Micromagentic simulation and Lorentz microscopy of curved ferromagnetic nanowires

Hristo Gergov

School of Physics and Astronomy
College of Science and Engineering
University of Glasgow

Submitted in fulfilment of the requirements for the Degree of Doctor of Philosophy

September 2024

Contents

List of Figures

Abstract

Ferromagnetic domain walls can be used to encode and propagate information in novel spintronic devices. However, to realize these devices, different materials and geometries that support stable and mobile domain walls need to be investigated. This thesis contributes to the effort by examining domain walls in nanowires with curved profiles using micromagnetic simulations and Lorentz microscopy.

Domain walls in head-to-head cylindrical segment nanowires were explored using micromagnetic simulations. The energy density (a measure of stability) of the resulting domain walls was recorded for each combination of nanowire geometry (half versus quarter cylinder) and nanowire composition (Fe vs. Co). A domain wall with a potential for the field of spintronics due to its narrow extent and strong out-of-plane component was found to stabilise in a wide range of nanowire sizes in both Co and Fe nanowires. Additionally, the effect of the interfacial Dzyaloshinskii-Moriya interaction (iDMI), on the domain wall formation in quarter cylinder nanowires was examined. That resulted in the stabilisation of another promising Néel-like domain wall with a simple one-dimensional rotation of the magnetisation - the 1D wall. Throughout the entire simulation space, the extent of the different domain walls was measured and recorded. Simulated experimental Fresnel mode and differential phase contrast (DPC) images were calculated and used in the quantification of the domain walls comparing magnetisation profiles to those from integrated induction. Finally, the effect of electrostatic phase on DPC and Fresnel image contrast was examined with respect to domain wall characterisation and classification.

Focused electron beam induced deposition (FEBID) was used to deposit physical Co and Fe nanowires of varying width and thickness with a profile similar to the one studied with simulations. The deposition conditions were optimised to produce defined magnetic nanowires with as high saturation magnetisation as possible. Domain walls were successfully nucleated in said nanowires with the application of an external magnetic field and identified using Fresnel mode microscopy. Differential phase contrast (DPC) imaging was then used to obtain accurate maps of the magnetic induction of the nanowires showing a more clear picture of the structure of the different domain walls. Finally, a combination of transmission electron microscopy (TEM), atomic force microscopy (AFM) and DPC imaging was used to obtain a measure of the saturation induction of the FEBID structures and thus infer their elemental purity.

1 Basics of Magnetism

Contents

1.1 Introduction

Over the recent decades, the study of magnetism on the nano and micro scales has been motivated by many impactful discoveries some of which have led to important applications both in academia and in industry. Examples of them include magnetic memories based on the Giant-Magneto-Resistance effect [1] and magnetic nanoparticle sensors used in biology [2]. In particular, ferromagnetic domain walls (DWs) have garnered the attention of researchers due to their many applications in the field of spintronics. Some of these include magnetic racetrack memories [3], shift registers [4], and DW logic devices [5]. Most of this research has been focused on planar guides or structures, which restrict the geometry of the devices to simple rectangular shapes. However, the recent developments in novel fabrication methods like Focused Electron Beam Induced Deposition (FEBID) and chemical synthesis (electroplating) and an increasing demand for cheaper and more efficient data storage schemes have made the extension of micromagnetic research to 3 dimensions not only possible but also necessary [6]. This extension brings to light new unusual spin configurations, which exhibit interesting physical effects. Cylindrical nanowires, in particular, have attracted a lot of attention [7]. They exhibit many properties similar to their planar counterparts, but numerical models and simulations have predicted that their curved geometry may counteract one of the major limiting factors in building successful magnetic nanowire devices [8] [9] - the Walker breakdown [10], which is characterised by an abrupt reduction in DW mobility and loss of DW integrity at a specific applied spin-polarised current or magnetic field. Successfully suppressing this limiting factor may allow for the possibility of cheap and efficient data transport via magnetic DWs. This thesis aims to contribute to the search for highly mobile and compact DWs by exploring nanowire geometries with a curved profile and a broken circular symmetry. It will do so by mapping the parameter space of DW in such nanowires via micromagnetic simulation and an empirical study, uncovering new DWs and creating a baseline for further study of this previously unexplored nanowire geometry. The nanowire types studied here are first introduced in Chapter 2 and further described in Chapter 4 and 5. This chapter (Chapter 1), gives an overview of the principal of magnetism on the micro and nanoscales and highlights the most important interactions responsible for the formation of domains and DWs. Additionally, it provides some of the background theory on which the micromagnetic simulations presented in Chapter 4 are based.

1.2 Basics of ferromagnetism

Magnetic fields arise from the motion of electrical charges. On the atomic scale the origin of magnetism can be attributed to a combination of the orbital motion of electrons around the nucleus and to their intrinsic spin. Classically an electron in orbital motion gives rise to a magnetic moment $\mathbf{m_L}$ proportional to its angular momentum $\mathbf{L}$ [11]. The magnitude of the magnetic moment is given by equation 1.1.

$$\boldsymbol{\mu}_l = -\frac{e}{2m_e} \cdot \boldsymbol{L} \tag{1.1}$$

Where e is the electron charge, $\hbar$ is the reduced Planck's constant and m_e is the mass of the electron. In addition to their orbital motion, electrons also possess an intrinsic angular momentum which is independent of their orbital motion. This quantity is the so-called electron spin and is often denoted as $\mathbf{S}$ [12]. The magnetic moment generated by the electron spin is given by equation 1.2.

$$\boldsymbol{\mu}_s = -g_s \frac{e}{2m_e} \cdot \boldsymbol{S} \tag{1.2}$$

Where g_s is a proportionality constant called the g-factor. For simplicity the two equations can be combined to give equation 1.3.

$$\boldsymbol{\mu} = \gamma \mathbf{J} \tag{1.3}$$

Where γ is a proportionality constant known as the gyromagnetic ration and $\mathbf{J}$ is the total angular momentum of the electron given by $\mathbf{J} = \mathbf{L} + \mathbf{S}$. This semi-classical description of atomic magnetism is achieved by applying Ampere's law to Bohr's model of the atom. A more complete description requires the full quantum mechanical treatment of the motion of electrons and the knowledge of the particular material's energy band structure. In a magnetic solid, there is a large number of magnetic moments, and it is, therefore, useful to define a quantity to describe their macroscopic behaviour. This is called the magnetisation $\mathbf{M}$ and is defined as the magnetic moment per unit volume. While in reality, $\mathbf{M}$ is a discrete quantity it can also be considered as a continuous function of time and position within the "continuum approximation" i.e. on a length scale large enough to make the graininess of individual magnetic moments insignificant. In linear magnetic materials, the relationship between the magnetisation and an externally applied magnetic field $\mathbf{H}$ is described the

following relation 1.4.

$$\mathbf{M} = \chi_m \mathbf{H} \tag{1.4}$$

Where the proportionality constant χ_m is called the susceptibility of the material. Most materials acquire magnetisation parallel (paramagnetic, $\chi > 0$) or anti-parallel (diamagnetic, $\chi < 0$) to the direction of the applied field. There are also materials in which the relationship between **M** and **H** is not linear and the susceptibility is not a constant value, but rather dependent on the strength of the applied field. In such materials, the individual magnetic moments can spontaneously align with their neighbours resulting in a non-zero magnetisation at **H = 0**. Materials with these properties are called ferromagnetic and can have magnetic susceptibility 5 orders of magnitude larger than their diamagnetic and paramagnetic counterparts. The alignment of magnetic moments is the result of the Heisenberg exchange interaction, which is a quantum mechanical effect arising from the Coulomb interaction of identical neighbouring particles with overlapping wavefunctions. It is described by the following Hamiltonian [13]:

$$\hat{\mathscr{H}} = -\sum_{ij} \mathscr{J}_{ij} \mathbf{S_i} \cdot \mathbf{S_j} \tag{1.5}$$

where $\mathscr{J}_{ij}$ is the exchange constant, which is a measure of the strength of the interaction and the sum is over all magnetic moments $\mathbf{S_i}$. The sign of the exchange constant $\mathscr{J}_{ij}$ determines the preferred orientation of the magnetic moments. $\mathscr{J}_{ij} > 0$ is associated with a parallel alignment of moments and a ferromagnetic configuration, whereas $\mathscr{J}_{ij} < 0$ favours an antiparallel configuration thus giving rise to antiferromagnetism [14]. For simplicity any further references to the exchange interaction will refer to ferromagnetic materials, as such materials are studied in this thesis. An intuitive and graphical way to describe the response of magnetic moments to an applied magnetic field is the hysteresis loop, an annotated example of which can be seen in Figure 1.1a. In the image one can see how the magnetisation (**M**) responds to the applied field (**H**) by increasing up to the maximum possible value called the saturation magnetisation M_s (1.1b. When the magnetic field **H** is switched off the magnetisation drops to a non-zero value called the remanent magnetisation ($\mathbf{M}_r$) and can be brought back down to 0 only after the application of the coercive field $\mathbf{H}_c$. It is important to note that the shape of the hysteresis loop is dependent on the size and shape of the magnetic sample. Additionally, the hysteresis loop shown here describes

major hysteresis, which illustrates the magnetic states of material starting from and ending with full magnetisation saturation [15]. As opposed to that minor hysteresis loops can be used to map the magnetic response to magnetic fields insufficiently strong to cause full saturation [16]. An important quantity mentioned several times above is saturation magnetisation. This is an intrinsic property of the material that varies with temperature. The relationship between the two for a ferromagnetic material is presented in Figure 1.1b. On the graph, we can see that the value of the saturation magnetisation is highest at T = 0 and declines with increasing temperate until it reaches zero at the Curie Temperature T_c [17]. Above this point, the thermodynamic energy is sufficient to cause the magnetic moments to misalign resulting in a paramagnetic behaviour. In the regions below the line, the magnetic moments in ferromagnetic materials can spontaneously align with each other. The materials considered in this thesis - Co and Fe are ferromagnetic at room temperature and have T_c of 1400 K and 1043 K.

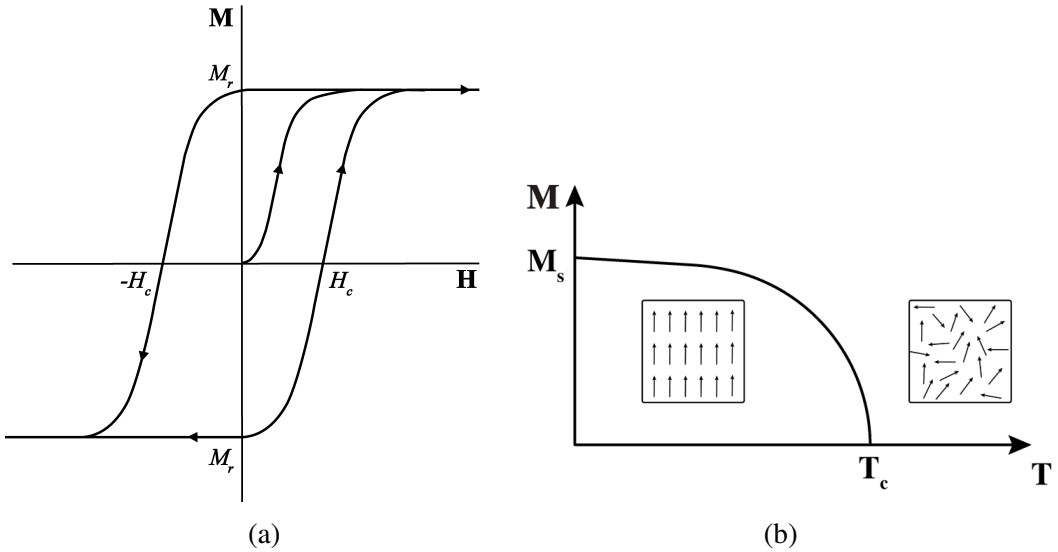

Figure 1.1: (a) Hysteresis Loop showing the response of Magnetisation M_s to an applied Magnetic Field H with remanent magnetisation M_r and coercive field H_c (b) Temperature dependence of saturation magnetisation showing the loss of ferromagnetic ordering above the Curie Temperature T_c.

1.3 Magnetic energy terms

While Heisenberg exchange is crucial to understanding ferromagnetism, energy contributions from different sources need to be considered in order to obtain a more comprehensive picture of the magnetisation configuration of a material. In ferromagnetic materials the total internal energy of the system U is the sum of several competing interactions. They are caused by separate physical phenomena but collectively contribute to the magnetic configuration of the material. Depending on the particular system the contribution of these phenomena can vary. The total internal energy U can be written as:

$$U = E_{ex} + E_m + E_k + E_z \tag{1.6}$$

where E_{ex} is the exchange energy, E_m is the magnetostatic energy, E_k is related to crystalline anisotropy and E_z is the Zeeman energy. There can be other interactions that contribute to the total energy of the system (e.g. magnetostriction), but they are not relevant to the systems studied in this thesis - namely bulk Co and Fe nanowires. The relevant interactions will be individually discussed in this section and related to the framework of micromagnetism, whose basic premise is that the magnetisation $\mathbf{M}(\mathbf{r})$ and dipole field $\mathbf{H_d}(\mathbf{r})$ of a magnet are continuously varying functions of the position ($\mathbf{r}$) [11]. Micromagnetism is considered a semi-classical model of magnetism as it integrates essential quantum mechanical effects like the exchange interaction to a continuous classical description of magnetisation. The main assumption of the model is that the length scale over which local neighbouring magnetic moments remain parallel is much larger than the inter-atomic lattice spacing for the given material [18] and thus atomic scale variation in the magnetic structure of the material can be ignored. This approach simplifies the mathematical treatment of complex magnetic interactions, such as exchange coupling, magnetostatic energy, and anisotropy effects, allowing for the analysis of domain structures, magnetic excitations, and dynamic processes within the material. By using this approximation, micromagnetic simulations, like the ones presented in Chapter 4, can effectively model and predict the behavior of magnetic materials. Further information on the theory on micromagnetism and micromagnetic simulations is presented in 1.5

1.3.1 Exchange energy

As described in Section 1.2 the ferromagnetic exchange is responsible for the parallel alignment of spins [13]. The strength of this interaction rapidly decreases with increased distance between atoms. Therefore, only the interactions between an atom and its nearest neighbours are sufficient to approximate the energy contribution given by equation 1.7.

$$E_{ex} = -2JS^2 \sum_{ij} cos\phi_{ij} \tag{1.7}$$

Here S is the magnitude of the spin vector and ϕ_{ij} is the angle between neighbouring spins and J is the so-called exchange integral. By assuming a continuous magnetisation unit vector $\mathbf{m}(\mathbf{r})$ such that $\mathbf{M}(\mathbf{r}) = M_s\mathbf{m}(\mathbf{r})$ and a small angle ϕ_{ij} between m_i and m_j one can re-express equation 1.7 the micromagnetic framework as follows:

$$E_{ex} = A \int_v ((\nabla m_x)^2 + (\nabla m_y)^2 + (\nabla m_z)^2) dV \tag{1.8}$$

Here the vector **m** represents the components of the magnetisation and A is the exchange stiffness constant given by equation 1.9.

$$A = \frac{JS^2}{a} n \tag{1.9}$$

In the equation above n is a number relating to the number of atoms in the unit cell and a is the lattice constant. An important quantity associated with the exchange energy is the exchange length l_{ex}, which is an approximation of the distance over which the magnetisation within a sample remains uniform [19]. It varies for different materials and is given by:

$$l_{ex} = \sqrt{\frac{2A}{\mu_0 M_s^2}} \tag{1.10}$$

In the equation above μ_0 is the permeability of free space and M_s^2 is the saturation magnetisation of the material. In soft magnetic materials, l_{ex} typically ranges from 2-5 nm and can be related to the sizes of the smallest entities of magnetisation.

1.3.2 Dzyaloshinksii-Moriya interaction

Another type of exchange interaction is the antisymmetric exchange, also known as the Dzyaloshinksii-Moriya Interaction (DMI) [20]. In materials where it is present, DMI competes with the standard Heisenberg exchange resulting in a gradual rotation (or canting) of the magnetic moments around the $\boldsymbol{D}_{ij}$ vector, the angle of which is dependent on the ratio between the two energies. Typically the strength of DMI is approximately 10 - 20% that of the Heisenberg exchange [21][22]. The microscopical cause for DMI is strong spin-orbit coupling (SOC) between two neighbouring magnetic atoms and a third non-magnetic one. This configuration can be seen in Figure 1.2. The term SOC refers to a relativistic interaction between the electron's spin and its orbital motion. The result is a slight change of the total angular momentum of the electron **J** depending on whether the spin is aligned with or against the orbital motion [23].

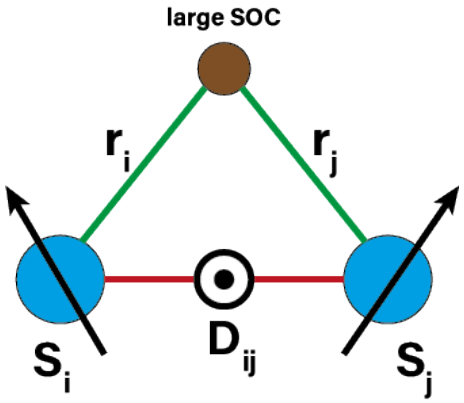

Figure 1.2: DMI interaction: Spin-orbit coupling (SOC) from heavy metal atom (brown) causes misalignment of between neighbouring spins (blue).$\boldsymbol{D}_{ij}$ vector points out of the page.

Energy contributions from DMI can be calculated using the Hamiltonian in equation 1.11

$$\hat{\mathscr{H}}_{\mathbf{dmi}} = -|\mathbf{D}_{ij}| \cdot \mathbf{S_i} \times \mathbf{S_j} \tag{1.11}$$

Where S_i and S_j are neighbouring spins and $\boldsymbol{D}_{ij}$ is the vector resulting from the strong spin-orbit coupling that causes the spins to stray from the parallel configuration resulting from the conventional exchange. Depending on atomic properties two different kinds of DMI can exist - bulk and interfacial (iDMI). The former is determined by the symmetry

in atomic lattice structures and arises in crystal structures which lack inversion symmetry i.e. in crystal structures that do not remain the same if inverted through a central point. An example of that is MnSi of the B20 crystal group [24]. The latter is present at interfaces between a magnetic material and heavy metals with strong spin-orbit coupling [25]. Examples include Pt/Co where the $\boldsymbol{D}_{ij}$ vector is positive [26] and Ir/Co interfaces [27] where the $\boldsymbol{D}_{ij}$ vector is negative. In such structures, the $\boldsymbol{D}_{ij}$ vector is parallel to the interface. Figure 1.3 shows a schematic of the magnetic moment rotation caused by positive and negative interfacial DMI. As stated before, DMI directly competes with the Heisenberg exchange and does not exist on its own. Its contribution to the energy of the magnetic system in the micromagnetic model is highly dependent on the crystal symmetries of the system and the particular expressions are derived using Lifshitz invariants [28] [29]. Equations 1.12 and 1.13 show the energy contributions for DMI in both thin film with interfacial DMI in the *x-y* plane and in materials in materials with bulk DMI respectively [30]. Typical values of the strength of iDMI in Ir/Ci and Pt/Co interfaces range from 1 - 2 $\mathrm{mJ/m^2}$ [31] [32]. DMI is essential in the stabilisation of chiral magnetic structures like magnetic skyrmions [33], which are particle like, topologically protected magnetic structures, and chiral DWs [34], which have applications in high-density data storage [35]. In this context the term chirality refers to the "handedness" of the magnetic structure and more precisely the direction of canting of the spins. For example a clockwise canting of the spins would result in a magnetic structure with different chirality compared to a counter-clockwise canted one. It can also induce exotic dynamic properties and transport phenomena with possible applications in future spintronic devices [36]. Some examples of that are provided in Chapter 2. The effects of interfacial DMI in Fe and Co nanowires are explored using micromagnetic simulations in Chapter 3.

$$E_{iDMI} = D(\mathbf{m} \cdot \nabla m_z - m_z \nabla \cdot \mathbf{m}) \tag{1.12}$$

$$E_{bulk} = D\mathbf{m} \cdot (\nabla \times \mathbf{m}) \tag{1.13}$$

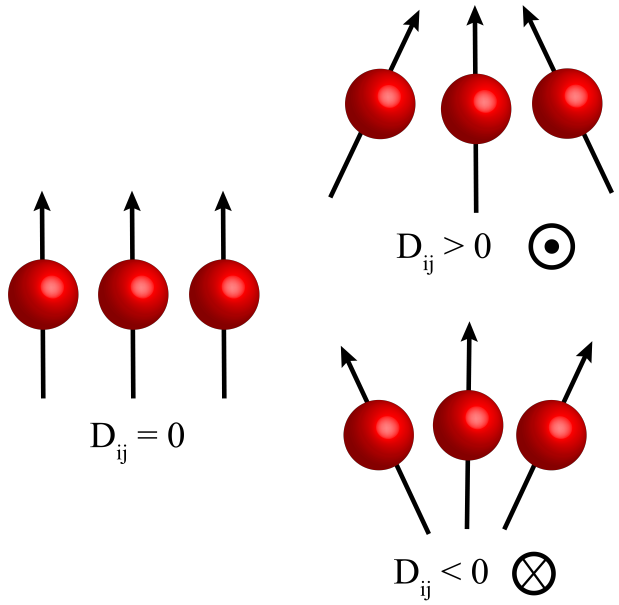

Figure 1.3: Magnetic moment rotation at a heavy metal / ferromagnetic material interface caused by positive (top) and negative magnitude of the $\boldsymbol{D}_{ij}$ vector

1.3.3 Magnetocrystalline anisotropy

Ferromagnetic materials can have a crystal structure that energetically favours the alignment of magnetisation parallel to a particular direction. This is called magnetocrystalline anisotropy and is also caused by the spin-orbit coupling phenomenon defined in Section 1.3.2. Here the magnetic moments become coupled to a specific crystal direction creating an energetically favourable direction of the magnetisation. This energetically favourable direction is commonly referred to as the easy axes. Depending on the crystal structure a material may have one or many easy axes. The energy contributions from magnetocrystalline anisotropy are dependent on an anisotropy constant K and the unit vector $\hat{e}$ pointing in the direction of the easy axis. The two most common examples are uniaxial anisotropy, where only one easy axis exists and cubic anisotropy, in which three orthogonal axes are the easy ones. Macroscopic energy contributions from magneto-crystalline anisotropy are often minimal for polycrystalline samples like those studied in this thesis due to the random directionality of individual crystallites. However, crystalline anisotropy can still result in small local variations in the magnetisation direction called magnetisation ripple [37].

1.3.4 Magnetostatic energy

In a magnetic material, each moment creates a dipole field. The macroscopic interactions between the dipole fields give rise to both internal (demagnetising field $\mathbf{H_d}$) and external (stray field) magnetic fields. $\mathbf{H_d}$ can be regarded as the gradient of some scalar potential $\Phi_\mathbf{r}$ i.e. $\mathbf{H_d} = -\nabla\Phi(\mathbf{r})$ and in an ideal uniformly magnetised sample it acts in a direction anti-parallel to the magnetisation. The form of the scalar potential for an ideal magnetic body, where the magnetisation is strictly defined in some region (V) and smoothly decays outside that region (δV) is given by equation 1.14 [38].

$$\Phi(\mathbf{r}) = \frac{1}{4\pi}\left(\int_V -\frac{\nabla'\cdot\mathbf{M}(\mathbf{r}')}{|\mathbf{r}-\mathbf{r}'|}d\mathbf{r}' + \int_{\delta V}\frac{\mathbf{n}\cdot\mathbf{M}(\mathbf{r}')}{|\mathbf{r}-\mathbf{r}'|}dS'\right) \tag{1.14}$$

Where the first integral is over the volume of the magnetic body, the second is over its surface and $\mathbf{n}$ is a unit vector normal to the surface. The energy associated with the demagnetising field $\mathbf{H_d}$ can be calculated by integrating over all magnetic moments in the sample volume V.

$$E_m = -\frac{\mu_0}{2}\int_V \mathbf{M}\cdot\mathbf{H_d}dV \tag{1.15}$$

In micro- and nanoscale magnets this energy is reduced when the effective magnetostatic surface and volume charges tend to zero. In magnetic samples, this is achieved by splitting the sample into regions of opposing magnetisation as pictured in Figure 1.4. The first schematic in the Figure (1.4 a)) displays a uniformly magnetised state in which the exchange energy is minimized due to the parallel alignment of neighbouring spins. This, however, comes at the expense of a large surface charge and an associated demagnetising energy. For these reasons, such a state is only stable within a strong external magnetic field or in samples with very high uniaxial anisotropy. If that is not the case the uniform state will split into oppositely pointing domains as pictured in Figure 1.4 b). There the demagnetising energy is significantly reduced, this time at the expense of increased exchange energy contribution. Such a state is associated with a high magnetocrystalline anisotropy along the long direction of the magnetic element. Without it, the magnetisation of the sample will form a flux closure state where the demagnetising energy is dramatically reduced for a comparatively smaller increase in the exchange energy.

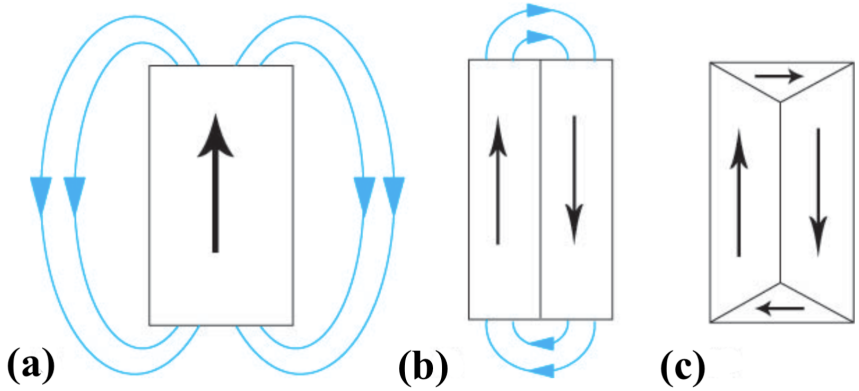

Figure 1.4: **a)** - Non-zero macroscopic magnetisation and a large related demagnetising field. **b)** - Magnetisation is split in domains to reduce demagnetising field .**c)** - Flux closure state.

It's worth noting that in smaller samples (on the order of the exchange length of the sample material) the increase in exchange energy makes the existence of flux closures impossible and the preferred magnetisation direction is along a single direction as depicted in Figure 1.4 c).

The magnetostatic energy is also the source of magnetic shape anisotropy. Much like magnetocrystalline anisotropy, shape anisotropy is characterised by a favourable direction of magnetisation. In the absence of any other interactions, the preferred magnetisation direction will be along the long axis. A typical example used to illustrate shape anisotropy is a magnetic ellipsoid - Figure 1.5. When the ellipsoid is magnetised along a direction opposing charges build up at the surfaces resulting in an internal field $\mathbf{H_d}$. When the magnetisation is along the long axis of the ellipsoid the distance between opposite charges is larger and $\mathbf{H_d}$ is reduced resulting in a more energetically favourable configuration. Within perfectly spherical samples the value of the $\mathbf{H_d}$ field is the same for magnetisation direction, making it the only geometry with no shape anisotropy. The energy contribution from shape anisotropy per unit volume in a thin magnetic film is given by equation 1.16.

$$E_{shape} = \frac{1}{2}\mu_0 M_s^2 cos^2(\theta) \tag{1.16}$$

Where the magnetisation is assumed to be with the magnitude of the saturation magnetisation of the material at an angle of θ to the film normal. Shape anisotropy competes with

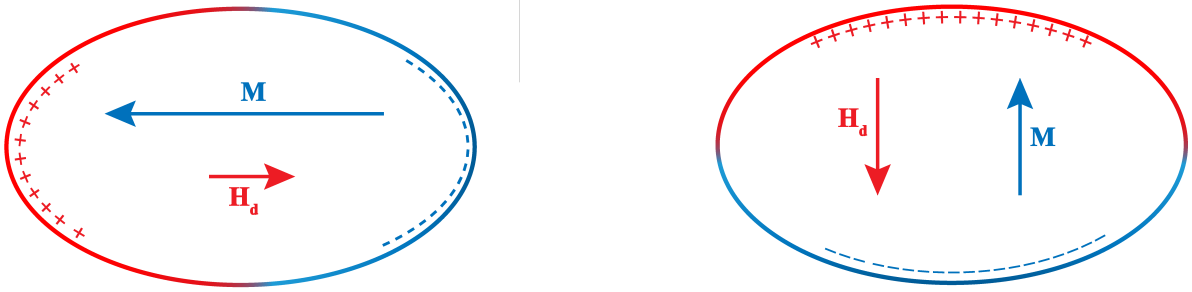

Figure 1.5: Shape Anisotropy in an elliptical element. The size of the arrows indicates the relative strength of the fields. In this case, magnetisation along the long axis is favourable.

magnetocrystalline anisotropy resulting in an effective anisotropy term K_{eff}. It is also an important factor in the formation of DWs in both planar and 3D magnetic nanowires.

1.3.5 Zeeman energy

The Zeeman energy is the result of an interaction of the magnetisation with an external field H_{ext}. It is given by equation 1.17 and is minimized when the individual magnetic moments align parallel with the external field lines.

$$E_z = -\mu_0 M_s \int \mathbf{H_{ext}} \cdot \mathbf{m} dV \tag{1.17}$$

Applying an external field causes magnetic domains aligned with the field direction to grow. At sufficiently high H_{ext} all the moments in the sample are aligned with field making resulting in an effectively saturated magnetisation.

1.4 Magnetic domains and domain walls in thin films

In ferromagnetic materials, the competition and interplay between the previously described interactions result in the formation of regions with uniform magnetisation called magnetic domains [39]. For magnetic samples with sizes comparable to the exchange length of the material l_{ex} single domain states are often favourable because of the relative strength of the Heisenberg exchange interaction [40]. As sample sizes increase so do the relative energy contributions of the dipolar interaction, magnetocrystaline and shape anisotropies. As

described in the previous section multiple magnetic domains are a way to minimize these energy contributions. The transition regions between domains, where magnetisation gradually changes direction, are called DWs. DW widths in continuous thin ferromagnetic films can vary between 1-200 nm [41]. They also have an associated energy cost related to them, which is proportional to the area occupied by the DW. There are two main types of DWs appearing in thin ferromagnetic films - Bloch and Néel, diagrams of which are shown in Figure 1.6. In Bloch walls the magnetisation rotates perpendicularly to the domain boundary as pictured in Figure 1.6 a). Bloch walls are also divergence-free and have no internal magnetostatic energy associated with the wall structure. They appear in thicker magnetic films and bulk materials. There are magnetic charges associated with Bloch walls at the top and bottom sample surfaces (indicated in Figure 1.6 as + and - signs), but for thicker samples, the charges are sufficiently separated to minimize the stray field contributions. As sample size decreases and surface charges are brought closer together the stray fields increase and the Bloch wall becomes more unfavourable. The critical point at which Néel walls become more favourable occurs at varying film thicknesses for different materials. For permalloy, which is an alloy of Nickel and Iron commonly used as an example, it is around 30 nm [13]. Néel walls are characterised by an in-plane rotation of magnetisation Figure 1.6 b). This type of rotation causes volume charges to build up within the material. Unlike Bloch walls Néel walls have a divergent magnetisation. Near the transition between Bloch and Neél walls a combination of the two can occur. This is called a cross-tie wall and is characterised by alternating vortex/antivortex pairs [42].

DWs can be propagated across mediums using external magnetic fields or spin-polarised currents. An important parameter associated with DW motion is DW mobility, which is defined as the rate of change of wall velocity under the influence of an external magnetic field. DWs with high mobility and velocities are highly desirable in the field of spintronics. An example of such a wall is a Neél wall with a fixed chirality. It has been shown experimentally that such walls can reach speeds up to 700 m/s in ferromagnetic multilayers [43], which is an order of magnitude faster than other DWs (e.g. the Bloch wall) [44], therefore making them ideal candidates for spintronic applications. Interfacial DMI has been shown to promote the formation Néel type walls in ferromagnetic multilayers [34] and that is why the effect of iDMI is also considered in this thesis. Section 4.3.2 in Chapter 4 explores the effect iDMI has on certain cylindrical segment Co and Fe nanowires through micromagnetic simulations.

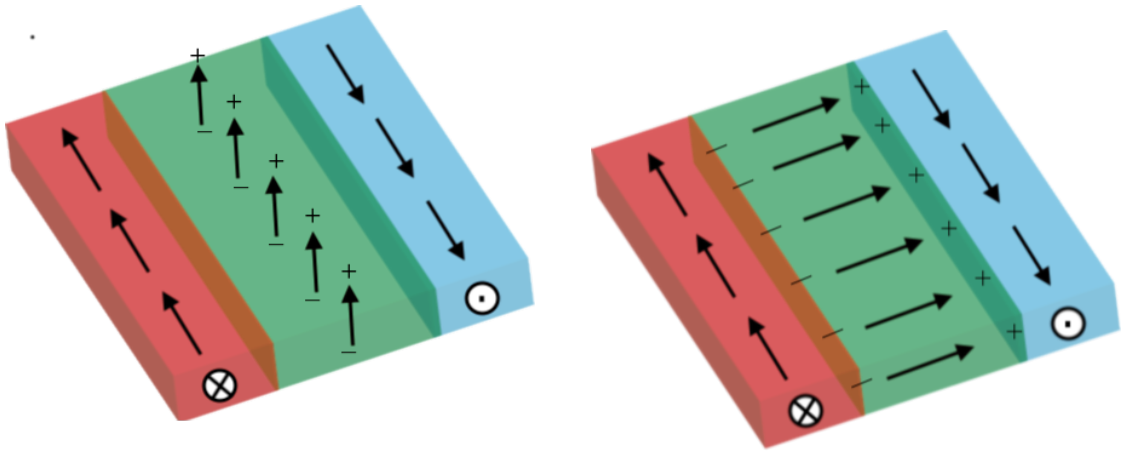

(a) Bloch DW (b) Néel DW

Figure 1.6: Diagram of the main DW types observed in thin magnetic films. Oppositely pointing domains are colored blue and red while the DW is colored green.

1.5 Micromagnetic simulations

Simulations are an essential tool for the study of magnetic structures on the nano and micro scales. They allow the user to explore and quantify different magnetisation states that can occur in a vast parameter space of sample geometry and composition. Additionally, they can be used to model magnetic behaviour and used to predict and interpret experimental results. Most simulation packages are based on the framework of micromagnetism which was discussed in earlier sections. Simulation packages utilising the micromagnetic approach are widely used because they allow the user to resolve subtle magnetisation changes in the transition regions between domains. Atomistic models [45] exist that provide a more comprehensive picture, but are not practical for the study of structures larger than a few nanometers. In the micromagnetic framework, the time evolution of magnetisation dynamics is calculated using the Landau-Lifshitz-Gilbert equation - (1.18). This is a phenomenological differential equation which calculates the response of the magnetisation to a torque created by an effective field [46].

$$\frac{\partial \mathbf{M}}{\partial t} = -\gamma \mathbf{M} \times \mathbf{H}_{eff} - \frac{\gamma \alpha}{|\mathbf{M}|} \mathbf{M} \times (\mathbf{M} \times \mathbf{H}_{eff}) \tag{1.18}$$

In the equation above γ is the ratio between a particle's magnetic moment and its angular moment (gyromagnetic ratio), α is the damping coefficient and $\mathbf{M}$ is the normalised magnetisation vector. $\mathbf{H}_{eff}$ is the effective magnetic field and can have contributions from the magnetostatic, exchange, anisotropy, DMI fields. It is given by:

$$\mathbf{H}_{eff} = \frac{1}{\mu_0}\frac{dU}{d\mathbf{M}} \tag{1.19}$$

where U is the total energy functional. The LLG equation has two terms, the first of which describes the rotation of the magnetisation $\mathbf{M}$ around the effective field $\mathbf{H_{eff}}$. The second term is related to damping and energy dissipation and describes the motion of magnetisation towards aligning with $\mathbf{H_{eff}}$. The motion caused by the two terms is illustrated in Figure 1.7. Most micromagnetic software packages, and most importantly the one used in this thesis, solve the LLG equation by subdividing the simulation space into discrete volume elements (cells) and assigning them a magnetisation vector. The LLG equation is then solved numerically for each cell. The simulation proceeds in discrete time steps, with the magnetization updated at each time step based on the current magnetization configuration and the effective magnetic field acting on each cell. The term influencing the effective magnetic field are described in Section 1.3. There are two main approaches to the subdivision of the simulation space - finite difference and finite element. In the first approach, each volume is cuboid-shaped. This makes the approach very efficient at simulating magnetic thin films or other shapes with sharp edges. In the finite element approach the volume elements are irregular tetrahedra, which allows for the simulation of more complex shapes at the cost of computational efficiency. It is important to note that for either of the approaches to yield significant and accurate results the size of the cell must be considered carefully. Usually, the exchange length (equation 1.10) of the simulated material is used as an upper limit on cell size [47]. In this thesis, the finite difference-based and GPU-accelerated Mumax3 was used for micromagnetic simulations of magnetic nanowires because it offered the best compromise between computational efficiency and accuracy. The simulations performed in this thesis do not take thermal effects into account [48]. This is not relevant to static simulations which aim to find the lowest energy state of the system. Additionally, the Curie temperatures of the simulated materials (1200-1600K for Co and 1200K for Fe [49]) are high enough to make any thermal contributions negligible [50]. In dynamic situations thermal effects may have a bigger impact on things like the field required to reverse

magnetisation or depin a magnetic DW. In addition to the lack of thermal effects, another limitation in the micromagnetic model is the assumption of material uniformity across the simulated structure. This limits the accuracy of the model for structures with inhomogeneities or defects. Furthermore since the results obtained from the micromagnetic model rely heavily on the material parameters used, significant care must be taken when choosing them. Further discussion on the micromagnetic package and different models used for this thesis are given in Chapter 4.

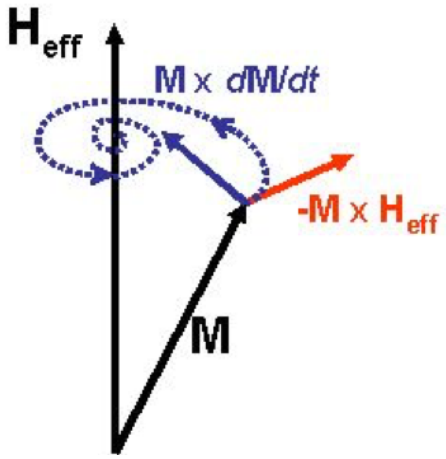

Figure 1.7: Visual representation of the precession (red) and damping (blue) terms of the LLG equation.

1.6 Thesis outline

The thesis continues with Chapter 2 where the focus is on ferromagnetic nanowires and their applications. There planar and cylindrical nanowires are introduced along with the DW structures they exhibit. Additionally, a brief introduction to the main spintronic applications of ferromagnetic nanowires and DWs is provided in order to highlight the motivation and provide some context for the research presented in this thesis. Chapter 3 delves into the experimental methods employed for this thesis. It provides a detailed outline of the fabrication techniques used for Co and Fe magnetic nanowires, including focused electron beam-induced deposition (FEBID) and DC magnetron sputtering. The chapter also explores the characterization techniques used to analyze these nanowires, encompassing both conventional and Lorentz mode electron microscopy and providing a theoretical

background where necessary. Chapter 4 presents a micromagnetic study of curved profile nanowires. This includes static simulations used to determine the various DW configurations that can be supported by half and quarter cylinder (HC and QC) nanowires along with a study of the effect of iDMI on QC nanowires. In order to supplement the micromagnetic study, simulated electron microscopy images were calculated for the different DW types and used in Chapter 5 to aid with the interpretation of TEM images of physical nanowires. The chapter results are summarized in a series of DW energy diagrams and provide a baseline picture of the DW types that can be expected in curved profile nanowires. Two of the observed DWs showed particularly promising characteristics, namely, a narrow profile and a simple spin structure, both highly desirable in the field of spintronics. Chapter 5 presents an empirical study of curved profile Co and Fe nanowires from fabrication via focused electron beam induced deposition (FEBID) through to structural and magnetic characterisation using electron microscopy. The fabricated nanowires, while not ideally QC and HC display similar cuvature and aspect ratios and are therefore comparable in shape to the ones simulated in Chapter 4. Their main magnetic characterisation was performed using Lorentz microscopy and the chapter presents a series of images of the DWs that were nucleated in the physical nanowires. Additionally, the chapter presents a quantitative DPC study used to obtain high - resolution images of the DWs and information of saturation induction and purity. Chapter 6 provides some final conclusions and discusses some of the pitfalls of the research along with some potential avenues of further research.

References

[1] Y. Tian and S. Yan. Giant magnetoresistance: history, development and beyond. *Science China Physics, Mechanics and Astronomy*, 56:2–14, 2012.

[2] A. Sobczak-Kupiec, J. Venkatesan, A. A. AlAnezi, D. Walczyk, A. Farooqi, D. Malina, S. H. Hosseini, and B. Tyliszczak. Magnetic nanomaterials and sensors for biological detection. *Nanomedicine: Nanotechnology, Biology and Medicine*, 12: 2459–2473, 2016.

[3] S. P. Parkin, M. Hayashi, and L. Thomas. Magnetic domain-wall racetrack memory. *Science*, 320(5873):190–194, 2008.

[4] J. Franken, H. Swagten, and B. Koopmans. Shift registers based on magnetic domain wall ratchets with perpendicular anisotropy. *Nature Nanotechnology*, 7:499–503, 2012.

[5] B. Dieny, R. C. Sousa, J. Hérault, C. Papusoi, G. Prenat, U. Ebels, D. Houssameddine, B. Rodmacq, S. Auffret, L. Prejbeanu-Buda, M. C. Cyrille, B. Delaet, O. Redon, C. Ducruet, J. P. Nozieres, and L. Prejbeanu. *Spintronic Devices for Memory and Logic Applications*, volume 19, pages 107–127. 2011.

[6] A. Fernández-Pacheco, R. Streubel, O. Fruchart, R. Hertel, P. Fischer, and R. P. Cowburn. Three-dimensional nanomagnetism. *Nature Communications*, 8:15756, 2017.

[7] M. Yan, A. Kákay, S. Gliga, and R. Hertel. Beating the Walker limit with massless domain walls in cylindrical nanowires. *Physical Review Letters*, 104:057201, 2010.

[8] J. A Fernandez-Roldan, A. De Riz, B. Trapp, C. Thirion, M. Vazquez, J. C. Toussaint, O. Fruchart, and D. Gusakova. Modeling magnetic-field-induced domain wall propagation in modulated-diameter cylindrical nanowires. *Scientific Reports*, 9:5130, 2019.

[9] M. Schoebitz, A. De Riz, S. Martin, S. Bochmann, C. Thirion, J. Vogel, M. Foerster, L. Aballe, T. O. Mentec, A. Locatelli, F. Genuzio, S. Le-Denmat, L. Cagnon, J. C. Toussaint, D. Gusakova, J. Bachmann, and O. Fruchart. Fast domain wall motion governed by topology and oersted fields in cylindrical magnetic nanowires. *Physical Review Letters*, 123:217201, 2019.

[10] A. Mougin, M. Cormier, J. P. Adam, P. J. Metaxas, and J. Ferré. Domain wall mobility, stability andWalker breakdown in magnetic nanowires. *Europhysics Letters (EPL)*, 78:57007, 2007.

[11] J. M. D. Coey. *Magnetism and magnetic materials*. Cambridge University Press, 2009.

[12] E. Merzbacher. *Quantum Mechanics*. J. Wiley & Sons, 3rd edition, 1998.

[13] A. Aharoni. *Introduction to the theory of ferromagnetism*. Oxford University Press, 2000.

[14] L. D. Landau. A possible explanation of the field dependence of the susceptibility at low temperatures. *Phys. Z. Sowjet*, 4:675, 1933.

[15] X. Liu, A. Berger, and M. Wuttig. Stability of the perpendicular magnetic anisotropy of ultrathin Ni films on Cu(100) upon multiple magnetization reversals. *Physical Review B*, 63:144407, 2001.

[16] D. Quach, D. Pham, D. Ngo, T. Phan, S. Park, S. Lee, and D. Kim. Minor hysteresis patterns with a rounded/sharpened reversing behavior in ferromagnetic multilayer. *Scientific Reports*, 8:4461, 2018.

[17] Charles K. *Introduction to Solid State Physics*. J. Wiley & Sons, 6th edition, 1986.

[18] C. Abert. Micromagnetics and spintronics: models and numerical methods. *The European Physical Journal B*, 92:120, 2019.

[19] M. Stano and O. Fruchart. *Magnetic nanowires and nanotubes)*, volume 27. Elsevier, 2018.

[20] I. Dzyaloshinsky. A thermodynamic theory of weak ferromagnetism of antiferromagnetics. *Journal of Physics and Chemistry of Solids*, 4:241–255, 1958.

[21] A. Fert and P. M. Levy. Role of anisotropic exchange interactions in determining the properties of spin-glasses. *Physical Review Letters*, 44:1538–1541, 1980.

[22] T. Moriya. Anisotropic superexchange interaction and weak ferromagnetism. *Physical Review*, 120:91–98, 1960.

[23] T. H. Llewellyn. The motion of the spinning electron. *Nature*, 117(2945):514, 1926.

[24] M. Bornemann, S. Grytsiuk, P. F. Baumeister, M. dos Santos Dias, R. Zeller, S. Lounis, and S. Blügel. Complex magnetism of B20-MnGe: from spin-spirals, hedgehogs to monopoles. *Journal of Physics: Condensed Matter*, 31:485801, 2019.

[25] S. Heinze, K. von Bergmann, M. Menzel, J. Brede, A. Kubetzka, R. Wiesendanger, G. Bihlmayer, and S. Blügel. Spontaneous atomic-scale magnetic skyrmion lattice in two dimensions. *Nature Physics*, 7:713–718, 2011.

[26] H. Yang, A. Thiaville, S. Rohart, A. Fert, and M. Chshiev. Anatomy of Dzyaloshinskii-Moriya interaction at Co / Pt interfaces. *Physical Review Letters*, 115:267210, 2015.

[27] A. Hrabec, N. Porter, A. Wells, M. Benitez, G. Burnell, S. McVitie, D. McGrouther, T. A. Moore, and C. H. Marrows. Measuring and tailoring the Dzyaloshinskii-Moriya interaction in perpendicularly magnetized thin films. *Physical Review B*, 90:020402, 2014.

[28] A. N. Bogdanov, U. K. Rößler, M. Wolf, and K. H. Müller. Magnetic structures and reorientation transitions in noncentrosymmetric uniaxial antiferromagnets. *Physical Review B*, 66:214410, 2002.

[29] L. D. Landau, E. M. Lifšic, and L. P. Pitaevskij. *Statistical physics, Part 1*. Springer, 3rd edition, 2008.

[30] D. Cortés-Ortuño, M. Beg, V. Nehruji, L. Breth, R. Pepper, T. Kluyver, G. Downing, T. Hesjedal, P. Hatton, and T. Lancaster. Proposal for a micromagnetic standard problem for materials with Dzyaloshinskii–Moriya interaction. *New Journal of Physics*, 20:113015, 2018.

[31] Y. Ishikuro, M. Kawaguchi, N. Kato, Y. Lau, and M. Hayashi. Dzyaloshinskii-Moriya interaction and spin-orbit torque at the Ir/Co interface. *Physical Review B*, 99:134421, 2019.

[32] O. Boulle, S. Pizzini, D. de Souza Chaves, A. Locatelli, T.O. Menteş, A. Sala, L.D. Buda-Prejbeanu, O. Klein, M. Belmeguenai, Y. Roussigné, A. Stashkevich, S. M.

Chérif, L. Aballe, M. Foerster, M. Chshiev, S. Auffret, I. M. Miron, and G. Gaudin. Room-temperature chiral magnetic skyrmions in ultrathin magnetic nanostructures. *Nature Nanotechnology*, 11:449–454, 2016.

[33] W. Kang, Y. Huang, X. Zhang, Y. Zhou, and W. Zhao. Skyrmion-electronics: An overview and outlook. *Proceedings of the IEEE*, 104:1–22, 2016.

[34] A. Thiaville, S. Rohart, É. Jué, V. Cros, and A. Fert. Dynamics of Dzyaloshinskii domain walls in ultrathin magnetic films. *EPL (Europhysics Letters)*, 100:57002, 2012.

[35] R. Camley and K. Livesey. Consequences of the Dzyaloshinskii-Moriya interaction. *Surface Science Reports*, 78(3):100605, 2023.

[36] A. Hirohata, K. Yamada, Y. Nakatani, I. Prejbeanu, B. Diény, P. Pirro, and B. Hillebrands. Review on spintronics: Principles and device applications. *Journal of Magnetism and Magnetic Materials*, 509:166711, 2020.

[37] H. W. Fuller and M. E. Hale. Determination of magnetization distribution in thin films using electron microscopy. *Journal of Applied Physics*, 31:238–248, 1960.

[38] D. Griffiths. *Introduction to electrodynamics*. Pearson, 2013.

[39] R. Schäfer. *Magnetic Domains*, pages 391–434. Springer International Publishing, Cham, 2021.

[40] A. Hubert. *Magnetic domains : the analysis of magnetic microstructures*. Springer, 1998.

[41] R. H. Wade. The determination of domain wall thickness in ferromagnetic films by electron microscopy. *Proceedings of the Physical Society*, 79(6):1237, 1962. doi: 10.1088/0370-1328/79/6/318.

[42] K. L. Metlov. Simple analytical description for the cross-tie domain wall structure. *Applied Physics Letters*, 79:2609–2611, 2001.

[43] T. H. Pham, J. Vogel, J. Sampaio, M. Vaňatka, J. C. Rojas-Sánchez, M. Bonfim, D. S. Chaves, F. Choueikani, P. Ohresser, and E. Otero. Very large domain wall velocities

in Pt/Co/Gdox and Pt/Co/Gd trilayers with Dzyaloshinskii-Moriya interaction. *EPL (Europhysics Letters)*, 113:67001, 2016.

[44] M. Hayashi, L. Thomas, C. Rettner, T. Moriya, Y. B. Bazaliy, and S. S. P. Parkin. Current driven domain wall velocities exceeding the spin angular momentum transfer rate in permalloy nanowires. *Physical Review Letters*, 98:037204, 2007.

[45] R. Evans, W. Fan, P. Chureemart, T. A. Ostler, M. Ellis, and R. Chantrell. Atomistic spin model simulations of magnetic nanomaterials. *Journal of Physics: Condensed Matter*, 26:103202, 2014.

[46] T. L. Gilbert. Classics in magnetics a phenomenological theory of damping in ferromagnetic materials. *IEEE Transactions on Magnetics*, 40:3443–3449, 2004.

[47] J. Leliaert and J. Mulkers. Tomorrow's micromagnetic simulations. *Journal of Applied Physics*, 125:180901, 2019.

[48] A. Vansteenkiste, J. Leliaert, M. Dvornik, M. Helsen, F. Garcia-Sanchez, and V. Waeyenberge. The design and verification of MuMax3. *AIP Advances*, 4:107133., 2014.

[49] K. H. J. Buschow. *Encyclopedia of Materials: Science and Technology*. Elsevier, 2001.

[50] M. Hahn. Temperature in micromagnetism: cell size and scaling effects of the stochastic Landau–Lifshitz equation. *Journal of Physics Communications*, 3(7): 075009, 2019.

2 Ferromagnetic Nanowires

Contents

2.1 Introduction

The term ferromagnetic nanowire refers to a thin and long strip of magnetic material with at least one dimension in the nanometer scale. Generally, such structures possess high aspect ratios, with their length being much larger than their width or thickness [1]. In the absence of a strong magnetocrystalline anisotropy, this results in a single domain magnetisation state orientated along the length of the nanowire [2]. If a domain wall (DW) is "forced" to nucleate in such a nanowire either by external factors, e.g. a strong magnetic field or by modifying the nanowire geometry (adding notches, kinks, or other defects), the resulting state is generally a head-to-head/tail-to-tail configuration with two domains separated by a 180° DW that differs significantly from the simple Bloch and Néel DWs described in Chapter 1. The size, shape, type and stability of these is highly dependent on the size and geometry of the nanowire they occupy. As mentioned in Chapter 1 the nanowire geometries studied in this thesis are characterised by a curved profile and a broken circular symmetry. Figure 2.1 shows examples of this geometry in c) and d). It is clear from the image that these geometries lie somewhere in between planar (a)) and cylindrical (b)) nanowires. It is therefore crucial to understand the DWs that form in each of these, before introducing the cylindrical segment nanowires. A summary of the DWs that form in cylindrical and planar nanowires is presented in Sections 2.2 and 2.3 and provides important background info that is later used to in the classification of the DWs of the curved profiles nanowires explored in this thesis. Furthermore, several of the main applications of ferromagnetic nanowires are discussed in Section 2.4 in order to provide context and the main motivation for the work.

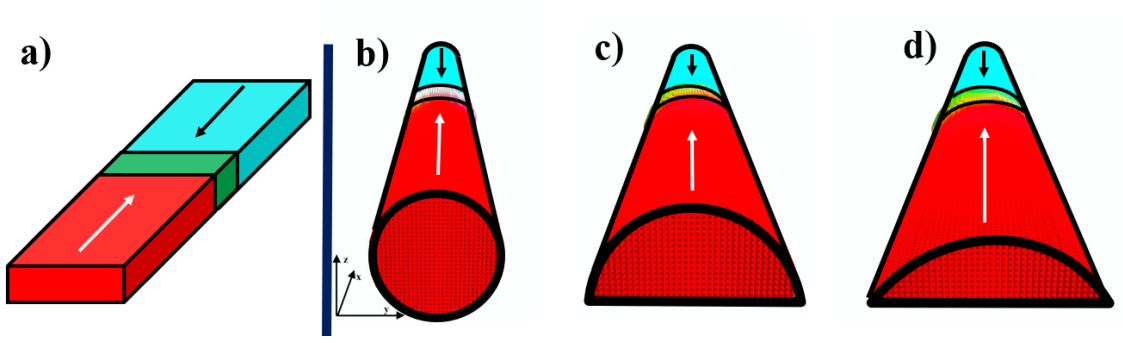

Figure 2.1: Example of the nanowires geometries. The images show a) planar, b) cylindrical, c) half-cylinder and d) quarter cylinder nanowires in head-to-head magnetisation configurations.

2.2 Planar nanowires

In the context of nanowires, the word planar is used to describe nanowires with a rectangular profile. These are the most researched nanowires and the easiest to fabricate with conventional methods like lithography [3], electrodeposition [4] and even ion beam irradiation [5]. The three main types of walls that can form in planar nanostrips are the following: transverse wall (TW), asymmetric transverse wall (ATW), and vortex wall (VW) [6] and can be seen in Figure 2.2. The TW can be likened to a pair of 90° Néel walls separated by a transverse magnetisation component (Figure 2.2 b)). This type of wall is formed in narrower and thinner (less than 50 nm wide for permalloy) magnetic nanowires because of its relatively low exchange cost. As the wire width increases, an asymmetrical component appears in the TW giving it a magnetisation component parallel to the wire axis (Figure 2.2 a)). This is the so called ATW, which is an almost mixed state between the pure TW and VWs but at intermediate dimensions. As the wire size increases further the VW becomes the most energetically favourable (Figure 2.2 c)). It is characterised by a rotation of the magnetisation around an out-of-plane component in the middle of the DW - the vortex core. Several more complex DW structures can occur in wider nanowires where the influence of shape anisotropy is reduced. These include extended, double and even triple vortices as described in [7]. Additionally, introducing notches, kinks or other imperfections within the geometry of the nanowire can not only act as pinning sites for the formation of DWs but also lead to a change in the DW geometry and size [8]. For example, periodic holes along the length of the nanowire have been shown to increase the achievable DW propagation speeds up to 900 m/s [9]. Further factors like sample composition, a strong external magnetic field or spin polarised current can also strongly affect the type and geometry of the DW [10].

2.3 Cylindrical nanowires

As opposed to their planar counterparts, the cylindrical nanowires have a circular profile which results into several unique properties. First of all, as mentioned in introductory chapter, the Walker breakdown phenomenon which limits DW propagation is suppressed [11] [12]. Secondly, cylindrical nanowires have been found to possess some magneto-chiral properties allowing them to support DWs which have different responses to magnetic field

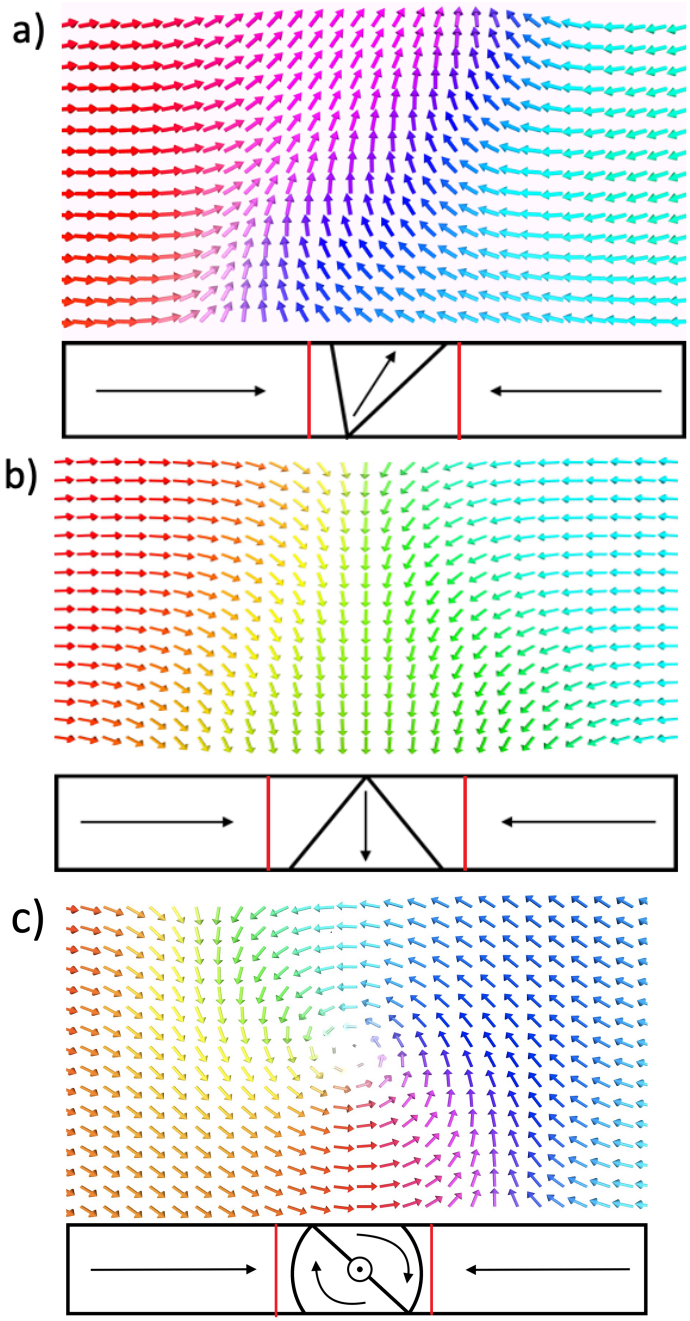

Figure 2.2: Spin vector diagrams and schematic illustrations of a) an ATW, b) a TW) and c a VW observed in planar nanowires in head-to-head magnetisation configuration. Red lines indicate position of the 2D vector plots.

depending on their chirality [11]. Finally, the curvature of the edge gives rise to the so-called curvature-induced DMI [13], which is characterised by spin canting without the presence of DMI inducing materials. This has been shown to promote chiral structures and skyrmion-like DWs and skyrmion tubes [14]. Several different methods exist to fabricate cylindrical nanowires including synthesizing the magnetic material within the pores of a nanoporous host material [15], electrodeposition within alumina templates [16], or using the FEBID technique [17], which is also employed in this thesis and will be discussed in more detail in Chapter 3. Similar to their planar counterparts, they can be magnetically characterised by many different methods including MOKE, magnetormetry, MFM and magnetic imaging within a transmission electron microscope (TEM) [18]. Their variable cross section, however, presents challenges to TEM imaging due to contrast from non magnetic sources due to thickness variations. A similar issue is present in the characterisation of cylindrical segment nanowires studied in this thesis and detail on that and how it can be addressed is available in Sections 3.5.2, 4.8.3 and 5.6.1. Finally, a very popular method utilised across the cylindrical nanowire research space is micromagnetic simulation as it provides a way to gain insight into specific problems and situations without the need for expensive fabrication and characterisation. In cylindrical nanowires, similar to planar nanowires, the supported DWs within the structure change as the lateral size of the nanowire increases. However, the circular symmetry of cylindrical nanowires results in slightly different types of DWs. In particular three different DW types have been observed in cylindrical nanowires - the TW, the Bloch-point wall (BPW) and the cylindrical ATW [19]. Schematics of them are displayed in Figure 2.3.

The TW (2.3a)) is very similar to its planar counterpart and is supported in narrow nanowires with a diameter under 50-60 nm. Its name is derived from the strong magnetisation component transverse to the long nanowire axis. Nanowires with larger diameters typically feature a BPW, which is characterised by a vortex-like rotation of magnetisation around the nanowire with a magnetic singularity in the centre, a Bloch point [20]. This particular wall has been shown to have an unexpected chirality. Depending on the direction of rotation of the wall when a magnetic field is applied to it, either normal motion or reversal of rotation followed by straight motion can be observed [21]. In larger nanowires (D > 50-60 nm) a third metastable DW can also be observed - the cylindrical ATW. It's characterised by a vortex-like rotation on the surface of the cylindrical nanowire. In order to preserve topological charge, this vortex is coupled to an antivortex structure on the opposite side of

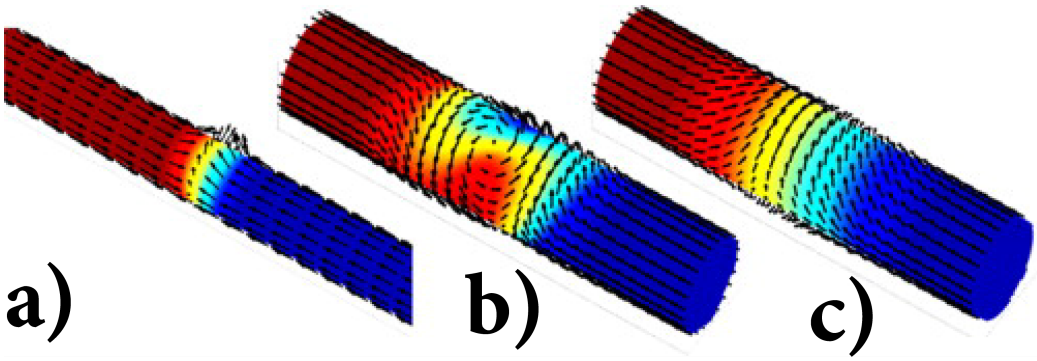

Figure 2.3: 3D representations of the a) TW, b) ATW and c) BPW observed in cylindrical nanowires. Arrows indicate the direction of magnetisation and the color change from blue to red indicates the M_z magnetisation component. *Reproduced from Ferguson et al. 2015.*

the nanowire. It is important to note that in some nanowire diameters close to the transition point listed earlier (50-60 nm), both BPW and TW can be supported with the BPW becoming the preferred state as the diameter increases further. Manipulating nanowire geometry is also a practice with cylindrical nanowires. M. Salem *et al.* [22] and C. Bran *et al.* [23] demonstrated the effect of diameter modulation on cylindrical nanowires, with the latter showing DW pinning in modulated and bamboo-like cylindrical nanowires. Nanowires composition also is an important factor for the DW formation. In [24] C. Bran *et al.* further determined that the magnetic state of segmented Ni and NiCo nanowires was highly dependent on the coupling between the adjacent segments.

2.4 Spintronics and nanowire based application

The main applications of ferromagnetic nanowires lie in the field of spintronics, which is an area of research focused on developing a new generation of nanoelectronic devices [25]. Spintronic devices aim to use the spin and magnetic moment of the electron in order to achieve higher device throughput, efficiency, and lower power consumption. An example of this is using magnetic domains and DWs to encode information and then access and manipulate this information through the propagation of DWs. The following sections describe some of the most common spintronics applications based on ferromagnetic DWs.

2.4.1 Spin polarised current

A popular method for manipulating magnetic domains and DWs is through an external magnetic field. However, when considering nanoscale spintronic devices the application of field has some limitations. For example applying a magnetic field is difficult to localise and it is therefore hard to target specific DWs (or even isolated device components) without unintentionally influencing others. Additionally, generating a magnetic field requires the inclusion of additional components to the device design. This creates additional fabrication difficulties, and increases the overall size and power consumption of the devices [26]. For these reasons, spin polarised current is often considered as a way to propagate DWs. This is simply an electric current, in which the flowing electrons have been modified so that their spins are aligned in a particular direction [27]. In a magnetic system this polarisation occurs when an electron spin carried by the current interacts with the magnetic layer. It is mediated by the exchange interaction and leads to torques between the spin and the magnetization. When a non-uniform magnetisation e.g. a DW is encountered by the current, the torque is transferred to it causing displacement [28]. This mechanism is commonly referred to as spin transfer torque or STT. Typically, the current is injected in pulses with times ranging from 10 ns to a few microseconds and varying current densities depending on the material composition of the system [29]. In the presence of heavy metals with strong spin orbit coupling another source of spin polarisation arises - spin orbit torque (SOT)[30] [31]. The origin of these effects can be due to different mechanism like the spin galvanic effect [32], or the spin Hall effect (SHE) [33], which causes a current spin polarisation in a direction perpendicular to the current flow. Either of the two can be present depending on the particular systems material parameters.

2.4.2 Racetrack memory

Perhaps the most important nanowire and DW-based device is magnetic racetrack memory. The initial concept was proposed and developed by Parkin *et al.* between 2003 and 2008 [34]. The operational principle is as follows: Magnetic domains with opposite magnetisation in a long thin strip of magnetic material are used to represent bits of information e.g. a domain with $\uparrow$ direction can represent a 1, while a $\downarrow$ domain can represent a 0. By shifting the domains through a specialised read/write device the magnetisation state can be recorded (read function) or altered (write function). A schematic of a single racetrack

memory can be seen in Figure 2.4.

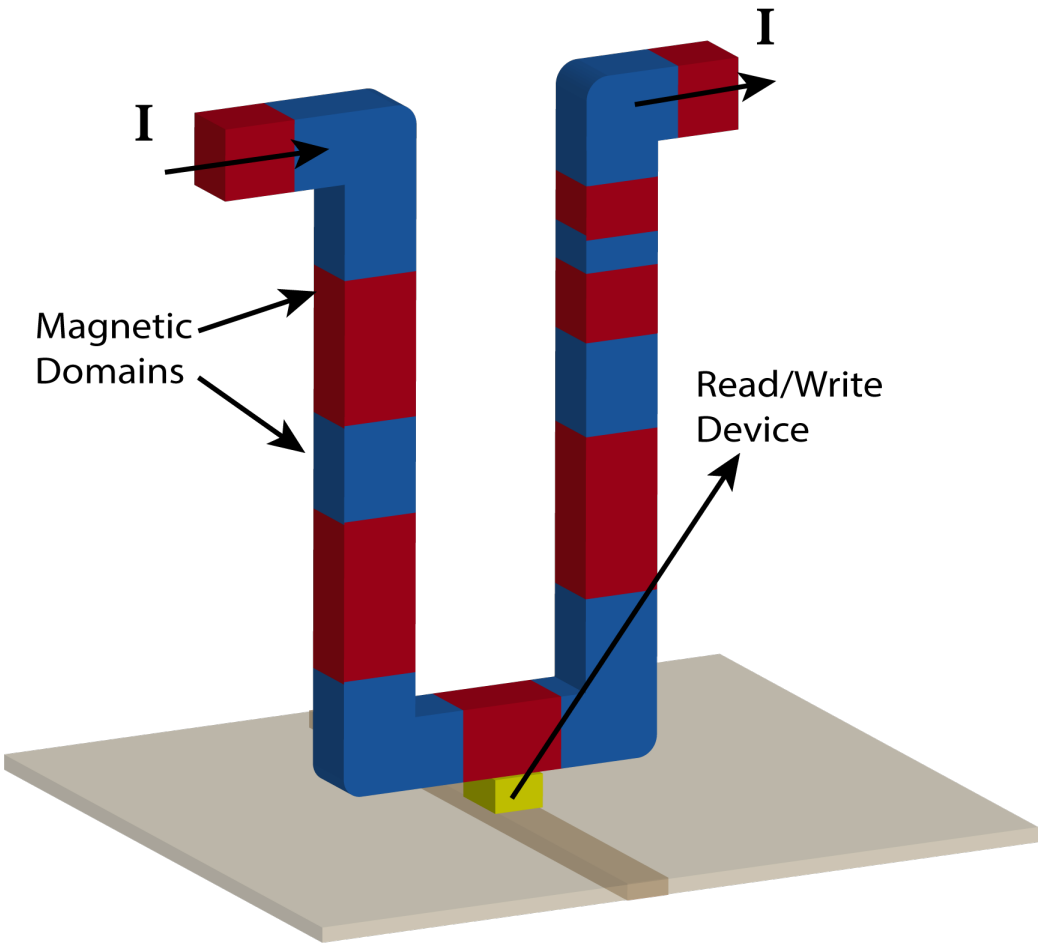

Figure 2.4: Schematic of magnetic racetrack memory. Blue and red colored regions represent opposite magnetic domains.

The propagation of the magnetic domains across the strip is achieved by manipulating the DWs that separate them. This can be done with a magnetic field, however, as mentioned earlier, this requires the addition of field generators in the device fabrication, which limits the size of the resulting devices and creates additional fabrication difficulties. For these reasons, the preferred approach for DW manipulation is using a spin-polarised current. Mechanisms based on STT were initially proposed, but recent research shows that

the performance of racetrack memory can be improved with the addition of DMI inducing layers [35], which facilitates highly mobile Néel-like DWs and the presence of SHE. The latter SOT based propagation was found to be much more efficient than the standard STT mechanism and resulted in DW speeds of up to 400 m/s. The read and write operation of the racetrack memory can be achieved by a variety magnetic sensors, with the most common method being implementation of magnetic tunnel junctions (MTJ) [36] as part of the nanostrip design. A detailed review on the advancement of the DW racetrack including novel material approaches using antiferromagnetic layers, device architecture and read/write mechanisms can be found in an article by R. Bläsing *et al.* [37].

2.4.3 Domain wall logic

Other spintronic devices that rely on DW propagation fall under the umbrella term "domain wall logic". These include magnetic nanowire based designs meant to replace common semiconductor components like shift registers and logic gates (NOT, NAND, NOR) [38]. A detailed description of all these devices is beyond the scope of this thesis, however, a basic understanding of the underlying principles can be obtained using the DW NOT gate. The function of a NOT gate is to simply invert the signal it receives i.e. if the NOT gate receives a signal representing a 1 it would output signal 0. A DW-based design for this is proposed in [39]. Similarly to the racetrack memory the DW NOT gate (and the other DW logic devices) relies on encoding bits of information in the magnetisation directions in the logic element and varying it the state by propagating a DW. The concept presented here relies on a counter-clockwise rotating magnetic field to do that. The operation is presented graphically in Figure 2.5.

In its initial state the magnetisation of the NOT gate is constant across all its terminals (P, Q, and R). As a domain is injected into the P terminal and propagated across the device the first magnetisation between P and Q becomes continuous and opposite to its initial state Figure 2.5 a) and b). Then as the magnetic field rotates the DW is driven out of the R terminal resulting in an effectively flipped magnetisation across the entire device. The DW propagation here is achieved using a magnetic field, however, current-driven motion has also been explored in [40]. Recently, also structures that include DMI effects have shown promise in the field [41].

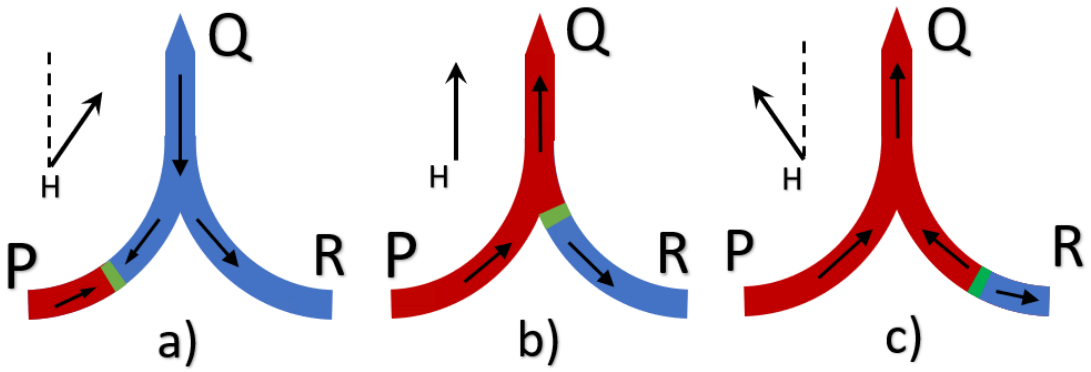

Figure 2.5: Schematic of DW based NOT gate. Blue and red colored regions represent opposite magnetic domains. a) shows injection of a DW in the device, b) shows the change in device magnetisation as the DW is propagated using an external field and c) shows the DW exiting the device and the resultant reversal of magnetisation.

2.4.4 Other domain wall based applications

Many other applications exist that depend on magnetic domains and the propagation of DWs and the response of nanowires. Some of these include sensors for magnetic fields or their components as described [42] or even for temperature [43]. DW also have found applications in the control and manipulation of secondary systems [44], where DWs were used to control magnetic nanoparticles for biological applications. Another application of magnetic DWs and nanowires is in Neuromorphic Computing, which refers to a novel computing architecture inspired by the human brain. In a neuromorphic computer, both the processing and memory functions are governed by a network of neurons connected using synapses [45]. The neuron elements take multiple signals as input and process them into a singular output, while the synapses work a connection between the neurons. Typically, the synapse connections between the neurons have adjustable weights associated with them, representing the strength of the connection between the neurons. These weights determine how much influence the output of one neuron has on the input of another. Adjusting the weights of the synapses allows neuromorphic systems to learn and adapt to different input data patterns. Magnetic DW-based devices like the DW-MTJ have been found to be promising candidates for neurons [46] and synapses [47] due to their tunability, non-volatility, and low power consumption. In the former, the presence and position of the DW

in the free layer of the MTJ can be used to encode information analogous to the firing state of a neuron in biological neural networks. The synaptic behaviour on the other hand is proposed to operate by modulating the resistance on the MTJ by oscillating the DW between pinning sites.

2.5 Skyrmion based spintronic nanowire applications

A different method to encode both magnetic logic and memory in nanowires and nanostrips is through the so-called magnetic skyrmions [48]. A magnetic skyrmion is a topologically protected, non-centrosymmetric magnetic quasi-particle exhibiting a vortex-like magnetization profile [49] . They stabilise in magnetic systems which exhibit DMI and have chiral characteristics, meaning that the rotation of their magnetisation can only be in one direction [50]. Much like DWs, they can be moved using electric currents via the SOT or STT mechanisms described earlier. Due to their inherent stability, they have been proposed as potential information carriers in spintronic systems [51]. Some of their application include skyrmion based logic and also neuromorphic computing [52] [53].

2.6 Limitations of domain walls based applications

One of the key research challenges of achieving such devices is the need for controllable high-speed DW propagation, as mentioned in Chapter 1. Strong magnetic fields are a way to achieve this in situation where a single DW needs to be propagated along a nanowire, but in multi-domain devices and components fields make it difficult to propagate DWs in a consistent manner. An alternative method is to apply a spin-polarised current as described in Section 2.4. Even with current driven DWs, there are limiting factors to the speed of DW propagation. The main one is Walker breakdown, a phenomenon in which anitvortex structures are periodically formed and annihilated an on the wire edges as the DW is propagated at high speeds [54]. This reduces the mobility of the DW and presents potential instabilities that can greatly limit DW-based applications. Multiple studies have been published on the suppression of Walker breakdown. Manipulation of the nanowire topology, such as the introduction of periodic holes [9] or modulation of the nanowire width [55], has shown a significant reduction of antivortex formation. Additionally, cylindrical nanowires have been shown to suppress Walker breakdown due to the lack of lateral edges [56]. An

unexplored gap in the research is a planar nanowire that lacks a lateral edge, i.e. a nanowire with a flat bottom but curved edge. This particular configuration is explored in this thesis.

References

[1] K. D. Sattler. *Handbook of Nanophysics*. CRC Press, 2010.

[2] A. Thiaville, J.M. Garcia, and J. Miltat. Domain wall dynamics in nanowires. *Journal of Magnetism and Magnetic Materials*, 242–245:1061–1063, 2002.

[3] J. I. Martín, M. Vélez, R. Morales, J. M. Alameda, J. V. Anguita, F. Briones, and J. L. Vicent. Fabrication and magnetic properties of arrays of amorphous and polycrystalline ferromagnetic nanowires obtained by electron beam lithography. *Journal of Magnetism and Magnetic Materials*, 249:156–162, 2002.

[4] P. Cojocaru, F. Muscolino, L. Magagnin, M. Vázquez, G. Badini-Confalonieri, and G. Carac. Electrodeposition of Ni/Co and Ni magnetic nanowires using allumina template. *ECS Transactions*, 25:147–153, 2010.

[5] M. Benitez, M.A. Basith, R. Lamb, D. McGrouther, S. McFadzean, A. MacLaren, D.and Hrabec, C. Marrows, and S. McVitie. Engineering magnetic domain-wall structure in permalloy nanowires. *Physical Review Applied*, 3:034008, 2015.

[6] Y. Nakatani, A. Thiaville, and J. Miltat. Head-to-head domain walls in soft nanostrips: a refined phase diagram. *Journal of Magnetism and Magnetic Materials*, pages 290–29, 2005.

[7] M. Kläui, M. Laufenberg, L. Heyne, D. Backes, U. Rüdiger, C. A. F. Vaz, J. A. C. Bland, L. J. Heyderman, S. Cherifi, A. Locatelli, T. O. Mentes, and L. Aballe. Current-induced vortex nucleation and annihilation in vortex domain walls. *Applied Physics Letters*, 88:232507, 2006.

[8] M. Kläui, H. Ehrke, U. Rüdiger, T. Kasama, R. E. Dunin-Borkowski, D. Backes, L. J. Heyderman, C. A. F. Vaz, J. A. C. Bland, G. Faini, E. Cambril, and W. Wernsdorfer. Direct observation of domain-wall pinning at nanoscale constrictions. *Applied Physics Letters*, 87:102509, 2005.

[9] R. Xu, M.and Li, D. Meng, J. Zhang, and M. Zhang. Suppression of Walker breakdown in nanowires with periodic holes. *Journal of Magnetism and Magnetic Materials*, 532:167988, 2021.

[10] M. Kläui. Head-to-head domain walls in magnetic nanostructures. *Journal of Physics: Condensed Matter*, 20:313001., 2008.

[11] R. Wieser, E. Y. Vedmedenko, P. Weinberger, and R. Wiesendanger. Current-driven domain wall motion in cylindrical nanowires. *Physical Review B*, 82(14):144430, 2010.

[12] A. Wartelle, B. Trapp, M. Staňo, C. Thirion, S. Bochmann, J. Bachmann, M. Foerster, L. Aballe, T. O. Menteş, A. Locatelli, A. Sala, L. Cagnon, J. C. Toussaint, and O. Fruchart. Bloch-point-mediated topological transformations of magnetic domain walls in cylindrical nanowires. *Physical Review B*, 99(2):024433, 2019.

[13] R. Hertel. Curvature-induced magnetochirality. *SPIN*, 03(03):1340009, 2013.

[14] M. Charilaou, H. Braun, and J. Löffler. Monopole-induced emergent electric fields in ferromagnetic nanowires. *Physical Review Letters*, 121(9):097202, 2018.

[15] G. Ji, S. Tang, B. Xu, B. Gu, and Y. Du. Synthesis of CoFe2o4 nanowire arrays by sol–gel template method. *Chemical Physics Letters*, 379(5–6):484–489, 2003.

[16] C. Bran, J. Fernandez-Roldan, R. del Real, A. Asenjo, O. Chubykalo-Fesenko, and M. Vazquez. Magnetic configurations in modulated cylindrical nanowires. *Nanomaterials*, 11:2079–4991, 2021.

[17] M. Huth, C. Porrati, F.and Schwalb, M. Winhold, R. Sachser, M. Dukic, J. Adams, and G. Fantner. Focused electron beam induced deposition: A perspective. *Beilstein Journal of Nanotechnology*, 3:597–619, 2012.

[18] M. Staňo and O. Fruchart. *Magnetic Nanowires and Nanotubes*, page 155–267. Elsevier, 2018.

[19] C.A. Ferguson, D.A. MacLaren, and S. McVitie. Metastable magnetic domain walls in cylindrical nanowires. *Journal of Magnetism and Magnetic Materials*, 381: 457–462, 2015.

[20] Y. Ivanov, M. Vázquez, and O. Chubykalo-Fesenko. Magnetic reversal modes in cylindrical nanowires. *Journal of Physics D: Applied Physics*, 46(48):485001, 2013.

[21] R. Hertel. Ultrafast domain wall dynamics in magnetic nanotubes and nanowires. *Journal of Physics: Condensed Matter*, 28(48):483002, 2016.

[22] M. Salem, P. Sergelius, R... Corona, J. Escrig, D. Görlitz, and K. Nielsch. Magnetic properties of cylindrical diameter modulated Ni80Fe20 nanowires: interaction and coercive fields. *Nanoscale*, 5(9):3941, 2013.

[23] C. Bran, J. Fernandez-Roldan, R. P. del Real, A. Asenjo, O. Chubykalo-Fesenko, and M. Vazquez. Magnetic configurations in modulated cylindrical nanowires. *Nanomaterials*, 11(3):600, 2021.

[24] C. Bran, J. Fernandez-Roldan, R. Del Real, A. Asenjo, Y. Chen, J. Zhang, X. Zhang, A. Fraile Rodríguez, M. Foerster, L. Aballe, O. Chubykalo-Fesenko, and M. Vazquez. Unveiling the origin of multidomain structures in compositionally modulated cylindrical magnetic nanowires. *ACS Nano*, 14(10):12819–12827, 2020.

[25] A. Hirohata, K. Yamada, Y. Nakatani, I. Prejbeanu, B. Diény, P. Pirro, and B. Hillebrands. Review on spintronics: Principles and device applications. *Journal of Magnetism and Magnetic Materials*, 509:166711, 2020.

[26] M. Hayashi, L. Thomas, R. Moriya, C. Rettner, and S. Parkin. Current-controlled magnetic domain-wall nanowire shift register. *Science*, 320(5873):209–211, 2008.

[27] J.C. Slonczewski. Current-driven excitation of magnetic multilayers. *Journal of Magnetism and Magnetic Materials*, 159(1–2):L1–L7, 1996.

[28] M. D. Stiles and J. Miltat. *Spin-Transfer Torque and Dynamics*, page 225–308. Springer Berlin Heidelberg.

[29] J. Currivan, Y. Jang, M. Mascaro, M. Baldo, and C. Ross. Low energy magnetic domain wall logic in short, narrow, ferromagnetic wires. *IEEE Magnetics Letters*, pages 3000104–3000104, 2012.

[30] K. S. Ryu, L. Thomas, S. H. Yang, and S. Parkin. Chiral spin torque at magnetic domain walls. *Nature Nanotechnology*, 8(7):527–533, 2013.

[31] L. Liu, O. J. Lee, T. J. Gudmundsen, D. C. Ralph, and R. A. Buhrman. Current-induced switching of perpendicularly magnetized magnetic layers using spin torque from the spin Hall effect. *Physical Review Letters*, 109(9):096602, 2012.

[32] S. Ganichev, E. Ivchenko, and V. Bel'kov. Spin-galvanic effect. *Nature*, 417(6890): 153–156, 2002.

[33] J. E. Hirsch. Spin hall effect. *Physical Review Letters*, 83(9):1834–1837, 1999.

[34] S. Parkin, M. Hayashi, and L. Thomas. Magnetic domain-wall racetrack memory. *Science*, 320(5873):190–194, 2008.

[35] K. S. Ryu, S. H. Yang, L. Thomas, and S. Parkin. Chiral spin torque arising from proximity-induced magnetization. *Nature Communications*, 5(1):3910, 2014.

[36] J. Zhu and C. Park. Magnetic tunnel junctions. *Materials Today*, 9(11):1369–7021, 2006.

[37] R. Bläsing, A. Khan, P. Filippou, C. Garg, F. Hameed, and S. Castrillon, J.and Parkin. Magnetic racetrack memory: From physics to the cusp of applications within a decade. *Proceedings of the IEEE*, 108(8), 2020.

[38] D. A. Allwood, G. Xiong, C. C. Faulkner, D. Atkinson, D. Petit, and R. P. Cowburn. Magnetic domain-wall logic. *Science*, 309(5741):1688–1692, 2005.

[39] D. A. Allwood, Gang Xiong, M. D. Cooke, C. C. Faulkner, D. Atkinson, N. Vernier, and R. P. Cowburn. Submicrometer ferromagnetic NOT gate and shift register. *Science*, 296:2003–2006, 2002.

[40] J. Currivan, M. D. Youngman J.and Mascaro, M. A. Baldo, and C. A. Ross. Low energy magnetic domain wall logic in short, narrow, ferromagnetic wires. *IEEE Magnetics Letters*, 3:3000104–3000104, 2012.

[41] Z. Luo, A. Hrabec, T. Dao, G. Sala, S. Finizio, J. Feng, S. Mayr, J. Raabe, P. Gambardella, and L. J. Heyderman. Current-driven magnetic domain-wall logic. *Nature*, 579(7798):214–218, 2020.

[42] J. Lenz and S. Edelstein. Magnetic sensors and their applications. *IEEE Sensors Journal*, 6(3):631–649, 2006.

[43] F. Klingbeil, S. D. Stölting, and J. McCord. Sensing of temperature through magnetooptical domain wall susceptibility. *Applied Physics Letters*, 118(9):092403, 2021.

[44] P. Vavassori, V. Metlushko, B. Ilic, M. Gobbi, M. Donolato, M. Cantoni, and R. Bertacco. Domain wall displacement in Py square ring for single nanometric magnetic bead detection. *Applied Physics Letters*, 93(20):203502, 2008.

[45] D. Ham, H. Park, S. Hwang, and K. Kim. Neuromorphic electronics based on copying and pasting the brain. *Nature Electronics*, 4(9):635–644, 2021.

[46] N. Hassan, X. Hu, L. Jiang-Wei, W. Brigner, O. Akinola, F. Garcia-Sanchez, M. Pasquale, C. H. Bennett, J. Incorvia, and J. Friedman. Magnetic domain wall neuron with lateral inhibition. *Journal of Applied Physics*, 124(15):152127, 2018.

[47] T. Leonard, S. Liu, M. Alamdar, H. Jin, C. Cui, O. Akinola, L. Xue, T. Xiao, J. Friedman, M. Marinella, C. Bennett, and J. Incorvia. Shape-dependent multi-weight magnetic artificial synapses for neuromorphic computing. *Advanced Electronic Materials*, 8(12):2200563, 2022.

[48] A. Fert, V. Cros, and J. Sampiao. Skyrmions on the track. *Nature Nanotechnology*, 8 (3):152, 2013.

[49] A. N. Bogdanov and U. K. Rößler. Chiral symmetry breaking in magnetic thin films and multilayers. *Physical Review Letters*, 87(3):037203, 2001.

[50] U. K. Rössler, A. N. Bogdanov, and C. Pfleiderer. Spontaneous skyrmion ground states in magnetic metals. *Nature*, 442(7104):797–801, 2006.

[51] M. Chauwin, X. Hu, F. Garcia-Sanchez, N. Betrabet, A. Paler, C. Moutafis, and J. Friedman. Skyrmion logic system for large-scale reversible computation. *Phys. Rev. Appl.*, 12:064053, 2019.

[52] Z. He and D. Fan. A tunable magnetic skyrmion neuron cluster for energy efficient artificial neural network. In *Proc. Conf. on Design, Automation & Test in Europe*, pages 350–355, Leuven, 2017. European Design and Automation Association.

[53] A. H. Lone and H. Fariborzi. Skyrmion-magnetic tunnel junction synapse with long-term and short-term plasticity for neuromorphic computing. *IEEE Transactions on Electron Devices*, 70(1):371–378, 2022.

[54] A. Mougin, M. Cormier, J. P Adam, P. J Metaxas, and J Ferré. Domain wall mobility, stability and Walker breakdown in magnetic nanowires. *Europhysics Letters (EPL)*, 78(5):57007, 2007.

[55] O. Lozhkina, R. Reeve, R. Frömter, and M. Kläui. Control of the Walker breakdown by periodical magnetic wire-width modulation. *Journal of Applied Physics*, 131(23): 233902, 2022.

[56] M. Yan, A. Kákay, S. Gliga, and R. Hertel. Beating the Walker limit with massless domain walls in cylindrical nanowires. *Physical Review Letters*, 104(5):057201, 2010.

3 Experimental techniques

Contents

3.1 Introduction

Throughout this project, various experimental techniques have been used to study the magnetic properties of curved-profile nanowires. This chapter includes a detailed account of the tools and methods that were essential to the research. The two main tools used were a scanning electron microscope (SEM) with a fitted focused ion beam (Helios PFIB) for sample fabrication and two transmission electron microscopes (TEM) - the Tecnai T20 and the JEOL atomic resolution microscope (ARM) for physical and magnetic characterisation. The Tecnai T20 was used for initial sample characterisation via techniques like bright-field imaging (Section 3.4.2) and for Fresnel mode Lorentz microscopy (Section 3.5.3). The JEOL ARM was mainly used for quantitative magnetic imaging via differential phase contrast (DPC) (Section 3.5.5). Section 3.2.1 of the chapter describes the basic operation of an SEM and the focused electron beam-induced deposition technique (FEBID) which was used in the fabrication of nanowires discussed in Chapter 4. The chapter continues with a brief description of magnetron sputtering which is a technique used for the deposition of functional thin films. Section 3.3 of the chapter outlines the physical characteristics of the TEM electron column and describes its basic operation. This is followed by a description of the structural imaging techniques including bright and dark field imaging and diffraction. The various magnetic imaging techniques which were used in the characterisation of the magnetic nanowires are discussed in section 3.5. Finally, section 3.5.6 presents tools used for the generation of Lorentz TEM images from micromagnetic simulation data.

3.2 Sample preparation and fabrication

The bulk of the magnetic and structural characterisation in this project is done using transmission electron microscopes, which requires the samples studied to be electron transparent i.e. the total thickness of the sample needs to be smaller than $\approx$ 100 nm. For this reason, the magnetic nanowires were patterned on top of thin Si_3N_4 membranes obtained from the James Watt Nanofabrication Centre at the University of Glasgow. The electron transparent window on which magnetic structures were deposited was square in shape with a side of 100 μm and thickness in the range between 30-50 nm. A schematic of the membranes is

shown in Figure 3.1. To avoid charging in the TEM protective layers of copper (Cu) were deposited on the membranes using DC magnetron sputtering before the nanowires were patterned. The sputtering process is discussed in more detail in Section 3.2.3 and in Section 5.2. the tools and processes needed for the fabrication of curved-profile nanowires are discussed.

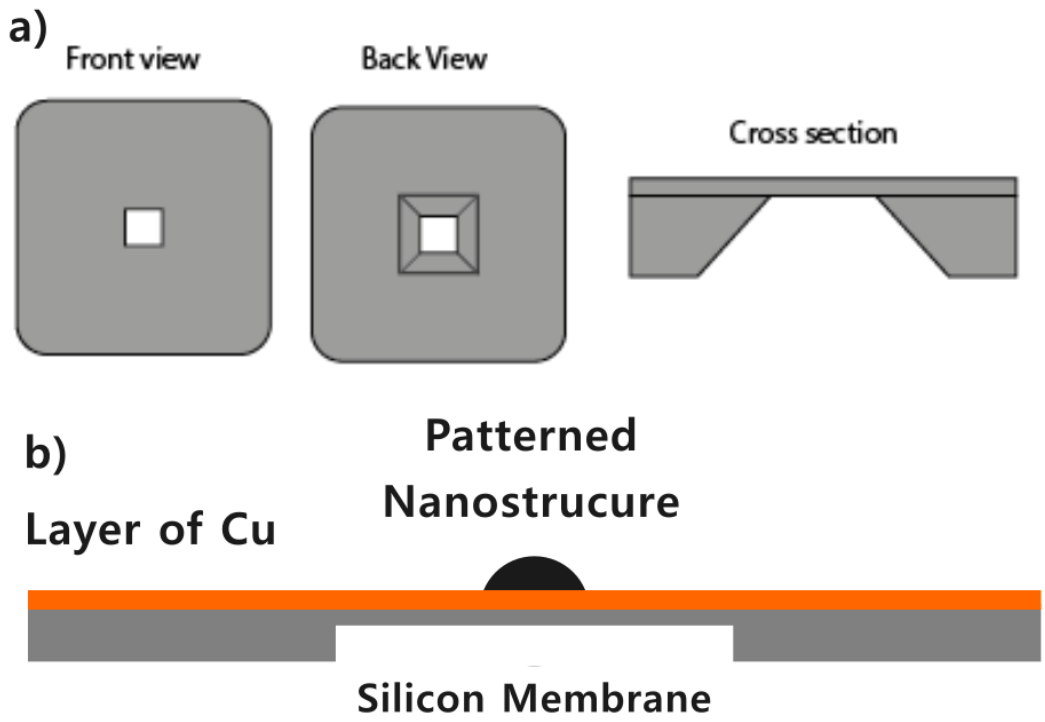

Figure 3.1: Schematic of TEM transparent Si_3N_4 membranes a) and a diagram of the fabrication process b). In a) the central electron transparent window that appears as a white square in the image (100 µm $\times$ 100 µm wide, 30-50 nm thick) is supported by a Si chip.in b) the orange layer represents the Cu layer, while the magnetic structure is the black semi-circle.

3.2.1 Scanning electron microscopy

For the patterning and initial imaging of ferromagnetic nanowires, a dual-beam system consisting of an SEM and a focused ion beam (FIB) was used. The specific instrument used in this project was the Helios xenon plasma FIB, referred to as PFIB for the rest of the thesis. A schematic of the instrument can be seen in Figure 3.2. In the Helios system, the ion column is at a 52° angle to the electron column which in turn is built perpendicular to the sample surface. Both columns have a similar internal structure consisting of an electron/ion source, followed by a set of apertures and lenses (magnetic for the electron column and electrostatic for the ion column), which are used to align the beam and condense it to a spot on the sample surface. During imaging either of the beams is rastered across the sample, which causes different particles to be ejected depending on the source. These are collected by a set of detectors, situated above the sample. The electron column can accelerate the primary electrons (PEs) coming from the electron source in the range between 1-30 keV. The particles produced when they strike the surface are photons, secondary electrons (SE) and backscattered electrons (BSE). SEs are weakly bound sample electrons ejected from the surface due to inelastic collisions with the PEs and the BSE are elastically reflected primary electrons ejected from deeper within the sample. The ejected particles are then collected by the detector to form an image [1]. For this project, several electron beam acceleration energies were used for the imaging and fabrication of the nanowires ranging from 3 kV to 15 kV. More detail on this is given in Chapter 4. Similarly to the electron beam, the ion beam can also be accelerated up to 30 keV but has a more destructive effect on the sample. In addition to the SEs, BSEs and photons when colliding with the surface the ions can eject sample atoms if the energy supplied by the ion is larger than the binding energy of the material [2]. This is known as milling and is widely for cross-sectional sample preparation for thin TEM samples. In the next section, the specific technique used for the fabrication of nanowires is described. It is important to note that while it is possible to perform the technique using both the ion and electron beams, the destructive nature of the ion beam makes it the less favourable option.

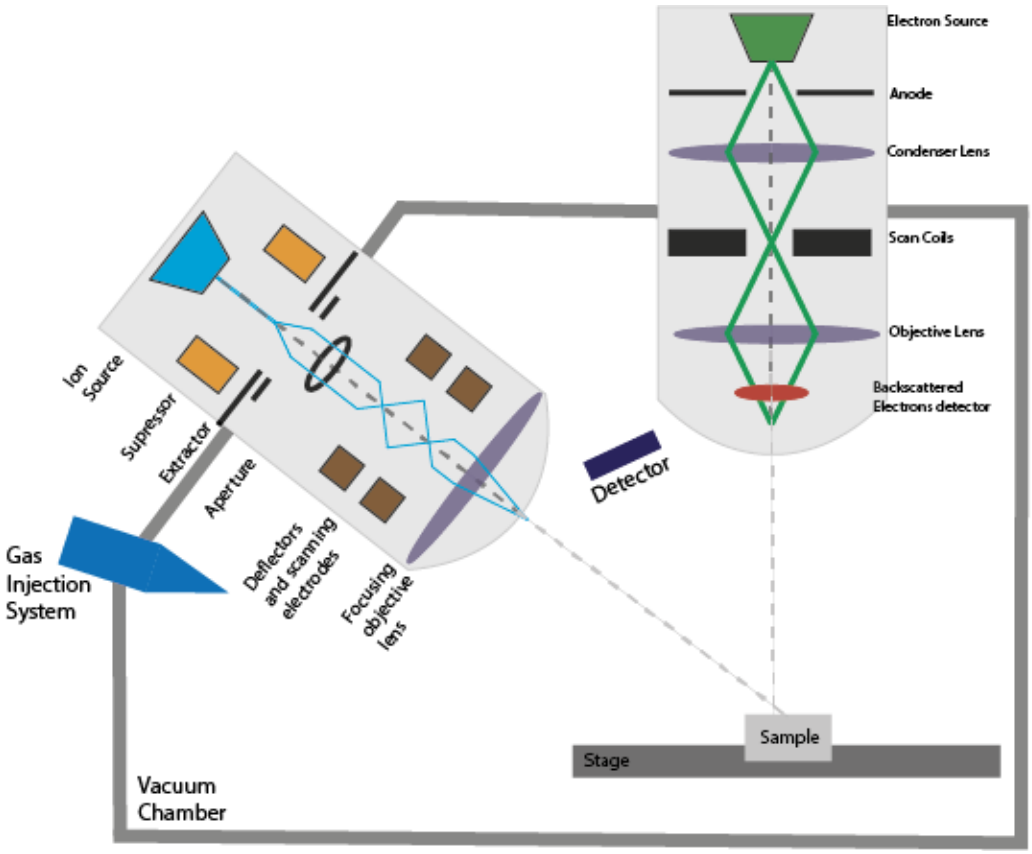

Figure 3.2: Schematic of a Dual-Beam SEM/FIB system, showing the orientation of the two columns and their basic components. Electron column is oriented perpendicular to the sample state, while the ion column is at 52°.

3.2.2 Focused electron beam induced deposition (FEBID)

A common occurrence when imaging with an SEM system is the formation of a dark region around the area of the sample that is exposed to the electron beam. The cause of this is the build-up of hydrocarbons on the sample surface facilitated by exposure to the electron beam. This negative effect can, however, be used to an advantage if instead of hydrocarbons a suitable precursor gas is present in SEM the chamber. This is the basic phenomenon on which the FEBID technique is based. By definition, FEBID is a chemical vapour deposition process that is assisted by a focused electron beam provided by a Scanning Electron Microscope [3]. It operates based on the electron-induced molecular dissociation of a gas

adsorbed on the sample surface. The gas is inserted into the SEM chamber near the substrate using a gas injection system (GIS). The focused electron beam decomposes the gas molecules resulting in the deposition of the remaining material on the sample surface and the evacuation of volatile fragments from the chamber via the vacuum system. This allows for the nano-scale patterning of custom shapes achieved by manipulating the path of the electron beam. An illustration of the FEBID technique can be seen in Figure 3.3. Because of the stochastic nature of the process which is due to the electrons interacting essentially randomly with precursor gas molecules the resulting structures have a naturally curved Gaussian-like profile. This is the main reason this technique was chosen for the fabrication of physical nanowires for this thesis. To control the shape and dimensions of the resulting structure the FEBID user can use basic shapes provided by the microscope interface, import mask patterns of the desired structure or even use so-called "stream" files which directly control the position of the electron beam and the time it remains on every single point of the raster [4]. Typically for the FEBID technique an organo-metallic precursor gas is used. Usually, those precursor gases are not fully broken up by the electron beam and some amount of hydrocarbons remain in the chamber and reduce the chemical purity of the final structure. For magnetic materials these impurities affect properties like the saturation magnetisation and exchange constant of the resulting structures [5]. Still using the right conditions significantly pure depositions are possible. For example, in Co structures a purity of 90 % is achievable with beam currents of 2 nA and above and around 80% if the beam current is smaller [6] [7]. The resolution of this technique is highly dependent on the spot size of the electron beam and the surface leaving secondary electrons. Recently it has been shown that using FEBID it is possible to build complex 3D and 2D structures with resolution of a few tens of nanometers and control their geometry during the deposition process [8]. Specific conditions in which nanowires for this project were grown are available in Chapter 4.

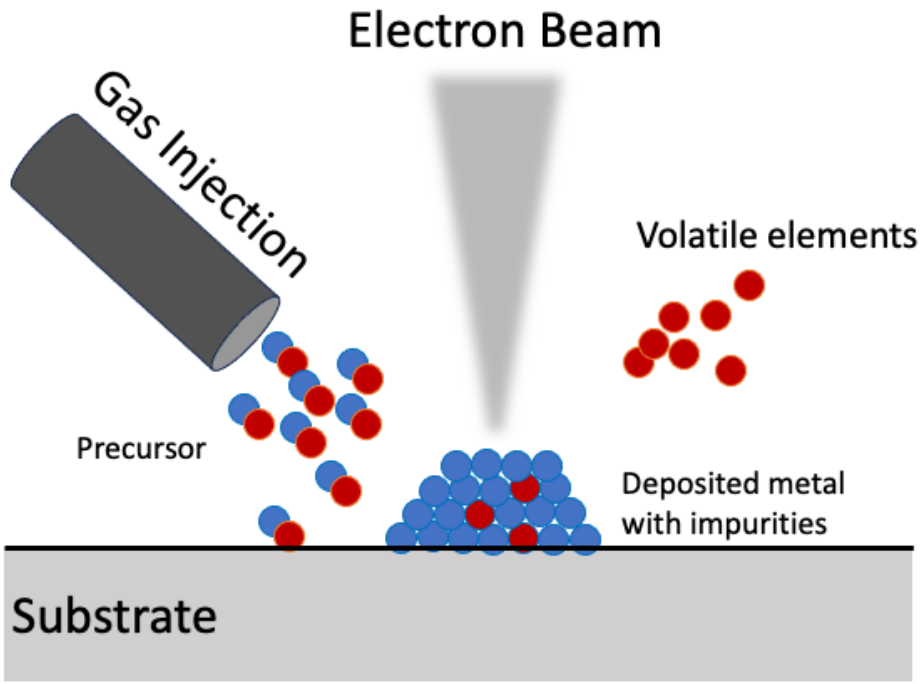

Figure 3.3: Schematic of the FEBID technique - Precursor gas molecules are inserted into the system via the GIS, adsorbed on the sample surface and broken down by an electron beam. This results in the deposition of the desired material with the volatile elements being ejected.

3.2.3 DC magnetron sputtering

While the Fe and Co structures patterned using FEBID for this project are conductive on their own, they are deposited on non-conductive Si_3N_4 membranes. This means that when they are imaged using a TEM they acquire a charge that cannot be conducted away from them which leads to difficulty in imaging. To circumvent that sputter deposition was used to deposit a thin (15 ± 2 nm thick) conductive film of copper (Cu) onto the membranes before the FEBID deposition. Sputter deposition is a physical vapour deposition (PVD) technique that is commonly used in the fabrication of high-quality polycrystalline thin films. The sputtering process works by striking a target material that needs to be deposited with high-energy ions from a glow-discharge plasma. Collisions with the ions cause the target atoms to be expelled from the surface, travel through the sputtering chamber and condense onto the sample forming a thin layer. The basic sputtering system consists of a

cathode situated at the target and an anode at the substrate which are held in a low-pressure vacuum chamber. To create the plasma an inert gas like Argon is released into the chamber and ionised by applying a high voltage between the cathode and anode. The positive ions are then accelerated towards the cathode resulting in the desired collisions. In addition to atoms, the ions colliding with the target also cause electrons to be ejected and accelerated away from the cathode, which makes them inefficient for sustaining the discharge [9]. By employing a magnetic field created by an array of magnets they can instead be deflected and confined near the target surface. This increases the electron density in the region where the plasma is formed and therefore the probability that an electron will ionize a neutral molecule. This increase in ionized material directly enhances sputtering yields and improves deposition rates [10]. A schematic is shown in Figure 3.4. The system used for this project was a manual DC sputter coater with an interchangeable target. As mentioned a Cu target was used at a current of 140 mA with Ar gas pressure of 5×10^{-2} mbar.

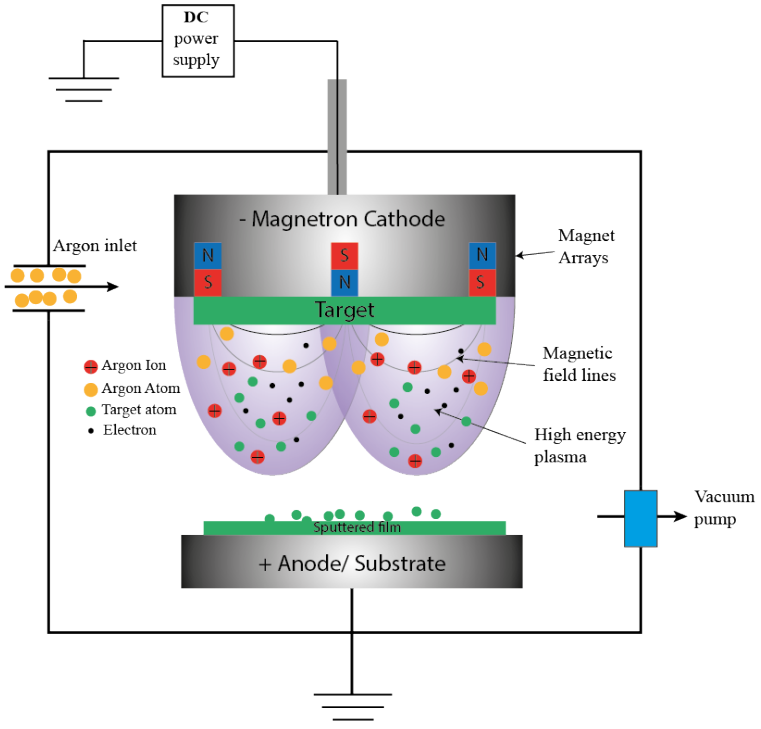

Figure 3.4: Schematic of a typical DC magnetron sputtering system used for the deposition of functional thin films.

3.3 Transmission electron microscopy

Direct imaging of domains and DWs is crucial to the study of magnetic nanowires. Domains sizes range from 10 nm to upwards of 100 nm and domain wall (DW) widths can be as small as one atomic repeat and also reach up to 100 nm. One of the best tools for imaging structures of that scale is the Transmission electron microscope (TEM), provided that the samples are thin enough to allow electrons to pass through them. For a TEM operated at an acceleration voltage of 200 kV, which is used throughout this project, the thickness at which materials are electrons transparent is $\sim$ 100 nm. One of the biggest factors in determining the resolution achievable in a TEM is the electron wavelength. Because the electron is a particle with a non-zero mass its wavelength is related to its momentum (p) via $\lambda = h/p$, where h is Planck's constant. This equation however neglects relativistic effects and can only be applied to TEMs with operating voltages under 100 kV. Both of the TEMs used for this thesis use accelerating voltages of 200 kV and therefore require a relativistic correction to be applied to the above formula in order to obtain an accurate wavelength. This is given in equation 3.1.

$$\lambda = \frac{h}{\sqrt{2m_0eV(1+\frac{eV}{m_0c^2})}} \tag{3.1}$$

Where c is the speed of light, m_0 is the electron mass and V is the accelerating voltage. Substituting V = 200 kV in equation 3.1 results in a wavelength $\lambda = 2.51$ pm [11].
In a microscope with a perfect lens system, the resolution would then only be limited by diffraction and given by Abbe's limit:

$$d = \frac{\lambda}{2nsin\theta} \tag{3.2}$$

where $nsin\theta$ is called the numerical aperture and relates to the refractive index n of the medium that the radiation travels through and θ is the semi-angle of the imaging probe. It is, however, impossible to reach this limit due to aberrations in the magnetic lenses used to focus the electrons. Examples of such aberrations are spherical aberration (C_s)

and chromatic aberration (C_c). The former is caused by the fact that off-axis electrons are more strongly deflected towards the optic axis than the electrons travelling near it. Chromatic aberration on the other hand is caused by a variation in the electron wavelength (or energy) in the electron beam. In TEM chromatic aberration can have several different causes including an imperfect electron gun system and electron energy loss due to inelastic scattering with thicker samples [12] [13]. Currently, the most sophisticated TEMs can achieve a resolution down to ~ 50 pm using a combination of high accelerating voltages and advanced lens aberration correction techniques, which increases convergence angle and thus reduces the value of d given by equation 3.2 [14]. While different TEM columns can vary in design and performance they all operate on the same principles and utilize the same basic components to form an image. Namely an electron gun, electromagnetic lenses, apertures and detectors. The electron gun is a device, whose function is to produce electrons and form a coherent electron beam. There are two main types of electron guns, based on the way they produce the electrons - thermionic and field-emission (FEG) [15]. In FEGs (as is the electron gun in the JEOL-ARM used in this project) the electrons are extracted from the tip of a sharp metal needle due to a strong electrostatic field gradient via a process called Fowler–Nordheim tunnelling [16]. Because of the very small area from which electrons are extracted (3 nm for cold FEG and 15 nm for Schottky FEG), the electron beams produced are usually highly coherent. The superior spatial and temporal beam coherence in particular is very important for imaging techniques which are based on phase contrast like some of the analytical Lorentz microscopy techniques discussed later in this chapter. Once the beam is formed it travels down the microscope column through a series of electromagnetic lenses and deflection coils, which are used to focus, tilt and shift it depending on the user's needs. Using these lenses the electron microscope can be configured to acquire images in two main modes - conventional and scanning transmission electron microscopy (CTEM and STEM) displayed graphically in Figure 3.5. In both modes, the first lens system the beam encounters is the condenser system whose role is to define important characteristics of the electron beam like the spot size and brightness.

3.3.1 Conventional TEM

In CTEM mode (Figure 3.5 a)) a combination of the condenser lens two and the upper objective lens is used to create an approximately parallel illumination of the sample. Once

the beam is transmitted through the sample it reaches the lower objective lens which is the main imaging lens in the microscope. Its role is to focus both the directly transmitted ray and any diffracted rays to its back focal plane where an objective aperture is placed. This aperture controls the angular spread of the beam and limits the number of highly scattered electrons reaching the electron detectors. Below the aperture is the intermediate lens system, which is used to select between diffraction and imaging modes. This is done by varying the strength of the first intermediate lens, which causes either the back-focal plane or the first image plane of the objective lens to be its object. The remaining projector lenses are used to further magnify the final image in image mode, or equivalently select the camera length when looking at diffraction patterns. Finally, the desired image can be seen on a viewing screen or recorded using a charge-coupled device (CCD) camera. In CTEM mode a detector or camera is used to collect either an image or a diffraction pattern. For this project, some the CTEM techniques used include bright-field imaging (Section 3.4.2) and Fresnel mode Lorentz microscopy (3.5.3.

3.3.2 Scanning mode TEM

In STEM mode (Figure3.5 b)) the condenser system is strongly excited in order to converge the electron beam to a focused probe, which is projected onto the sample. The imaging then happens by rastering the probe across the sample with a series of scanning coils. The scanning coils also ensure that the probe remains parallel to the sample surface, which is crucial, because if the angle of incidence of the electron beam varied, the scattering processes within the sample would be affected, making the resulting images difficult to interpret. In contrast to CTEM mode, where the whole image is recorded at once, in STEM mode, the image is collected pixel-by-pixel by a detector at the bottom of the microscope column. Some detectors used in STEM are discussed in Section 2.5.4. It is important to note that in STEM mode the microscope is always in diffraction mode and the projector system is responsible for selecting the camera length. STEM mode was mainly used to acquire quantitative magnetic images of the samples via the DPC technique described in Section 3.5.5.

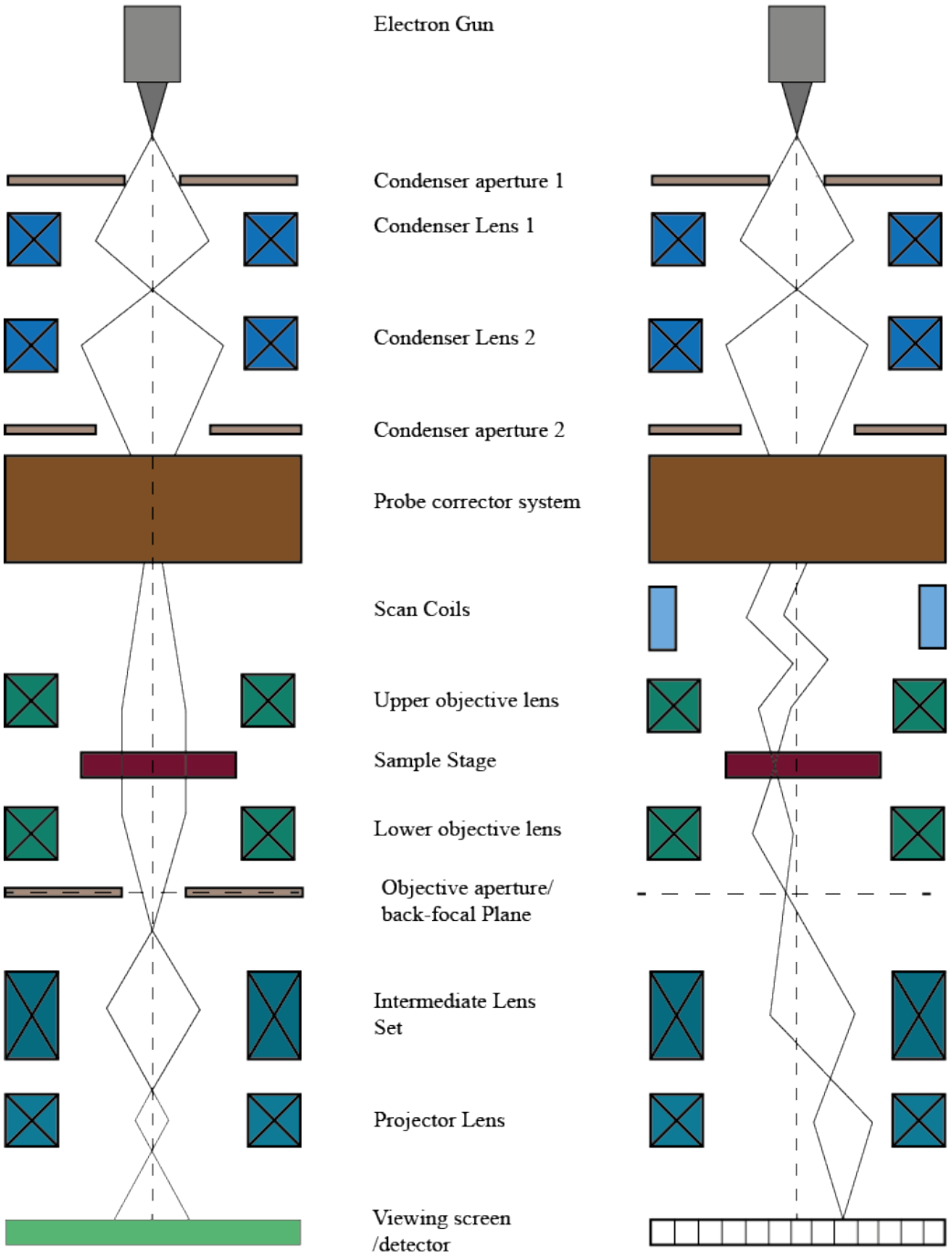

Figure 3.5: Ray diagrams for a TEM configured in conventional mode or CTEM (a)) and scanning mode or STEM (b)). In CTEM the electron beam reaches the sample as a plane wave, whereas in STEM mode the beam is condensed to a probe.

3.3.3 TEM image formation principles

In a TEM the electron beam can be regarded as a plane wave described as some wavefunction ψ_{e^-}. When passing through a thin sample the plane wave experiences a change in both amplitude and phase due to interactions with the sample resulting in the sample wavefunction $\psi(\mathbf{r}_\perp)$ given by equation 3.3:

$$\psi(\mathbf{r}_\perp) = a(\mathbf{r}_\perp)e^{i\phi(\mathbf{r}_\perp)} \tag{3.3}$$

where $a(\mathbf{r}_\perp)$ and $\phi(\mathbf{r}_\perp)$ are the amplitude and phase of the electron wavefunction at position $\mathbf{r}_\perp$. After the sample the electron wavefunction $\psi(\mathbf{r}_\perp)$ passes through the objective system and enters the back focal plane of the objective lens, where the electron distribution can be described by the Fourier transform of $\psi(\mathbf{r}_\perp)$, denoted as $\Psi(\mathbf{k}_\perp)$. Passing through the objective system further modifies the phase of the electron wave due to the aberrations in the main imaging lens of the microscope. In reciprocal space, this effect can be quantified using the phase-distortion function $\chi(\mathbf{k}_\perp)$ given by equation 3.4.

$$\chi(\mathbf{k}_\perp) = \pi\Delta f\lambda|\mathbf{k}_\perp|^2 + \frac{1}{2}\pi C_s\lambda^3|\mathbf{k}_\perp|^4 \tag{3.4}$$

Where Δf is the defocus and C_s is the spherical aberration constant of the imaging lens. Other than the phase-distortion function the electron wavefunction is also modified by the coherence of the electron beam and chromatic effects. The effects of this can be included in the electron wavefunction through multiplication with an envelope function $p(\mathbf{k}_\perp)$ given by equation 3.5.

$$p(\mathbf{k}_\perp) \approx \frac{(\pi\theta_c\Delta f)^2}{ln2}|\mathbf{k}_\perp| \tag{3.5}$$

Where θ_c is the beam divergence angle defined as the angular half-width of the intensity distribution of the electron source. Finally, $p(\mathbf{k}_\perp)$ and $\chi(\mathbf{k}_\perp)$ can be combined with aperture function $A(|\mathbf{k}_\perp|)$, which has a value of 1 inside an aperture and 0 otherwise to give the contrast transfer function $H(\mathbf{k}_\perp)$, which determines how different spatial frequencies are transferred from the sample to the final image $G(\mathbf{k}_\perp)$. In reciprocal space, this is represented mathematically via equation 3.6.

$$G(\mathbf{k}_\perp) = \Psi(\mathbf{k}_\perp)H(\mathbf{k}_\perp) \tag{3.6}$$

Where $H(\mathbf{k}_\perp)$ has the following form :

$$H(\mathbf{k}_\perp) = A(|\mathbf{k}_\perp|)e^{-ip(\mathbf{k}_\perp)}e^{-i\chi(\mathbf{k}_\perp)} \tag{3.7}$$

The projection system then applies an inverse Fourier transform to produce the final image function - $g(\mathbf{r}_\perp)$ in the image plane. This is represented mathematically in equation 3.8.

$$g(\mathbf{r}_\perp) = \psi(\mathbf{r}_\perp) \otimes h(\mathbf{r}_\perp) \tag{3.8}$$

Here the $\otimes$ sign denotes a convolution of the sample $\psi(\mathbf{r}_\perp)$ and a point spread function $h(\mathbf{r}_\perp)$, which is the inverse Fourier transform of $H(\mathbf{k}_\perp)$. Finally, detectors in the image plane of the microscope can record the intensity of the final image function $I(\mathbf{r}_\perp)$, given by:

$$I(\mathbf{r}_\perp) = g(\mathbf{r}_\perp)^* g(\mathbf{r}_\perp) = |g(\mathbf{r}_\perp)^2| \tag{3.9}$$

Where the $g(\mathbf{r}_\perp)^*$ is the complex conjugate of $g(\mathbf{r}_\perp)$. The mathematical formalism outlined above is mostly derived from [17][18] and although abstract, it is also useful in understanding and interpreting TEM images. Additionally, it forms the basis of the methods used for the calculation of simulated experimental images in Chapter 4 and for the quantification of Fresnel image defocus in Chapter 5. More detail on both is given in the following sections and chapters.

3.4 Structural imaging

Structural imaging in a TEM refers to obtaining information about the atomic, crystalline or geometric makeup of the studied material. This can be done by studying the image or diffraction pattern of the sample in both CTEM and STEM modes of operation. In the following sections, three different structural imaging techniques are discussed - bright-field (BF) imaging, dark-field (DF) imaging and electron diffraction. Simplified ray diagrams for three techniques for CTEM can be seen in Figure 3.6.

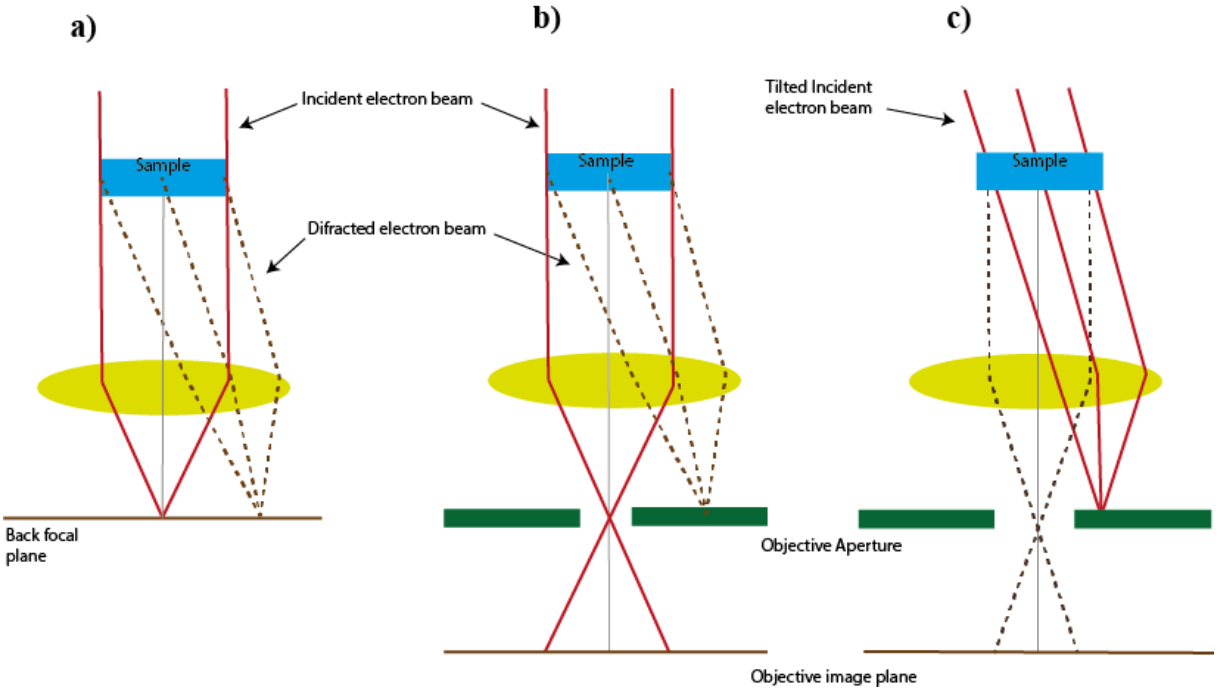

Figure 3.6: Schematics of electron diffraction (a)), BF imaging (b)) and tilted DF imaging (c)). The solid red lines represent the straight-through, unscattered electron beam while the brown dotted line represents the diffracted beam.

3.4.1 Diffraction

Diffraction imaging is a technique used for the characterisation of the crystal structure of a particular sample through the study of its diffraction pattern. In crystalline and poly-crystalline materials a diffraction pattern is formed when electron waves scattered from successive atomic planes interfere constructively. This occurs only if the Bragg condition is satisfied.

$$n\lambda = dsin(\theta) \tag{3.10}$$

Where θ is the electron scattering angle, d is the atomic spacing of the material, n is an integer and λ is the electron wavelength. For a 200 kV TEM with λ=2.51 pm equation 3.10 gives a scattering angle of $\approx$ 10mrad. The diffraction pattern forms in the back focal plane of the objective lens and vary based on the crystallinity of the sample. For a single crystal, the diffraction pattern is a series of symmetric spots, while for polycrystalline samples in which multiple crystal directions are present, like the ones studied in this thesis,

the diffraction pattern consists of a central bright spot surrounded by a series of concentric rings. An example of such a diffraction pattern can be seen in Figure 3.7. Diffraction imaging is commonly used for structural characterisation and to obtain information about sample crystallinity like atomic lattice constants and crystal symmetries [19]. For this thesis diffraction imaging was used to check the structure of the deposited Co and Fe nano structures and Cu films.

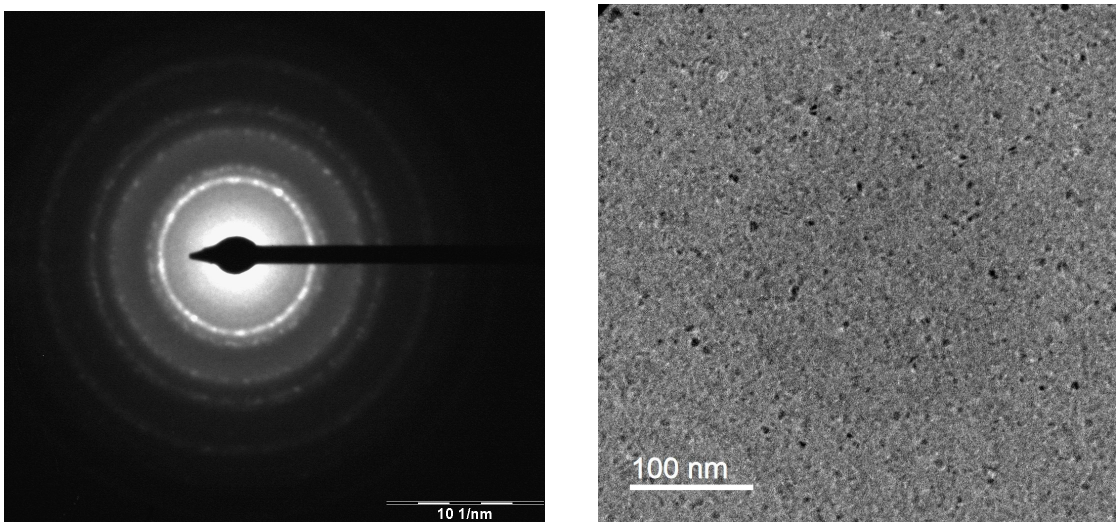

(a) Diffraction pattern (b) BF image

Figure 3.7: Diffraction pattern of a sample area over which a 10nm thick copper film was deposited a) and the corresponding BF image b).

3.4.2 Bright and dark-field imaging

The two most common modalities of TEM imaging - BF and DF imaging are fundamentally derived from electron diffraction. To form a BF image only the directly transmitted electrons i.e. the ones in the central spot of the diffraction pattern are projected onto the image plane. An aperture is used to filter out any electrons scattered by sample interactions. In the diffraction pattern presented in Figure 3.7a this corresponds to the central region of the image covered by the beam block. A dark field image on the other hand is formed by only collecting the scattered electrons in a specific diffraction spot or annular range. In the diffraction pattern shown in 3.7a this corresponds to the concentric rings present in the pattern. This is achieved by tilting the incident beam in such a way that the scattered electrons

travel along the optic axis of the microscope and through the objective aperture. The contrast in BF and DF images arises from the variation of electron scattering in the sample. In BF images, for example, any electrons that undergo sufficient scattering to meet any of the Bragg diffraction conditions will not appear in the final image therefore darkening areas where a lot of elastic scattering can occur. Factors that influence this are sample thickness and composition with thicker, more dense or higher-atomic number materials resulting in more scattering and therefore darker regions in the final image. On the other hand, in DF imaging, areas of high scattering will appear bright as the electrons that form the DF image are precisely the ones that have undergone scattering and meet the Bragg conditions. DF imaging is particularly useful for the multilayer systems with different materials because the different atomic number layers will appear differently in the final image [20]. The described methods for obtaining BF and DF images are valid only for CTEM mode. In STEM the microscope is always in diffraction mode and there is no objective aperture to choose which sections of the beam are transmitted. Instead, information is collected by detectors placed in the following configuration. A standard detector like a CCD camera collects the straight-through beam to form the BF image while an annular dark field (ADF) and a high angle annular dark field (HAADF) ring-shaped detectors collect the scattered beam. In this project, BF imaging was commonly used to visually inspect new samples, search for defects and for the measurements of critical dimensions of the nanomagnetic structures deposited using FEBID.

3.5 Magnetic imaging in the TEM

Within a TEM the electron beam can experience deflections due to the magnetic induction produced by the sample magnetisation of ferromagnetic material. These deflections can be used to obtain qualitative and quantitative information about the magnetic structure of a sample. Their study and imaging within a TEM is referred to as Lorentz microscopy. Both of the TEMs used for the characterisation of magnetic samples in this thesis is equipped with the capability to perform Lorentz microscopy and image magnetic structure with a nanometer-scale resolution. The following subsections first describe the requirements to achieve magnetic imaging a TEM, then the underlying theory Lorentz TEM and finally the main Lorentz microscopy imaging techniques used in this thesis.

3.5.1 Field-free imaging and in-situ experiments

In TEM samples are placed in between the pole pieces of the objective lens. The strong magnetic field it produces (1-2T) can easily erase any magnetic structure that one would want to image. This is why in Lorentz microscopy the current in the objective lens is switched off (or significantly reduced) and its function in the microscope is replaced with two weaker Lorentz mini lenses. In the JEOL ARM used for this project they are called the condenser and objective mini lenses and are placed above and below the sample. Switching off the objective lens has two main consequences. First, a reduction of the achievable resolution of the microscope. This is because Lorentz lenses exhibit spherical aberrations that are up to three orders of magnitude greater than those of standard imaging objective lenses, which have a spherical aberration constant (C_s) of only a few millimetres [21]. This can be limited with aberration correction and it has been shown that a resolution of 1 nm is possible for field-free mode in STEM mode for the 200 kV JEOL ARM used in this thesis [22]. Secondly, even when switched off the objective lens has a remanent field of 80-150 Oe. By applying a degaussing current to the objective lens this residual field can be reduced to < 1 Oe using a specialised piece of hardware designed especially for the JEOL ARM - the "Warwick Box" [23]. Despite the strong fields it can produce the objective lens can still be used in magnetic imaging. It is a very useful tool for in-situ magnetisation experiments. Because of its position in relation to the sample it can be partially excited to produce a magnetic field perpendicular to the sample plane and parallel to the optic axis of the microscope. Then by tilting the stage as illustrated in Figure 3.8, one can utilise the component of the field that is parallel to the sample plane for a variety of magnetisation experiments. An expression for the magnitude of the plane-parallel component of the field in terms of the objective field H and the stage tilt angle α_t is given by equation 3.11. It must be noted that the out-of-plane component of the magnetic field can also affect the samples, however, the nanowires studied in this thesis have strong in-plane shape anisotropy, which restricts the sample magnetisation. Additionally, while the sample lies in a tilted position in order for it to be affected by the external field, for the experiments performed in this thesis, the external field is always switched off and the sample returned to the zero tilt position for imaging. This is done to ensure that only stable states of the structures studied are imaged.

$$H_{\parallel} = Hsin(\alpha_t) \tag{3.11}$$

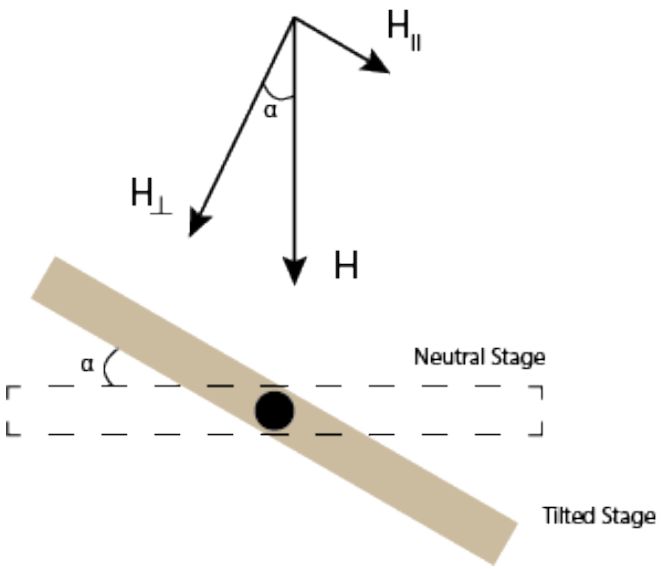

Figure 3.8: Tilting the sample stage by an angle α in order to apply an in-plane field to sample. The field is created by exciting the objective lens.

In this thesis, this method of applying an external magnetic field was used to induce different magnetisation states in the ferromagnetic nanowires patterned using FEBID. These included saturating the nanowires along their long dimension and nucleating magnetic DWs. Both of these applications along with more detail on their purpose and execution are provided in Chapter 4. The next sections provide more context on both the physics behind magnetic imaging in a TEM and specific techniques used in this project.

3.5.2 Theory of Lorentz TEM

The deflections experienced by electrons travelling through a magnetic field can be quantified using two approaches - classical and quantum mechanical. The classical explanation is based on the Lorentz force $\mathbf{F_L}$. For an electron with charge e the expression for it is given by 3.12:

$$\mathbf{F_L} = -e(\mathbf{v} \times \mathbf{B}) \tag{3.12}$$

Where $\mathbf{B}$ is the magnetic induction and $\mathbf{v}$ is the electron velocity. At this point, it is important to make a distinction between sample magnetisation $\mathbf{M}$ and induction $\mathbf{B}$. The quantity of interest is usually the former, however, it is the latter that can be directly imaged and

quantified with Lorentz microscopy. The two are related through the equation 3.13 ,

$$\mathbf{B} = \mu_0(\mathbf{H} + \mathbf{M}) \tag{3.13}$$

where **H** is the demagnetising field. Furthermore due to the cross-product present in the expression only the components of magnetic induction normal to the direction of the electron beam will exert the Lorentz force and cause deflections. The angle of these deflections for a uniform magnetised and with unvarying thickness t can be obtained from equation 3.14 and is displayed graphically in Figure 3.10.

$$\beta = \frac{e\lambda B_s t}{h} \tag{3.14}$$

Here λ is the electron wavelength, h is Planck's constant and B_s is the saturation induction of the sample. In the situation described **H** = 0 and the induction is directly proportional to the magnetization i.e. $\mathbf{B} = \mu_0\mathbf{M}$. A commonly given example for the scale of deflections due to Lorentz's force is that of a uniformly magnetised thin film. For example, a permalloy film with $B_s = 1$ T and $t = 20$ nm imaged using a 200 kV TEM deflects the beam by $\beta = 12.7$ µrad [12], which is orders of magnitude smaller than the typical deflections caused by Bragg scattering.

While in the paragraphs above we provided a classical description, it is essential to also consider a quantum mechanical wave optical approach to quantifying the effect magnetic induction has on the electron beam, as it provides us with a deeper understanding of the physical processes behind magnetic imaging. This is done through the Aharomov-Bohm effect, which describes the influence of an electromagnetic potential $(\mathbf{A})$ on the phase (ϕ) of charged particles [24]. To illustrate the Aharomov-Bohm effect the following thought experiment is often used. Two electrons are travelling on either side of an infinitely long magnetic element and interfering afterwards. Despite the fact that their paths do not directly go through an area with magnetic induction the electrons gain a phase difference because they each experience a different magnetic vector potential. This is illustrated in Figure 3.9. It should be noted that while in the specific case discussed here, the electrons only encounter a potential the same treatment can be applied to any arbitrary closed path inside or outside the sample. That being said the phase shift due to magnetic vector

potential(ϕ_m) is given by equation 3.15.

$$\phi_m = -\frac{e}{\hbar}\oint_C \mathbf{A}\cdot dl \tag{3.15}$$

Where the integration is along the closed loop (C) defined by the paths of the two electrons in Figure 3.9. This phase shift can be directly related to the magnetic induction $(\mathbf{B})$ by using Stokes theorem and substituting $B = \nabla \times \mathbf{A}$ resulting in equation 3.16.[25]

$$\phi_m = \frac{e}{\hbar}\int \mathbf{B}\cdot dS \tag{3.16}$$

Where the surface integral describes the magnetic flux through the surface enclosed between the trajectories of the two electrons. Evaluating this integral along the z direction in the scenario depicted in Figure 3.9, i.e., the sample is within the path traced by the electrons and has a uniform thickness and saturation induction, gives equation 3.17 [26].

$$\phi_m = \frac{e}{\hbar}B_s t x \tag{3.17}$$

Finally, taking the gradient of 3.17 along the x-direction shows the proportional relationship between the gradient of the phase and the Lorentz deflection angle (equation 3.18) thus reconciling the classical and quantum approaches [27]. It's worth noting that experimental image calculations (as the ones described in the final sections of this Chapter) usually utilise the latter.

$$\nabla_\perp \phi = \frac{2\pi\beta}{\lambda} = \frac{2\pi e B_s t}{h} \tag{3.18}$$

In addition to the magnetic phase, and regardless of whether a sample is magnetic or not, a further phase change occurs when electrons pass through a sample with variations in thickness (t) and/or in the mean inner potential of the material (V) [28]. This is referred to as the electrostatic phase and is given by:

$$\phi_e = \frac{\pi V t}{\lambda E} \tag{3.19}$$

Where E is the electron accelerating voltage. For samples in this thesis quantifying and minimizing ϕ_e has been a challenging task, as the samples studied have often had consid-

erable thickness variations.

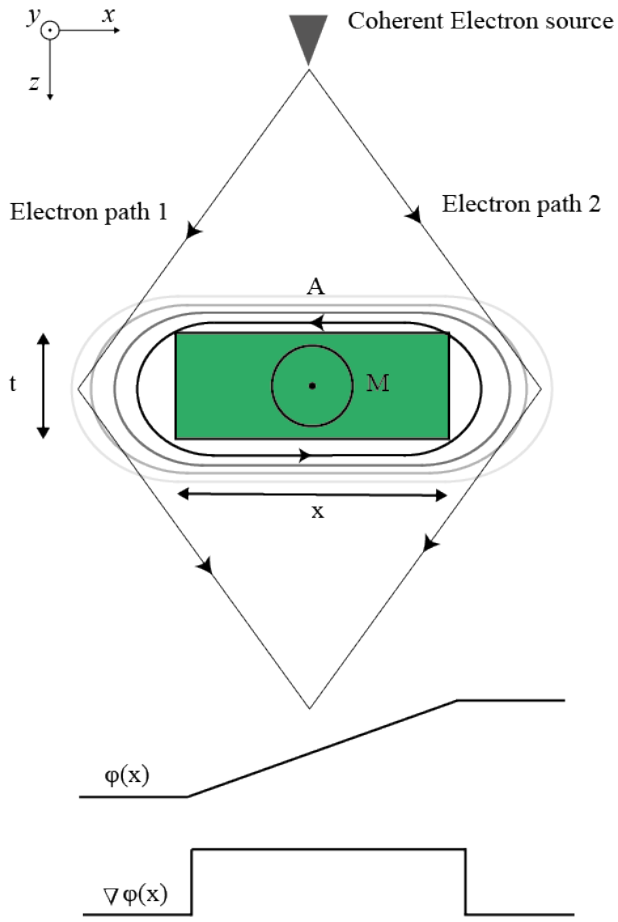

Figure 3.9: Illustration of the Aharomov-Bohm effect for two electrons taking different paths around a magnetic element with an associated magnetic vector potential A. Also included are profiles of the resulting phase and phase gradient.

3.5.3 Fresnel mode Lorentz microscopy

The only perceptible contrast differences in a standard in-focus bright field TEM image are amplitude (or diffraction) contrast even when imaging magnetic samples. This is because the phase changes that the electron beam experiences when passing through a magnetic potential are insufficient to produce visible contrast during in-focus imaging. This is why in order to obtain magnetic contrast in CTEM mode it is necessary to introduce further

aberrations to the contrast transfer function (3.7). This is done by using a non-zero defocus value - Δf of the main imaging lens and in such a way selecting to image a plane below or above the sample plane (underfocus and overfocus respectively). This method of imaging is referred to as Fresnel mode Lorentz microscopy and is a simple but powerful CTEM technique for the imaging of magnetic structures like DWs, magnetic vortexes, or skyrmions [29] [30][31]. As described at the start of the section this type of imaging is generally performed with the objective lens off, however, it is possible to utilize the method of creating in-plane fields by slightly exciting the objective lens described in Section 3.5.1 during Fresnel imaging. In this thesis, Fresnel mode was used to image magnetic structure during in-situ magnetisation experiments and was one of the main techniques used for identifying DWs in the Co and Fe nanowires. A schematic of Fresnel mode imaging in the cases of a multi-domain thin film (a)) and a single-domain nanowire (b)) are shown in Figure 3.10. There it can be seen that the Lorentz deflections of the electron beam cause bright or dark fringes in areas where the electrons converge or diverge respectively. In the multi-domain example such areas are the DWs, while in the case of single-domain nanowires Fresnel contrast can be seen on the edges of the wire (Figure 3.10 b)). In the second example this is because of the difference in deflection between electrons passing through the domains within the wire and the ones passing through free space. Due to the low magnitude of the Lorentz deflections to the electron beam it is often necessary to use very high levels of defocus (up to a few mm) to observe clear magnetic contrast during Fresnel imaging. It must be noted that Fresnel mode is a phase contrast imaging technique and Fresnel images contain electrostatic contributions to contrast due to the mean inner potential and thickness of the imaged structures. Additionally, Fresnel mode microscopy (and other techniques that rely on the phase of the electron beam to extract magnetic information) are not sensitive to magnetisation components parallel to the electron beam as mentioned in 3.5.2. components of magnetisation Chapter 4 describes the method that was used to decouple the magnetic and electrostatic contributions.

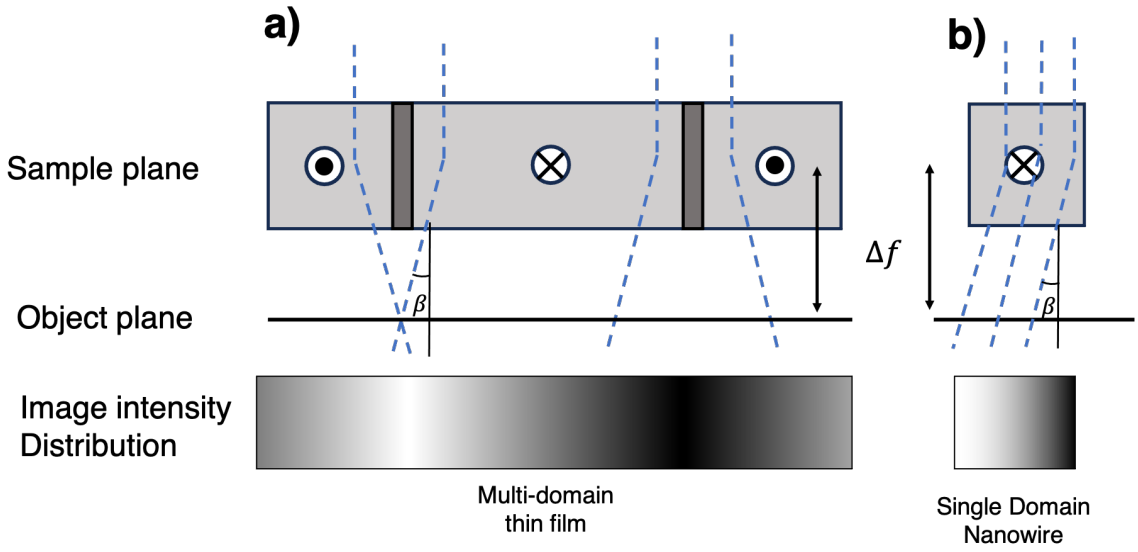

Figure 3.10: Diagram of Fresnel Imaging mode in the case of a multi-domain thin film (a)) and a single domain nanowire (b)). Incoming electrons are deflected resulting in dark areas when diverging and bright areas when converging.

An example of a Fresnel mode image of several magnetic structures can be seen in Figure 3.11. In the images, flux-closure structures are clearly visible in the squares and as stated earlier only regions of varying magnetisation (in this case the so-called low-angle DWs and the flux-closure core) cause Fresnel contrast. The direction of magnetisation in the sample can be inferred from this contrast and is indicated in the image using the blue arrows. In areas of constant magnetisation what we can see is simply amplitude or diffraction contrast. Magnetic contrast is also visible around the edges of the squares and the nanowires. In the latter the continuity of the bright and dark fringes on either edge of the nanowires indicates unchanging magnetisation along the length of the structure.

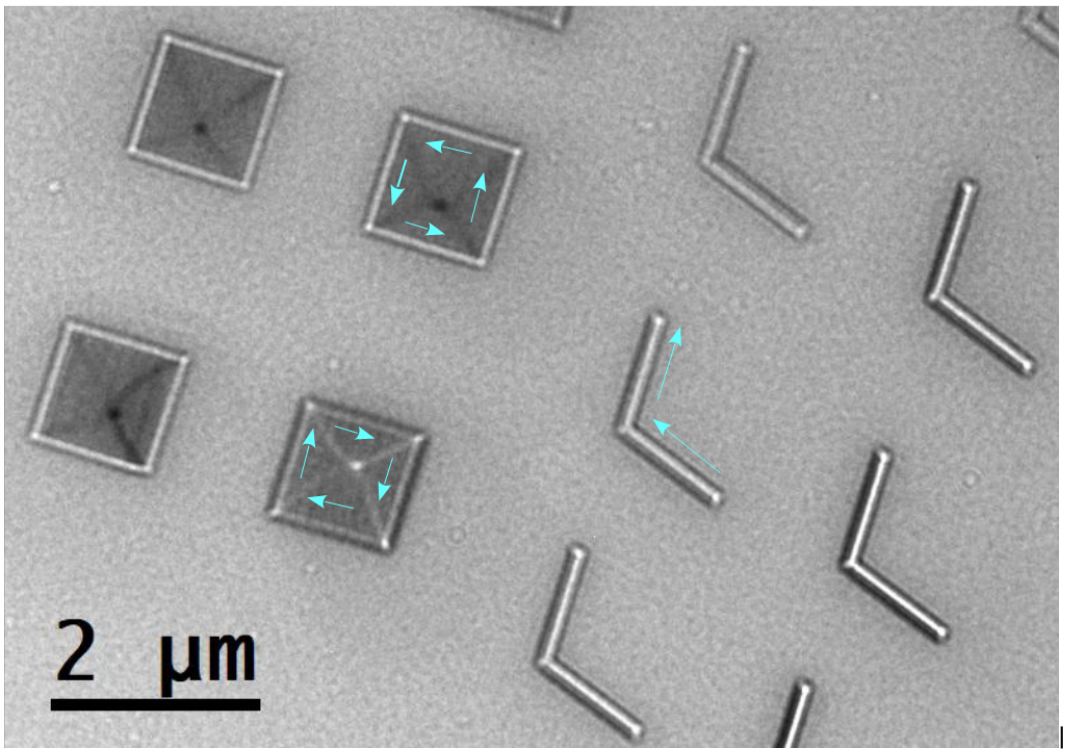

Figure 3.11: Fresnel Images of Co squares and nanowires. One can clearly see the magnetic flux closure structure in the squares and the dark contrast on the side of the nanowires indicating a saturated state. The inferred direction of the magnetisation is indicated using the blue arrows.

3.5.4 Calculation of Fresnel defocus

In order to interpret and quantify Fresnel mode images it is necessary to be aware of the image defocus. In the T20 and JEOL ARM microscopes, a defocus figure is provided for the objective lens. However, this is not the case for the mini (Lorentz) lens. Because of that, it was necessary to calculate it image post-acquisition using the Fresnel images. The way to do that is by using the contrast transfer function (CTF) $H(\mathbf{k}_\perp)$ (3.7) and the phase distribution function $\chi(\mathbf{k}_\perp)$ (3.4) in reciprocal space. For Fresnel imaging the relationship between the two can be simplified to the following form [18]:

$$H(\mathbf{k}_\perp) \approx sin(\chi(\mathbf{k}_\perp) \approx sin(\pi \Delta f \lambda |\mathbf{k}_\perp|^2) \tag{3.20}$$

To arrive at this expression we have assumed a highly convergent beam ($\theta_c \approx 0$) and that the other aberration contributions to $\chi(\mathbf{k}_\perp)$ are minimal compared to the one from the defocus Δf. This is true for most Fresnel imaging scenarios due to high defocus used. In the expression above there is clear relationship between defocus and the CTF. By setting the left hand side of the equation to zero ($H(\mathbf{k}_\perp) = 0$) it is possible to analytically solve the equation and obtain a defocus value. Clearly equation 3.20 evaluates to zero when the term inside the $sin()$ function is an integer multiple of π i.e when $\pi\Delta f\lambda|\mathbf{k}_\perp|^2 = n\pi$. Rearranging allows us to obtain an equation that directly links the defocus Δf to the spatial frequency $\mathbf{k}_\perp$ where the CTF equates to zero:

$$\Delta f = \frac{n}{\lambda|\mathbf{k}_\perp|^2} \tag{3.21}$$

In practice, the zeros of the CTF $H(\mathbf{k}_\perp)$ correspond to spatial frequencies ($\mathbf{k}_\perp$) not being transferred to the final image. These spatial frequencies can be accessed directly from the Fourier transform of the Fresnel image, where they appear as dark concentric rings. To accurately find the spatial frequency of the zeros ($\mathbf{k}_\perp$) an average radial profile is taken of the Fourier image, which is shown in Figure 3.12. There the spatial frequencies corresponding to zeros of the CTF can be seen as local minima and are indicated as red dots. Finally a measure of the defocus can be obtained by substituting the obtained values for $\mathbf{k}_\perp$ in equation 3.21. This process of quantifying defocus is used in Chapter 4 during the analysis of Fresnel images of several DWs.

3.5.5 Differential phase contrast

DPC imaging is a technique used in STEM, which provides quantitative information on the integrated magnetic induction of the sample [32] [33]. The basic principle behind it is that the electron beam deflections (β) due to the sample integrated induction ($B_s t$) are proportional to the gradient of the phase gained by the electrons transmitted through the sample ($\nabla\phi$) due to the Aharomov-Bohm effect shown in equation 3.18. In practice, DPC imaging is realised by rastering a converging probe onto the sample surface using a pair of scan coils. The probe is then deflected by the magnetic induction of the sample and finally directed back to the optic axis by additional de-scan coils located post-specimen. A specialized detector is used to collect the incoming electrons that form the image. A

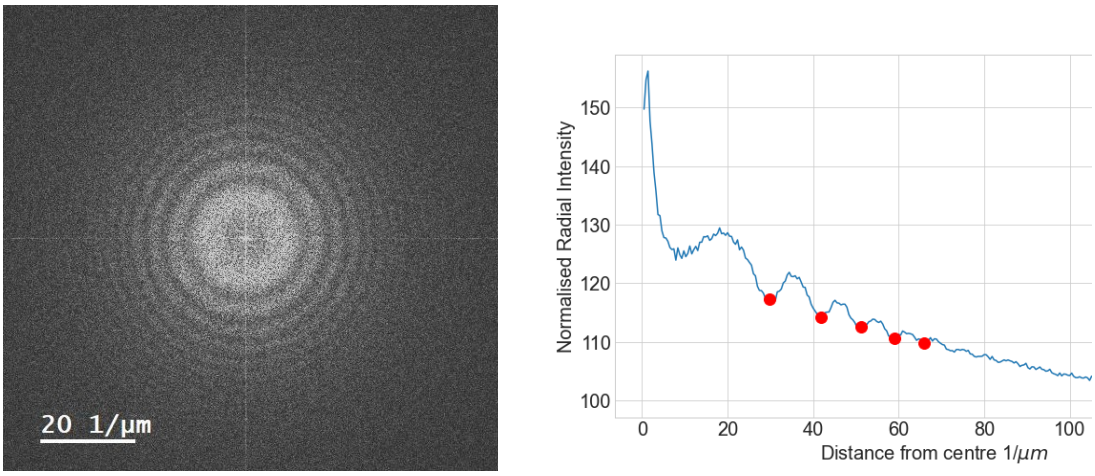

(a) (b)

Figure 3.12: FFT of image 3.11 showing zeros of the CTF $H(\mathbf{k}_\perp)$ as dark rings (a)) and a calculated radial profile of 3.12a (b)), where the same zeros are indicated with red dots.

diagram showing the DPC imaging process can be seen in Figure 3.13. In conventional DPC either a 4 or 8 quadrant segmented detector is used. The deflections in the beam due to the induction are then measured by summing the electrons incident on each segment (or the outer segments in the 8-quadrant detector) and taking the difference between opposing quadrants or halves of the detector. This results in two orthogonal integrated induction maps. By summing the electron illumination from each quadrant one can also obtain the equivalent of a bright field image of the sample allowing for the simultaneous acquisition of magnetic and structural data. This method of imaging is possible only if the magnetic deflections are small enough compared to the probe convergence angle α i.e $\beta < 0.1\alpha$. Another assumption of segmented detector DPC is that the electron beam incident on the detector produces a disk of constant intensity. This is not true for crystalline samples, in which diffraction due to Bragg scattering introduces variations in the contrast within the disk, making the images difficult to process and interpret. In recent years the advancement of detector and read-out technology [34] has facilitated the use of pixelated detectors for magnetic DPC imaging [35] along with other applications [36] [37]. For this thesis, pixelated DPC was one of the primary tools for quantitative magnetic imaging of the FEBID deposited nanostructures. The imaging was done on the JEOL ARM and the detector used was the 256×256 pixel Medipix3 [38] direct electron detector (DED) equipped with a Merlin readout system [34]. There are several advantages to using this

particular system. First, DEDs boast superior frame rates. The Medipix3 system, for example, captures images at up to 1200 frames per second (fps), vastly exceeding the typical 10 fps of conventional CCD cameras. This speed difference stems from the readout mechanism. The Medipix3 employs a readout device on each pixel, allowing for immediate signal processing. CCDs, on the other hand, utilize a charge-shifting system that requires moving the charge to a dedicated readout register, introducing a bottleneck. Fast readout speed directly translates to more efficient data acquisition and to fewer artefacts due to microscope instability and stage drift. An additional advantage of the Medipix3 system is the better signal-to-noise ratio. DEDs offer better signal-to-noise ratio (SNR) and less noise compared to CCD cameras mostly due to the absence of a scintillation layer. In CCDs, a scintillation layer converts electrons to photons, which are then registered by the detector [12]. This can sometimes lead to signal interference between adjacent pixels during charge transfer. Conversely, the direct readout mechanism in DEDs significantly reduces the possibility of charge spreading to neighboring pixels, minimizing crosstalk and noise. For this project the Medipix3 was used for the collection of 4D STEM DPC data sets, meaning a 2D image of the electron diffraction disk was collected at every point of a 2D scan. These were very large (up to 35 GB each) but provided the in-depth information necessary for advanced processing methods like cross-correlation edge filtering which allows for the filtering of unwanted structural information. The technique works by overlaying an image of an "ideal" disk edge to every disk recorded during the DPC scan and computing the offset which gives a direct measure of the Lorentz deflection described in Section 3.5.2 [35]. For this project the ideal disk edge is obtained from an average of disk images taken from points in the scan where the electron beam does not pass through with the sample. This method was preferred over alternative approaches that utilise the entire disk intensity, because it computes the shifts of the transmitted beam solely based on the shift of the disk edge. This filters out most of the unwanted structural information that appears as variation in intensity within the transmitted disk. This technique was implemented using the Python based FPD library and the phase_correlation() processing function [39].

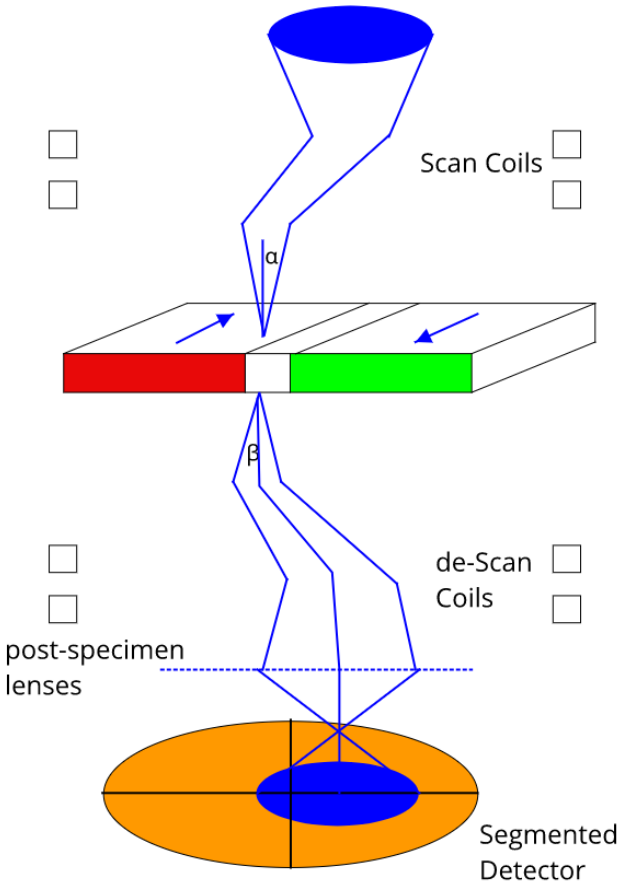

Figure 3.13: DPC imaging - the probe is rastered across the specimen using scan coils, the beam is deflected by the magnetic induction and the resulting signal is transmitted to a segmented detector.

Example images obtained using 4D STEM and processed using a cross-correlation method can be seen in Figure 3.14. The figure displays three images of the same 1 µm × µm Co square deposited using FEBID. The first image (a)) is the sum bright field image which shows the grainy and speckled structure of the sample, while b) and c) show the maps of the integrated induction in the directions signified by the arrows.

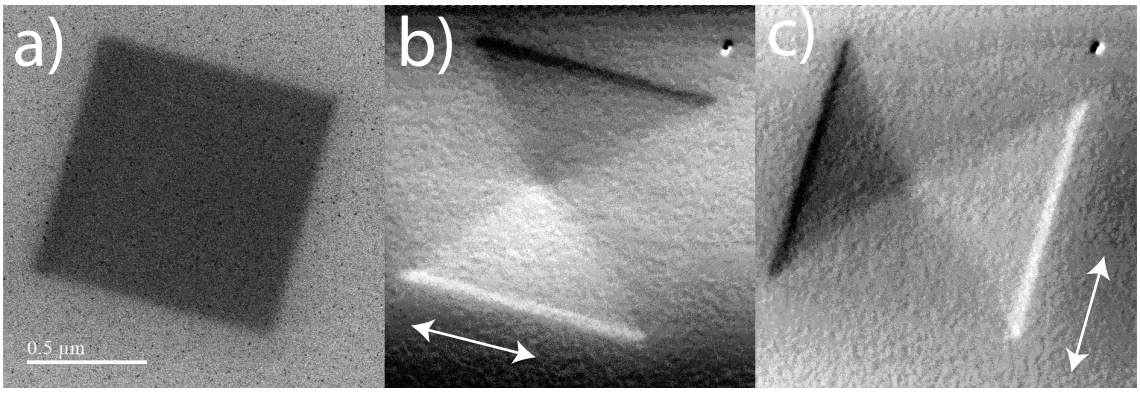

Figure 3.14: Pixelated DPC images of a 1 µm × 1 µm Co square with a vortex magnetic structure. a) shows the bright field sum image, b) and c) show the integrated induction in the directions specified by the arrows.

3.5.6 Simulated Lorentz microscopy images

Correct image interpretation is a key issue in the world of electron microscopy. This is also true for Lorentz microscopy. As mentioned in the previous chapter a tool that can aid with that is the micromagnetic simulation. In particular, it is possible to generate accurate DPC and Fresnel mode images using results from micromagnetic simulations that can help with the interpretation of images containing complex or obscured by electrostatic contrast magnetisation configurations. In this thesis, simulated Lorentz microscopy images of Co and Fe nanowires were generated using the "FPD" software package ([39]), which is a Python code base providing various tools for the analysis of pixelated detector data. It was used in the calculation of simulated experimental images in both Chapters 3 and 4. The formation of these images relies on computing the phase of an electron beam passing through the simulated magnetic structure. In the "FPD" package, two-dimensional (2D) datasets of the in-plane magnetization components (m_x and m_y) are utilized to derive this phase. This is accomplished by employing the method outlined by M. Beleggia *et al.* ([40]) and the following mathematical relationship:

$$\Phi_m = \frac{h}{2e} i\pi\mu_0 t \frac{M_x k_y - M_y k_x}{k_x^2 + k_y^2} \tag{3.22}$$

Where k_x and k_y are the x and y components of the reciprocal space vector $\mathbf{k}_\perp$ and Φ_m , M_x and M_y are the numerically calculated Fast Fourier transforms (FFT) of the magnetic

phase contribution ϕ_m and the in-plane magnetisation components m_x and m_y. A 2D image of the phase due to the magnetisation of the simulated structure can then be obtained simply by computing an inverse Fourier transform of the result of the above equation. This is implemented in FPD in the mag_phase() function. Electrostatic contributions to the phase (ϕ_e) can also be included in the calculation to give the total phase change due to the sample ($\phi_t = \phi_e + \phi_m$) by simply defining the thickness of the desired structure $t(x,y)$ and the mean inner potential V_0 and computing via equation 3.19. The process of obtaining $t(x,y)$ for the nanowires that are the subject of this thesis is described in Section 4.8.3. After having obtained an image of the phase (3.15b) it is only required to numerically calculate its gradient in 2 orthogonal directions in order to derive simulated DPC images (3.15c and 3.15d). This can be achieved with in-built functions in the FPD package or by using external image and data processing libraries. Examples of DPC images for a simulation of a 500 nm $\times$ 500 nm $\times$ 30 nm permalloy square with cell dimension of 2 nm $\times$ 2 nm $\times$ 2 nm are shown in Figure 3.15. In addition to DPC, it is also possible to obtain simulated Fresnel mode images using the phase from equation 3.22. Figure 3.16 shows Fresnel images calculated using two different defocus values (Δf = 10 µm (a)) and Δf = 400 µm (b)) of the same square depicted in 3.15. These were calculated using the mag_tools.fresnel() function in FPD. The wavelength and beam divergence values used in the image calculation were $\lambda = 2.51$ pm $\theta_c = 10^{-6}$ rad respectively. In order to describe how these are computed we refer back to Section 3.3.3. There the final image intensity $\left(I(\mathbf{r}_\perp)\right)$ recorded by a TEM was shown to be the squared convolution of the microscope transfer function - $h(\mathbf{r}_\perp)$ and the electron wave function exiting the sample - $(\psi(\mathbf{r}_\perp)$ i.e. equation 3.9. In order to avoid calculating a complex convolution both the wavefunction and contrast transfer function are converted to reciprocal space using a fast Fourier transform resulting in the following expression:

$$I(\mathbf{r}_\perp) = |g(\mathbf{r}_\perp)^2| = \mathscr{F}^{-1}\left|H(\mathbf{k}_\perp)\Psi(\mathbf{k}_\perp)\right|^2 \tag{3.23}$$

For Fresnel imaging the first term in this equation has the following form :

$$H_{Fr}(\mathbf{k}_\perp) = e^{-i\pi\Delta\lambda|\mathbf{k}_\perp|^2} e^{-\frac{(\pi\theta_c\Delta)^2}{ln(2)}|\mathbf{k}_\perp|^2} \tag{3.24}$$

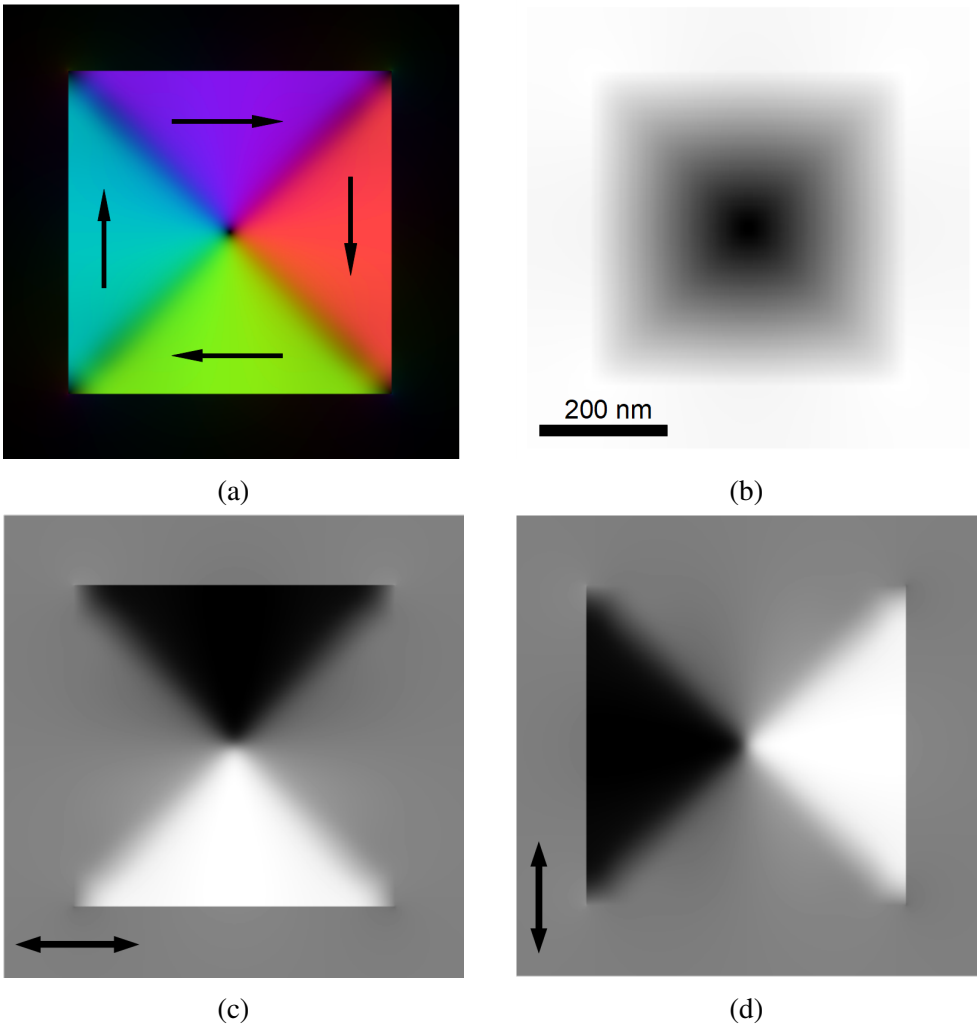

Figure 3.15: Calculated DPC images showing two orthogonal induction components (3.15c and 3.15d) and an image of the magnetic phase (3.15b) from simulation of a 500 nm × 500 nm × 30 nm permalloy square in a flux closure magnetisation configuration (3.15a).

In equation 3.24 the spherical aberration $\left(C_s\right)$ contribution to the phase distortion function $\left(\chi(\mathbf{k}_\perp)\right)$ in 3.4 has been ignored. This is a valid assumption for most magnetic imaging scenarios because the magnitude of the Lorentz deflections of the electron beam is typically too small ($\sim$ 5 - 20 µrad) for spherical aberration to have a negative effect on the images. The envelope function (3.5) has remained unchanged. The second quantity of interest i.e the sample wavefunction $\psi(\mathbf{r}_\perp)$ is described by its amplitude $\left(a(\mathbf{r}_\perp)\right)$ and phase$\left(\phi(\mathbf{r}_\perp)\right)$ - 3.3. In Fourier space it has the following representation:

$$\Psi(\mathbf{k}_\perp) = \mathscr{F}\left|\psi(\mathbf{r}_\perp)\right| = \mathscr{F}\left|a(\mathbf{r}_\perp)e^{i\phi(\mathbf{r}_\perp)}\right| \tag{3.25}$$

In the current calculation, only the magnetic phase given by 3.22 is considered. The electrostatic contributions to phase are ignored, as in this scenario they would only introduce variation in contrast on the edges of the square. For the amplitude function because of the unchanging thickness of the structure in question, we assume a constant value of 0.8 inside the square and 1 outside it, which in practice represents 80 % transmission of the electron beam through the sample. For the simulated Fresnel images in Chapter 4 a custom amplitude function is assigned to each different nanowire based on its geometry and thickness. This function is constructed in a similar manner to the one for the square above, however due to the varying thickness of the nanowires the percentage of the transmitted beam is also varied accordingly across the geometry. The code used to generate it is available in Appendix A.2. Having obtained expressions for both the contrast transfer function and the sample wavefunction the final step to obtaining simulated Fresnel images is to plug them into equation 3.23 and calculate the inverse Fourier transform. The simulated images presented here show good agreement with the experimental data presented in the Fresnel imaging section of the chapter in the central areas of the square. However, to properly describe the contrast on the edges of the square the electrostatic contributions need to be considered. The following chapters describe how the techniques and methods presented so far are used to study magnetic DWs in nanowires with curved profiles. Chapter 4 focuses on micromagnetic simulations of cylindrical segment nanowires and calculation of experimental images, while Chapter 5 presents an empirical study of nanowires with curved profiles fabricated by FEBID and characterised by Lorentz mode TEM.

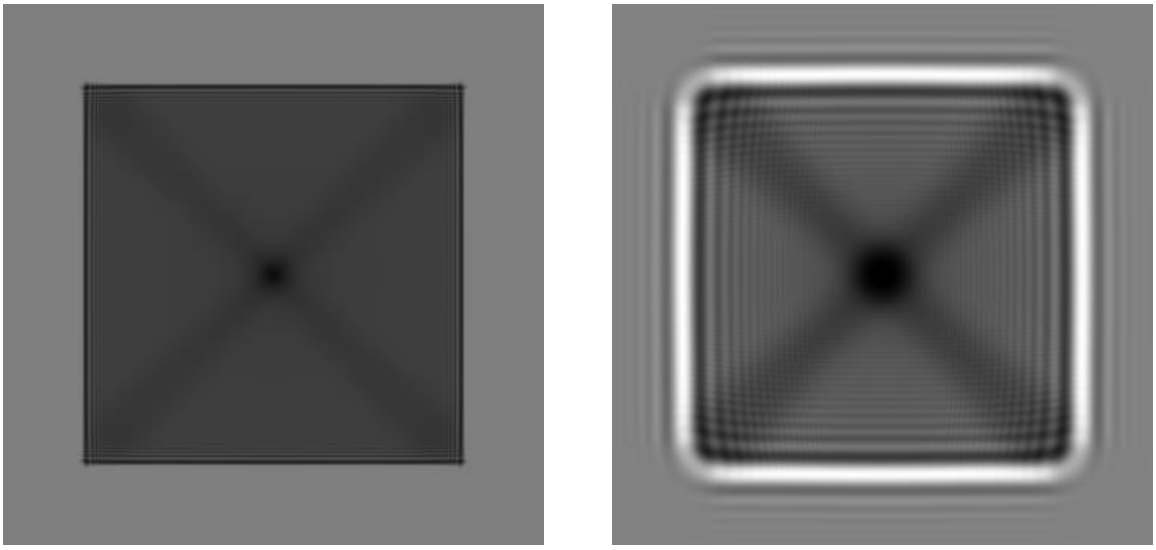

(a) (b)

Figure 3.16: Calculated Fresnel images with $\Delta f = 10$ µm (a)) and $\Delta f = 400$ µm (b)) obtained from a simulation of 500 nm $\times$ 500 nm $\times$ 20 nm permalloy square in a flux closure magnetisation configuration (3.15a).

References

[1] J. Goldstein. *Scanning Electron Microscopy and X-ray Microanalysis*. Springer US, 2003.

[2] J. Orloff. *High resolution focused ion beams : FIB and its applications*. Kluwer Academic/Plenum Publishers, 2003.

[3] W. F. van Dorp and C. W. Hagen. A critical literature review of focused electron beam induced deposition. *Journal of Applied Physics*, 104(8):081301, 2008.

[4] L. Skoric, D. Sanz-Hernández, F. Meng, C. Donnelly, S. Merino-Aceituno, and A. Fernández-Pacheco. Layer-by-layer growth of complex-shaped three-dimensional nanostructures with focused electron beams. *Nano Letters*, 20(1):184–191, 2019.

[5] E. Nikulina, O. Idigoras, P. Vavassori, A. Chuvilin, and A. Berger. Magneto-optical magnetometry of individual 30 nm cobalt nanowires grown by electron beam induced deposition. *Applied Physics Letters*, 100(14):142401, 2012.

[6] A. Fernandez-Pacheco. *Studies of Nanoconstrictions, Nanowires and Fe3O4 Thin Films*. Springer Berlin Heidelberg, 2011.

[7] A. Fernández-Pacheco, J. M. De Teresa, R. Córdoba, and M. R. Ibarra. Magnetotransport properties of high-quality cobalt nanowires grown by focused-electron-beam-induced deposition. *Journal of Physics D: Applied Physics*, 42(5):055005, 2009.

[8] R. Winkler, B. B. Lewis, J. D. Fowlkes, P. D. Rack, and H. Plank. High-fidelity 3D-nanoprinting via focused electron beams: Growth fundamentals. *ACS Applied Nano Materials*, 1(3):1014–1027, 2018.

[9] P. J. Kelly and R. D. Arnell. Magnetron sputtering: a review of recent developments and applications. *Vacuum*, 56(3):159–172, 2000.

[10] J. T. Gudmundsson. Physics and technology of magnetron sputtering discharges. *Plasma Sources Science and Technology*, 29(11):113001, 2020.

[11] D. J. Smith. Progress and perspectives for atomic-resolution electron microscopy. *Microscopy and Microanalysis*, 11(S02):159–166, 2005.

[12] L. Reimer. *Transmission electron microscopy : physics of image formation and microanalysis*. Springer, 2008.

[13] C. B. Carter and D. B. Williams. *Transmission electron microscopy : diffraction, imaging, and spectrometry*. Springer, 2016.

[14] C. Kisielowski, B. Freitag, M. Bischoff, H. van Lin, S. Lazar, G. Knippels, P. Tiemeijer, M. van der Stam, S. von Harrach, and M. Stekelenburg. Detection of single atoms and buried defects in three dimensions by aberration-corrected electron microscope with 0.5 Å information limit. *Microscopy and Microanalysis*, 14(5):469–477, 2008.

[15] J. Orloff. *Handbook of Charged Particle Optics (2nd ed.)*. CRC Press, 2008.

[16] R. H. Fowler and L. Nordheim. Electron emission in intense electric fields. *Proceedings of the Royal Society A*, 119(781):173–181, 1928.

[17] M. de Graef. Lorentz microscopy: Theoretical basis and image simulations. *Elsevier*, pages 27–67, 2001.

[18] D. B. Williams and C. B. Carter. *Transmission Electron Microscopy*. Springer US, 2009.

[19] P. B. Hirsch, A. Howie, R. B. Nicholson, D. W. Pashley, and M. J. Whelan. *Electron Microscopy of Thin Crystals*. Butterworths, 1965.

[20] M. T. Otten. High-angle annular dark-field imaging on a TEM/STEM system. *Journal of Electron Microscopy Technique*, 17(2):221–230, 1992.

[21] B. Freitag, M. Bischoff, H. Mueller, P. Hartel, and H. Harrach. Sub-nanometer resolution in field-free imaging using a titan 80-300 with lorentz lens and image cs-corrector at 300kv acceleration voltage. *Microscopy and Microanalysis*, 15:184–185, 2009.

[22] S. McVitie, D. McGrouther, S. McFadzean, D.A. MacLaren, K.J. O'Shea, and M.J. Benitez. Aberration corrected Lorentz scanning transmission electron microscopy. *Ultramicroscopy*, 152:57–62, 2015.

[23] A. Kohn and A. Habibi. Adapting a JEM-2100F for magnetic imaging. *JEOL News*, 47(1):17–22, 2012.

[24] Y. Aharonov and D. Bohm. Significance of electromagnetic potentials in the quantum theory. *Phys. Rev.*, 115:485–491, 1959.

[25] S. McVitie and G. S. White. Imaging Amperian currents by Lorentz microscopy. *Journal of Physics D: Applied Physics*, 37(2):280–288, 2003.

[26] S. McVitie and M. Cushley. Quantitative Fresnel Lorentz microscopy and the transport of intensity equation. *Ultramicroscopy*, 106(4-5):423–431, 2006.

[27] J. N. Chapman, I. R. McFadyen, and S. McVitie. Modified differential phase contrast Lorentz microscopy for improved imaging of magnetic structures. *IEEE Transactions on Magnetics*, 26:1506–1511, 1990.

[28] J. C. H. Spence. On the accurate measurement of structure-factor amplitudes and phases by electron diffraction. *Acta Crystallographica Section A*, 49(2):231–260, 1993.

[29] J. N. Chapman. The investigation of magnetic domain structures in thin foils by electron microscopy. *Journal of Physics D: Applied Physics*, page 623, 1984.

[30] J. N. Chapman, E. M. Waddell, P. E. Batson, and R. P. Ferrier. The Fresnel mode of Lorentz microscopy using a scanning transmission electron microscope. *Ultramicroscopy*, 4(3):283–292, 1979.

[31] D. Ngo and S. McVitie. Visualization of vortex core polarity in NiFe nanodots by tilted Fresnel images. *Ultramicroscopy*, 111(8):1276–1285, 2011.

[32] N. Shibata, S. D. Findlay, Y. Kohno, H. Sawada, Y. Kondo, and Y. Ikuhara. Differential phase-contrast microscopy at atomic resolution. *Nature Physics*, 8(8):611–615, 2012.

[33] J. N. Chapman, P. E. Batson, E. M. Waddell, and R. P. Ferrier. The direct determination of magnetic domain wall profiles by differential phase contrast electron microscopy. *Ultramicroscopy*, 3:203–214, 1978.

[34] R. Plackett, I. Horswell, E. N. Gimenez, J. Marchal, D. Omar, and N. Tartoni. Merlin: a fast versatile readout system for Medipix3. *Journal of Instrumentation*, 8(01): C01038, 2013.

[35] M. Krajnak, D. McGrouther, D. Maneuski, V. O' Shea, and S. McVitie. Pixelated detectors and improved efficiency for magnetic imaging in STEM differential phase contrast. *Ultramicroscopy*, 165:42–50, 2016.

[36] T. J. Pennycook, A. R. Lupini, H. Yang, M. F. Murfitt, L. Jones, and P. D. Nellist. Efficient phase contrast imaging in stem using a pixelated detector. Part 1: Experimental demonstration at atomic resolution. *Ultramicroscopy*, 151:160–167, 2015.

[37] H. Yang, T. J. Pennycook, and P. D. Nellist. Efficient phase contrast imaging in stem using a pixelated detector. Part II: Optimisation of imaging conditions. *Ultramicroscopy*, 151:232–239, 2015.

[38] R. Ballabriga, M. Campbell, E. Heijne, X. Llopart, L. Tlustos, and W. Wong. Medipix3: A 64k pixel detector readout chip working in single photon counting mode with improved spectrometric performance. *Nuclear Instruments and Methods in Physics Research Section A: Accelerators, Spectrometers, Detectors and Associated Equipment*, 633:S15–S18, 2011.

[39] G. Paterson. Fpd: Fast pixelated detector data storage, analysis and visualisation. https://gitlab.com/fpdpy/fpd. Accessed 20/05/2020.

[40] M. Beleggia, M. A. Schofield, Y. Zhu, M. Malac, Z. Liu, and M. Freeman. Quantitative study of magnetic field distribution by electron holography and micromagnetic simulations. *Applied Physics Letters*, 83(7):1435–1437, 2003.

4 Simulations of cylindrical segment nanowires

Contents

4.1 Introduction

Micromagnetic simulations are an invaluable tool for the study of novel physics in the field of magnetism. They can be used to explore the magnetisation in complex geometries, provide insight into experimental results and aid experimental design. They are an invaluable tool in the study of the magnetic properties of nanowires [1] [2] [3]. As mentioned in Chapter 1, the simulation package used is the finite-difference based mumax3. It has in-built functionalities that allow for simple geometric shapes to be scaled, rotated, moved and combined to form complex parametric shapes, for which the resulting magnetisation can be calculated. All of this is achieved by simple scripting in the Go programming language developed by Google and allows the user to easily customize and alter the simulation based on the research requirement. On top of that, mumax3 utilises GPU acceleration to speed up calculations and reduce the overall simulation time. Recently micromagnetic simulations have been widely used for the research of curved ferromagnetic structures like toruses [4] and cylindrical nanowires [5]. The latter are particularly interesting for devices based on DW propagation because it has been shown that the Walker breakdown phenomenon which limits DW velocity can be suppressed for some magnetisation configurations within cylindrical nanowires [6]. In this chapter, we further explore nanowires with curved edges, but with the addition of broken cylindrical symmetry, which may favour different DW types. We do so by performing micromagnetic simulations of cylindrical segment nanowires and analysing the resulting magnetisation states. The purpose of this is to search for stable and narrow domain walls (DWs) facilitated by the curvature of the nanowires. The following sections discuss the initialisation of the simulations, the DWs observed in different cylindrical structures, their stability and their size. Finally, we discuss how simulated Lorentz TEM images of the different magnetisation states are calculated and used in the characterisation and identification of states within physical nanowires.

4.2 Simulation initialisation

To begin a micromagnetic simulation the user of mumax3 is required to provide a set of material parameters and a geometry. For this thesis, the selection of those was influenced by the fact that physical versions of the simulated nanowires would be fabricated using the FEBID technique described in Section 3.2.2. Because FEBID is a complex deposition

process, which involves the use of a precursor gas and possible hydrocarbon contamination in the microscope chamber, the resulting nanostructures have a variable composition [7] [8]. There were two magnetic precursor materials available for deposition - $Co_2(CO)_8$ and $Fe(CO)_5$ in the University of Glasgow FEBID-equipped PFIB system. For these materials under standard deposition conditions the resulting nanostructures are polycrystalline and with a typical metal purity of $\sim 75\%$ [9] [10]. Based on this figure the following two sets of starting parameters are used for the simulations - $M_{s1} = 1300 \times 10^3$ A/m, $A_1 = 1.5 \times 10^{-11}$ J/m [11] [12] and $M_{s2} = 900 \times 10^3$ A/m, $A_2 = 1.3 \times 10^{-11}$ J/m [13] with the first set representing 70% pure polycrystalline Co and the second 70% pure polycrystalline Fe. Because of this no magnetocrystalline anisotropy contribution to the energy of the system was included in either set of the starting parameters. As stated in Chapter 1 of the thesis, in micromagnetic simulations the simulated geometry is subdivided into cuboid cells with each cell being assigned a magnetic moment of fixed magnitude. In a micromagnetic framework it is assumed that this magnetic moment represents the magnetisation for the entire volume of the cell. This is why it is important to choose a cell size smaller than the exchange length (l_{ex}) of the simulated material. Typical values for Fe and Co are $l_{ex} = 2.3$ nm and $l_{ex} = 3.8$ nm respectively [14]. For this thesis, a universal cell size of 2 nm $\times$ 2 nm $\times$ 2 nm was chosen. With these parameters, several sets of straight and L-shaped quarter cylinder (QC) and half cylinder (HC) nanowire geometries were initialised. These geometries were generated using the mumax3 language by manipulating the readily available basic shapes like cuboids, cylinders and spheres. An example of the code used to generate nanowire geometries and run the simulations is available in the Appendix. Figure 4.1 shows 2D cross-sections of the simulated geometries and Figure 4.2 shows the difference between the L-shape and straight geometries. The reason L-shaped nanowires were chosen was because the shape naturally allows for the formation of a DW in the vertex of the L, making DW in L-shaped nanowires easy to produce experimentally. In contrast, straight nanowires offer a different advantage. Their uniform geometry allows observation of a wider variety of DW types and provides a platform to study how edge curvature influences DW formation within cylindrical segment nanowires. Additionally, by simulating both QC and HC structures, it is possible to see the effect of larger nanowire curvature and thickness on DW formation. For each combination of nanowire profile and shape (e.g. straight HC, L-shape QC etc.) a set of simulations with varying sizes was performed. The length (size in the x-direction) of the simulated nanowires was chosen to

be 2 µm (each arm of the L-shape geometry was set to 1 µm) and the thickness ranged from $t_{QC} = 10$ - 50 nm for the QC nanowires and $t_{HC} = 20$ - 100 nm for the HC ones with the width (w) varying proportionally with the thickness. These lengths were chosen in order to cap the nanowire width at 200 nm for bot the QC and HC geometries. Doing this ensured reasonable simulation times and an appropriate aspect ratio between the maximum nanowire width and length.

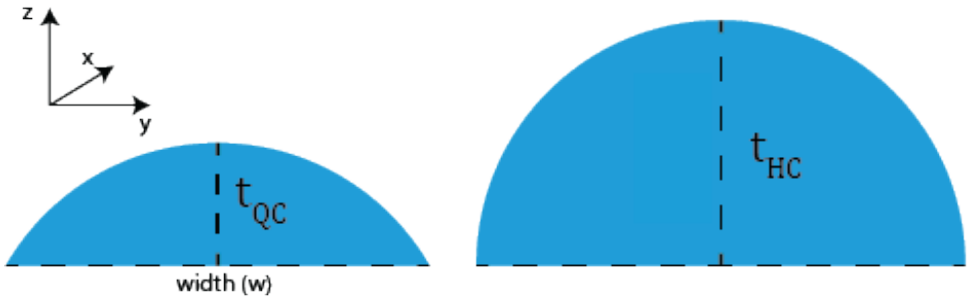

Figure 4.1: Example cross-sections of the nanowires geometries studied in this thesis - QC and HC with the nanowire dimensions denoted as thickness (t) and width (w).

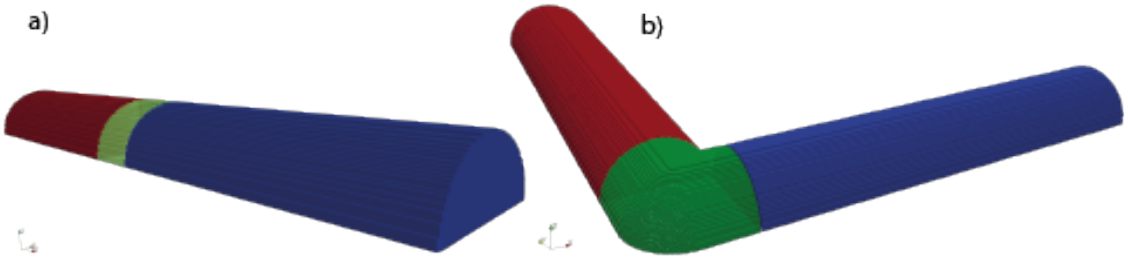

Figure 4.2: Simulated nanowire geometries - Straight (a)) vs. L-shape (b)) nanowire. Red and blue regions represent oppositely oriented domains, while green represents the DW region.

The goal of the simulations was to map the different DWs that can exist as metastable structures in the described nanowire geometries. To do that the nanowire simulation was

set up in a head-to-head magnetisation configuration with two oppositely pointing domains and a DW region in between. In order to maximise the chances of finding all the possible DW states for every given simulation, several different starting magnetisation states were considered in the DW region in the middle of the wire. Figure 4.3 depicts 2D vector representations of the various initial states under consideration, with a focus on the central region of the nanowires. These include an in-plane transverse magnetisation state (a) and d)), an out-of-plane transverse magnetisation (b) and e)) and a vortex state magnetisation state (c) and f)) for a straight and an L-shaped nanowire respectively. It should be noted that the the diagrams in Figure 4.3 display a sub-sampled version of the simulation with increased vector sizes and decreased vector density to aid with the visualisation of the state. Additionally, while only single slices of the 3D structures are provided, the magnetisation structure they show is representative for the entire volume. Examples of how the DW magnetisation varies along the nanowire thickness are shown in Figure 4.5 a)-d) for QC geometries and 4.9 for HC geometries. For each nanowire size, a simulation was performed with each of these starting states. In the situations considered in this project, namely looking for equilibrium magnetisation states, the magnetization vector is mainly adjusting to minimize the system's free energy. This adjustment happens through the damping term in the LLG equation, while the spiral motion introduced by the precessional term is less relevant. Therefore the relax() numerical solver, which allows the effective field to point towards a state of decreasing energy and disables the precesional term of the LLG equation, was used. The Gilbert damping parameter was set to an artificially high $\alpha = 0.5$ in order to reduce the time it takes for the system to reach a stable state [15]. Similarly high damping parameters were used in the simulation of Fe and Co spheres - [16] $\alpha = 0.1$ and thin films-[17] $\alpha = 1$. It must be noted that normally finite-difference software is not ideal for the simulation of curved structures like the ones discussed here. This is due to the staircase effect which appears when trying to approximate curvature with cuboid cells. In mumax3 this is corrected by an in-built function (EdgeSmooth = n) that sub-divides cells on the surface of the geometry n^3 times in order to better approximate the curvature of the shape. For this project, the highest possible subdivision with n = 8 was chosen to achieve the best possible approximation of a smooth curved edge. Examples of the simulation files used in this thesis are available in Appendix A.1.

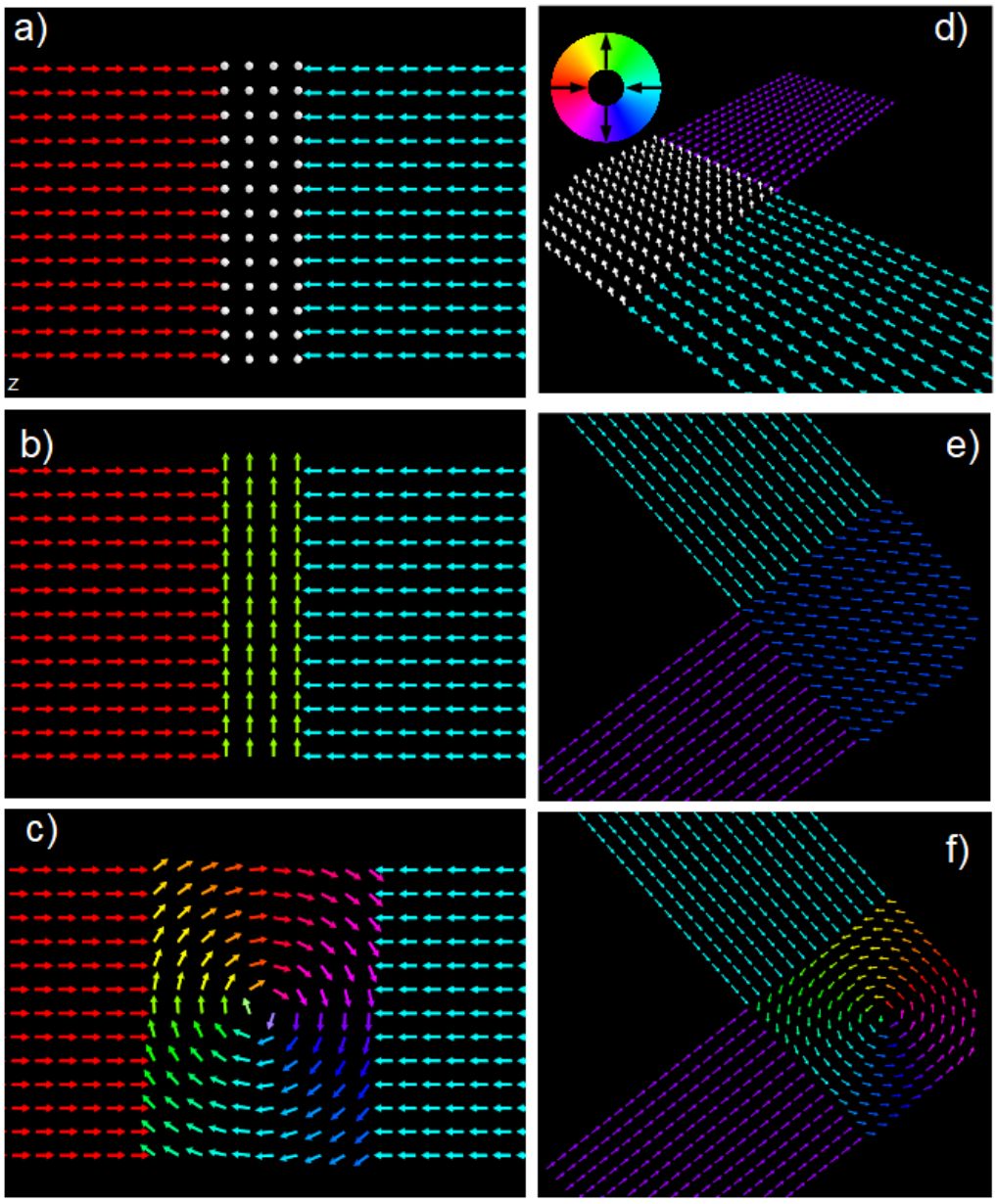

Figure 4.3: Simulation starting states for straight (a) through c)) and L-shape (d) through f)) nanowire simulations. a)- straight wire out-of-plane wall state, b)-straight wire in-plane transverse wall state, c)-straight wire vortex wall state, d)-L-shaped wire Out-of-plane wall state, e)-L-shaped wire in-plane transverse wall state, f)-L-shaped wire vortex wall state. Diagrams of L-shaped nanowires are rotated to best display the magnetisation state. The colour wheel and vectors directions apply to all images. White color represents out-of-plane magnetisation.

4.3 Domain walls in quarter cylinder nanowires

The first simulation results presented here are from nanowires with QC profiles. Static, energy-minimisation simulations were conducted as described in Section 4.2 using the stated parameters and dimensions for QC nanowires. The QC nanowires were found to support both states that were similar to ones observed in planar nanowires (described in Section 2.2) and some unique ones. 2D diagrams of the different DWs observed can be seen in Figure 4.4.

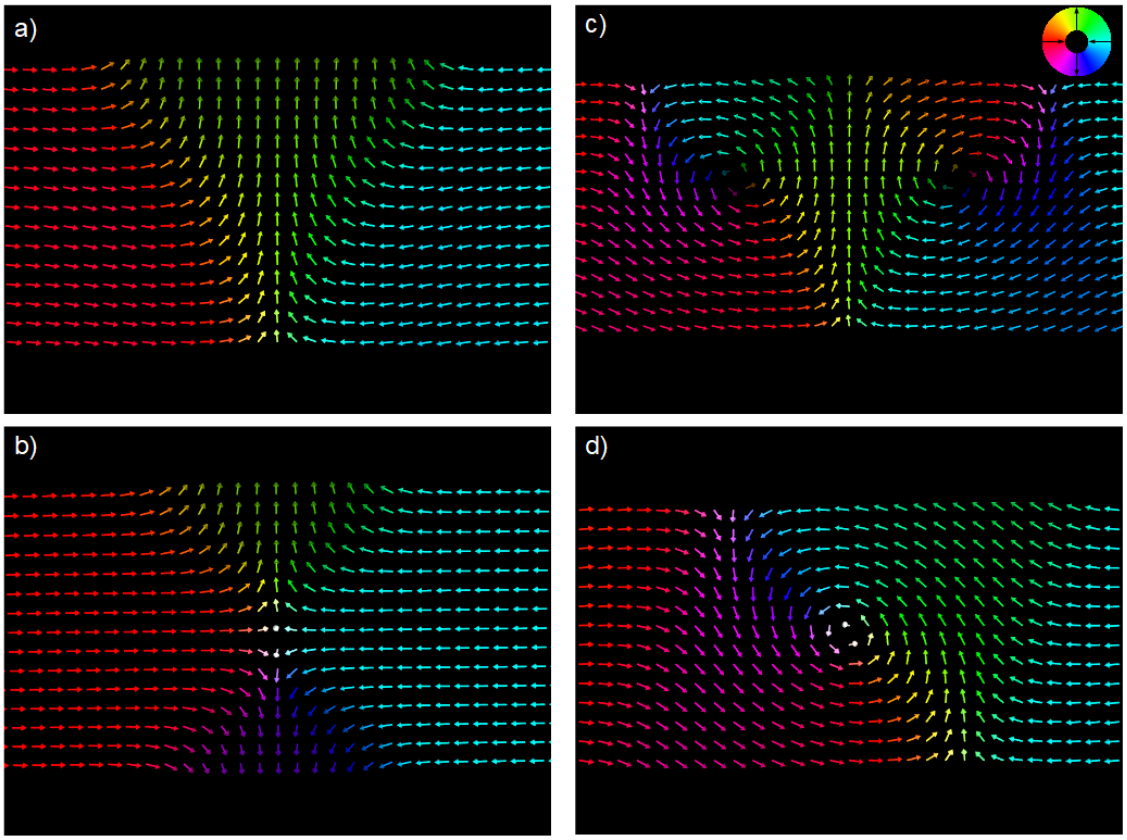

Figure 4.4: 2D vector diagrams of DW types observed in QC nanowires: a) - TW, b) - FSW, c) - TDVW, d) - VW. Colours represent longitudinal and transverse magnetisation components, with white representing out-of-plane magnetisation direction. a), b) and d) are obtained from a 100 nm $\times$ 25 nm QC nanowire, c) is obtained from a 120 nm $\times$ 30 nm QC nanowire.

The DWs shown in a) and d) strongly resemble the transverse wall (TW) and vortex wall (VW) described for planar nanowires in Chapter 2, suggesting they are of the same type. In Figure 4.4 a) (the TW) the magnetisation forms a roughly triangular region oriented perpendicular to the long axis of the wire. This DW has two degenerate states of equivalent energy cost depending on the transverse direction of the central region. Their profiles, which show how the DW varies throughout the nanowire thickness, can be seen in Figure 4.5 a) and b). In the VW, pictured in 4.4 d), the magnetisation rotates around a central vortex core pointing out-of-plane of the wire axis. It also has four degenerate states based on the direction of the core and also the rotation (clockwise or anticlockwise) of the magnetisation (Figure 4.5 e)). The flower state wall or FSW (Figure 4.4 b)) is a metastable DW [18] with a structure that resembles the transverse DWs observed within cylindrical nanowires. It is characterised by an out-of-plane central region surrounded by two transverse "petals", which in turn appear as two oppositely pointing TWs. It also has two degenerate states based on the direction of the out-of-plane region in the centre. Profiles of both are pictured in Figure 4.5 c) and d). The FSW is a wall of particular interest due to its divergent nature, relatively simple shape and compact size (compared to the other walls). Finally, Figure 4.5 c) displays the transverse/double-vortex hybrid wall (TDVW). Compared to the other three, it is the most complex one and is characterised by a triangular transverse central region at the upper end of which the magnetisation begins to curl on either side forming two vortices. Much like the regular TW the TDVW also has a degenerate state, in which the direction of the transverse region is reversed and so is the direction of the vortex rotation - Figure 4.5 f). It is possible that other degenerate states exist based on the orientation of the vortex cores, but none were observed in the simulations conducted here. It should be noted that while the images shown in Figure 4.4 were chosen to be the most representative of the DWs and clearly show their structure, they fail to fully capture the 3D nature of the DWs and the slight rotation of magnetisation due to the curvature of the nanowire geometry. This can be seen in Figure 4.5 a) through d) which display cross-sections through the TW and FSW degenerate states as described earlier. This presence of curvature in the nanowire profile is the most likely cause of the stabilisation of the FSW as it reduces the number of axes of symmetry in the structure and introduces a so-called effective DMI, without the presence of interfacial DMI-inducing materials [19]. In cylindrical nanowires and nanotubes, this effect of curvature has been linked to the formation of novel magnetisation states [20] [21]. In the next section, the stability and size of the different DWs are examined with respect to

the dimensions of the QC nanowires.

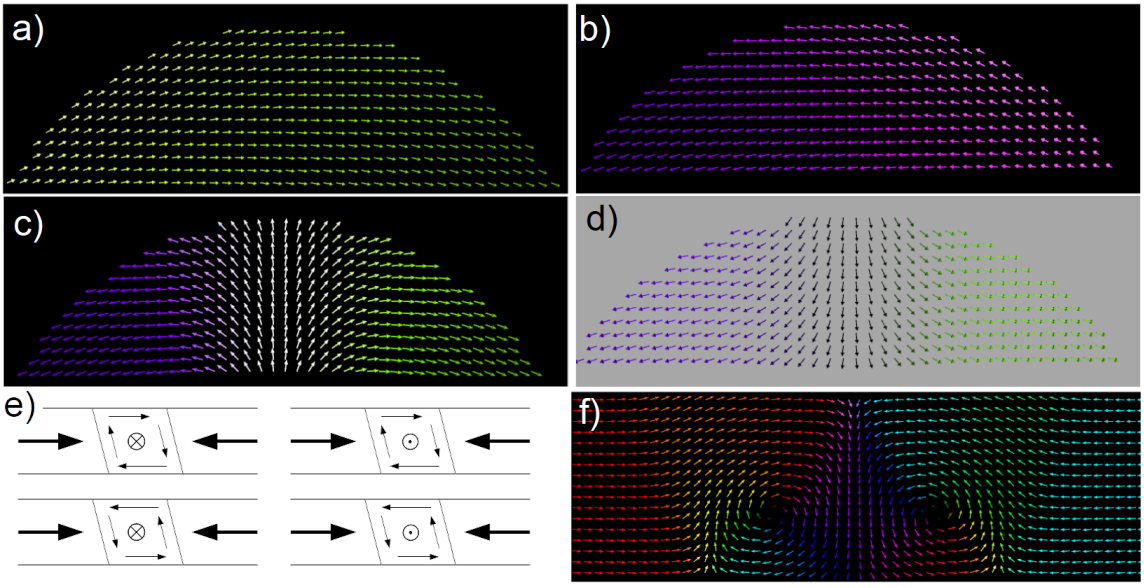

Figure 4.5: Degenerate states and profiles of the different DWs observed in QC nanowires: a) and b) represent vector diagrams of the profiles of a TW, c) and d) are the profiles of the degenerate states of a FSW, e) shows diagrams of the four equivalent vw configurations and f) is a vector diagram of the alternative state of the TDV wall. In e) the circle with a cross and dot represent magnetisation direction into and out of the page respectively.

4.3.1 Stability of domain walls in quarter cylinder nanowires

The total energy density of the simulation was the metric used to represent the stability of DWs. It is defined as the energy per unit volume and encapsulates the contributions from the magnetostatic and exchange interactions described in Section 1.3. It was directly obtained as an output of the simulation and then plotted for various DW types against the width of the nanowire occupied by each wall. Energy density was chosen because it allows for a straightforward comparison of stability regardless of nanowire size. The resultant plots for Co and Fe alloy nanowires can be seen in Fig. 4.6 a) and 4.6 b) respectively. It is clear from the graphs that the initial material parameters affect the energy density quite strongly, with the values nearly doubling for the Co alloy nanowires with 1300×10^3 A/m. Additionally, the results from the simulations showed the relationship between the simulation starting and relaxed states. When the initial state closely resembled the ground

state (the most stable configuration), the simulation invariably relaxed to that ground state. For instance, the starting state depicted in Figure 4.3 b) always converged to a TW (4.4 a) or a TDVW 4.4 c). A similar behaviour was observed with the out-of-plane (4.3 a)) and vortex (4.3 c)) starting states relaxing into FSW and VWs respectively. As expected the ground state configuration for the smaller nanowires for each set of material parameters is the TW, denoted by a green triangle on the diagrams. However, the transition point at which the VW becomes more stable differs depending on the material parameters. For the 900×10^3 A/m wires, the VW was first recorded to have a lower average energy density at wire dimensions of w = 120 nm (with maximum thickness t = 30) nm, while for the 1300×10^3 A/m wires, the change in the ground state first occurs at w = 80 nm (t = 20 nm). The width and thickness figures here refer to the definitions in Figure 4.1. A similar transition point was observed in permalloy nanostrips in [22]. The simulations predict that the TW and VW can both form across the full range of nanowire sizes, however, for the Co alloy nanowire and the VW remains the more energetically favourable one for the remaining nanowire sizes. In the case of the Fe alloy wires, the simulations show that TW and VW can only coexist within wires with widths smaller than 100 nm. For any larger size, the TW no longer stabilised and was replaced by the metastable TDVW described in Section 4.3. This was surprising despite there being a similarity between the TW and TDVW (the main component of both is an extended triangular region with parallel magnetisation) as the presence of two vortices does not intuitively suggest stability. The TDVW, however, only relaxed in larger wires where it is most likely preferable to the TW because of the combined effects of nanowire curvature and the reduction of the magnetostatic energy contribution from the vortices. Interestingly, simulations showed that the TDVW even becomes the ground state in Fe alloy nanowires above w = 120. The last remaining wall in the diagram, the FSW, appeared as a metastable state across the entire simulation range for the QC regardless of material parameters. In the smaller Fe alloy nanowire it was observed to have lower total energy than the VW, however, still larger than that of the TW. That being said, the energy density differences between the ground state and least energetically favourable wall types for all sizes are relatively small, ranging from 9 % to 15 % for the Co alloys nanowires and 7 % to 12 % for the Fe alloy ones. This implies that the metastable walls may nucleate in physical nanowires in the presence of additional factors like crystalline anisotropy, physical imperfections that may cause the pinning of a particular state, field history or the presence of interfacial DMI. The effect of the latter is discussed in the next

section.

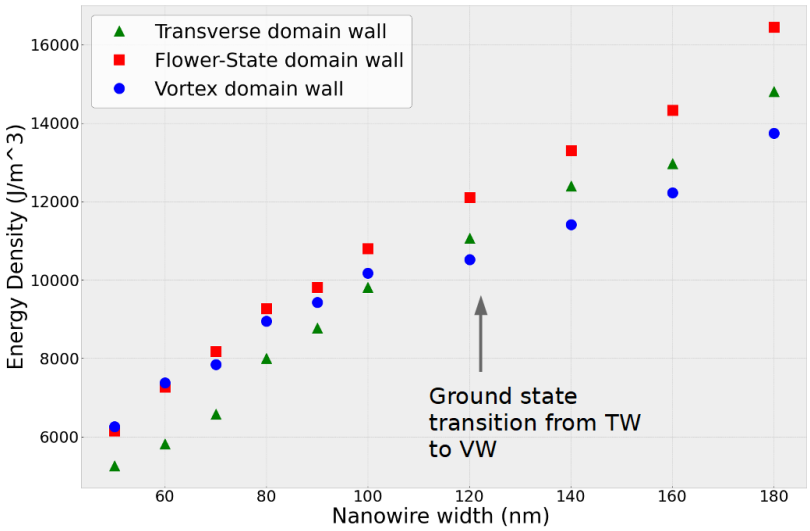

(a) Total energy density diagram for Co ($M_s = 1300 \times 10^3$ *A/m*) QC nanowires

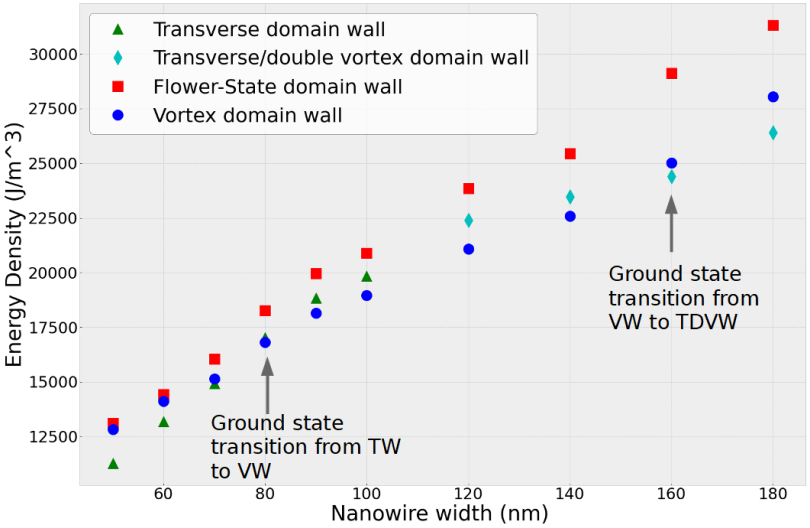

(b) Total energy density diagram for Fe ($M_s = 900 \times 10^3$ *A/m*) QC nanowires

Figure 4.6: Total energy density of Co (a)) and Fe (b)) QC nanowires plotted in relation to nanowire width (size in y-dimension). Different markers represent the different DWs.

4.3.2 Effect of DMI on quarter cylinder straight nanowires

As mentioned in Chapter 1, iDMI aids in the stabilisation of chiral Néel-like DWs which have been shown to achieve propagation speeds of up to 700 *m/s* in Co multi-layers [23]. Here we examine the effect of iDMI on the DW structures in combination with the QC nanowire curvature. iDMI was implemented in the simulations by adding a single layer adjacent to the nanowire geometry with no magnetic properties but with an effective interfacial DMI (iDMI) strength of D = 1×10^{-3} J/m^2 similar to the method employed in [24]. This value was chosen as it is experimentally achievable with the addition of a 4 nm Pt layer to thin Co/Al films [25]. [26] further quotes iDMI strength varying between 0.1 and 3.5×10^{-3} J/m^2 for different configuration of Co and Pt thin films. It should be noted however that the value is only a realistic estimate of what the true iDMI strength would be in the system studied. A more accurate value would require a further experimental study. The simulations were then initialised in the same manner as the ones without iDMI. Once the simulations were completed iDMI was found to have the largest effect on DWs within the smaller sizes of nanowires (up to 70 nm) - in particular on the ones with an out-of-plane component - the FSW and the VW. Figure 4.7 shows this effect on the structure of an FSW, which is completely transformed into the so called one-dimensional wall or 1DW (a)) and on the VW (b)). The images shown in the figure are from a simulation of a Co alloy nanowire of w = 60 nm.

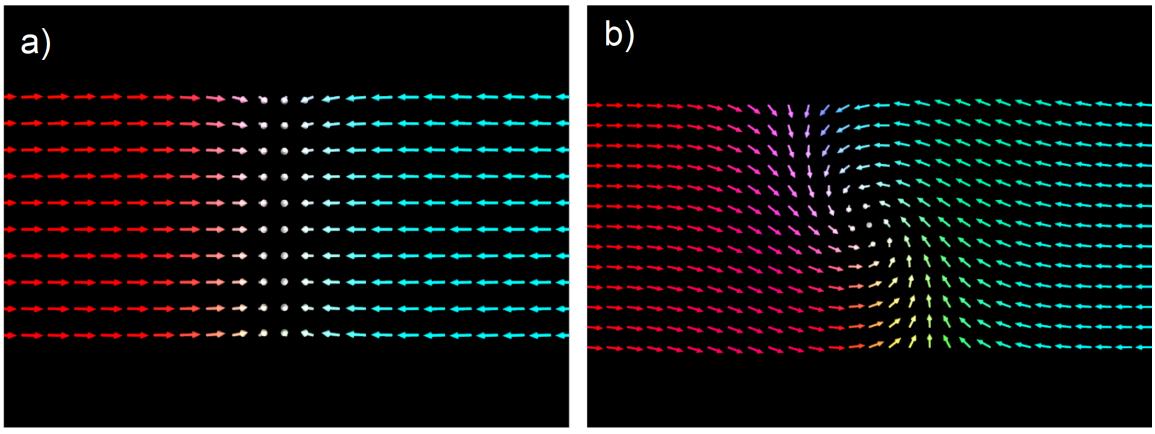

Figure 4.7: 2D vector diagrams of QC nanowires of w = 60 nm with a 1DW (a)) and VW (b)) in the presence of DMI, with D = 1×10^{-3} J/m^2.

In the case of the VW iDMI had the effect of significantly broadening the vortex core and introducing a divergent component to the magnetisation rotation. The resulting state is very similar to the transition state between a circular and radial vortex reported in [27] at similar values of iDMI. The effect of iDMI on the FSW within Co alloy nanowires with $w < 70$ nm is much more pronounced. As can be seen in Figure 4.7 a) the DW structure is completely transformed with the in-plane triangular regions disappearing and the entire DW becoming a continuous region of out-of-plane magnetisation. This makes it appear much more like a one-dimensional structure, hence this particular wall will be referred to as the 1DW later in the thesis. Additionally, this DW was found to have the smallest extent out of all the DWs observed during the simulations, a property that is highly desirable in the field of spintronics. As the size of the simulated nanowire was increased the effect of iDMI was diminished and within Co alloy nanowire with $w > 70$ nm the DWs pictured in Figure 4.7 a) no longer stabilised and was replaced by the FSW pictured in Figure 4.4. An additional effect of iDMI was the prevention of the formation of the degenerate state of the FSW described in Section 4.3. Meanwhile, in the Fe alloy nanowires, iDMI was not found to have such a strong effect on the magnetisation configuration of the FSW. It also did not lead to the stabilisation of the 1DW. It did, however, result in the same broadening of the vortex core in VWs.

Similarly to Section 4.3.1 the average energy density of the different magnetisation states was recorded and plotted for each nanowire size. The resulting plots can be seen in Figure 4.8. The same relationship between starting and final state was also observed with the starting states shown in 4.3 a), b) and c) converging to DWs they closely resemble i.e. FSW, TW/TDVW and VW respectively. Over the range of simulations, iDMI was found to reduce the average density for the different walls by 10 % in both Co and Fe alloy nanowires. In addition, there are also a couple of other subtle differences. Firstly, one can see that no vortex state relaxed at the smallest size of nanowire and a TDVW stabilised at the largest simulated nanowire of $w = 180$ nm. This state did not stabilise at all in Fe alloy nanowires without the presence of iDMI. The transition between TW and VW being the ground state occurred at $w = 100$ nm. For Fe alloy nanowires transitions between ground states were recorded at $w = 80$ nm (from TW to VW) and again at $w = 180$ nm (from VW to TDVW). In addition, no FSW was able to stabilise in Fe alloy nanowire in the presence of iDMI at nanowire widths greater than 140 nm with the only remaining states at that size being the VW and TDVW.

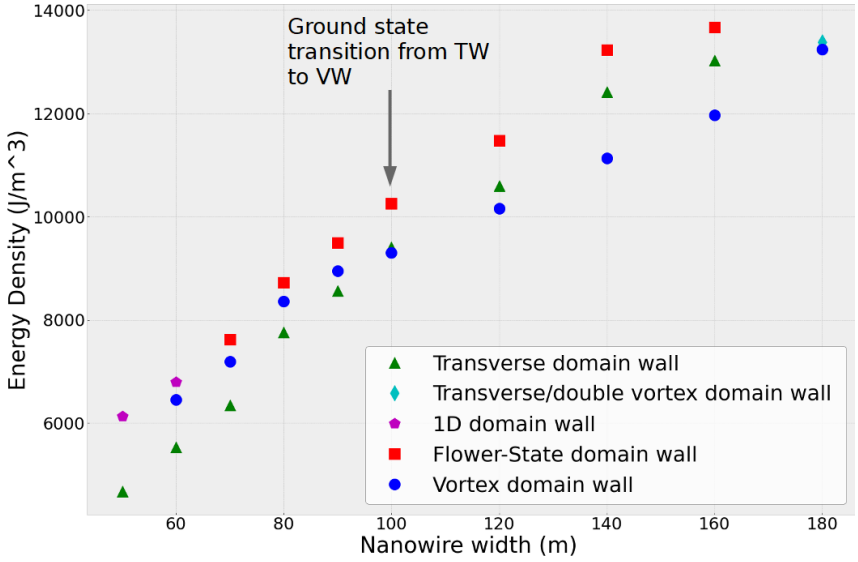

(a) Total energy density diagram for Co QC nanowires with iDMI

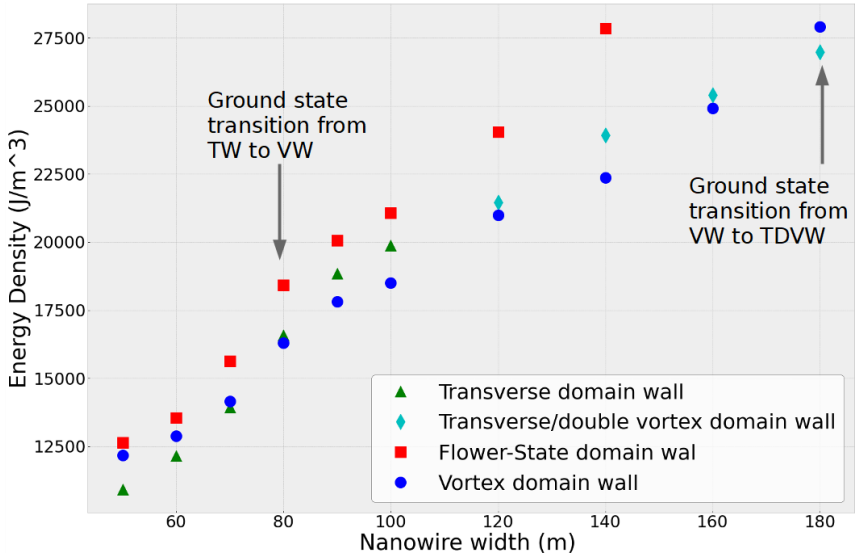

(b) Total energy density diagram for Fe QC nanowires with iDMI

Figure 4.8: Total energy density of Co (a)) and Fe(b)) QC nanowires with interfacial DMI plotted in relation to nanowire width (size in y-dimension). Different markers represent the different DWs.

For both sets of starting material parameters and over the entire simulation range the FSW remained a metastable state. Overall, the inclusion of iDMI yielded interesting results - an overall decrease in the energy of cost DWs and in particular the appearance of the DW pictured in 4.7 a). Its nearly one-dimensional profile, chiral nature and compact size make

it an interesting candidate for spintronic devices. However, more studies are needed to quantify its stability and practicality. Examples of such may include static simulations on materials with favourable crystalline anisotropy [28] and experimentation with higher values of iDMI strength and dynamical simulations to quantify its propagation [29].

4.4 Domain walls and their stability in half cylinder nanowires

The next set of simulations was performed on straight HC nanowires. In these, the width and length of the nanowires were kept identical to their QC counterparts, which resulted in the thickness of the wire and consequently the curved surface area being increased. Overall the same DWs were observed as in the QC nanowires - TW, VW, FSW, and TDVW (Figure 4.4) albeit with small topological differences to account for the increased curvature. An example of this is the strengthening of the out-of-plane component of the magnetisation around the outer surface of the nanowire - this can clearly be seen in Figure 4.9 a) and b) which display cross-section vector diagrams of the FSW and TW respectively. In addition to the ones listed above a new type of DW emerged in some of the larger nanowires. It can be seen in Figure 4.10. It strongly resembles the VW in structure, but the magnetisation is not symmetrical around the vortex core, therefore, invoking the name for it - asymmetric vortex wall or AVW. The AVW observed here is also very similar to the so-called Landau DW found in permalloy nanostrips wider than 200 nm [30], which is also characterised by magnetisation rotating around an extended vortex core. A notable feature of the AVW observed here is its size. In the Fe alloy nanowire simulations, as the wire width increased, the extent of this wall began spanning a big proportion of the nanowire. Co HC nanowires were simulated up to a width of 180 nm and Fe wires up to 160 nm. Beyond that point, the resulting magnetisation configurations ceased to be head-to-head with a DW and instead turned into complex multi-domain configurations. The energy density again was used as a measure of DW stability. The starting states had a similar effect on the final states as discussed in Sections 4.3.1 and 4.3.2 with one notable difference. The out-of-plane starting state (4.3 a)) relaxed into the AVW state for Co nanowires wider than 120 nm and Fe nanowires larger than 140 nm.

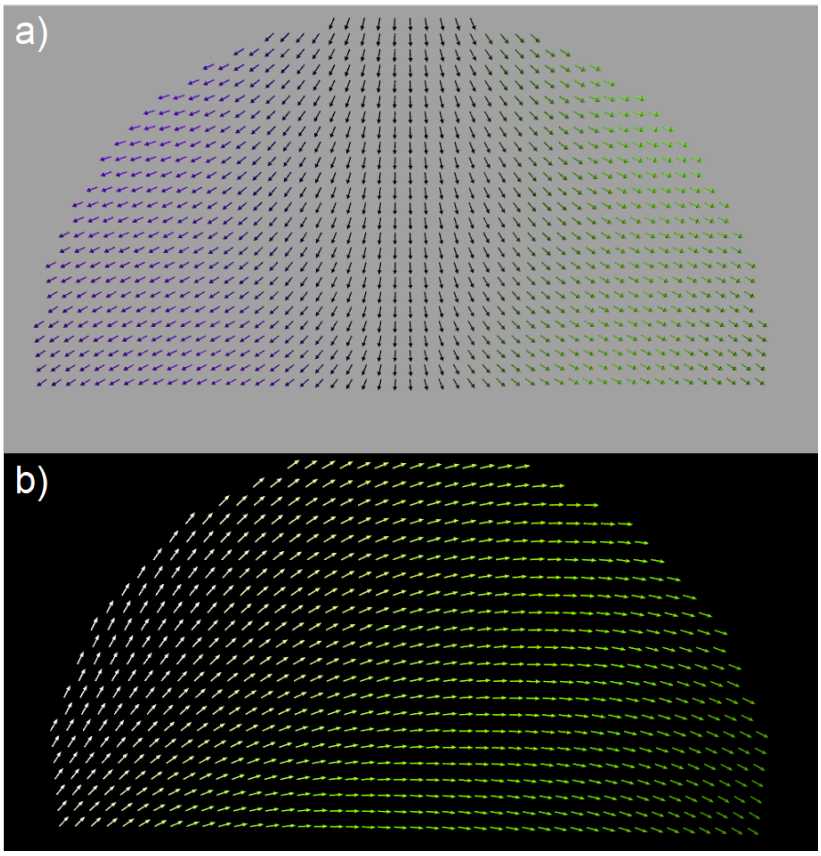

Figure 4.9: Vector diagrams displaying the profiles of a FSW (a)) and TW (b)) for 100 nm wide HC Co nanowire.

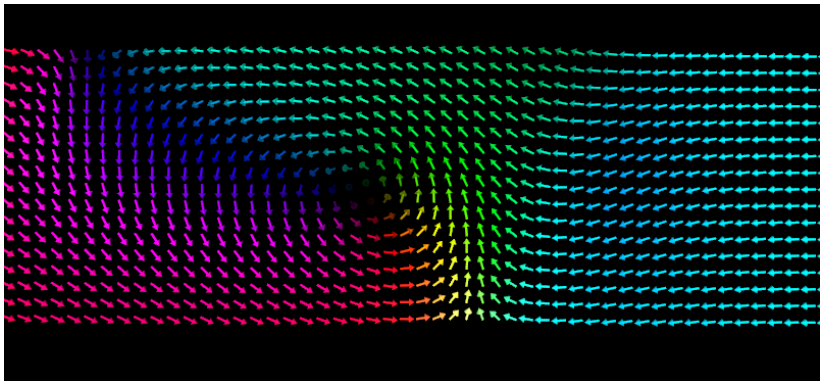

Figure 4.10: 2D vector diagram of a AVW obtained from a 140 nm wide Fe HC nanowire.

The plots for Co and Fe HC nanowires can be seen in Figure 4.11. The average energy density across all HC wire sizes was found to be slightly higher than that of their QC

counterparts. For both sets of material parameters used the TW was found to be the most favourable DW for the smallest nanowire sizes. As larger nanowires are simulated the first phase transition occurred at a nanowire width of 80 nm (t = 40 nm) for the Co nanowires and at 70 nm (t = 35 nm) for the Fe nanowires. At this point, the VW became the ground state DW. In square permalloy ($M_s = 800 \times 10^3$ *A/m*) nanowires a similar transition between a TW and BPW was found to occur at a nanowire width of 40 nm [31]. Similarly in cylindrical nanowires transitions between TW and BPW were reported at diameters of 30 nm for $M_{s1} = 1300 \times 10^3$ *A/m* and of 55 nm for $M_{s2} = 900 \times 10^3$ *A/m* [32]. In the Co alloy nanowires the VW remained the ground state for all sizes up to 140nm where the AVW took its place as the most low-energy state. Interestingly, the VW and AVW were found to coexist at wires with widths between 120 and 140 nm. This leads to the conclusion that the AVW is not an "adaptation" of the VW more favourable within larger wire sizes, but a completely different wall altogether. In the Fe alloy nanowires, the VW remained the ground state in wires with widths up to 100 nm. Then in wires with width between 100 nm and 140 nm the ground state was found to be the TDVW. In the Fe alloy nanowires, there was one final phase transition at w = 140 nm. At this point, the AVW became the most energetically favourable DW. Regardless of the material parameters, the energy differences between the VW, AVW and TDVW in nanowires with a width greater than 120 nm were very small, implying that either one may be observed in physical nanowires. In the HC simulations, the FSW was also found as a metastable wall with the highest energy cost. Unlike in the QC simulations, it did not appear across the entire simulation range. Instead, it relaxed in wires with widths up to 100 nm in Co alloy nanowire and 120 nm in Fe alloy nanowires. A noticeable feature of the FSW is how its energy cost changes with wire width. In smaller nanowires, its energy density was found to be very close to that of the ground state wall for the particular wire size. As the wire size increases so does the energy gap between the FSW and the other DWs. This led to the conclusion that an FSW would most likely be observed in smaller nanowires with widths smaller than 70 nm. Like in the case with QC nanowires the effects of iDMI were also examined here. However, the introduction of iDMI with a strength of $D = 1 \times 10^{-3}\ J/m^2$ resulted in no significant change in the spin structure of the DWs in the HC nanowires and did not affect the ground-state transition points. This is most likely due to the increased nanowire thickness of the HC as compared to the QC nanowire and the fact the iDMI strength decays exponentially with the distance from the inducing layer [33].

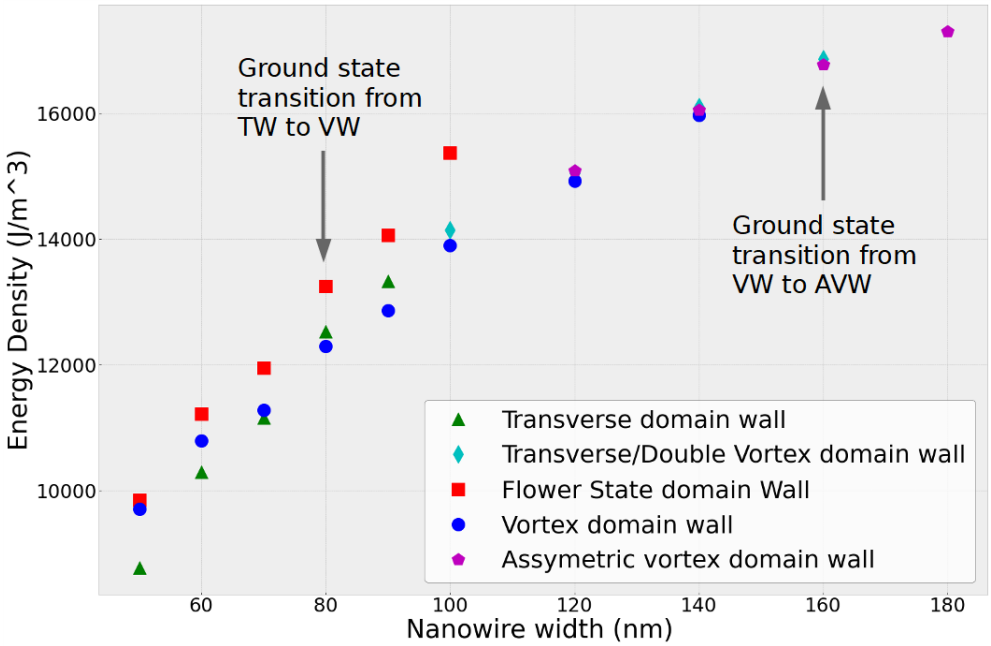

(a) Total energy density diagram for Co HC nanowires

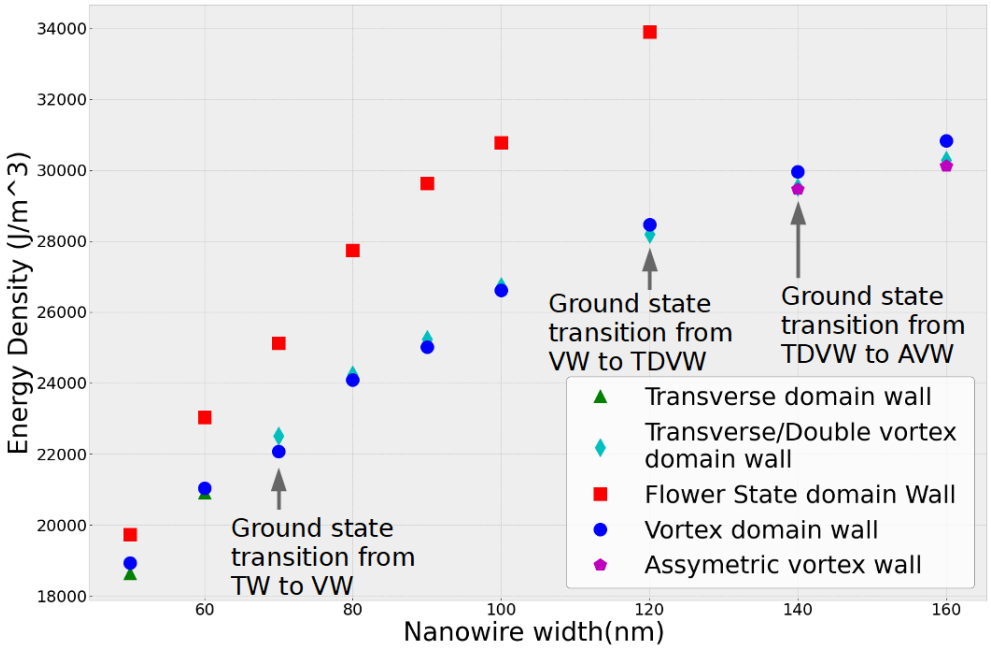

(b) Total energy density diagram for Fe HC nanowires

Figure 4.11: Total energy density of Co alloy (a)) and Fe alloy (b)) HC nanowires plotted in relation to nanowire width (size in y-dimension). Different markers represent the different DWs.

4.5 L-shaped nanowire simulation results

Nucleating DWs in physical straight nanowires is not easily achievable without the introduction of defects like notches or thickness modulation [34][35]. This is why a curved or L-shaped nanowire design is often used. Here simulations are conducted of L-shaped HC and QC nanowires to explore the range of DWs that can stabilize in such structures. Again the material parameters for Co and Fe alloys described in Section 4.2 were used and the simulated nanowire sizes ranged from w = 60 nm to w = 200 nm. Each simulation was initialised with the states described in Section 4.2. Figure 4.12 shows 2D vector diagrams of the two DW observed in both the HC and QC L-shape simulations. In comparison to the straight nanowire, a much smaller number of unique DWs was observed - only a TW 4.12 a) and an extended VW with a transverse component - Figure 4.12 b). The cause of this is the strong shape anisotropy associated with the L-shaped nanowire geometry and the fact that the simulations are initialised in a head-to-head configuration. These factors constrain the DWs to the vertex of the "L", where the geometry significantly differs from the straight nanowire, in which the nanowire edges are parallel. This constraint also resulted in a different relation between the starting and final state to the one observed in the straight nanowire simulations. Here each nanowire simulation of a particular size resulted in an identical final state. Despite the topological differences between the straight and L-shaped nanowires there are also similarities. In particular the TW in L-shape nanowire is quite similar to the one observed in the straight nanowire in terms of the overall spin orientation. The shape, however, is different. Whereas in straight nanowires the TW was found to have a triangular shape, here the shape of the wall is dictated by the shape of the vertex. The other VW found during the simulations appeared only in the larger nanowires. Here the VW is quite asymmetric with an extended core much like the AVW from Section 4.4. In nanowires where this wall appears the vortex is localised in one of the "arms" of the L, while in the other the magnetisation is mostly transverse. This is because the geometry of the VW and the nanowire vertex are not compatible.

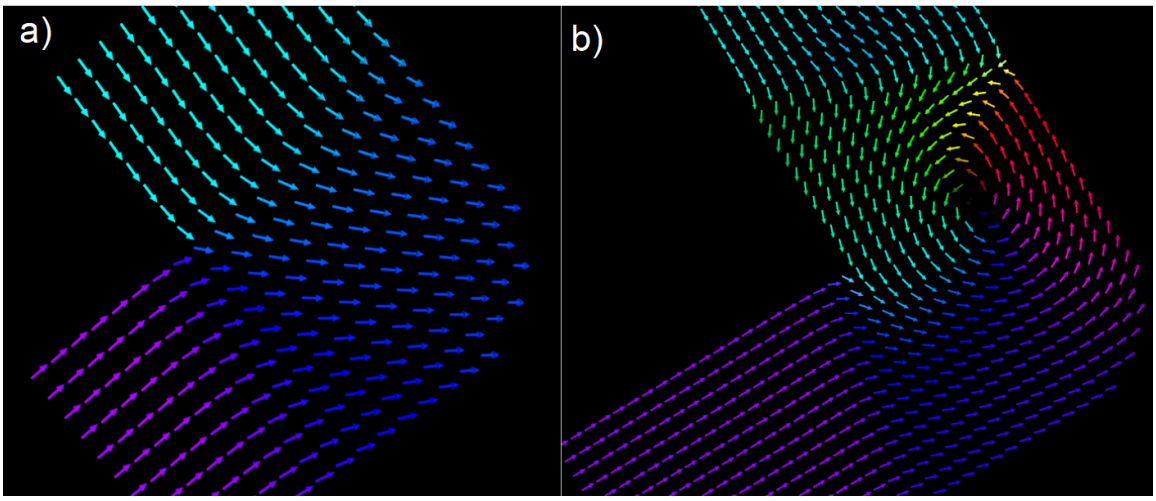

Figure 4.12: 2D vector diagrams of Fe alloy QC L- shape nanowires displaying the TW (a)) and VW (b)). a) is relaxed from an 80 nm wide nanowire, while b) is obtained from an 140 nm wide nanowire. The same DW configurations were observed in the Co alloy nanowires.

The energy density graphs that represent the stability of the different walls for the L-shape nanowires can be seen in Figure 4.13. There one can see that the TW is the most commonly occurring DW. In the Co alloy QC simulations, it was the only DW that appeared across the entire simulation range. In the Fe alloy simulations, the situation was similar with the exception of the two largest simulated nanowires where it was replaced by the VW. In the HC L-Shape nanowires, the transition between TW and VW happened at w = 140 nm for Co alloy and 100 nm for Fe alloy. Furthermore, the size range where head-to-head DWs were able to relax at all was quite limited. Beyond the sizes pictured in Figure 4.13b and 4.13c, the resulting magnetisation followed the shape of the "L" and was mostly uni-directional with the exception of a slight rotation at the bent region of the L. Simulations with included iDMI of value $D = 1 \times 10^{-3} J/m^2$ were performed on the QC and HC L-shape geometries, the effect of which was a flat decrease in the exchange energy density of the configuration as can be see in Figure 4.13. In these simulations, no changes were observed in the ground-state transitions or the overall spin structure of the walls. An interesting observation about the L-shape simulations that distinguishes them from the straight ones is the fact that no metastable walls were found to stabilise. Furthermore, the simulation starting state was not observed to affect the final DW that formed. For each nanowire size regardless of which starting state was used (Figure 4.3 d)-f) the result was always the same

- the ground sate DW of that particular nanowire configuration. Again this is most likely due to constraint imposed by the L-shape geometry.

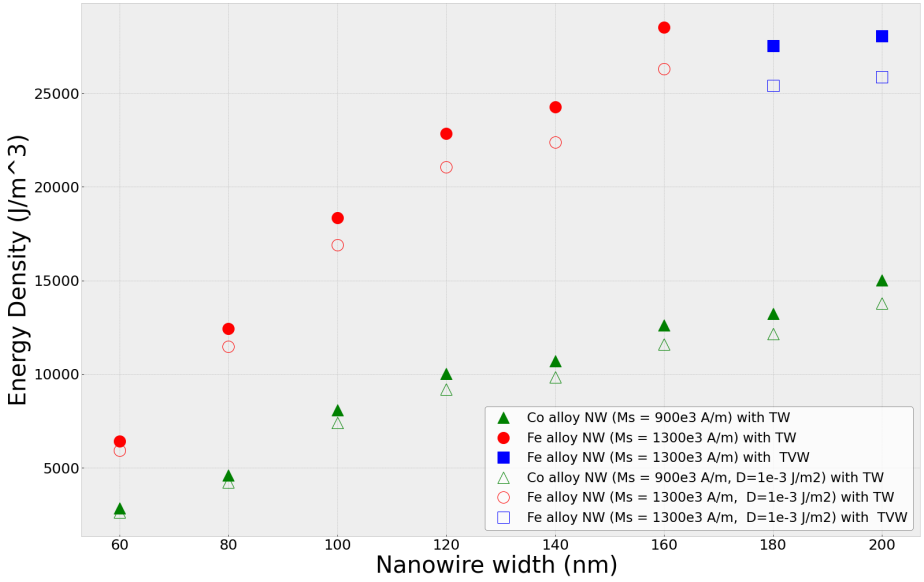

(a) Total energy density diagram for both Co and Fe QC L-shape nanowires

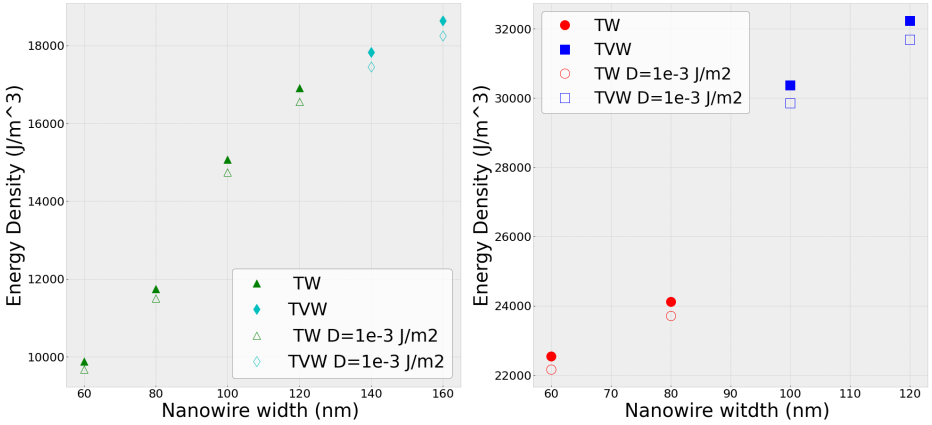

(b) Total energy density diagram for Co HC L-shape nanowires

(c) Total energy density diagram for Fe HC L-shape nanowires

Figure 4.13: Total energy density of QC and HC L-shape nanowires versus nanowires width. 4.13a shows the results for both QC Co alloy and Fe alloy, while 4.13b and 4.13c display the results for HC Co alloy and Fe alloy nanowire respectively. Different markers represent the different DWs. Hollow markers represent results from simulation with iDMI.

4.6 Domain wall extent in cylindrical segment nanowires

As mentioned in Chapter 2, an important characteristic for a DW is its width or extent along the long dimension of the nanowire. Here are presented the extents of the DWs discussed in Sections 4.3 through to 4.5. The main challenge in obtaining a measurement of the DW extents for the simulations outlined here is the complex spin structure of some of the DWs in which the magnetisation can vary across two or even all three dimensions of the nanowire. Because of this employing conventional methods for calculating DW widths from magnetisation, such as fitting the longitudinal component to a hyperbolic tangent function (as outlined in [36]), which only work effectively on one dimensional DWs, are not applicable here. Instead, the following approach is used. First, the longitudinal component (m_x) of the magnetisation is extracted from the simulation. The resulting three-dimensional dataset is then summed and averaged along the nanowire thickness (z-dimension) and normalised to give a 2D image of the m_x component of the nanowire. Line profiles are then taken across this image to provide measurements of the DW extent. Because the DWs observed here can vary in across the transverse dimension of the nanowire (the y-dimension) several profiles 5 nm apart were taken and averaged to give the final DW extent measurement. A schematic of the process is shown in Figure 4.14, where the red dotted lines indicate where line profiles are measured.

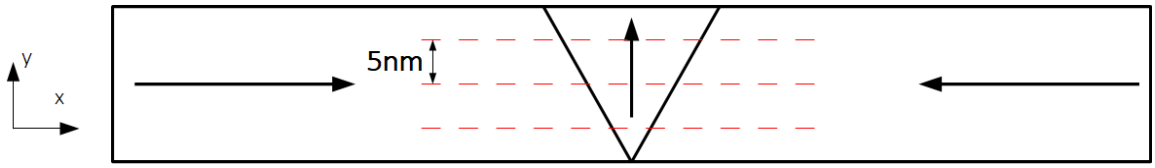

Figure 4.14: Schematic of how an average DW extent is calculated for a TW. The red dotted lines indicate the locations where line profiles were taken across the 2D image of the longitudinal magnetisation of the nanowire.

From the line profiles a measurement of the extent of the DW packet was taken by measuring the region over which the normalised longitudinal magnetisation was in the range between 0.95 and -0.95. Areas with magnitude outside that range was considered to be part of domain, rather than part of the DW. This range was chosen as it was found to be the most representative of the DW. For the L-shape nanowires, a similar approach was used

with an extra step. Because of the slightly more complex shape, two different profiles were taken along each arm, meeting in the midpoint of vertex of the L. The two profiles were then concatenated giving a single continuous line profile. Again several line profiles were take in this manner with a spacing of 5 nm and the extent measurement method was then used on the resulting profiles. Images of the profiles of the different DWs along with a 2D image of their normalised m_x component can be seen in Figure 4.15. The red line in the images represents the location where the corresponding profile was taken. It should be noted that all the "simpler" DWs (FSW, TW and 1DW) had very similar profiles (Figure 4.15a) that closely resembled the hyperbolic tangent profiles in 1D DWs mentioned earlier. Despite that the same method of DW extent measurement was used in order to preserve the consistency of the data. The process of DW extent measurement described above was repeated for the different DWs in each nanowire. The results were then organised by DW shape and can be seen in Figure 4.16. When looking Figures 4.16 and 4.15 it is important to note that no direct comparison can be made between some of the different DWs. Good examples of this are the TW and the TDVW. Although they have some similar characteristics, they are structurally very different with the latter one being more of a composite DW packet rather than a conventional DW. That being said a few conclusions can be drawn from examining the graphs. One is that DWs in HC wires are wider than their QC counterparts regardless of nanowire shape or material parameters. This can be attributed to a combination of the increased thickness and increased curved surface of the nanowire [29] [30] . In straight nanowires (both in HC and QC) the most compact walls were found to be the 1DW and FSW with extents ranging from 9 nm to 11 nm for the 1DW and 20 nm up to 160 nm for the FSW - 4.16 a). Similar sizes were reported for DWs in nanostrips in the presence of iDMI [24]. Their narrow extent makes them both suitable candidates for spintronic devices, which require a lot of densely packed spin structures as discussed in Chapter 2. The 1DW has the additional advantage of a fixed chirality, which is also a desirable quality. The TW was also one of the more narrow DWs with an extent ranging from 15 nm to 100 nm 4.16 b). It is also easy to stabilise and was found to be the ground state in all nanowires smaller than 70 nm.

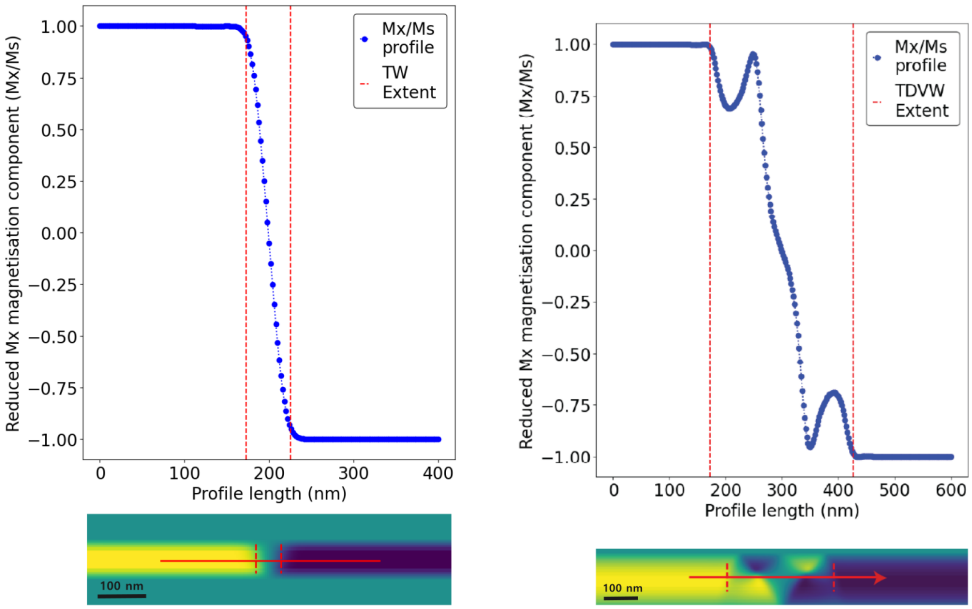

(a) TW wall profile

(b) TDVW profile

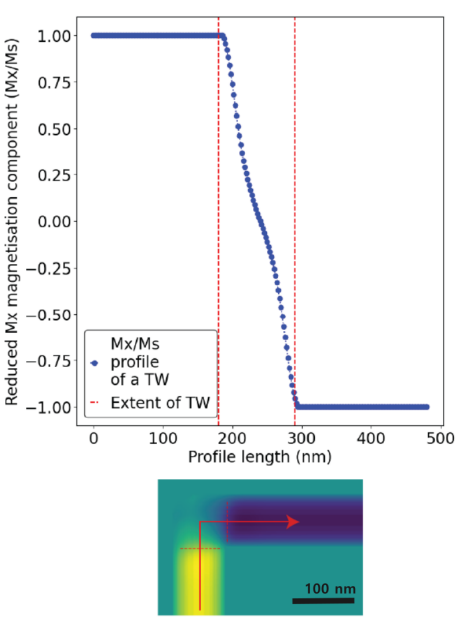

(c) TW profile L shape

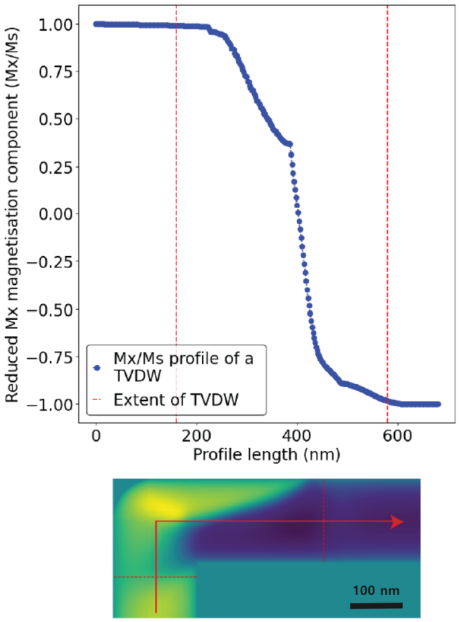

(d) VW profile L shape

Figure 4.15: Line profiles taken along the longitudinal normalised magnetisation component for straight nanowires with TW 4.15a b), TDVW 4.16 and L-shaped nanowires with TW 4.15c and VW 4.15d. The profiles are plotted along with a 2D image of the corresponding magnetisation component. The red line in the magnetisation image corresponds to the location where the profile was taken, while the red dotted lines represent the DW width that was obtained from that profile.

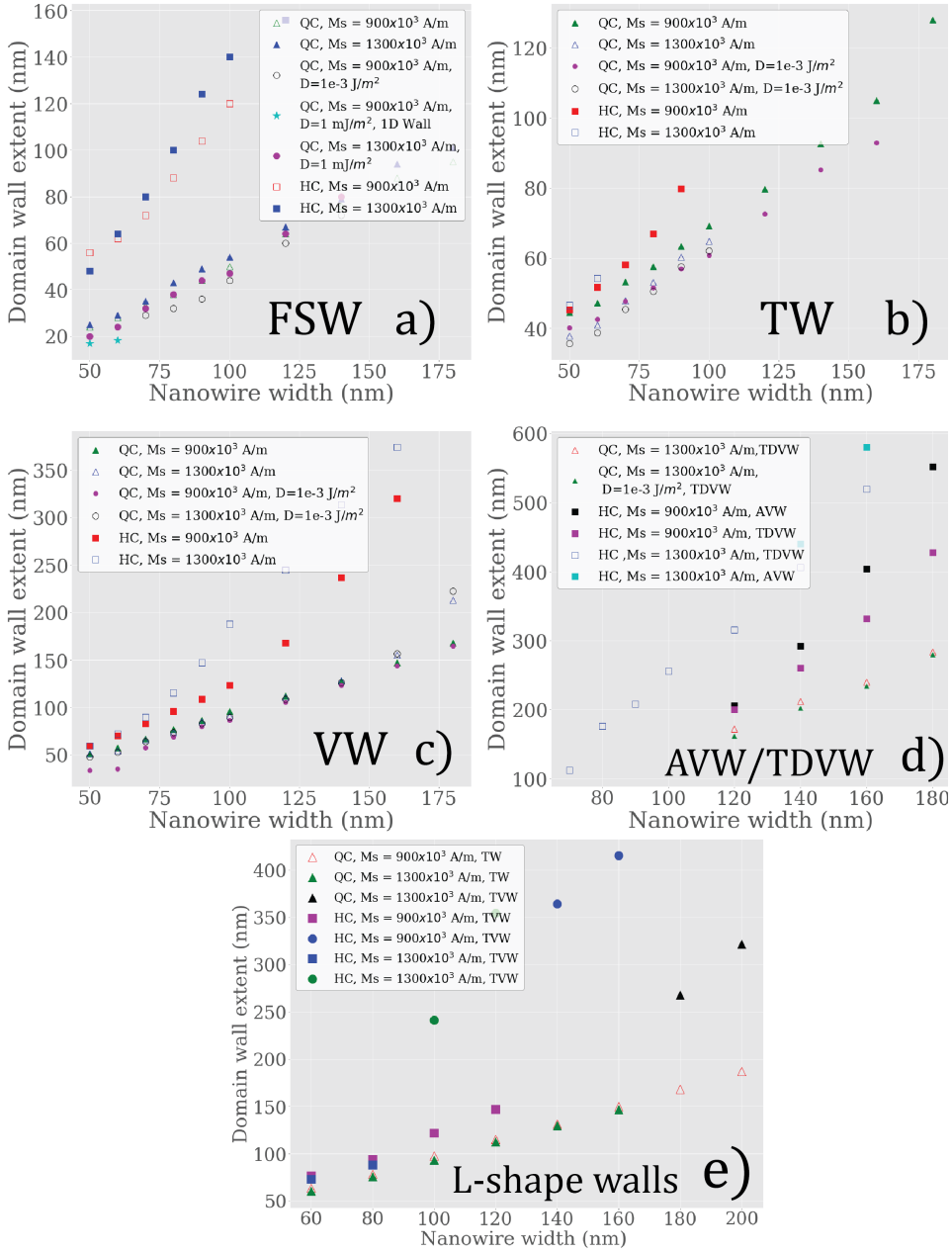

Figure 4.16: DW extent for various DWs plotted against nanowire width. a) - d) show the extents of DWs for QC and HC straight nanowires with a) showing FSW extents, b) TW, c) VW and d) a combination of AVW and TDVW, e) shows the extents of all TW and VW wall types observed in L-shape geometries.

Naturally, the more complex DW packets in the larger nanowires were found to occupy a larger proportion of the nanowire length. In particular, the extent to which the magnetisation was found to change in the widest HC nanowires with AVW and TDVW reached up to 34% of the length of the whole nanowire. Such complex structures while interesting can be unstable and are also more likely to suffer from Walker breakdown. An interesting observation can be made on the increase of DW extent of the different DWs with nanowire size. In the simpler DWs like the FSW and TW, the DW extent seems to increase in a linear fashion with the corresponding nanowire dimensions, while in the more complex nanowire, this relationship is closer to exponential - as can be seen for the VW in Figure 4.16 c). The introduction of iDMI also had an effect on the size of some of the DWs in QC nanowires. Overall it led to a significant decrease in the extent of the TW and FSW. In L-shape nanowires a similar trend is present. The TW (the simpler wall) is much narrower and is further contained by the shape of the nanowire. In the nanowire sizes over which it appears, it spans the bent region of the L and increases linearly with nanowire size. Moreover, there is only a fractional difference in size between DWs in Fe and Co alloy L-shaped nanowires. On the other hand, the more complex VW "spills" outside the bent region and into the arms L-shape. Its complex structure and its incompatibility with the L-shape make it less likely to stabilize. The introduction of iDMI to the L-shaped nanowires had little to no effect on the DW extent in the studied range. This was also most likely due to shape of the nanowire and the fact that the DW is constrained to the bent region of the L effectively forcing its shape and size.

4.7 Simulation results summary

The last few sections presented the results from simulating cylindrical segment nanowires with different geometries and material parameters. These include images and descriptions of a variety of DWs that can stabilise in such geometries as well as a record of their stability and extent. Table 4.1 provides a summary of the different DWs across the simulation space. The data presented here is organized by nanowire type (e.g. QC Co nanowire) and width, with the DWs for each entry appearing in descending order by their total energy density. The table shows a wide variety of DWs across the cylindrical segment parameter space. As expected simpler and narrower DWs like the FSW, 1DW stabilised in the narrower structures, while for larger nanowires complex DWs like the TDVW and AVW dominated. For

the L-shaped nanowire simulations the trend was different with a TW being the only DW present across almost the entire simulation range. An additional outcome was the iDMI-aided stabilisation of a one-dimensional chiral DW in Co nanowires. Although it was not the ground state wall for the particular combination of nanowire dimension and parameters, its narrow profile and chiral nature do make it a desirable candidate for spintronic applications. Further studies involving varying the simualtion parameters can be used to search for a particular configuration where this wall is the ground state. For example, varying the crystalline anisotropy of the nanowires has been shown to affect the magnetic properties and reversal processes in Co and CoFe nanowires [1]. A more detailed discussion on potential ways to achieve this is presented in Chapter 6. A limitation of this simulation study is the fact that all simulations performed here were static. Further studies exploring the dynamics of the observed walls under external magnetic fields or spin polarised currents would provide insight into their stability and applicability in spintronics. The dynamic effects can also be explored in the pressence of DMI, which can also have an effect on the dynamic behaviour of the DWs [37]. Overall, the results presented here can be used as a baseline for developing further experimental and simulation studies on nanowires with curved profiles or as a reference point for further study of any of the unique DWs that are presented here.

Table 4.1: DW types observed in straight Co and Fe nanowire simulations

Nanowire width	**50 nm**	**60 nm**	**70 nm**	**80 nm**	**90 nm**	**100 nm**	**110 nm**	**120 nm**	**130 nm**	**140 nm**	**150 nm**	**160 nm**	**170 nm**	**180 nm**
QC Co nanowire	TW FSW VW	TW FSW VW	TW VW FSW	TW VW FSW	TW VW FSW	TW VW FSW	VW TW FSW	VW TW FSW	VW TW FSW	VW TW FSW	VW TW FSW	VW TW FSW	VW TW FSW	VW TW FSW
QC Fe nanowire	TW VW FSW	TW VW FSW	TW VW FSW	TW TW FSW	VW TW FSW	VW TW FSW	VW TW FSW	VW TDVW FSW	VW TDVW FSW	VW TDVW FSW	VW TDVW FSW	TDVW VW FSW	TDVW VW FSW	 VW FSW
QC Co nanowire with DMI	TW 1DW	TW VW 1DW	TW VW FSW	TW VW FSW	TW VW FSW	VW TW FSW	VW TW FSW	VW TW FSW	VW TW FSW	VW TW FSW	VW TW FSW	VW TW FSW	VW TW FSW	VW TDVW
QC Fe nanowire with DMI	TW VW FSW	TW VW FSW	TW VW FSW	VW TW FSW	VW TW FSW	VW TW FSW	VW TW FSW	VW TDVW FSW	VW TDVW FSW	VW TDVW FSW	VW TDVW FSW	VW TDVW FSW	VW TDVW	TDVW VW
HC Co nanowire	TW VW FSW	TW VW FSW	TW VW FSW	VW TW FSW	VW TW FSW	VW TDVW FSW	VW TDVW FSW	VW AVW AVW	VW AVW TDVW	VW AVW TDVW	VW AVW TDVW	AVW VW TDVW	AVW VW TDVW	AVW TDVW
HC Fe nanowire	TW VW FSW	TW VW FSW	VW TDVW FSW	VW TDVW FSW	VW TDVW FSW	VW TDVW FSW	VW TDVW FSW	TDVW VW FSW	TDVW VW FSW	AVW TDVW VW	AVW TDVW VW	AVW TDVW VW		
QC L-shaped Co nanowire	TW	TW	TW	TW	TW	TW	TW	TW	TW	TW	TW	TW	TW	TW
QC L-shaped Fe nanowire	TW	TW	TW	TW	TW	TW	TW	TW	TW	TW	TW	TW	TW	VW
HC L-shaped Co nanowire	TW	TW	TW	TW	TW	TW	TW	TW	VW	VW	VW	VW		
HC L-shaped Fe nanowire	TW	TW	TW	TW	TW	VW	VW	VW						

4.8 Simulated Lorentz microscopy images

For micromagnetic simulations to be more useful and provide better insight into the magnetic properties of the simulated structure it is necessary to be able to relate them to experimental results. Such an approach is widely used in the interpretation of experimental Lorentz TEM images [38] [39], where DPC and Fresnel mode image simulations are used to identify and characterise DWs. Simulated Lorentz TEM images have also been applied in stand-alone studies simulation like [40], where they are used to generate the contrast produced by magnetic skyrmions at different angles of electron beam illumination. Several methods have been developed to calculate experimental Lorentz microscopy images from micromagnetic simulations. An example of this is a method based on the calculation of the magnetic vector potential (equation 3.15) developed by [41]. Here experimental images of the straight and L-shaped nanowires were computed using the "FPD" software package [42] using the m_x and m_y components of magnetisation via the methods described in 3.5.6 . As described there the formation of these simulated experimental images is based on the phase of an electron beam as it passes through the simulated magnetic structure. This calculated phase image is then used to obtain simulated DPC and Fresnel mode images of the different nanowires described in Sections 4.4 and 4.3. For the nanowires studied here the 2D images of the m_x and m_y components of magnetisation are obtained by summing along the nanowire thickness (z-direction). This effectively "flattens" the 3D structure to a 2D representation. The summation is done in this way to retain the magnitude of the magnetisation for each simulation layer.

4.8.1 Calculated Fresnel Images

First, we present the calculated Fresnel mode images of the different nanowires. For the images calculated here, the following parameters were chosen to plug into equation 3.24 - the electron beam wavelength was set to 2.51 pm and the beam divergence θ_c was set to 10^{-6} rad [43] in order to simulate a beam from a coherent 200 kV FEG electron source. The aperture function was set to 1 everywhere to simulate imaging conditions where the electron beam is not obstructed by apertures. The phase was obtained from a calculation using the FPD mag_ phase() function from the 2D images of the in-plane magnetisation components m_x and m_y of the simulation and the amplitude function was obtained from its geometry. While the magnetisation components are readily available as a result of the

micromagnetic simulation the amplitude function needs to be calculated separately. The value of the amplitude function is based on the transmittance of the electron beam through the sample. For the curved nanowires, we assume a smoothly varying amplitude proportional to the sample thickness. Figure 4.17 shows an example of an amplitude function for a 20 nm thick QC nanowire, which was assumed to have a value of 0.9 at the maximum thickness corresponding to 90 % beam transmittance. The surrounding area was assumed to have no effect on the amplitude of the electron wave and its value was set to 1. A similar value was reported in [44], however, an accurate estimate would require further Monte Carlo simulations based on the particular system and material parameter [45].

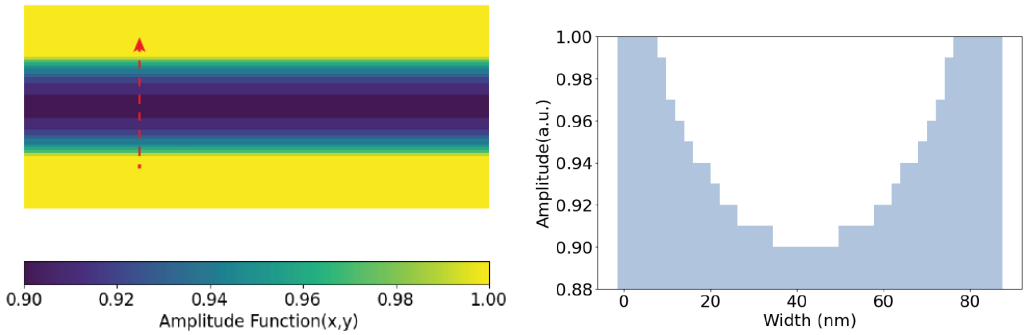

Figure 4.17: Amplitude function (a)) and profile across it (b)) of an 80 nm wide QC nanowire used for the calculation of simulated Fresnel mode images. Red dotted line indicates direction of the profile. The shape and magnitude shown in b) are constant across the wire.

Common lens defects like spherical and chromatic aberrations were not considered in the image calculations, because their contribution to the contrast in the final image is dwarfed by that of the high defocus values. Images were calculated for each of the DWs presented in Sections 4.3 - 4.5 using three different defocus values - 0.1 mm, 0.5 mm and 2 mm. These parameters were chosen so that the simulated Fresnel images can be readily used for comparisons to a variety of experimental images. In them, one can see unique defining features of the DWs that may be useful in identifying and classifying them in physical nanowires. The calculated Fresnel mode images for straight nanowires are displayed in Figure 4.18, while the L-shaped ones can be seen in Figure 4.19.

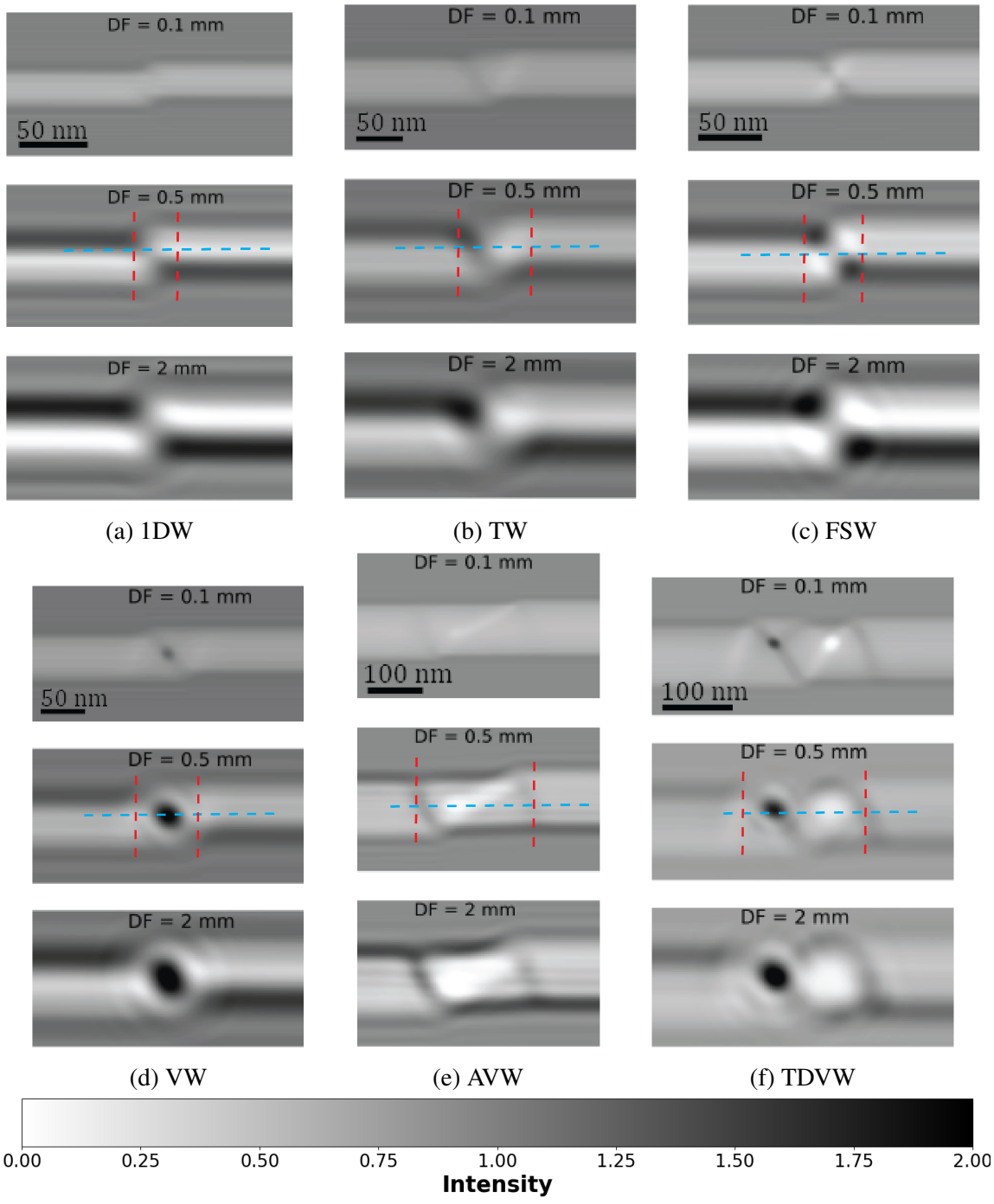

(a) 1DW (b) TW (c) FSW

(d) VW (e) AVW (f) TDVW

Figure 4.18: Fresnel images of the different DWs appearing in straight nanowires. The 1DW (4.18a) was from a 60 nm QC simulation, while the TW (4.18b), FSW (4.18c) and VW (4.18d) stabilised an 80 nm wide QC nanowire. The AVW (4.18e) and TDVW (4.18f) stabilised in a 120 nm Co QC nanowire. The images were calculated for 3 different defocus parameters - 0.05 mm, 0.2 mm and 0.5 m. Blue and red dotted lines indicate locations for profiles displayed in Figure 4.21.

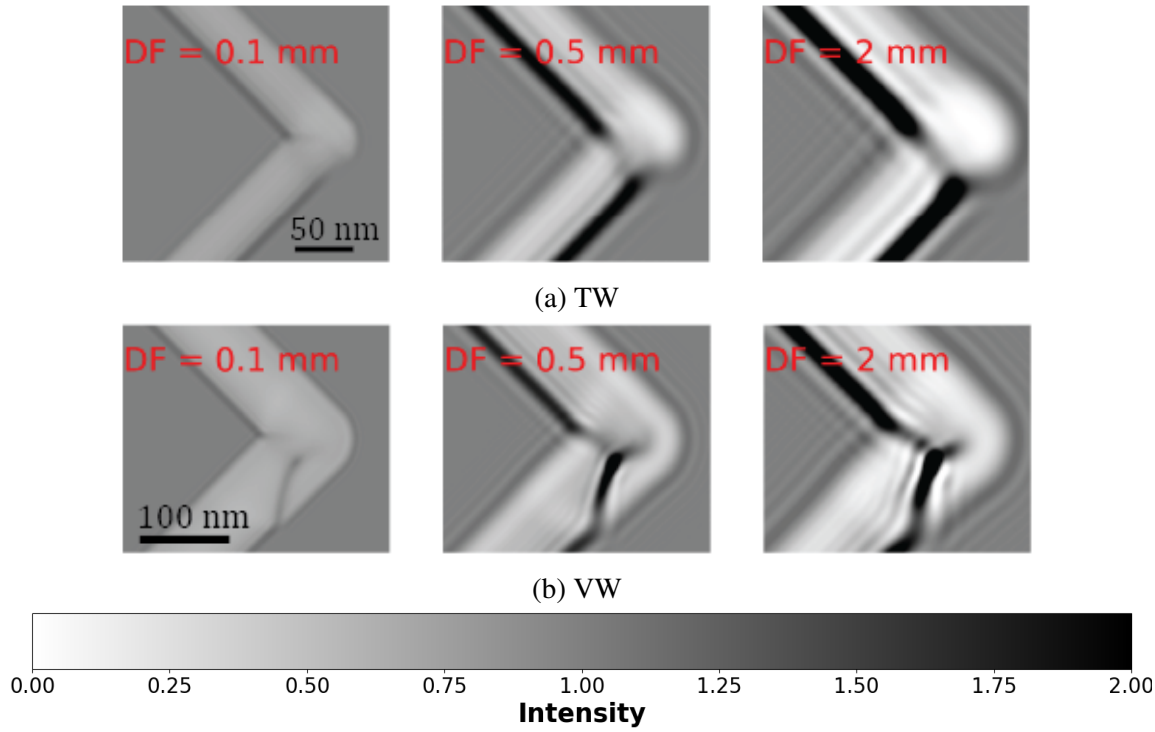

(a) TW

(b) VW

Figure 4.19: Fresnel images of the different DWs appearing in L-shaped nanowires. The TW (4.19a) stabilised an 80 nm wide QC nanowire while the VW (4.19b) stabilised in a 100 nm wide Co HC nanowire. The images were calculated for three different defocus parameters - 0.2 mm, 0.5 mm and 2 mm.

In the images shown, one can clearly see the dark and bright contrast on the wire edges that switch on either side of the DW which is typical of Fresnel microscopy of head-to-head or tail-to-tail nanowires. In the FSW and TW, this contrast changes symmetrically around the centre of the nanowire, while for the VW and AVW, the change of edge contrast occurs on either end of the DW packet. This may be useful when trying to identify DWs experimentally. An interesting change in edge contrast can be seen on the TDVW (4.18f). On the top edge of the nanowire, the contrast changes symmetrically about the centre of the nanowire, but on the bottom edge, there appear to be two transitions where the contrast alternates from bright to dark. In the images of the L-shaped nanowires, the edge contrast is also useful for identifying the DW state. In the TW (4.19a) the dark contrast on the left-hand side of the nanowire only extent to the beginning of the nanowire bent, while in the VW state (4.19b) it continues around the bent reaching the edge of the DW packet on the other side. In addition, the extended vortex core seen in the VW appears to have a very

similar structure to the AVW seen in straight nanowires. To aid in the visualization of the DWs and the edge contrast of the nanowire associated with them, simplified schematics of the Fresnel contrast for the different DWs are presented in Figure 4.20. The images shown there are simple pictorial representations that clearly display the most unique and identifiable features of each DW that can be captured using Fresnel mode imaging.

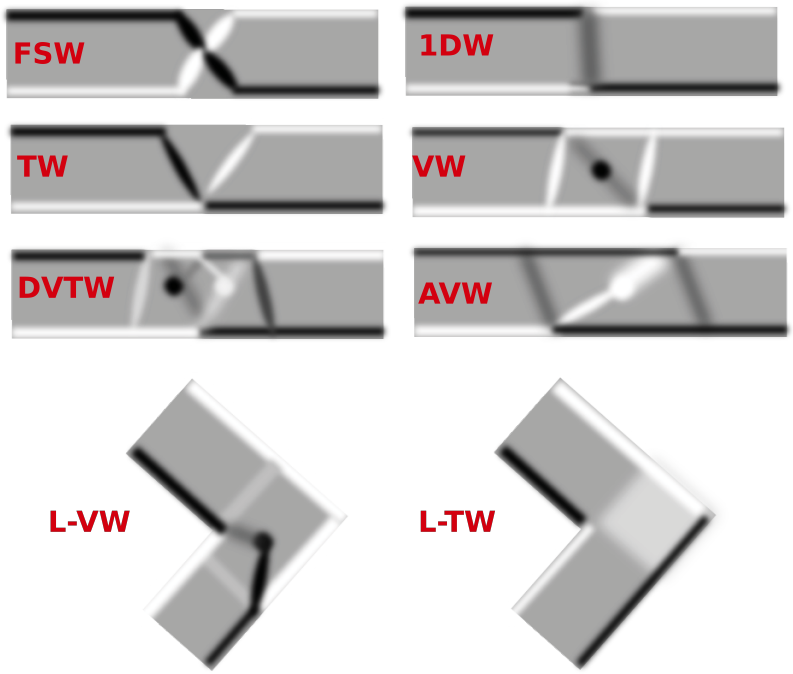

Figure 4.20: Simplified schematics of the Fresnel contrast associated with the different DW.

In addition to qualitative identification of the walls, Fresnel images can be used in a semi-quantitative manner to obtain measurements of DW extents. Figure 4.21 shows line profiles obtained from the Fresnel images of the different DWs shown in Figure 4.19 and 4.18 at a defocus of 2 mm. In the profiles, DWs appear as a series of intensity peaks which correspond to dark and bright contrast in the image. The domains, however, have no variation of intensity in the image. For this reason the method for obtaining DW extent from the magnetisation described in Section 4.6 cannot be applied to the simulated Fresnel images and the two cannot be directly compared. The commonly used Python scipy.find_peaks() function was used to detect the peaks and record their width at the half-maximum

point. This width was then used as a measurement of the DW extent. An example of that can be seen in Figure 4.21a where the red lines represent the calculated DW extent of 1DW in a 60 nm QC nanowire imaged with a defocus of 2 mm. For the more complex walls where multiple peaks were present, the extent was taken as the horizontal distance at FWHM of the first and final peaks that appear in the intensity image. In situations where the DW varied in width across the wire (e.g. the TW pictured Figure 4.21 c)) this measurement was repeated across the nanowire and the result averaged.

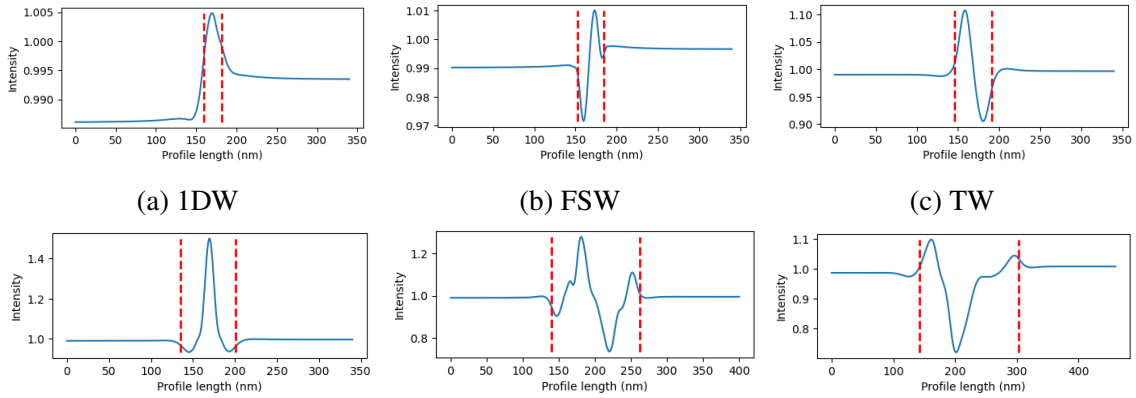

(a) 1DW (b) FSW (c) TW

(d) VW (e) TDVW (f) AVW

Figure 4.21: Average line profiles across DWs in calculated Fresnel mode images Images were taken with a defocus value of 0.5 mm. The red lines indicate the extent of the particular DW.

In the images shown in Figures 4.18 and 4.19 one can clearly see that as the defocus increases so does the apparent extent of the DW. This correlation is visually represented in Figure 4.22, where the extent of a VW, as measured from calculated Fresnel images with defocus ranging from 500 nm to 5 mm, is plotted against the corresponding defocus value. The values shown here are obtained from images of an 80 nm wide Co QC nanowire, but a similar relationship was observed for different nanowire sizes and shapes and for different DW types. The error bars in the figure represent uncertainty obtained from the peak finding algorithm combined with the pixel spacing (2 nm). There are two distinct regions in the plot separated by the red line located between defocus values of Δf = 400 µm and Δf = 500 µm. The region on the left of it represents the so called linear Fresnel imaging regime, where the Fresnel image intensity can be directly related to the out-of-plane component of the curl of the magnetisation, pictured in Figure 4.23 [46]. A similar

result was reported in [47]. The similarity is clear when comparing the VW Fresnel image presented in Figure 4.18 d) and its corresponding profile (4.21) to the images shown in 4.23. Additionally, the VW extent values measured from simulated Fresnel images in the linear regime range from 93 nm to 95 nm $\pm$ 5 nm, which is in good agreement with the value of 93 nm obtained from an average line profile across Figure 4.23a, shown in 4.23b. Beyond defocus values of Δf = 500 µm the measured DW extent begins to rapidly increase and no clear quantitative relation can be made between the contrast in the Fresnel image and the sample magnetisation for the structures in question. Images obtained with defocus in the non-linear do still contain the key features of the DW as can be seen in the 2 mm defocus images shown in Figures 4.18 and 4.19.

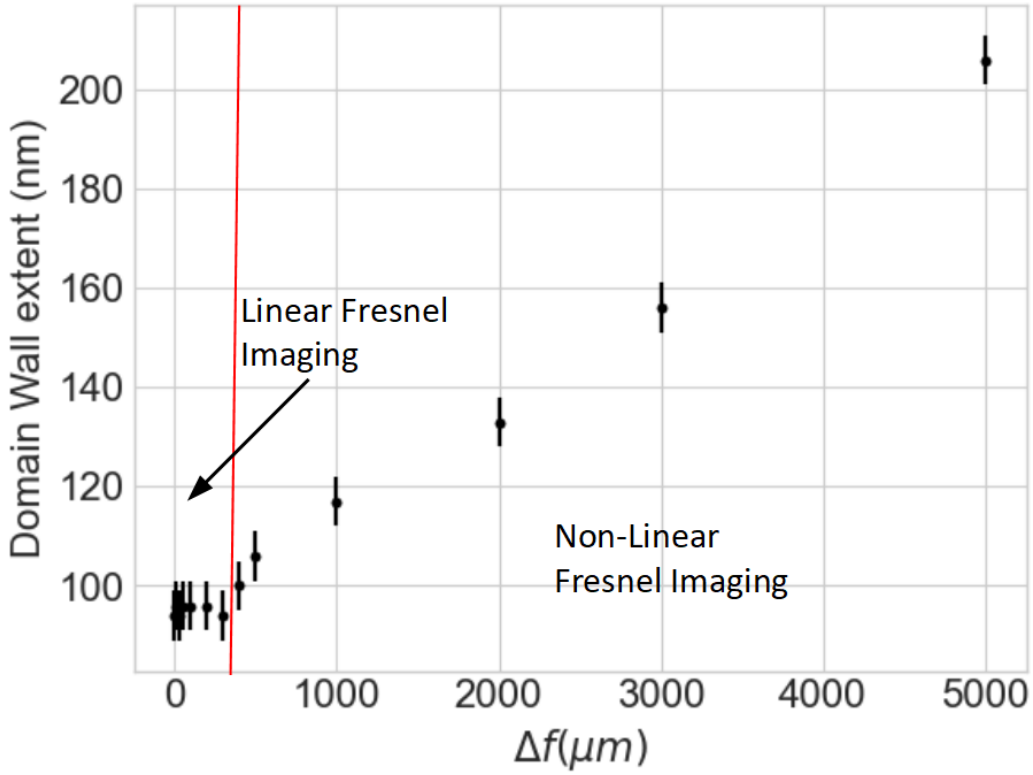

Figure 4.22: Relationship between extent of VW, calculated from Fresnel image and defocus (Δf). Red line separated linear and non-linear regimes of Fresnel imaging.

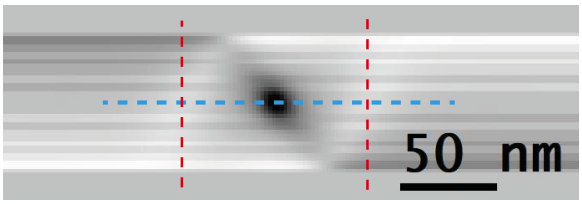

(a) Out-of-plane curl of M

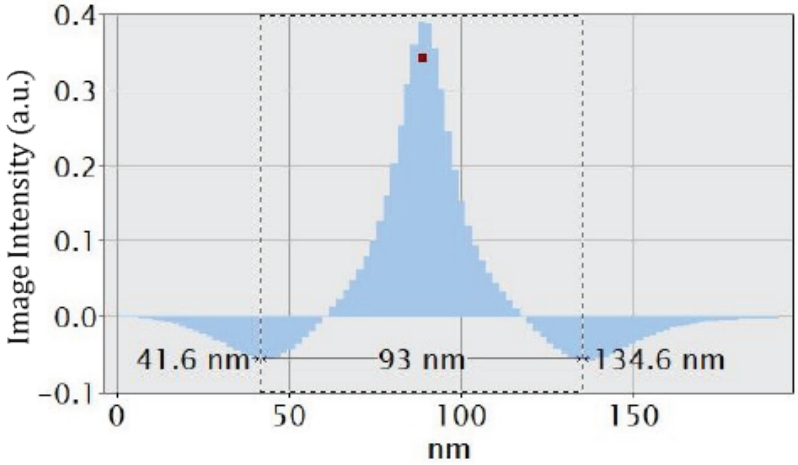

(b) Average profile across a)

Figure 4.23: Out-of-plane component of the curl of magnetisation for a 80 nm wide QC nanowire with a VW (a)) and an average line profile across it (b)). Blue line in a) represents the central location of the line profile while the red lines show the extent of the DW and correspond to the dotted lines in b).

In conclusion, the simulated Fresnel images presented here show a relatively clear picture of the different DWs with easily distinguishable features. Additionally, the relationship between defocus and DW extent presented above can be used to semi-quantitatively obtain a measure of the DW extent for an actual experimental image if the defocus value is known. The word "semi" is an important distinction, because the simulated Fresnel images shown here represent an ideal imaging scenario which is not realistically achievable. Additionally, this section does not include the effects of electrostatic contrast, which is an important issue when imaging structures with variable thickness. This is addressed in Section 4.8.3, where an attempt is made to simulate electrostatic contributions to the phase.

4.8.2 Calculated DPC Images

An alternative way to identify DWs and measure them quantitatively from experimental images would be using DPC imaging as described in Section 3.5.5. In this technique quantitative information about the magnetic induction of the sample is extracted directly from the phase. In particular, the gradient of the phase is proportional to the deflection of the electron beam caused by the magnetic induction of the sample - Equation 4.1. In the absence of an external magnetic field (as is the case for the simulated nanowires) this gives a direct probe into the magnetisation of the sample.

$$\nabla\phi = \frac{2\pi}{\lambda}\beta \tag{4.1}$$

Where ϕ is the phase of the electron beam, β is the deflection of the electron beam due to sample magnetisation and λ is the electron wavelength. To obtain simulated DPC images of the nanowires simulated in Sections 4.3 through to 4.5 the FPD package is again used to obtain the 2D gradient of the phase image, which can be selected as an output of the mag_phase() function, a detailed description of which is available in Section 3.5.6. This function takes as input 2D images of the m_x and m_y magnetisation components obtained using the method described in 4.8 and outputs a pair of images that map two orthogonal components of the integrated induction of the sample. Example DPC images calculated from simulations containing all the different DWs observed in L-shaped and straight nanowires can be seen in Figure 4.25 and 4.24. These include a composite colour phase image along with two maps of the orthogonal components of the integrated induction of the sample in the directions indicated by the arrows. The colour images are obtained by combining the two orthogonal induction component and coloring the resultant image based on its grey-scale value. Combined with the color wheel, they show a more intuitive representation of the variation of the sample induction. For comparison 2D representations of the in-plane magnetisation components are also included.

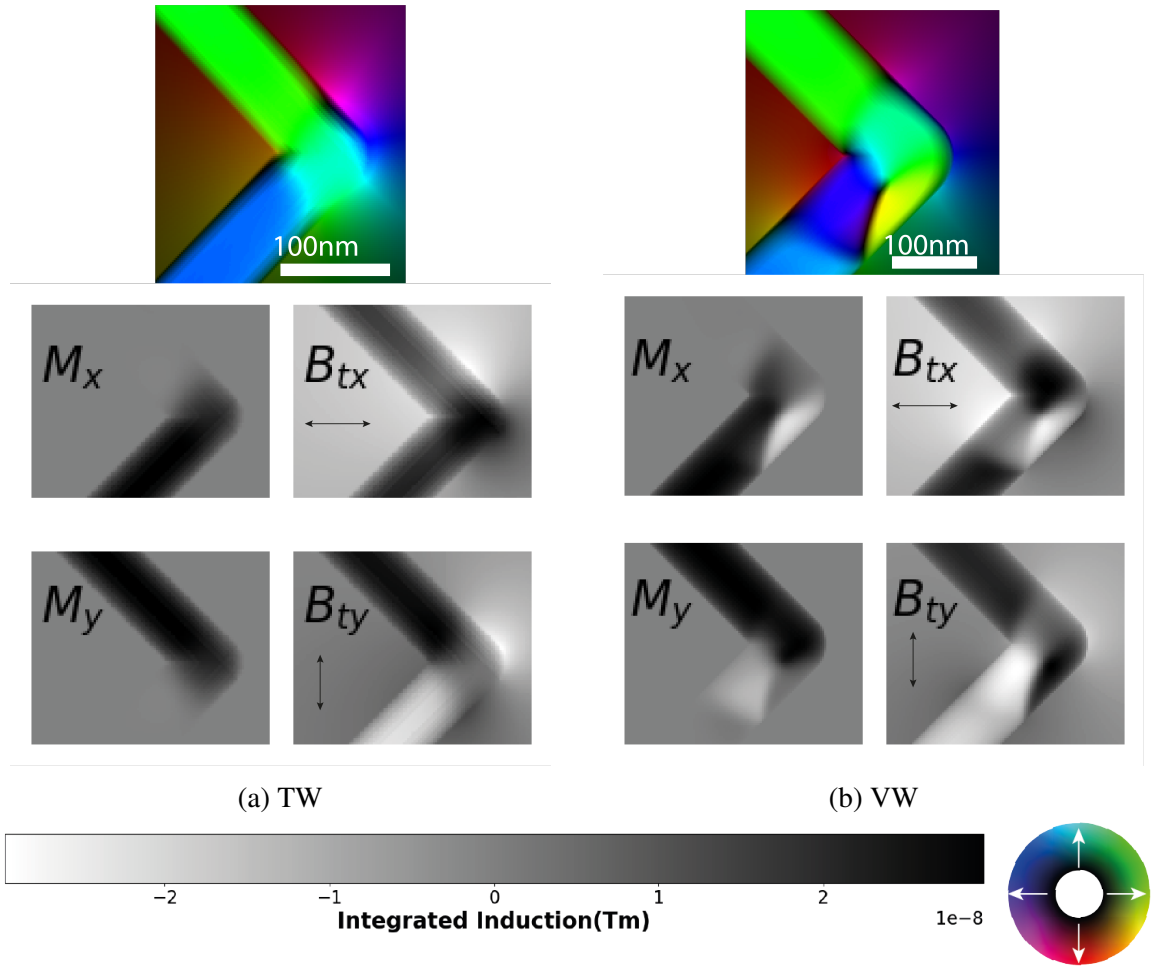

(a) TW (b) VW

Figure 4.24: Calculated DPC images of the different DWs appearing in L-shaped nanowires. The TW (4.19a) stabilised an 80 × 20 nm wide Fe QC nanowire while the VW(4.19b) stabilised in a 100 × 50 nm wide Co HC nanowire. The images for each DW display a composite colour phase image (middle) and two orthogonal components of the integrated induction in directions indicated by the arrows.

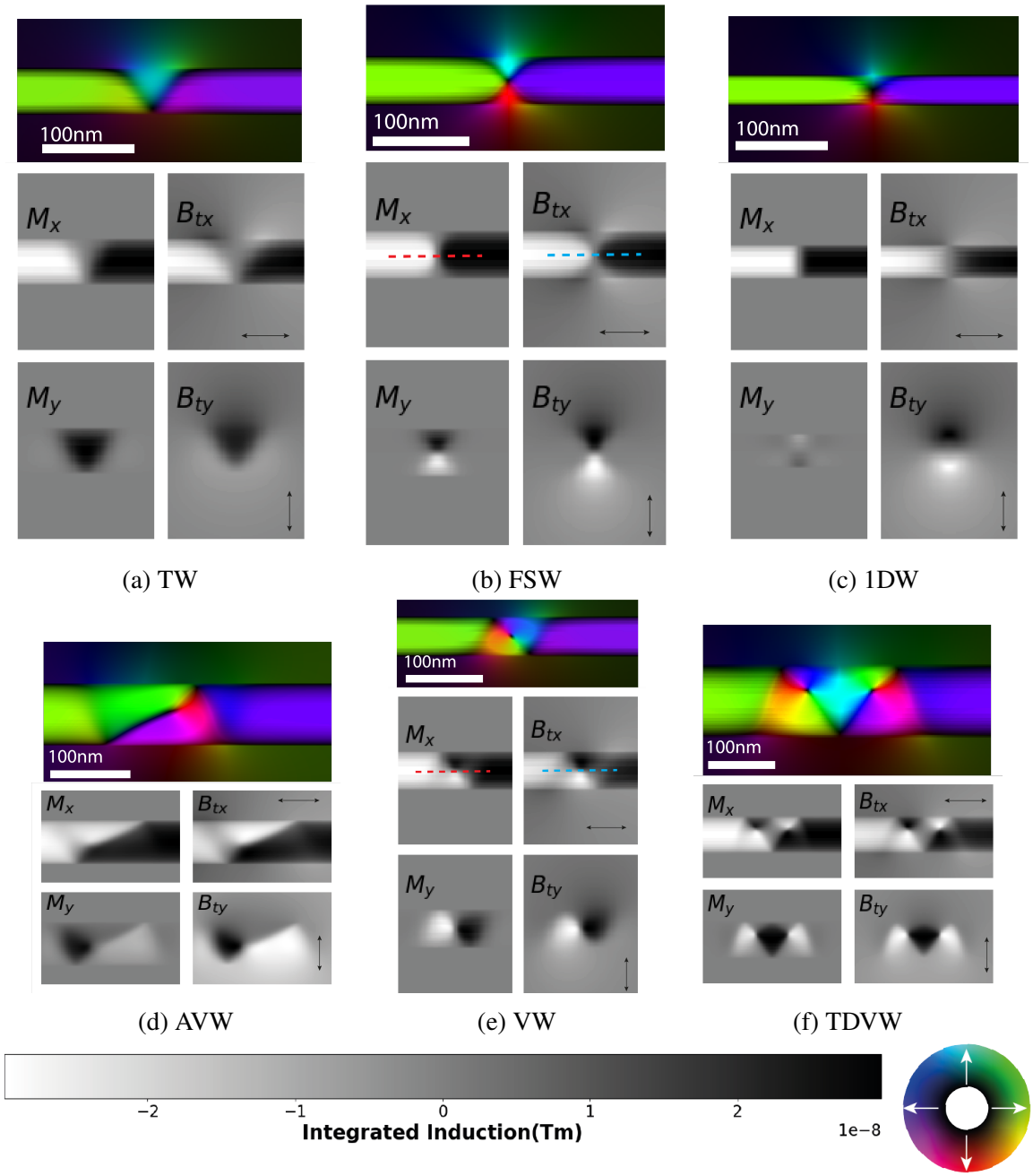

Figure 4.25: Calculated DPC images of the different DWs appearing in straight nanowires. The TW (a)), FSW (b)), and VW (e)) stabilised in an 80x20 nm wide Co QC nanowire, the 1DW(c)) in a 60 × 15 nm wide Co QC nanowire, while the AVW (d)) and TDVW (f)) stabilised in a 120 × 40 nm Fe QC nanowire w. The images for each DW display a composite colour phase image, the two components of magnetisation and the equivalent two orthogonal components of the integrated induction in directions indicated by the arrows. Blue and red dotted lines in b) and e) indicate line profile locations shown in Figure 4.26.

In the images shown here, there are clear distinctive features of all the different DWs. As can be seen, there are only subtle differences between the magnetisation from the simulations and the calculated DPC images. The main one is the presence of stray fields generated by the DWs outside the geometry of the nanowires. The effect of these is also visible within the nanowires, where they appear to make the DWs wider. This is most clearly visible in the images of the TW (4.25 a)), FSW (4.25 b)) and 1DW (4.25 c)). The similarities and differences between the integrated induction and magnetisation are further pictured in Figure 4.26, which displays side by side line profiles obtained from DPC and magnetisation component images for a FSW and VW using the method outlined in 4.6 i.e. several line profiles were taken from the resultant DPC images along the long dimension of the nanowire. The location where the line profiles were taken are displayed as red dotted lines for the magnetisation (**M**) and blue dotted lines for the integrated Induction ($\mathbf{B_{tx}}$) in Figure 4.25 b) and e).

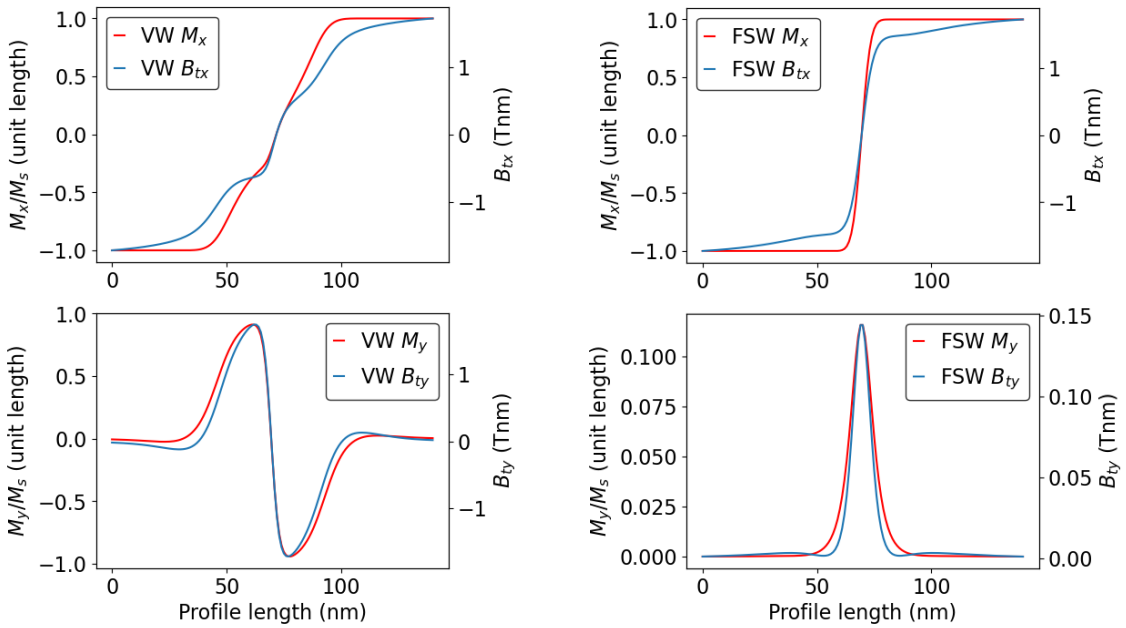

(a) VW (b) FSW

Figure 4.26: Average line profiles showing the difference between the in-plane (x and y) components of magnetisation (**M**) and integrated Induction ($\mathbf{B_{tx}}$) for a VW (a)) and FSW (b)).

Finally, the extent of the DWs (DWs) from the DPC images was measured from these line profiles and compared to the DW extents obtained directly from magnetisation. Figure 4.27 shows this comparison between VWs and FSWs for both HC and QC nanowires. Clearly, the extents obtained from the integrated induction are consistently larger across the different nanowire sizes. This is most likely due to the stray fields caused by the DW, which are also captured in the DPC images. The average difference in DW extent calculated from magnetisation and from integrated induction is 9.5% for the QC nanowires and 8.4% for the HC ones.

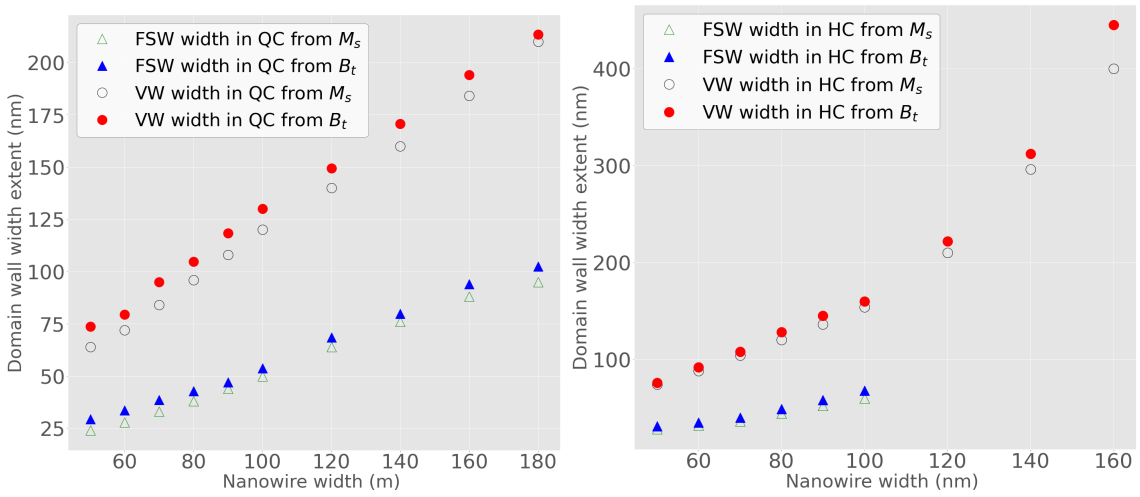

(a) QC (b) HC

Figure 4.27: DW extent for FSWs and VWs calculated from Integrated induction images compared to measurements from the magnetisation. a) shows the comparison for QC nanowires, while b) shows it for HC nanowires.

4.8.3 Effect of electrostatic contrast

As mentioned in Sections 3.5.2 and 3.5.6, the variable thickness of the nanowire simulated here gives rise to strong electrostatic contrast that might obscure the desired magnetic information in Lorentz microscopy. Here an attempt is made to introduce an electrostatic component to the phase with which the simulated images are calculated in order to better relate simulated images to future experimental results. The electrostatic phase ϕ_e from a sample is related to its thickness function - t(x,y) (Equation 3.19). For the simulations performed here, t(x,y) is obtained by calculating the $t = 2 \times 10^{-9}\sqrt{m_x^2 + m_y^2 + m_z^2}$ sum for

each cell in the simulation and averaging the resulting 3D dataset along the wire thickness (z-dimension) to obtain a 2D thickness image - $t(x,y)$ - pictured in Figure 4.28. The code used to achieve this is available in available in Appendix A.2.

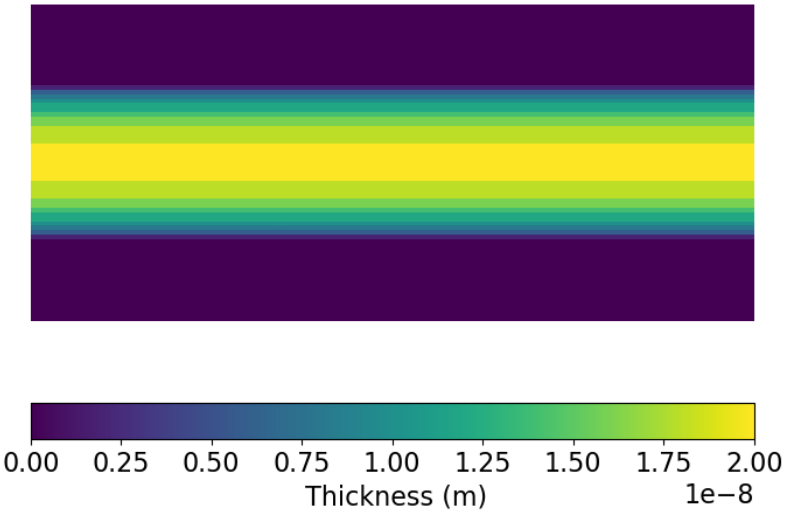

Figure 4.28: Thickness function of an 80 $\times$ 20 nm QC nanowire used in the calculation of the electrostatic phase.

This image is then used to calculate the electrostatic phase ϕ_e using Equation 3.19 as discussed in Section 3.5.6. The mean inner potential values used were 21 V for the Co nanowires and 23 V, obtained from several external sources [48] [49] [50]. The final result is added to the already calculated magnetic phase (ϕ_m) giving the total phase $\phi_t = \phi_m + \phi_e$ from which a new set of simulated Lorentz microscopy images are obtained. Figure 4.29 shows DPC images with an included electrostatic phase of several L-shaped and straight nanowires. In Figure 4.29 one can see that the magnetic contrast is considerably obscured by the electrostatic contributions. The main features of the DWs, however, are still distinguishable. In addition, Figure 4.30 shows a comparison between images of the longitudinal magnetisation (M_x/M_s), the integrated induction (B_{tx}) and the integrated induction with electrostatic contributions included. The main difference in the three is the extra bright/dark contrast on the wire edges that can be seen in the DPC image with included EC. To better visualise the difference vertical line profiles were taken across the simulated DPC of a QC and HC nanowire of the same width (100nm) with and without the electrostatic contributions.

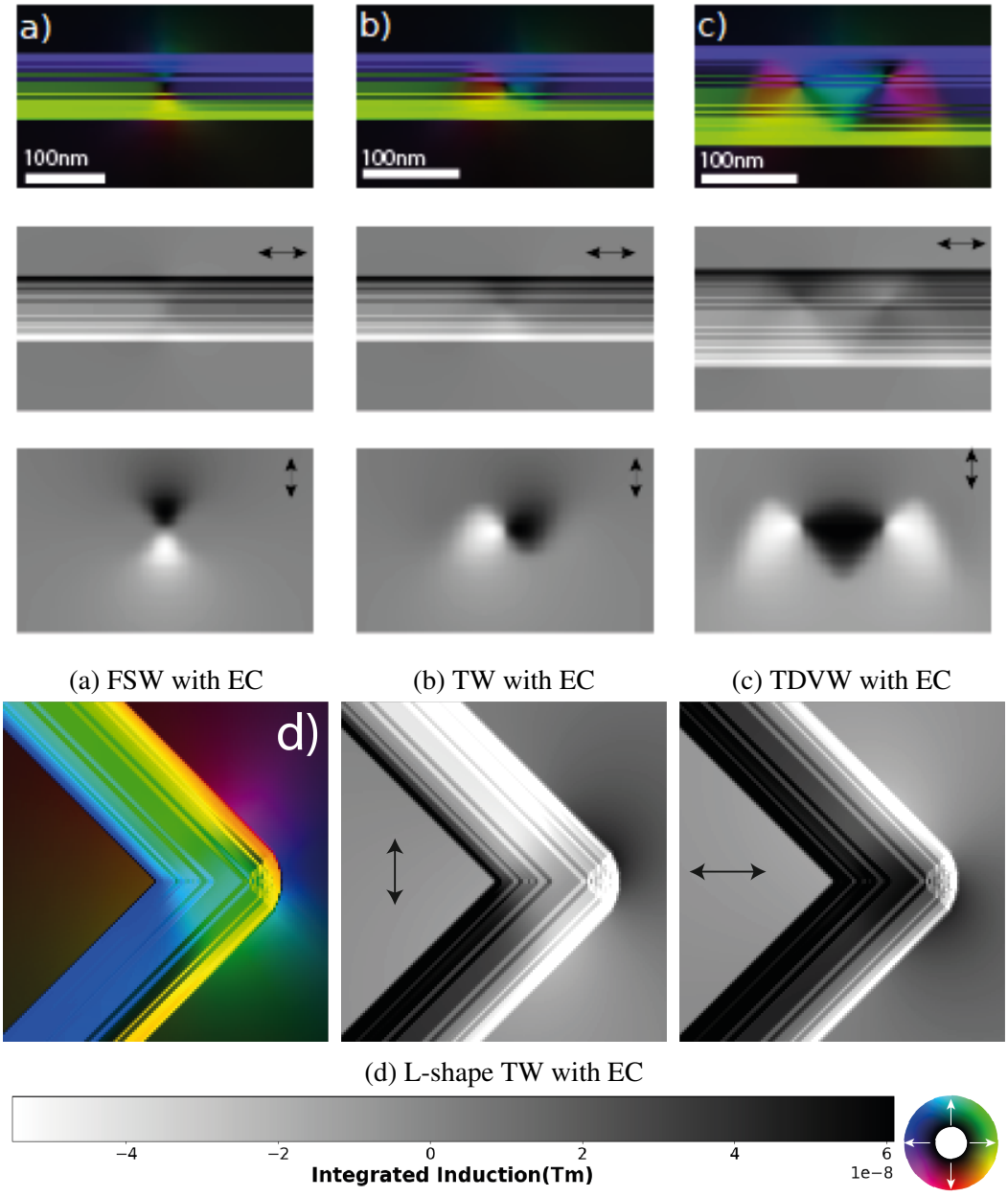

(a) FSW with EC (b) TW with EC (c) TDVW with EC

(d) L-shape TW with EC

Figure 4.29: Calculated DPC images of a FSW (4.29a), VW (4.29b), TDVW (4.29c) and L-shape TW (4.29d) with included electrostatic phase. Images show a composite colour phase image (top image) along with two composite integrated induction images.

The profiles were taken across the y-dimensions of the nanowires and in the domain region. They can be seen in Figure 4.31. There one can see a clear distinction between the profiles of a QC and HC nanowire by examining the size of the peaks on either end of the profile in

the images with included electrostatic phase. These are much taller in the case of the HC because of the higher curvature. On the other hand, the profiles showing only the magnetic contrast have a shape closely resembling the shape of the nanowire. This observation is used in the DPC imaging section of Chapter 4 as a way to qualitatively determine whether decoupling the electrostatic and magnetic contributions to phase has been successful. As a final remark, it should be noted that while including electrostatic contributions to the simulated Lorentz microscopy images had an effect on image quality it did not affect the apparent size of the different DWs. This is because DW extents are measured using a line profile along the long dimension of the nanowire, which has no variation in thickness.

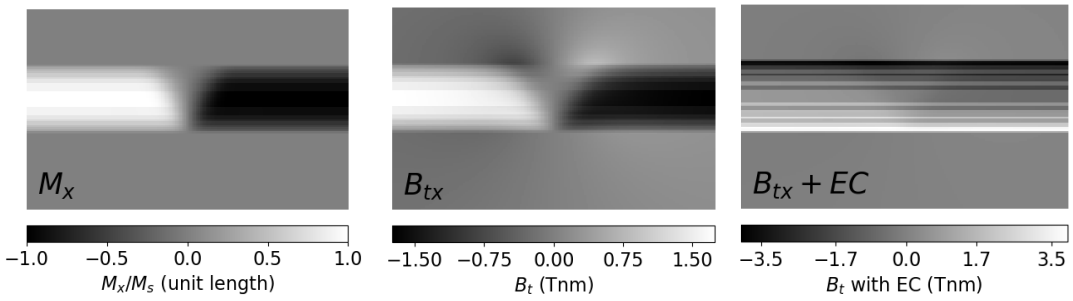

(a) Normalised M_x (b) Integrated Induction (c) Integrated Induction + EC

Figure 4.30: Comparison between the M_x (a)), B_{tx} Component of a calculated DPC image (b)) and the same B_{tx} component with electrostatic phase included in the calculation of an 80 nm wide QC nanowire with a TW.

In addition to the DPC images, Fresnel images with included electrostatic phase were calculated for QC and HC nanowires. Example images showing a VW and TW in straight 100 nm wide QC and HC nanowires can be seen in Figure 4.32. These images were calculated with a defocus value of 1 mm and the same imaging conditions described in Section 4.8.1. A major feature present in all the images is the reduction of magnetic edge contrast in the domains. Despite that, there are clear identifying features that can be used to label the different DWs. In the examples given one such feature is the high-intensity central dot corresponding to the vortex core of the VW pictured in Figures 4.32c and 4.32d. Additionally, as was the case for the simulated DPC images, the electrostatic contrast modelled in this way had no effect on the measured DW extent calculated from Fresnel images as the large defocus value strongly overshadowed any variations due to the electrostatic contrast.

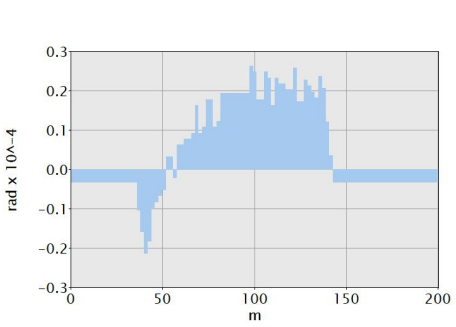

(a) Profile across QC nanowire with EC EC

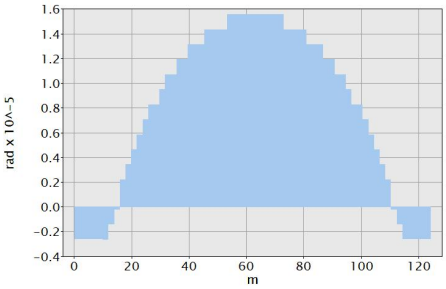

(b) Profile across QC nanowire without

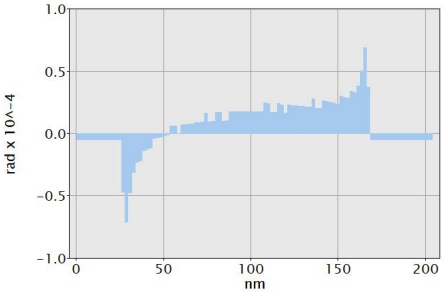

(c) Profile across HC nanowire without EC

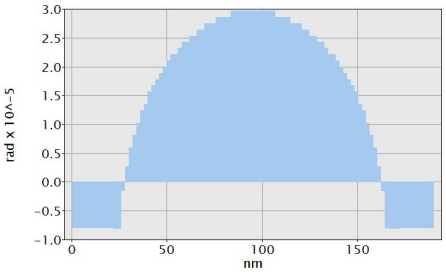

(d) Profile across HC nanowire without EC

Figure 4.31: Profiles taken across calculated DPC images of a QC and HC nanowires with (4.31a - QC and 4.31c-HC) and without (4.31b - QC and 4.31d - HC) electrostatic phase.

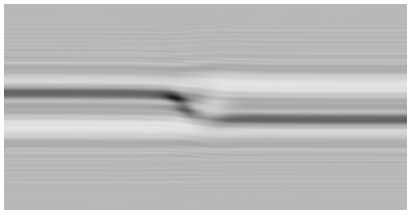

(a) TW in QC

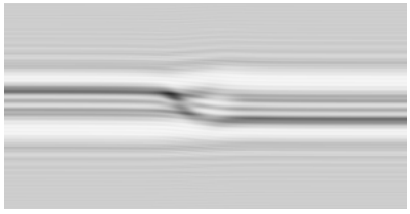

(b) TW in HC

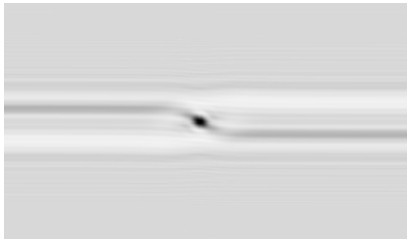

(c) VW in QC

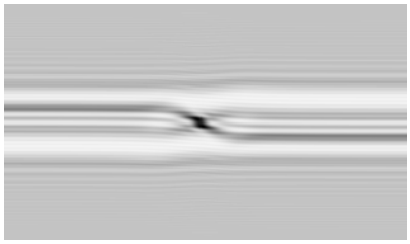

(d) VW in HC

Figure 4.32: Calculated Fresnel images with defocus of 1 mm of QC (a) and b)) and HC (c) and d)) Co nanowires with TW and VW with included electrostatic phase.

4.9 Summary

An extensive series of micromagnetic simulations of cylindrical segment nanowires was performed. The results demonstrated the formation of a wide variety of different DWs with unique features. In particular, the metastable FSW and 1DW show potential for spintronic devices due to their compact size and chirality. A probe was made into the stability of the different DW by extracting the average density of the different nanowire and several plots were constructed showing the evolution of the ground state DW in different nanowires. The effect of iDMI on QC nanowires was examined and was found to have the greatest effect on thinner and narrower nanowires. iDMI was found to amplify the out-of-plane component of DWs and also led to the stabilisation of the narrow 1DW. The sizes of different DWs were calculated and recorded. Several factors were found to affect the DW widths including nanowire profile (HC vs QC), material parameters and the presence of iDMI. Overall, significantly more different DWs stabilised in straight nanowires as opposed to L-shaped ones. However, in physical experiments nucleating a DW in a straight nanowire would be quite challenging because, in the lowest energy state, the magnetisation in the wire would simply point along the long dimension of the nanowire or form a flux closure state if nanowire is wide enough to support it. Creating a head-to-head magnetisation would be much easier in an L-shaped nanowire due to its geometry. In order to be able to relate the simulations to experimental results simulated Lorentz microscopy images were calculated for the different DWs. In these, the effect of the nanowire shape was considered with the inclusion of a calculation of the electrostatic phase in the image calculation. The results showed that using Fresnel mode imaging for distinguishing different DWs is possible even with high defocus imaging and for structures with strong electrostatic contrast. Similarly, in DPC imaging even with the inclusion of the electrostatic phase most of the distinctive features of the different DWs remained visible. While the simulations performed here form a good basis for experimental studies, the parameter space that can be further explored is vast. For example, a wider range of material parameters (M_s and A) can be examined along with a more comprehensive study of iDMI in order to look for a set of parameters for which the most interesting DWs (FSW and 1DW) are also the ground state ones. This topic is further discussed in Chapter 6, where several avenues of future research are suggested.

References

[1] C. Bran, Y. P. Ivanov, D. G. Trabada, J. Tomkowicz, R. P. Del Real, O. Chubykalo-Fesenko, and M. Vazquez. Structural dependence of magnetic properties in co-based nanowires: Experiments and micromagnetic simulations. *IEEE Transactions on Magnetics*, 49(8):4491 – 4497, 2013.

[2] K. M. Lebecki and M. J. Donahue. Frustrated magnetization in co nanowires: Competition between crystal anisotropy and demagnetization energy". *Phys. Rev. B*, 82: 096401, 2010.

[3] L. Vila, M. Darques, A. Encinas, U. Ebels, J. George, G. Faini, A. Thiaville, and L. Piraux. Magnetic vortices in nanowires with transverse easy axis. *Phys. Rev. B*, 79:172410, 2009.

[4] S. Vojkovic, V. L. Carvalho-Santos, J. M. Fonseca, and A. S. Nunez. Vortex-antivortex pairs induced by curvature in toroidal nanomagnets. *Journal of Applied Physics*, 121(11):113906, 2017.

[5] Y. P. Ivanov and O. Chubykalo-Fesenko. Micromagnetic simulations of cylindrical magnetic nanowires. In Manuel Vázquez, editor, *Magnetic Nano- and Microwires*, pages 423–448. Woodhead Publishing, 2015.

[6] M. Yan, A. Kákay, S. Gliga, and R. Hertel. Beating the Walker limit with massless domain walls in cylindrical nanowires. *Physical Review Letters*, 104(5):057201, 2010.

[7] I. Utke, J. Michler, Ph. Gasser, C. Santschi, D. Laub, M. Cantoni, P.th A. Buffat, C. Jiao, and P. Hoffmann. Cross section investigations of compositions and substructures of tips obtained by focused electron beam induced deposition. *Advanced Engineering Materials*, 7(5):323–331, 2005.

[8] A. Botman, J. J. L. Mulders, and C. W. Hagen. Creating pure nanostructures from electron-beam-induced deposition using purification techniques: A technology perspective. *Nanotechnology*, 20(37):372001, 2009.

[9] A. Fernández-Pacheco, L. Skoric Luka, J. M. De Teresa a, J. Pablo-Navarro, M. Huth, and O. V. Dobrovolskiy. Writing 3D nanomagnets using focused electron beams. *Materials*, 13:3774, 2020.

[10] J. M. De Teresa, A. Fernández-Pacheco, R. Córdoba, L. Serrano-Ramón, S. Sangiao, and M. R. Ibarra. Review of magnetic nanostructures grown by focused electron beam induced deposition (FEBID). *Journal of Physics D: Applied Physics*, 49(24): 243003, 2016.

[11] R. Lavrijsen, R. Córdoba, F. J. Schoenaker, T. H. Ellis, B. Barcones, J. T. Kohlhepp, H. J. M. Swagten, B. Koopmans, J. M. De Teresa, C. Magén, M. R. Ibarra, P. Trompenaars, and J. J. L. Mulders. Fe:O:C grown by focused-electron-beam-induced deposition: magnetic and electric properties. *Nanotechnology*, 22(2):025302, 2010.

[12] M. W Grinstaff, M. B. Salamon, and K.S. Suslick. Magnetic properties of amorphous iron. *Phys. Rev. B*, 48:269–273, 1993.

[13] S. Sangiao, C. Magén, D. Mofakhami, G. de Loubens, and J. M. De Teresa. Magnetic properties of optimized cobalt nanospheres grown by focused electron beam induced deposition (FEBID) on cantilever tips. *Beilstein Journal of Nanotechnology*, 8:2106–2115, 2017.

[14] G. S. Abo, Y. Hong, J. Park, J. Lee, W. Lee, and B. Choi. Definition of magnetic exchange length. *IEEE Transactions on Magnetics*, 49(8):4937–4939, 2013.

[15] G. M. Macauley. Skating on spin ice: On the application of Lorentz microscopy and numerical techniques to characterise phase transitions and non-equilibrium phenomena in artificial spin ices. 2020.

[16] C. Kurniawan, A. Widodo, and D. Djuhana. The diameter effect on the magnetization switching time of sphere-shaped ferromagnets using micromagnetic approach. 902: 012060, 2020.

[17] M. Gusenbauer, H. Özelt, J. Fischbacher, A. Kovacs, P. Zhao, T. Woodcock, and T. Schrefl. Extracting local nucleation fields in permanent magnets using machine learning. 6:89, 2020.

[18] R. D. McMichael and M. J. Donahue. Head to head domain wall structures in thin magnetic strips. *IEEE Transactions on Magnetics*, 33(5):4167–4169, 1997.

[19] R. Streubel, E. Y. Tsymbal, and P. Fischer. Magnetism in curved geometries. *Journal of Applied Physics*, 129(21):210902, 2021.

[20] J. A. Fernandez-Roldan, A. De Riz, B. Trapp, C. Thirion, M. Vazquez, J.-C. Toussaint, O. Fruchart, and D. Gusakova. Modeling magnetic-field-induced domain wall propagation in modulated-diameter cylindrical nanowires. *Scientific Reports*, 9(1): 5130, 2019.

[21] M. Charilaou, Ha. Braun, and J. F. Löffler. Monopole-induced emergent electric fields in ferromagnetic nanowires. *Phys. Rev. Lett.*, 121:097202, 2018.

[22] Y. Nakatani, A. Thiaville, and J. Miltat. Head-to-head domain walls in soft nanostrips: a refined phase diagram. *Journal of Magnetism and Magnetic Materials*, 290-291:750–753, 2005.

[23] T. H. Pham, J. Vogel, J. Sampaio, M. Vaňatka, J C. Rojas-Sánchez, M. Bonfim, D. S. Chaves, F. Choueikani, P. Ohresser, E. Otero, A. Thiaville, and S. Pizzini. Very large domain wall velocities in Pt/Co/Gdox and Pt/Co/Gd trilayers with Dzyaloshinskii-Moriya interaction. *Europhysics Letters*, 113(6):67001, 2016.

[24] M. D. DeJong and K. L. Livesey. Domain walls in finite-width nanowires with interfacial dzyaloshinskii-moriya interaction. *Phys. Rev. B*, 95:054424, 2017.

[25] M. J. Benitez, A. Hrabec, A. P. Mihai, T. A. Moore, G. Burnell, D. McGrouther, C. H. Marrows, and S. McVitie. Magnetic microscopy and topological stability of homochiral néel domain walls in a Pt/Co/Al trilayer. *Nature Communications*, 6(1): 8957, 2015.

[26] M. Kuepferling, A. Casiraghi, G. Soares, G. Durin, F. Garcia-Sanchez, L. Chen, C. H. Back, C. H. Marrows, S. Tacchi, and G. Carlotti. Measuring interfacial dzyaloshinskii-moriya interaction in ultrathin magnetic films. *Rev. Mod. Phys.*, 95: 015003, 2023.

[27] G. Siracusano, R. Tomasello, A. Giordano, V. Puliafito, B. Azzerboni, O. Ozatay, M. Carpentieri, and G. Finocchio. Magnetic radial vortex stabilization and efficient manipulation driven by the Dzyaloshinskii-Moriya interaction and spin-transfer torque. *Physical Review Letters*, 117(8):087204, 2016.

[28] H. Sepehri-Amin, T. Ohkubo, M. Gruber, T. Schrefl, and K. Hono. Micromagnetic simulations on the grain size dependence of coercivity in anisotropic Nd–Fe–B sintered magnets. *Scripta Materialia*, 89:29–32, 2014. ISSN 1359-6462.

[29] J. A. Fernandez-Roldan, A. De Riz, and B. Trapp. Modeling magnetic-field-induced domain wall propagation in modulated-diameter cylindrical nanowires. *Scientific Reports*, 9(1):5130, 2019.

[30] V. D. Nguyen, O. Fruchart, S. Pizzini, J. Vogel, J.-C. Toussaint, and N. Rougemaille. Third type of domain wall in soft magnetic nanostrips. *Scientific Reports*, 5(1):12417, 2015.

[31] S. Jamet, N. Rougemaille, J.C. Toussaint, and O. Fruchart. Head-to-head domain walls in one-dimensional nanostructures: An extended phase diagram ranging from strips to cylindrical wires. In *Magnetic Nano- and Microwires*, pages 783–811. Woodhead Publishing, 2015.

[32] R. Moreno, V. L. Carvalho-Santos, D. Altbir, and O. Chubykalo-Fesenko. Detailed examination of domain wall types, their widths and critical diameters in cylindrical magnetic nanowires. *Journal of Magnetism and Magnetic Materials*, 542:168495, 2022.

[33] S. Woo, K. Litzius, B. Krüger, M.-Y. Im, L. Caretta, K. Richter, M. Mann, A. Krone, R. M. Reeve, M. Weigand, P. Agrawal, I. Lemesh, M. A. Mawass, P. Fischer, M. Kläui, and G. S. D. Beach. Interfacial dzyaloshinskii-moriya interaction: effect of heavy metal layer thickness. *Nature Materials*, 15(5):501–506, 2016.

[34] S. Da Col, S. Jamet, M. Staňo, B. Trapp, S. Le Denmat, L. Cagnon, J. C. Toussaint, and O. Fruchart. Nucleation, imaging, and motion of magnetic domain walls in cylindrical nanowires. *Applied Physics Letters*, 109(6):062406, 2016.

[35] G. Venkat, D. A. Allwood, and T. J. Hayward. Magnetic domain walls: types, processes and applications. *Journal of Physics D: Applied Physics*, 57(6):063001, 2023.

[36] C. Stoner Edmund. Ferromagnetism: magnetization curves. *Reports on Progress in Physics*, 13(1):83–183, 1950.

[37] A. Di Pietro, F. García-Sánchez, and G. Durin. Domain wall statics and dynamics in nanowires with arbitrary dzyaloshinskii-moriya tensors. *Phys. Rev. B*, 108:174427, 2023.

[38] D. Petit, T. Zeng, J. Sampaio, E. Lewis, L. O'Brien, A. Jausovec, D. Read, P. Cowburn, K.J. O'Shea, S. McVitie, and J. N. Chapman. Magnetic imaging of the pinning mechanism of asymmetric transverse domain walls in ferromagnetic nanowires. *Applied Physics Letters*, 97(23):233102, 2010.

[39] S. Da Col, S. Jamet, N. Rougemaille, A. Locatelli, T. O. Mentes, B. S. Burgos, R. Afid, M. Darques, L. Cagnon, J. C. Toussaint, and O. Fruchart. Observation of bloch-point domain walls in cylindrical magnetic nanowires. *Phys. Rev. B*, 89: 180405, 2014.

[40] R. Cheng, M. Li, A. Sapkota, A. Rai, A. Pokhrel, T. Mewes, C. Mewes, D. Xiao, M. de Graef, and V. Sokalski. Magnetic domain wall skyrmions. *Phys. Rev. B*, 99: 184412, 2019.

[41] M. Mansuripur. Computation of electron diffraction patterns in Lorentz electron microscopy of thin magnetic films. *Journal of Applied Physics*, 69(4):2455–2464, 1991.

[42] G. Paterson. FPD: Fast pixelated detector data storage, analysis and visualisation. https://gitlab.com/fpdpy/fpd. Accessed 20/05/2020.

[43] M. de Graef. Lorentz microscopy: Theoretical basis and image simulations. pages 27–67, 2001.

[44] A. A. Sousa, M. F. Hohmann-Marriott, G. Zhang, and R. D. Leapman. Monte carlo electron-trajectory simulations in bright-field and dark-field STEM: Implications for tomography of thick biological sections. *Ultramicroscopy*, 109(3):213–221, 2009.

[45] D. C. Joy. Monte carlo modeling for electron microscopy and microanalysis. *Journal of the American Chemical Society*, 9(13):3324–3324, 1995.

[46] S. McVitie and G. S. White. Imaging amperian currents by Lorentz microscopy. *Journal of Physics D: Applied Physics*, 37(2):280–288, 2003.

[47] S. McVitie and M. Cushley. Quantitative Fresnel Lorentz microscopy and the transport of intensity equation. *Ultramicroscopy*, 106(4-5):423–431, 2006.

[48] R. I. Anishchenko. Calculation of the mean inner potential of a crystal in the statistical theory. *Physica status solidi (b)*, 18(2):923–928, 1966.

[49] R. E. Dunin-Borkowski, M. R. McCartney, D. J. Smith, and S. Parkin. Towards quantitative electron holography of magnetic thin films using in situ magnetization reversal. *Ultramicroscopy*, 74(1-2):61–73, 1998.

[50] M. de Graef, N. T. Nuhfer, and M. R. McCartney. Phase contrast of magnetic cobalt spheres. *Microscopy and Microanalysis*, 5(S2):34–35, 1999.

5

Lorentz Microscopy of curved nanowires fabricated using FEBID

Contents

5.1 Chapter Outline

In Chapter 4, a detailed micromagnetic simulation study was used to analyse the different magnetic domain walls (DWs) that may exist in cylindrical segment ferromagnetic nanowires. In this chapter, the examination of DWs in nanowires with a curved profile is continued by an empirical study of physical nanowires using a variety of electron microscopy techniques. The first section details the fabrication process of the nanowires including the patterning using FEBID and preparation for electron microscopy using DC magnetron sputtering. The chapter continues with a discussion of the structural and magnetic properties of the nanowires obtained using a variety of microscopy techniques. These include bright field, Fresnel mode and DPC mode electron microscopy as well as atomic force microscopy (AFM). BF imaging and AFM were used to measure the critical sizes of the nanowires and provide an insight into the quality of the fabrication. Fresnel mode was used for a qualitative study of their magnetic structure and STEM DPC used to obtain quantitative information about the magnetic properties of the nanowires and the DWs that they support. Additionally, the chapter presents a method to decouple the electrostatic and magnetic contributions to the electron phase change in DPC images which leads to improved and more easy to interpret images.

5.2 Nanowire fabrication

The FEBID technique described in Chapter 3 was chosen to fabricate the nanowires. It provided flexibility in the nanowire shape prototyping with the possibility of directly creating nanowire patterns using the in-built microscope tools or importing pre-made patterns either in bitmap image or textual file form. In addition, it allowed direct control over the fabrication process and the ability to immediately vary deposition parameters according to the user's needs. For this project, the deposition was achieved on a Helios plasma focused ion beam instrument with the use of either $Co_2(CO)_8$ or $Fe(CO)_5$ metal-organic precursor gases. The nanowires were deposited on 40 nm thick Si_3N_4 membranes. Before each deposition, a 10 -15 nm layer of Cu was deposited on the membranes using DC Magnetron Sputtering at a current of 140 mA with Ar gas pressure of 5×10^{-2} mbar. This was done to avoid charging when the sample is imaged in a TEM. Several candidate materials were considered, but in the end, Cu was chosen because of its consistent and

pure deposition quality in the particular sputtering setup used. As a result of the stochastic nature of FEBID, the patterned nanowires had naturally curved (Gaussian-like) profiles, very similar to the cylindrical segment profiles of the simulated nanowires in Chapter 4 as shown in Figure 5.2 c). As the main goal of this project is to examine DWs that can occur in such nanowires their shapes were chosen to promote DW nucleation when an external magnetic field is applied. For simple straight nanowires, like the ones described in Chapter 4, applying a field would result in a single domain state along the long dimension of the nanowire. For this reason the straight geometry had to be slightly modified. The closest approximation to it that would allow for the nucleation of a DW without the introduction of edge defects is a slightly curved C-shape. In this configuration the edges are kept intact and approximately parallel over a small portion of the nanowire, while allowing for the nucleation of a DW in the centre of the "C" [1]. In addition to the "C" shape an "S" shape was also considered with the goal of increasing the likelihood of DW nucleation by doubling the number of potential pinning locations. The "L" shape geometry was also reproduced and supplemented by a "Z" shape, which has a similar topology, but an additional DW pining site. For both of these the goal was to nucleate DWs in the vertices [2][3]. Figure 5.1 displays the different geometries considered along with the intended locations of DW and domains when an external field is applied.

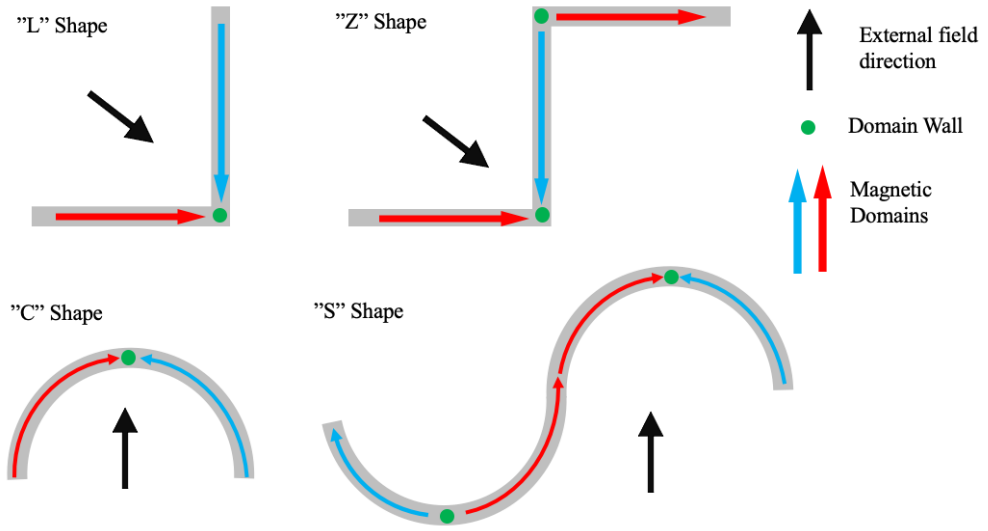

Figure 5.1: Schematics of the nanowire shapes considered for FEBID including the proposed positions of DWs when an external field is applied.

In order to best study the parameter space nanowires with a variety of sizes were fabricated using the method described in Section 3.2.2. Bitmap mask patterns were used for the "C" and "S" shapes, while the "L" and "Z" shapes were directly constructed using the microscope patterning function. The lengths of the different wires were kept constant - 1.5 μm for the "C" and "L" shaped nanowires and 2.3 μm for the "S" and "Z" shaped nanowires. The dimensions of the nanowires that varied were the width and the thickness. For the width, this was done by altering the pattern used for the deposition. For each different shape, patterns of different widths ranging from 50 nm to 200 nm were considered. These values were chosen to comply with the simulations conducted in Chapter 4 and later confirmed using measurements from BF TEM images in Section 5.3. The nanowire thickness was controlled by changing the deposition time with longer deposition times naturally resulting in thicker wires. This was confirmed visually during deposition as thicker wires appeared to show stronger contrast in the SEM. Subsequent AFM measurements showed the maximum thickness in the nanowires varied between 18 nm and 30 nm. No thicker nanowires were considered in order to keep the samples electron-transparent and to avoid long deposition (>3 minutes) which often resulted in uneven or skewed structures due to beam drift. Multiple nanowires of the same size were deposited during each session in order to increase the chances of nucleating a stable DW that retains its position once the magnetic field used to nucleate is switched off. In Figure 5.2 one can see a typical example of a nanowire array fabricated by FEBID, where a) shows an SEM image of a set of different nanowires with varying thickness, b) a higher magnification image of a single 120 nm wide L-shaped nanowire and c) an average line profile across a) clearly showing the curved, Gaussian-like nanowire geometry. It should be noted that while the profiles of the nanowires presented here differ slightly from the geometries described in Chapter 4, the thickness variation and curvature that are the properties of interest are still present. Furthermore, because of the dimensions listed above, most of the nanowires produced for this thesis can be likened to the quarter cylinder (QC) ones described in Chapter 4, due to their similar width-to-thickness ratio ($\approx$ 4:1). There are, of course, some exceptions, namely the nanowires that are simultaneously with narrow width (w < 70 nm) and high maximum thickness (t > 30 nm), which can be approximated to a half cylinder (HC), which corresponds to a width to thickness aspect ratio of 2:1. Additionally, nanowires wider than 170 nm and thinner than 25 nm have profiles which also differ from a QC, as at such high thickness-to-width ratios curved surface area of the nanowire is significantly reduced.

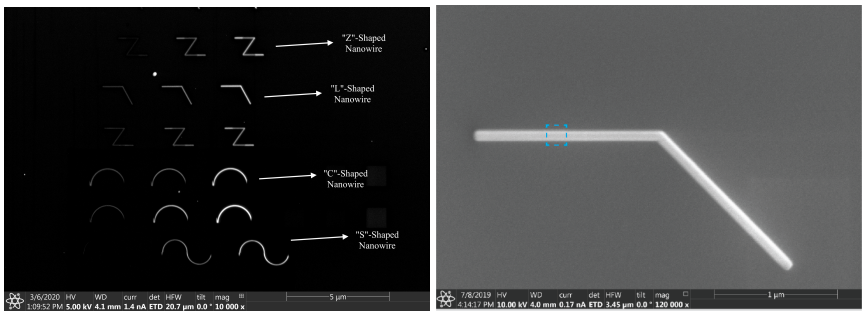

(a) Array of various nanowires (b) 120nm wide Co L-shaped nanowire

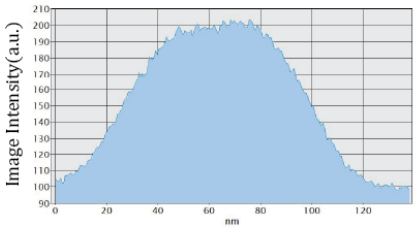

(c) Average line profile across b)

Figure 5.2: Typical sample fabricated by FEBID with a) showing array of diversely shaped Co nanowires, b) - an SEM image of an "L" shaped nanowire and c) - the curved profile of the nanowire obtained from the SEM image in b). Location where the profile was taken is marked by a blue dotted line.

The nanowire fabrication process using FEBID was a challenging process due to the many factors that can affect both the chemical makeup and geometry of the final deposits. These include the electron beam parameters, the type of precursor used, the substrate material and also the environmental factors at the time of the deposition (SEM chamber pressure, temperature and presence of contaminants) [4]. In the past high-quality deposition for Co (>85 %) and Fe (>70 %) nanowires has been achieved with an electron beam voltage of 5 kV and beam current in the range 0.4 nA to 1.6 nA [5][6]. Higher purity is possible with higher beam currents (in the range of a few nA) [7] but the higher currents result in a larger electron beam and therefore bigger structures [8]. Through a trial-and-error method the following parameters were found to produce the best-defined nanowires in the required thickness range. The electron accelerating voltage was set to 5 kV and the beam current to 0.69 nA. The distance between the substrate and the electron column was kept at 4.1 mm and the magnification at x25k which resulted in a working window of 8.2 µm. Nanowires

were deposited in groups of 4 with a pitch of 1 μm both vertically and horizontally, which ensured no overlap of deposition between different structures. Patterning duration ranged from 30s up to 3 min depending on the desired dimension of the nanowire. To avoid unwanted deposition after each set of wires was patterned the electron beam was blanked or moved away from the deposit site until the chamber pressure returned to its original value indicating that the amount of precursor gas left in the chamber is minimal. In addition to the nanowires, a set of 1 μm $\times$ 1 μm squares with thicknesses ranging from 15 nm to 35 nm was deposited at the beginning of each session. Their purpose was to quickly check whether the deposition rate and the system vacuum were suitable for patterning by examining the squares dimensions and morphology directly in the SEM. If deposition quality was low with undefined structures or very low deposition rates, steps like purging the gas injection system or improving the vacuum in the SEM chamber were taken. Figure 5.3 shows an image of 4 Fe squares deposited in the configuration explained above. The squares were also a useful tool during the nanowire characterisation process. During Fresnel mode imaging they provided a quick indication that the structures were magnetic due to their easily recognisable flux-closure structure. In addition, their uniform thickness proved useful when determining the saturation induction of the FEBID-deposited structures. It's important to note that the conditions used for deposition were rarely the best for SEM imaging. For this reason, the SEM imaging done to obtain the images shown in 5.3 and 5.2 was performed at the end of a deposition session at which point the microscope parameters were adjusted to obtain useful images.

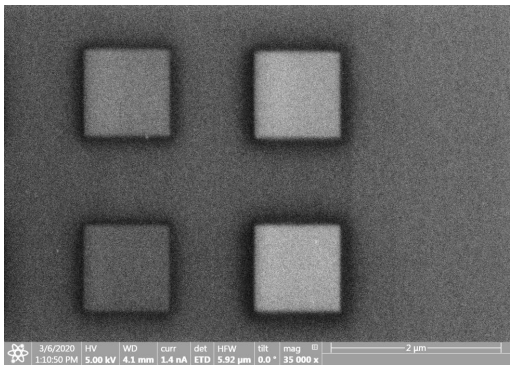

Figure 5.3: SEM image of four 1 μm $\times$ 1 μm Fe squares deposited with a pitch of 2 μm. The change, in contrast, represents a different thickness of the squares.

5.3 Fresnel mode imaging and domain wall nucleation

Initial imaging of the magnetic structure of the nanowires fabricated by FEBID was achieved using Fresnel mode Lorentz microscopy. The main tool for obtaining Fresnel mode images was the Tecnai T20, however, some Fresnel images were also acquired on the JEOL ARM. The choice of microscope depended on factors like uptime and availability, with both being able to produce high quality Fresnel mode images. A challenging aspect of the imaging was the high electrostatic contrast resulting from curved profiles of the nanowires, which obscured the bright/dark Fresnel contrast originating from varying magnetisation. Because of that initial imaging was performed on a set of squares deposited in identical conditions to the nanowires. They exhibited an easily recognisable flux closure pattern and due to their relatively uniform cross-section (except very near the edges), electrostatic contrast was not an issue. Fresnel mode and BF images showing the flux closure pattern are presented in Figure 5.4 a) and b) respectively.

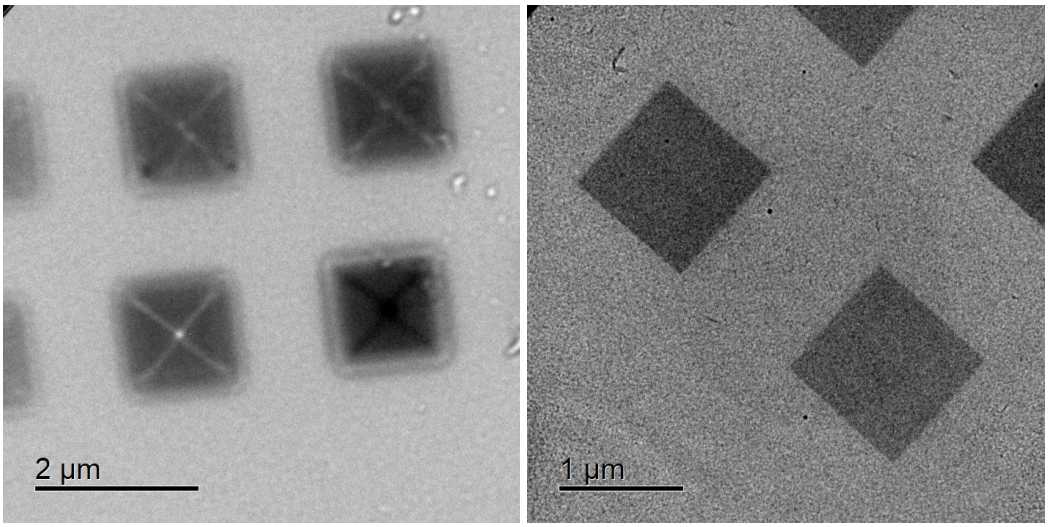

(a) (b)

Figure 5.4: Fresnel image of 1 $\times$ 1 µm Co squares exhibiting characteristic flux closure pattern (a))) along with a BF TEM image showing the polycrystalline structure of the deposits (b).

Once the squares were confirmed to be magnetic, an experiment was conducted to test the response of the nanowires to an external magnetic field. The experiment involved applying an external magnetic field of 1100 Oe along the long dimension of the nanowires by exciting the objective lens of the microscope and tilting the sample stage as described in Section 3.5.1. This resulted in saturating the magnetisation of the nanowire. By tilting the sample stage in the other direction the magnetisation was reversed. Figure 5.5a and 5.5b show an example of the procedure using Co "S" shape nanowire whose magnetisation is reversed using this method. In the images, this magnetisation reversal is clearly indicated by the reversal of bright and dark contrast on the edges of the nanowire. The main purpose of this was to determine whether the nanowires would retain any particular magnetic configuration when the external field is switched off. To that end, the experiment was successful as both of the images shown here were obtained at zero tilt of the sample stage and in the absence of an external magnetic field. This method of collecting images of a nanowire saturated in opposite directions can also be used to filter the electrostatic contribution to the contrast, however, because at the time of image acquisition Fresnel mode was meant to only provide qualitative images of the nanowires, not enough images were acquired to perform it. Once it was clear that the magnetic configuration of the FEBID-deposited nanowires was controllable by an external field attempts were made to nucleate DWs within them . This was done by applying the magnetic field in a direction perpendicular to their longitudinal dimension [9] [10]. Figure 5.5c shows a domain nucleated in this manner in a Co "S" shaped nanowire. In the image the direction the external field was applied in is indicated with a blue arrow. The presence is determined by two factors - a discontinuity in the nanowire contrast that is not present when it is in a single-domain state and a reversal of bright and dark contrast on each side of the discontinuity. Here the images were also obtained at zero tilt and no applied field. The following section (5.4) presents different DWs nucleated using this method. Each of its subsections describe the imaging of a different DW type and the type of nanowire in which it was observed in and imaged. This is done to highlight the contrast produced by each DW and how it compares to a simulated one. The Fresnel images are also accompanied by BF image, which is used to measure the nanowire width and a simulated Fresnel mode image obtained from a micromagnetic simulation. The results from all the Fresnel imaging along with the BF image measurements are then summarised in Table 5.1.

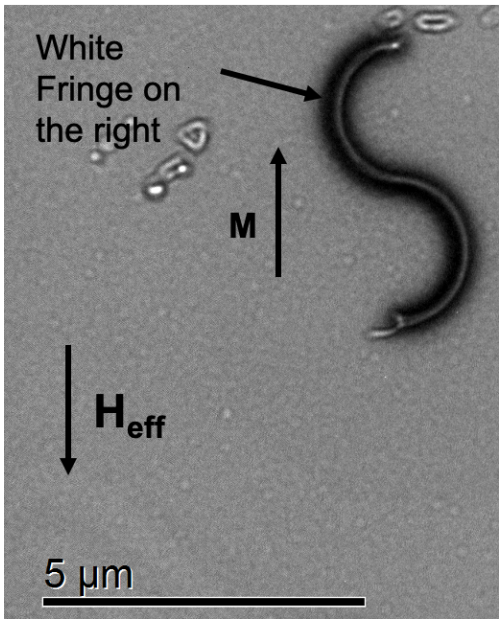

(a) S-shaped nanowire in a saturated state

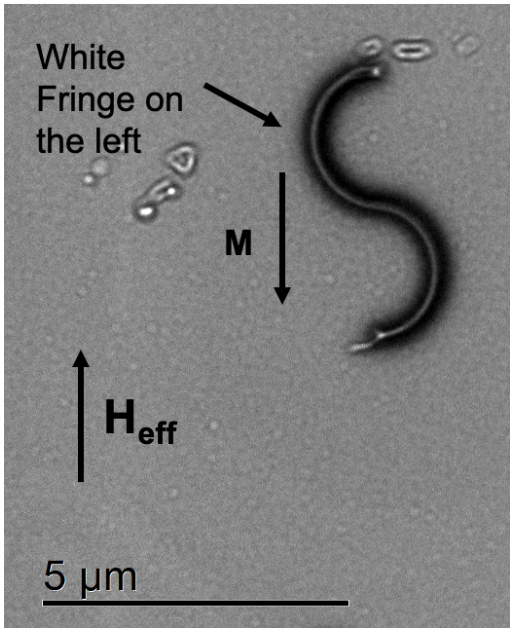

(b) Same S-shaped Nanowires with reversed magnetisation

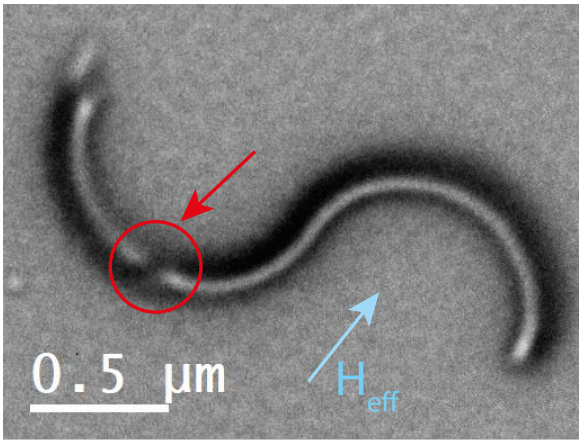

(c) DW stabilised in S-shape nanowire

Figure 5.5: Fresnel images of S-shaped nanowires in 3 different magnetisation configurations. a) and b) show the wire in two opposite saturated states and c) shows a two-domain configuration with a DW in between them. The arrows represent the direction of the sample magnetisation and the direction in which an external field was applied to achieve each magnetic configuration.

5.4 Domain wall imaging and identification

Chapter 4 presented simulated Fresnel mode images that show the magnetic contrast that would be produced by different DW types in nanowires with cylindrical segment geometries. A concise recap of these can be seen in Figure 5.6, where a Fresnel image of each different wall obtained at $\Delta f = 2$ mm from QC nanowire simulations is shown. This relatively high defocus value was chosen for easier comparison with the experimental Fresnel images, which were usually obtained at $\Delta f > 1$ mm . The other imaging parameters were the same as the one used in the Chapter 4, namely a 200 keV electron beam with beam divergence $\theta_c = 10^{-6}$ rad. Again the effects of lens aberrations were not considered due to the high defocus. In the following subsections, the simulated Fresnel images will be used as a tool to identify and label the different DWs observed in the experimental images.

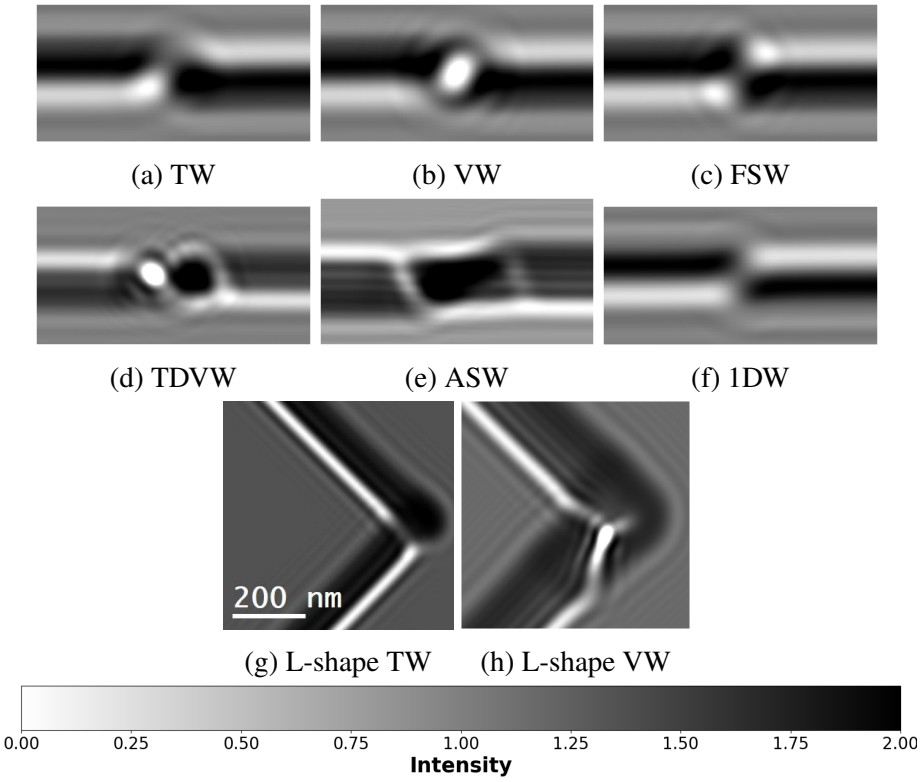

Figure 5.6: Fresnel mode images of the different DWs observed during simulations of curved nanowires. All images were obtained from QC simulations and calculated with $\Delta f = 2$ mm and $\theta_c = 10^{-6}$ rad.

5.4.1 Transverse Wall in L-shaped nanowire

The first DW that will be discussed can be seen in Figure 5.7. The first panel of Figure 5.7a shows a Fresnel image of a 1.2 μm long Fe L-shaped nanowire. There the presence of a DW is strongly indicated by the reversal of bright and dark contrast on each side of the vertex of the L. Along with the Fresnel image in the figure, one can also see a BF TEM image of the nanowire (5.7c), which was used to measure its width of 110 nm. This measurement was based on the edge-to-edge distance of the nanowire as observed on the BF image (indicated in cyan in 5.7c). The same edge-to-edge measurement was performed on the Fresnel image in the both of the domain regions of the nanowire and resulted in a nanowire width of 160 nm $\pm$ 15 nm . The source of this discrepancy is the "stretched" magnetic contrast around the nanowire edges. No direct measurement was performed on the thickness of this particular nanowire, however, based on the aspect ratio between its measured width and the nanowire thickness range of (15-35 nm) listed in the previous section its shape is most likely more similar to a QC. Based solely the contrast in the Fresnel image (5.6a) it is difficult to identify the DW with certainty. There is no evidence of a vortex core, which would appear as a bright or dark circular region (as pictured in 5.6b and 5.6d), meaning the magnetisation is mostly uniform. This suggest that the most likely DW imaged here is a transverse wall (TW). To support this assumption a simulated Fresnel image with included electrostatic contrast of a 110 nm Co L-shaped nanowire with a TW is displayed in 5.7b. The image was calculated with a defocus of 1 μm and shows the same reversal of contrast on either side of the vertex of the L-shape and similar contrast variation in the region of the DW. Additionally, a similar relationship was found between the actual simulated nanowire width (110 nm) and the one measured from the calculated Fresnel image (156 $\pm$ 15 nm). To further highlight the similarities between the simulated and experimental Fresnel images, average line profiles measured using the Digital Micrograph software and plotted along the central regions of the nanowires in both. These are displayed in panels d) and e) of Figure 5.7. The locations where the profiles were obtained are indicated with a blue dotted line in 5.7 a) and b). It's important to note that while the profiles pictured in d) and e) are indicated with a single line in both a) and b) in reality they represent an average line profile covering most of the nanowire width.

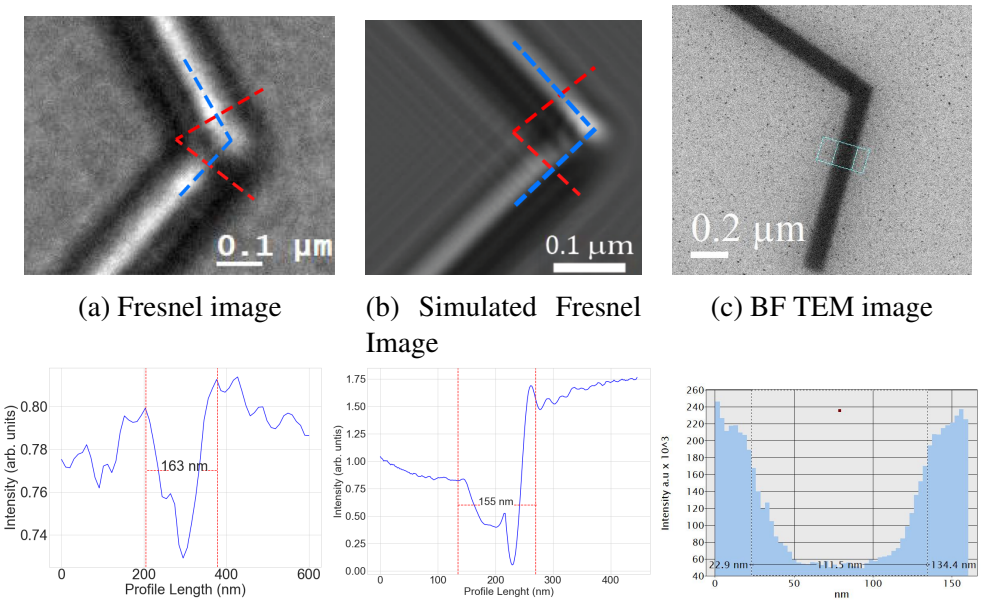

(a) Fresnel image (b) Simulated Fresnel Image (c) BF TEM image

(d) Profile across DW in a) (e) Profile across DW in b) (f) Profile across c)

Figure 5.7: Fresnel mode (a)), simulated Fresnel mode (b)) and TEM BF (c)) images of a 1.2 µm long, 110 nm wide Co L-shaped nanowire with a TW. d) and e) show line profiles across the DW region of a) and b) respectively , while f) shows a line profile across one of the arms of the L-shape in c). The red lines in a) and b) represent the boundaries of the DW and correspond to the red lines in d) and e), while the blue lines in a) and b) show the location where the line profiles were obtained. The black dotted lines in f) represents the edge-to-edge width of the nanowire as measured from c).

An additional use of the profiles was to measure the extent of DWs in both the experimental and simulated images. This was done using the FWHM of the peaks method shown in Section 4.8.1. This method was also used for all the DW width calculations in subsections from 5.4.2 to 5.4.4. For the images shown in 5.7 the resulting extents were found to be 163 nm $\pm$ 15 nm for the experimental image and 155 $\pm$ 10 nm for the simulated one. For both the error originates from the pixel size of the image (3 nm for a) and 2 nm for b)) of the image combined with the defocus. The locations of the proposed DW start and end points used to obtain these measurements are indicated with the red lines in the Fresnel images and their respective profiles. Much like the nanowire width value, the DW extent value measured here is also inflated due to the defocus. The actual DW extent is likely similar in size to the vertex of the L, as the DW is confined in that region by the geometry of the nanowire. This was also the relationship observed for both QC and HC simulations

of L-shaped nanowires presented in the Chapter 4 and for the simulation presented here. To better interpret the experimental image presented in Figure 5.7 it is important to know at what defocus it was obtained. A method to measure that, based on the wave optical formalism described in Chapter 3, is presented in detail in Section 3.5.4. In short, a value the defocus is obtained using $\Delta f = \frac{n}{\lambda k_n^2}$ where Δf is the defocus λ the electron wavelength and k_n^2 is the n-th zero of the contrast transfer function. Figure 5.8 illustrates the process for the Fresnel image presented in 5.7a. There 5.8a shows the FFT of Figure 5.7a, the radial profile obtained from it (5.8b) and the plot of λk_r^2 versus n whose gradient gives the defocus (Δ) value of the image (5.8c). In 5.8a the dark concentric circles are the zeros of the CTF. Their locations are also indicated as red dots on the average radial profile. Performing the calculation results in a defocus of 0.95 $\pm$ 0.08 µm. The error mostly due to uncertainty in the measurement of the locations of the zeros from the FFT, but also represents the statistical error from the fit.

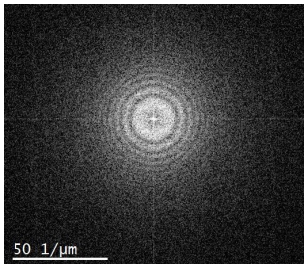

(a) FFT of 5.7a

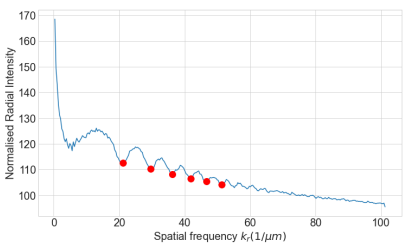

(b) Average Radial Profile of the FFT of 5.7a

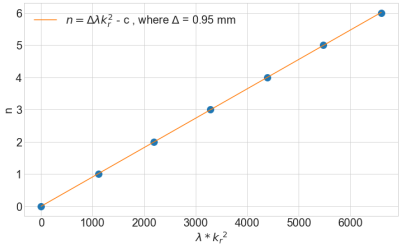

(c) Plot of k_r^2 against n

Figure 5.8: Calculation of the defocus (Δf) of the Fresnel images in 5.7. Zeros of the CTF were found by examining the average radial profile obtained from the contrast in the FFT of the image (5.8b) and indicated in red. The spatial frequencies were plotted against corresponding integer values giving the defocus (Δf) as the gradient of the line- (5.8c).

5.4.2 Vortex wall

The next DW type was nucleated in an 80 nm wide Co nanowire with a maximum thickness of 24 nm and is presented in Figure 5.9. Similarly to the nanowire in Figure 5.7 this one can also be compared to a QC nanowire based on its width-to-thickness ratio. The Fresnel image shown in Figure 5.9a was obtained using the Tecnai T20 microscope and unfortunately, at the magnification used, it was not possible to obtain a measurement of the defocus (Δf) as no zeros of the CTF appeared in the FFT of the image. However, based on similar images obtained using the JEOL ARM it is most likely that the defocus is in the range between 3-5mm. This is also suggested by the discrepancy between the actual nanowire width (80 nm) obtained from the BF image (5.9c) and the one measured from the Fresnel image (134 $\pm$ 15 nm). In the Fresnel image, the DW is characterised by an extended white "dot", which is indicative of a vortex wall (VW) structure. This is further supported by comparison with a calculated Fresnel image from a micromagnetic simulation of a 80 nm QC nanowire pictured in Figure 5.9b. The simulated Fresnel image presented here was calculated with a defocus of Δf = 4 µm and the nanowire edge-to-edge width measured from it was 128 $\pm$ 15 nm. This is in good agreement with the same measurement from the experimental image. Additionally, the contrast variations in both the DW and the domain regions of the simulated image are visibly similar to the ones in the experimental image. The similarities are even more apparent when comparing their average line profiles pictured in (Figure 5.9d) (5.9e) respectively. In order to quantify the images presented here measurement of the DW extent were obtained from the average line profiles of both the experimental (176 $\pm$ 15 nm) and simulated Fresnel images (163 $\pm$ 10 nm). The DW extent measurements were based on the FWHM method presented in Section 4.8.1. Of course, these values are inflated due to the high defocus, with the latter representing a true VW extent of 92 nm $\pm$ 5 nm . This measurement was obtained directly from the magnetisation used to generate the simulated Fresnel mode image using the method presented in Section 4.6. Although the same comparison cannot be made for the nanowire in the experimental image, the actual extent of the VW in it is likely to be between 80 nm and 100 nm assuming the contrast around it is stretched similarly to the contrast around the nanowire edges.

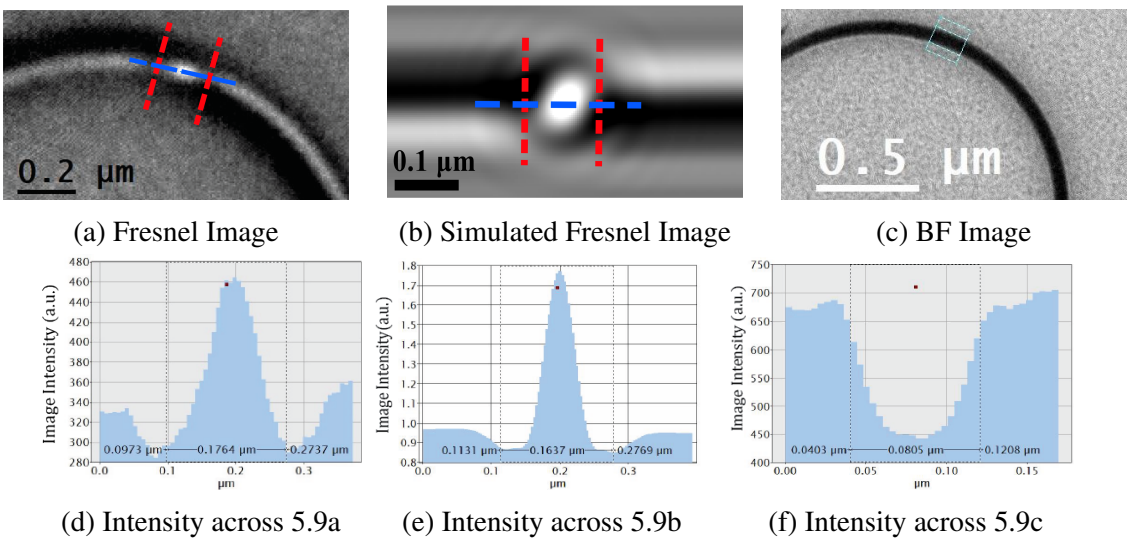

(a) Fresnel Image (b) Simulated Fresnel Image (c) BF Image

(d) Intensity across 5.9a (e) Intensity across 5.9b (f) Intensity across 5.9c

Figure 5.9: Fresnel mode (a)), simulated Fresnel mode (b)) and a BF (c)) image of a 80 nm wide C-shaped Co nanowire with a VW. d) and e) show line profiles across the DW region of a) and b) respectively, while f) shows a line profile across the nanowire width. The blue lines in a) and b) represent the location where the line profiles were taken, while the red lines indicate boundaries of the DW region and correspond to the dotted lines in d) and e). The cyan marked region in c) shows the location where the profile in e) was obtained, while the black lines in e) show the edge-to-edge width of the nanowire.

5.4.3 Transverse/double vortex wall

In Figure 5.10 one can see a series of images of a 64 nm nm wide Co-S-shape nanowire with a maximum thickness of 19 nm obtained from AFM measurements. Similarly to the other two nanowire presented in Sections 5.4.1 and 5.4.2 this one also has a shape closer to a QC based on its width to thickness ratio. The Fresnel image of it (5.10a) was also obtained using the Tecnai T20 and similarly to the image shown in 5.9, the exact value of the defocus is unknown but can be assumed to be in the range between 3 mm and 5 mm. Again the measurement of the nanowire width from the Fresnel image (117 ± 15 nm) was much larger than the one from the BF image of it shown in Figure 5.10c. The contrast signature of the DW, seen in Figure 5.10, significantly differs from the ones shown so far. It is characterised by a peak followed by a dip in the intensity of a similar extent. This is a pattern characteristic of a double vortex wall, where each of the vortices rotates

in opposite directions. Again a calculated Fresnel mode image (with $\Delta f = 4$ µm) from a micromagnetic simulation of a transverse/double vortex wall (TDVW) is included for comparison (Figure 5.10b). It shows features very similar to the ones in the actual Fresnel image with the exception of the ripple-like contrast around the vortices. Additionally, any contrast due to the transverse component of the TDVW is barely visible due to the high defocus in both the experimental and simulated images. It should be noted that the simulation used for comparison was from a 70 nm wide Fe HC nanowire, as the TDVW was not found to stabilise in QC Co nanowires narrower than 100 nm. Like in the case of the VW, the extent of the TDVW was measured from the average intensity profile from the experimental Fresnel image (5.10d) and found to be 237 $\pm$ 15 nm. This likely corresponds to a TDVW extent between 120 nm and 140 nm if the contrast stretching in the DW region is comparable to the one in the nanowire edges. Similarly the extent of the TDVW from the simulated Fresnel image was found to be 204 $\pm$ 15 nm, which corresponds to an extent of 118 $\pm$ 6 nm obtained directly from magnetisation that was used to generate the simulated image. It should be noted that there is no direct comparison between the extent of the TDVW from the simulated and experimental Fresnel images due to the differences between the two listed above.

5.4.4 Transverse wall in C-shaped nanowires

Finally, a third type of wall, observed in another 60 nm wide Fe C-shaped nanowire, is presented in Figure 5.11. Based on its width measurement obtained from a BF image (5.11c) and maximum thickness of 27 nm from an AFM measurement the nanowire geometry can be likened to a HC. A Fresnel mode image of the nanowire can be seen in 5.11a. Similarly to the images presented in 5.4.2 and 5.4.3 the defocus used here was also in the range between 3 mm and 5 mm. The nanowire width, measured from the Fresnel image was 112 $\pm$ 15 nm. Much like the DW observed in the L-shape nanowire this one is also difficult to identify. Unlike the VW and double vortex walls, which have very distinct features, this one appears just like a discontinuity between the two domains with only a slight increase in intensity on the left-hand side of the DW. Comparing these features to the micromagnetic simulations show that the one it resembles most is the TW.

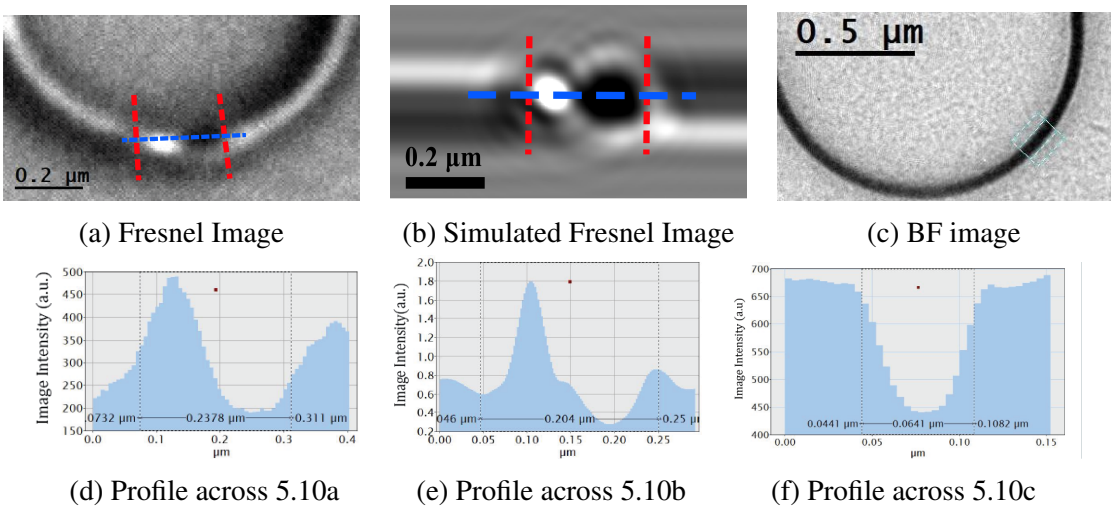

(a) Fresnel Image (b) Simulated Fresnel Image (c) BF image

(d) Profile across 5.10a (e) Profile across 5.10b (f) Profile across 5.10c

Figure 5.10: Fresnel mode (a)), simulated Fresnel mode (b)) and a BF (c)) image of a 64 nm wide S-shaped Co nanowire with a TDVW. d) and e) show line profiles across the DW region of a) and b) respectively, while f) shows a line profile across the nanowire width. The blue lines in a) and b) represent the location where the line profiles were taken, while the red lines indicate boundaries of the DW region and correspond to the dotted lines in d) and e). The cyan marked region in c) shows the location where the profile in e) was obtained, while the black lines in e) show the edge-to-edge width of the nanowire.

A simulated Fresnel image of one from a 60 nm wide HC Fe nanowire calculated at a defocus of 3 µm is presented in 5.11b. A similar contrast is present on the left-hand side of the flower state wall (FSW) (5.6c) and one-dimensional wall (1DW) (5.6f), however, for those the contrast is symmetrical on either side of the DW, which is not observed in the experimental image. The DW extent from the experimental Fresnel image was measured and found to be 140 $\pm$ 15 nm, while the one from the simulation - 113 $\pm$ 15 nm. The reason for this large difference is the irregular contrast variation in the experimental image. This is a problem specific for this DW as it has no strong contrast producing features (i.e. vortex cores), whose boundaries can be easily determined. For this reason it is also difficult to estimate the actual DW extent.

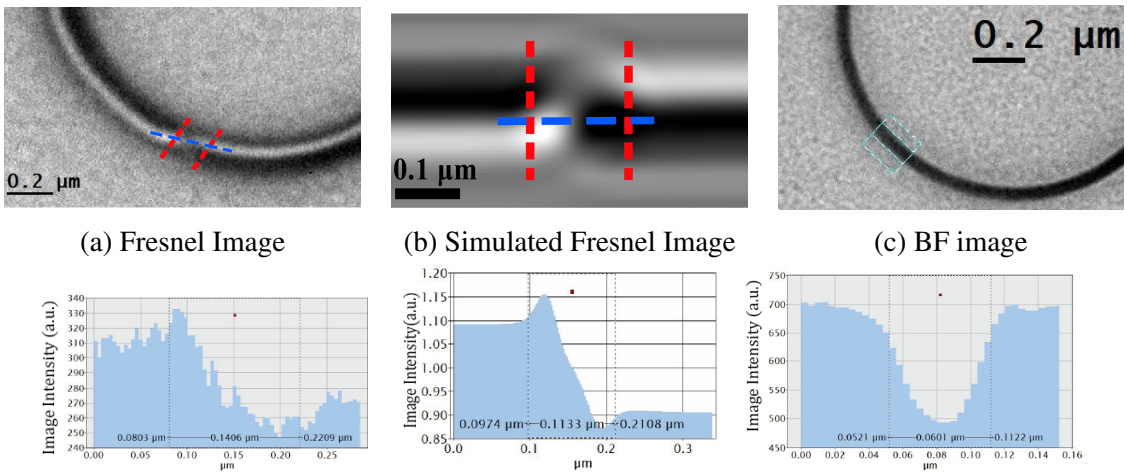

(a) Fresnel Image (b) Simulated Fresnel Image (c) BF image

(d) Profile across DW in 5.11a (e) Profile across DW in 5.11a (f) Profile across 5.11c

Figure 5.11: Fresnel mode (a)), simulated Fresnel mode (b)) and a BF (c)) image of a 64 nm wide C-shaped Co nanowire with a TW. d) and e) show line profiles across the DW region of a) and b) respectively, while f) shows a line profile across the nanowire width. The blue lines in a) and b) represent the location where the line profiles were taken, while the red lines indicate boundaries of the DW region and correspond to the dotted lines in d) and e). The cyan marked region in c) shows the location where the profile in e) was obtained, while the black lines in e) show the edge-to-edge width of the nanowire.

5.5 Fresnel mode summary

By using the methods above DWs were nucleated and classified in a range of nanowire sizes and shapes. A summary of the results is presented in Table 5.1, which lists the DW types that were observed in Co and Fe nanowires at different sizes. The QC, HC and N/A comments after each nanowire width refer to the shape the nanowire most closely resembles, with N/A referring to nanowires wider than 170 nm that have a significantly smaller curved surface than a QC. As mentioned in Section 5.2 this is inferred from the width-to-thickness ratio of the particular nanowire. For nanowires where a direct thickness measurement is not available the maximum thickness range listed in Section 5.2 is used to make an educated assumption.

For each of the nanowire width entries in the table above there were multiple occurrences of the listed DW. This is the case because the nanowires were deposited in arrays and as

Table 5.1: DW types observed in curved Co and Fe nanowires fabricated using FEBID as observed by Fresnel imaging

	Co		**Fe**	
	Width (nm)	DW type	Width (nm)	DW type
L-shaped nanowire	72 HC	TW	220 N/A	TW
	110 QC	TW	250 N/A	TW
	150 QC	TW		
Z-shaped nanowire	60 HC	TW	180 N/A	TW
	71 HC	TW	200 N/A	TW
	110 QC	TW	251 N/A	TW
	130 QC	TW		
C-shaped nanowire	50 HC	TW	230 N/A	VW
	64 HC	TW		
	72 HC	VW		
	83 QC	VW		
	90 QC	TDVW		
S-shaped nanowire	60 HC	TDVW		
	120 QC	TW		

expected multiple nanowires of the same array acquired the same magnetisation under an applied field. It should be noted that reaching a stage where the Fresnel imaging of a DW was successful was dependent on multiple factors. Even after the FEBID deposition parameters were optimised sometimes the deposition rate and purity were insufficient to build samples that show magnetic contrast in the TEM. Additionally, since DWs in nanowires of the dimensions studied here are inherently metastable they often disappeared when the external field used to generate them was switched off or when the sample was returned to the zero tilt position. That being said all of the entries in Table 5.1 represent DWs that were stable at zero tilt and zero external field. A clear limitation of the study was the high values of defocus used. On one hand, using high defocus values was necessary to provide a clear contrast, facilitating the DW classification. On the other hand, such high defocus values clearly fall into the non-linear imaging regime [11], likely causing the DW extent figures to be inflated. An additional difficulty while imaging was the curvature of the nanowires, which is a source of electrostatic contrast. While it is possible to correct that during post-processing by acquiring multiple images of the same structure in opposite

magnetisation states, this was not performed for the images shown due to the time constraints of the project. An attempt to decouple magnetic and electrostatic phases, however, is presented for DPC data in the next section. There we provide information about the magnetic properties of the nanowires and a more clear look into the structure of some of the DWs that they can support.

5.6 Quantitative DPC imaging

So far in Sections 5.3 and 5.4, Fresnel imaging was shown to be an effective tool employed during the nucleation of DWs and for identifying different DW types. Additionally, it was used to obtain semi-quantitative measurements of the extent of the DWs. But since it is an out-of-focus technique it is not ideal for quantitative measurements and obtaining detailed information about the magnetic structure of the nanowires. For that purpose DPC is a much better candidate as it provides a direct probe into the sample induction. Here DPC images of several DWs in both Co and Fe nanowires are presented. Furthermore the DPC data is used to obtain a direct measurement of the saturation induction of the FEBID fabricated nanowires. The data sets were obtained using a JEOL ARM equipped with a Merlin detector using a 5 μm aperture at a magnification of x150k and a camera length of 800 cm. This resulted in a probe semi-angle of 2.15 mrad. Due to the high level of diffraction contrast present in the nanowires, (nanocrystalline cobalt and layers of crystalline copper) pixelated DPC was the chosen imaging technique. The data processing was done using the FPD package using an edge cross-correlation method [12], a short description of which, is available in Section 3.5.5 of Chapter 3.

5.6.1 Removal of electrostatic contrast

Before performing any quantitative analysis on the magnetic structure of the nanowires using DPC images, the electrostatic contribution to the phase must be removed leaving behind only the deflections due to magnetic induction. The following method was employed to achieve this. First the nanowire is saturated in either direction using the methodology described in Section 3.5.1. For both saturated states a DPC dataset is collected. Once the datasets are processed and calibrated, the resulting pair of DPC images (I_1 and I_2) can be said to have the following contributions from magnetic and electrostatic phases, provided

the magnetisation of the nanowire was successfully reversed.

$$I_1 = \nabla(\phi_e + \phi_m) \tag{5.1}$$

$$I_2 = \nabla(\phi_e - \phi_m) \tag{5.2}$$

By carefully aligning I_1 and I_2, it is then possible to separate the electrostatic ($\nabla\phi_e = (I_1 + I_2)/2$) and magnetic ($\nabla\phi_m = (I_1 - I_2)/2$) contributions to the phase. This is a commonly used method to separate the magnetic phase that can also be applied for Fresnel mode imaging [13] [14]. Figure 5.12 shows an example of the process for DPC images of a 110 nm wide Co L-shaped nanowire. For simplicity only one of the DPC components is shown. In 5.12a and 5.12b one can see the same nanowire in two opposite magnetisation configurations, which correspond to I_1 and I_2. Panel 5.12c shows the electrostatic contribution to phase obtained from the average sum of 5.12a and 5.12b, while panel 5.12d shows the magnetic contribution given by their average difference. Additionally, a line profile which shows the magnitude of the deflections in radians is plotted with each image. The red arrows in 5.12a, 5.12b and 5.12d indicate the direction of magnetisation in the nanowire, while the dotted lines in all images show the region where the line profile was obtained and the black double-headed arrows indicate the field mapping directions. An useful outcome of this procedure is that once calculated the electrostatic contributions can be subtracted from any DPC image of the same nanowire (as long as the imaging conditions are the same and the images are properly aligned) to leave behind only the magnetic information. The effect of subtracting the electrostatic contribution from datasets of the same nanowire where a TW is nucleated can be seen in Figure 5.13. Panel 5.13a of the figure shows the original DPC image, while 5.13c shows an induction map of the nanowire where the electrostatic contrast has been removed. The difference between the two images is highlighted in 5.13b, which shows line profiles across the top and bottom domain regions of both 5.13a (red line) and 5.13c (blue filled area). The locations where the profiles were taken are indicated with red dotted lines in both images. The most significant effect is near the edges of the nanowire. There the high-magnitude deflections due to the rounded geometry of the nanowire have been filtered out. Upon closer examination of the line profiles in 5.12c it can be seen that their shape is similar to the shape of the cross-section of the nanowire. The same result was observed in calculated DPC images in Section 4.8.3 indicating that the process of filtering out the electrostatic contribution was successful.

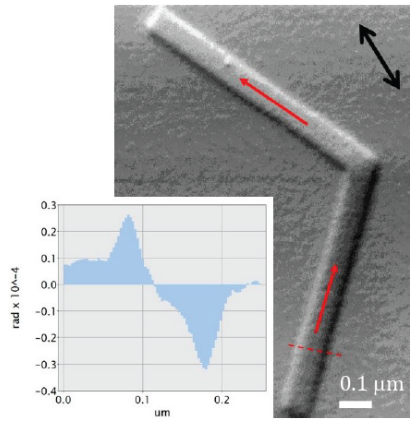

(a) DPC image of "up" saturated L-shaped nanowire (I_1)

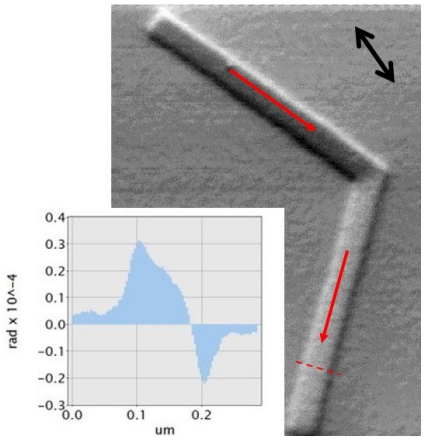

(b) DPC image of "down" saturated L-shaped nanowire (I_2)

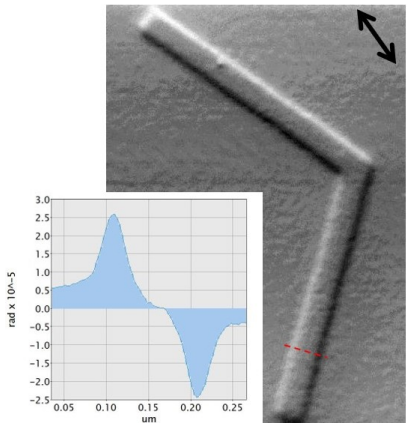

(c) $\nabla\phi_e = (I_1 + I_2)/2$

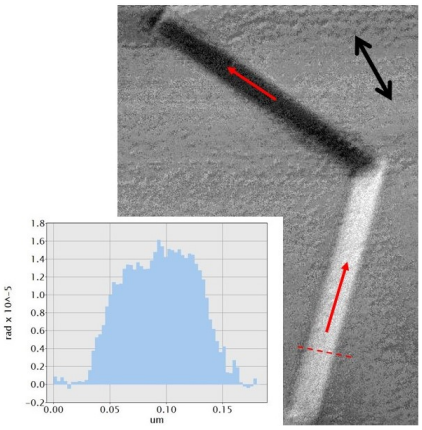

(d) $\nabla\phi_m = (I_1 - I_2)/2$

Figure 5.12: DPC images showing a 110 nm Co L-shaped nanowire nanowire. In a) and b) the magnetisation of the nanowire points in opposite directions. c) shows a map of the electrostatic contrast obtained the average sum of a) and b), while d) shows the magnetic induction obtained from their average difference. Average line profiles showing the magnitude of the deflections is plotted beside each DPC image. Red arrows indicate the proposed direction of the magnetisation, while black double sided arrows show the magnetic induction mapping directions.

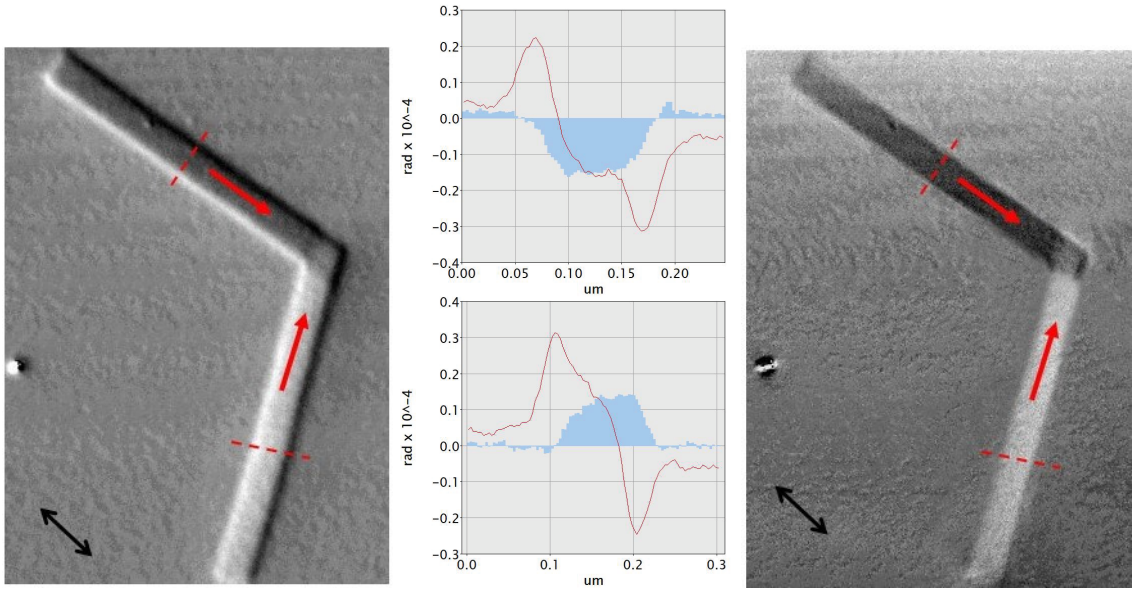

(a) L-shape nanowire with EC (b) Overlaid line profiles of a) and c) (c) L-shape nanowire without EC

Figure 5.13: DPC images of a 110 Co nanowire with a TW, where the EC is still present (a) and filtered out (c). The DPC images are accompanied by average line profiles (b)) showing the difference between the originally obtained (red) and purely magnetic deflections(blue).

This particular technique is used in Section 5.6.2 to obtain an accurate quantitative value of the saturation induction of the FEBID fabricated nanowires.

5.6.2 Saturation induction of the FEBID patterned structures

As mentioned in Section 3.5.2, the deflections of the electron beam that are recorded using DPC are due not only to the magnetic induction of the sample but also due to its thickness and mean inner potential. One of the ways to decouple the two was presented in Section 5.6.1. Here that process is applied to an 82 nm wide Fe nanowire with a maximum thickness of 26 nm. The AFM profile, from which the thickness was measured, along with a BF image of the nanowire can be seen in Figure 5.14.

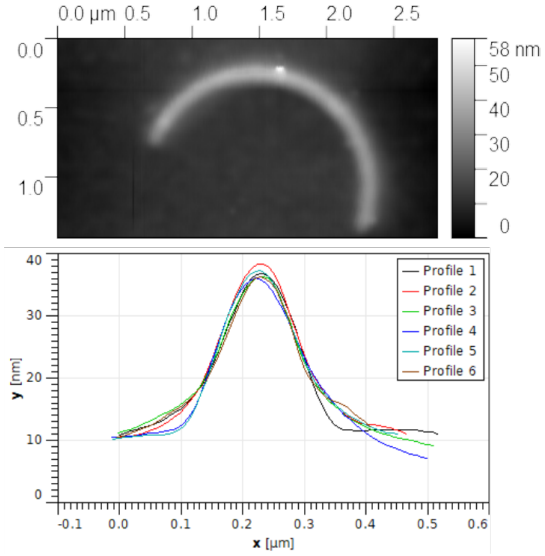

(a) AFM image and profiles

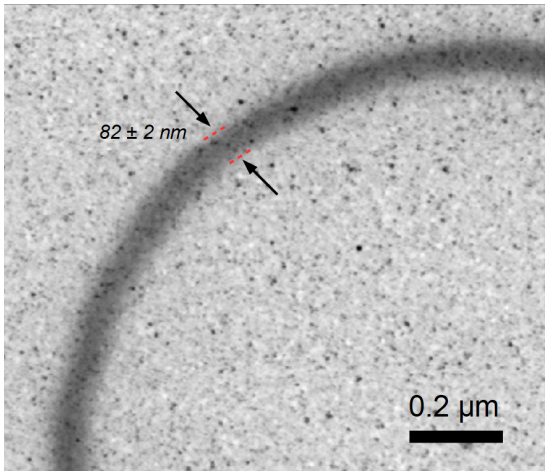

(b) BF image

Figure 5.14: Images used for the measurement of the dimensions of a C-shaped Fe nanowire. a) shows an AFM micrograph with several lines profiles across different positions in the nanowire. b) is a BF image used to measure the nanowire width.

For this particular nanowire, only two datasets of different magnetisation configurations were available. In the first one, the nanowire was in a saturated state and in the second in a head-to-head magnetisation state with a VW. Figures 5.15a and 5.15b show one of the DPC image components for both datasets. In the images, it can clearly be seen that the magnetisation below the DW in the head-to-head state is in the same direction as the magnetisation in the saturated state. This means that using the method described in the previous section it is only possible to obtain the electrostatic contrast for the top section of the nanowire (above the DW), where the magnetisations of the different datasets are opposite. This is reflected in the final deflection image in Figure 5.15d.

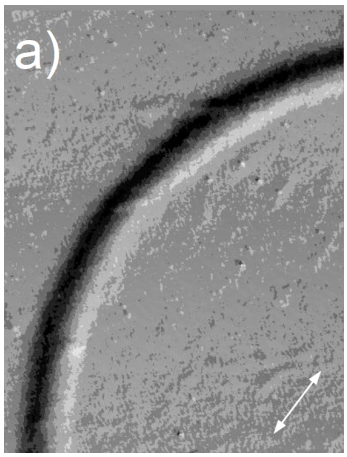

(a) βt_y of saturated nanowire

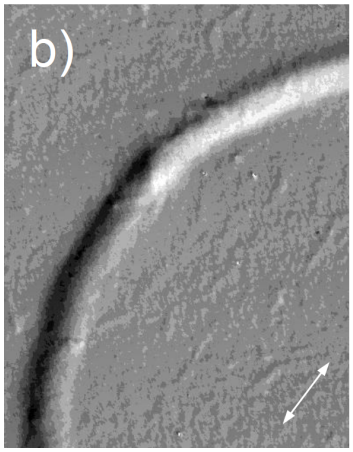

(b) βt_y of nanowire with VW

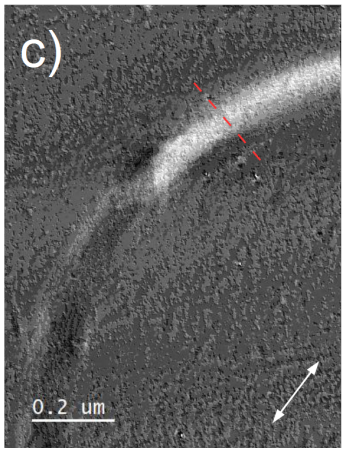

(c) βt_y of nanowire without EC

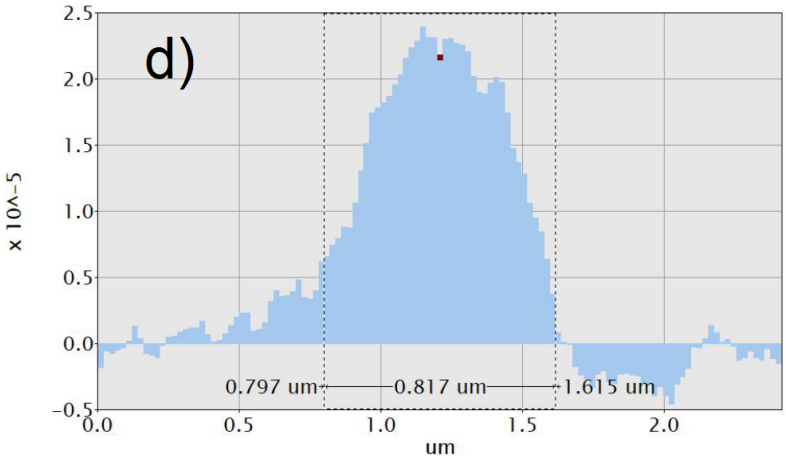

(d) Average line profile across C

Figure 5.15: DPC images and a profile across a C-shaped 82 nm wide nanowire used to calculate its saturation induction. a) and b) show said nanowire in saturated and head-to-head magnetisation states, while c) shows the nanowire in the same configuration as b), but with electrostatic contrast contributions to the phase removed. d) is an average line profile across the nanowire in c) quantifying the deflections of the electron beam due to the sample's magnetic induction.

There we see that on the bottom section of the nanowire, where the induction direction of both datasets is the same, any contrast due to the nanowire has been removed. On the other hand, in the top section of the nanowire, where the magnetisation was opposite, what remains is a clear image of deflections purely due to the induction. Their magnitude is

shown in the line profile in (5.15d). To obtain the saturation induction (B_s) the maximum values of the deflections (β) from the DPC image and thickness (t) from the AFM profile were plugged into equation 5.3.

$$B_s = \frac{h\beta}{e\lambda t} \tag{5.3}$$

This resulted in a value of 1.5 $\pm$ 0.1 T for the nanowire saturation induction, which corresponds to 68% of the bulk Fe value of 2.1 T [15]. From this measurement, a Fe elemental purity of 68% can be estimated. Similar deposit purity is also reported in [16][17] [18]. In order to consolidate this finding a further measurement of the saturation induction is obtained from a 1 µm $\times$ 1 µm $\times$ 32 nm Fe square from the same sample. Similarly to Figure 5.14 Figure 5.16 also displays an AFM profile of the square along with a BF image.

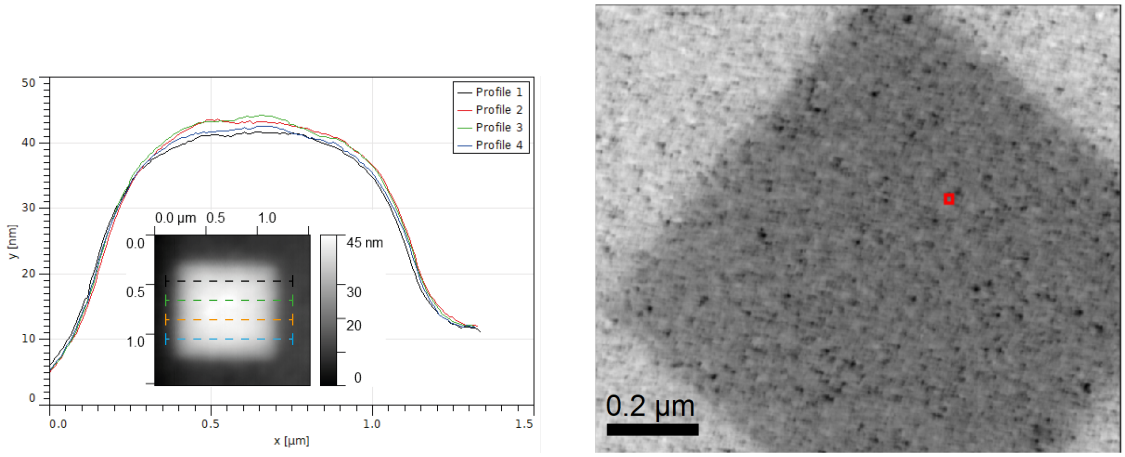

(a) AFM image and profiles

(b) BF image

Figure 5.16: Images used for the measurement of the dimensions of a 1 µm $\times$ 1 µm $\times$ 32 nm thick Fe square. a) shows an AFM micrograph with several lines profiles across different positions in the square. b) is a BF image.

In the AFM profile, one can see that even in the square deposits a light curvature and thickness variation are present around the edges of the structure. This can also be inferred from the bright fringes on the edges of the square that can be seen in the DPC image in Figure 5.17.

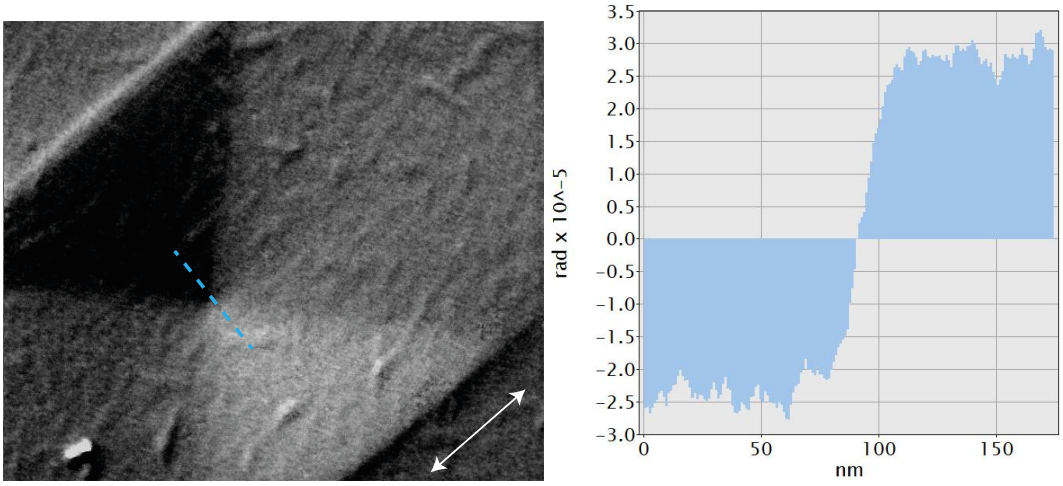

(a) DPC component 1

(b) Line profile across a)

Figure 5.17: DPC induction map (a)) and a line profile showing the magnitude of deflections due to magnetic induction (b)) of a 1 µm × 1 µm × 32 nm Fe square. The blue line indicated in a) indicates the location of the line profile.

On the other hand, an examination of the central region of the square in both the DPC and AFM images reveals that it has a mostly uniform thickness, meaning the electrostatic contributions to the contrast in the DPC image are minimal. This allows us to directly obtain a measure of the saturation induction from the line profile across the square pictured in Figure 5.17b by substituting the average values in the equation 5.3. The "jagged" peaks in the profile are most likely due to diffraction contrast from Cu crystallites that were not filtered by the cross-correlation algorithm. For the thickness, the average measurement from the AFM profile of 32 nm is used. This results in an average B_s value of 1.5 $\pm$ 0.13 T, which is in good agreement with the value recorded from the nanowire shown in Figure 5.15. Having obtained a measurement for the saturation induction of a Fe square the same method was repeated for a Co square with an average thickness of 24 nm. The AFM profile along with one of the DPC components and average line profile showing the deflections is pictured in Figure 5.18.

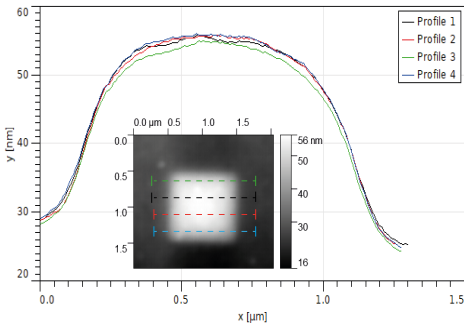

(a) AFM image and profiles

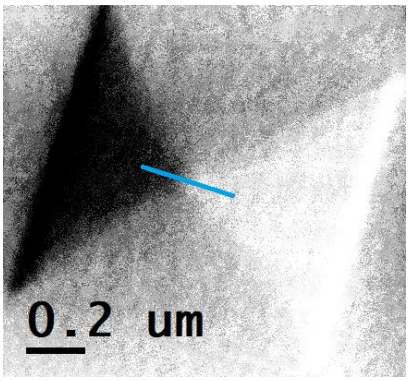

(b) BF image

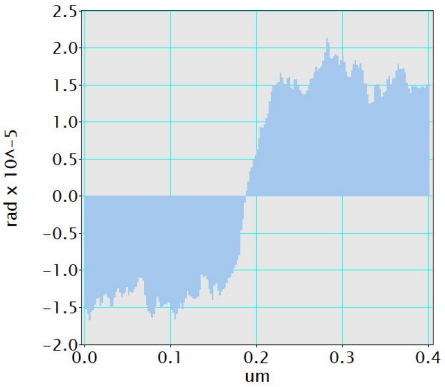

(c) BF image

Figure 5.18: Images used for the measurement of the dimensions of a 1 µm × 1 µm × 24 nm Co square. a) shows an AFM micrograph with several lines profiles across different positions in the square. b) is the y - component DPC image of the same square and c) shows the average line profile across b).

Repeating the calculation results with the values presented in Figure 5.18 c) results in a B_s value of 1.2 T $\pm$ 0.1 for the Co square which corresponds to $\sim$ 70% of the bulk Co value of 1.7 T [19]. Much like for the Fe deposits, this value is within the expected elemental purity range for similar FEBID fabricated structures [20] [21]. Unfortunately, it is not possible to provide a direct secondary measurement of the B_s value from an nanowire. This is because although an EC-corrected induction map of a Co nanowire is available (Figure 5.13c) its thickness is unknown as no AFM was performed on that sample. However, using the limits of nanowire thickness described in Section 5.2 - (18-35 nm) would give a B_s value ranging from 0.7 to 1.4 T corresponding to 51 % to 79 % of the bulk Co value. Having demonstrated a method to remove EC from nanowires and used it to quantitatively determine the saturation induction of the FEBID nanowires and squares, the next sections

present some DPC images of different DWs and attempt to classify their type.

5.6.3 Vortex wall in C-shaped nanowire

The first DW and the easiest to identify is a VW. Figure 5.19 shows the EC corrected DPC images of one nucleated in a 210 nm wide Fe nanowire with a maximum thickness of 26 nm in a head-to-head magnetisation state. Panels 5.19 (a) and b)) of the figure display two orthogonal components of the magnetic induction with the mapping directions indicated by the white arrows. The third panel displays a composite colour image calculated from a) and b), which clearly shows the variation of induction across the nanowire. In d) one can see a virtual bright field image of the nanowire and the area around it obtained from the summed signal from of all points in the DPC scan. There the polycrystalline copper grains that cause the bulk of diffraction contrast in DPC are easily visible. The final image (e)), is an average line profile across the DW, which was obtained from the induction component pictured in b). In this plot the region between the two dotted lines shows the variation of the electron beam deflections due to the magnetisation in the DW and the measurement of 295 $\pm$ 15 nm shows its extent. The locations of the start and end of the DW are also displayed in b) with the help of the cyan dotted lines. The contrast in the DPC images and the DW profile shape presented in e) closely resemble ones obtained from calculated DPC images of micromagnetic simulation - Figure 5.19 f) and g). The only difference is the irregularly sized peaks present in the plot. These are most likely caused by the upper-mentioned copper crystallites. The simulation used for comparison here is of a 80 nm wide QC Fe nanowire and comparing the line profiles of the experimental and simulated images shows good agreement between the deflection variations in the two. In addition to the one shown here, DPC datasets of VWs were also collected for 84 nm and 103 nm wide Fe nanowires. Their extents were measured to be 111 $\pm$ 11 nm and 126 $\pm$ 11 nm respectively.

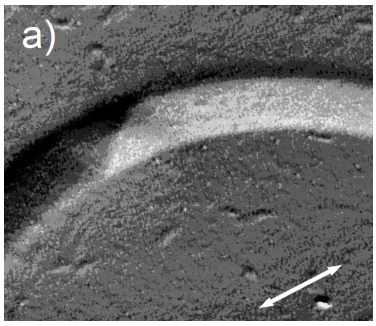

(a) DPC component 1

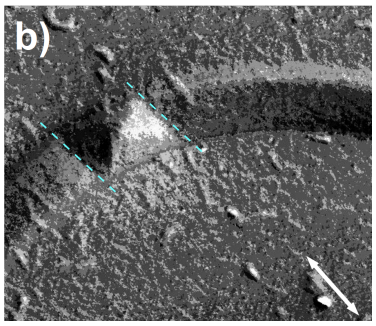

(b) DPC component 2

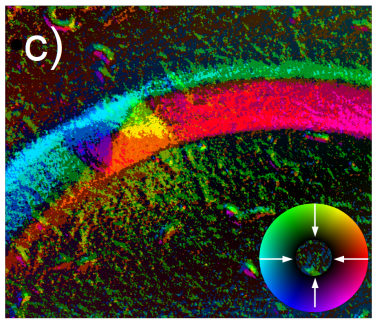

(c) Composite color image

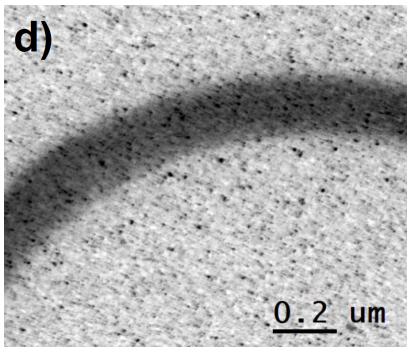

(d) DPC sum image

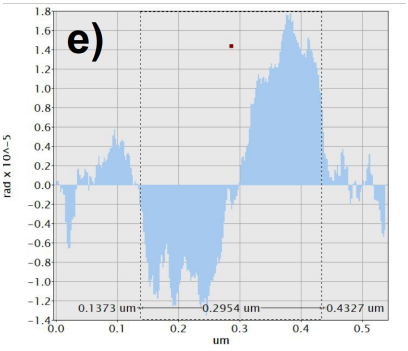

(e) Profile across DW in 5.19b

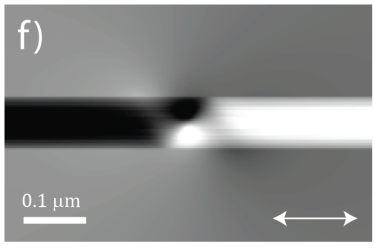

(f) Simulated DPC component 1

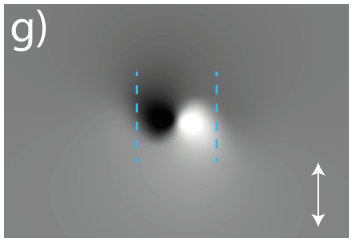

(g) Simulated DPC component 2

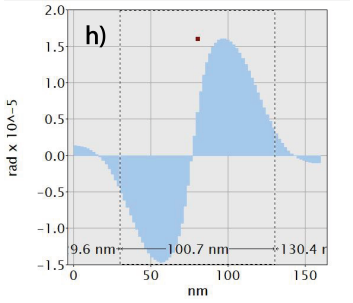

(h) Profile across DW in 5.19g

Figure 5.19: DPC images of a VW nucleated in a 210 nm wide Fe nanowire. a) and b) show the two induction components with the white arrows representing the induction mapping directions. c) shows a composite image of the a) and b) and is used to clearly visualise the change of induction within the nanowire. d) shows the DPC sum image and e) is line profile measurement across the DW used to measure its extent. f) and g) show simulated DPC images of a VW from 80 nm $\times$ 20 nm FE nanowire. h) shows the line profile across g).

5.6.4 Asymmetric vortex wall in C-shaped nanowire

A different type of DW was also observed in two of the other Fe nanowires (82 nm and 90 nm wide). Figure 5.20 shows an image of one nucleated in a 90 nm wide C-shaped nanowire. The images in the figure are organised in the same way as the ones in Figure 5.19. The DPC images presented there have not been EC corrected as there are no additional datasets of the nanowire in different magnetisation states and no direct measurements of its thickness. Unfortunately, this makes the images more difficult to interpret. Despite that, some identifying characteristic of the DW are still visible. The first ones are the bright and dark contrast regions on either end of the DW that can be seen in 5.20b. These indicate induction in either a parallel or anti parallel orientation to the transverse dimension of the nanowire and the mapping direction of the DPC scan marked by the white arrow. They also somewhat resemble similar regions in the VW pictured in 5.19b. Here, however, they are not symmetric around the centre of the nanowire, with the dark region being closer to the bottom edge and the bright region closer to the top one. Additionally, the bright and dark regions appear further from each other than would be expected for a VW in a nanowire of this size. Another feature that is helpful in identifying the DW is the extended region over which the induction appears to change in the centre of nanowire pictured in 5.20a. There the induction again appears to be separated in 2 regions with parallel and anti parallel orientation to the longitudinal dimension of the nanowire. These two observations indicate that the DW pictured likely has an asymmetric vortex structure. Such an asymmetric vortex wall (AVW) was observed in the HC nanowire simulations and was discussed in 4.4. A simulated DPC images of an AVW can be seen in Figure 5.20 f) and g). There one can see clear similarities between the contrast in both of the DPC components. The extent of the AVW pictured here was measured from the average line profile across it (5.20e) and found to be 251 ± 15 nm. This is in agreement with the extents of AVW observed in simulation (4.16 d), which often spanned areas more than twice the nanowire width. It must be pointed out that the nucleation of this wall was surprising both because of its complicated extended nature and the fact that in the simulation it relaxed exclusively in HC nanowires wider than 130 nm. Its appearance in the smaller physical nanowires here implies that it is a stable structure and that not only size but also nanowire shape and curvature play a critical role in its formation.

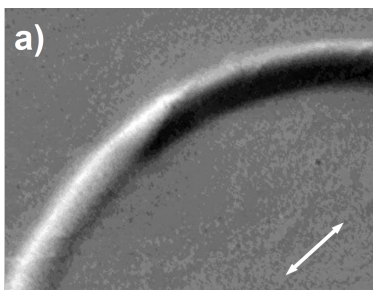

(a) DPC Component 1

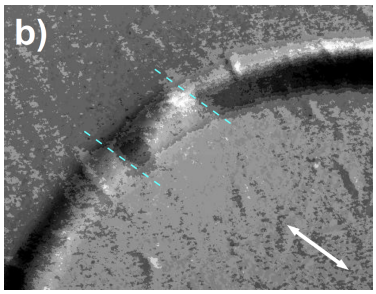

(b) DPC Component 2

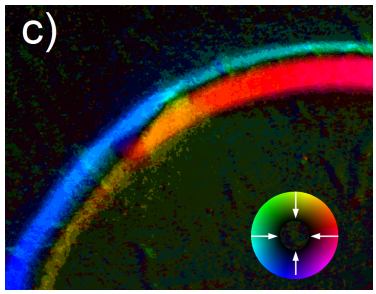

(c) Composite color image

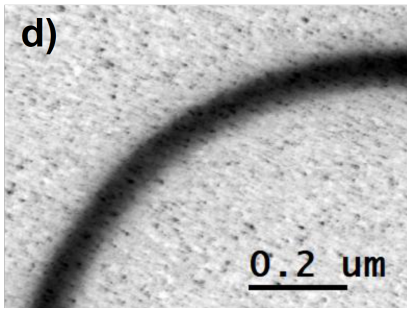

(d) DPC sum image

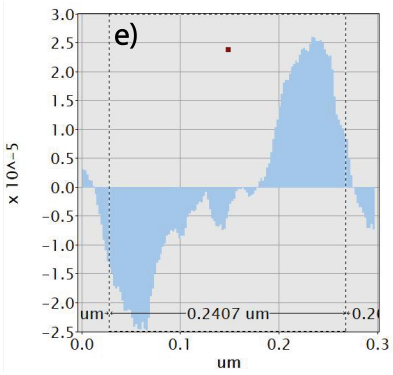

(e) Profile across DW

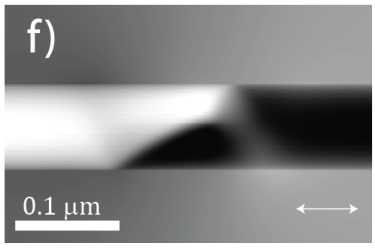

(f) Simulated β_x image of AVW

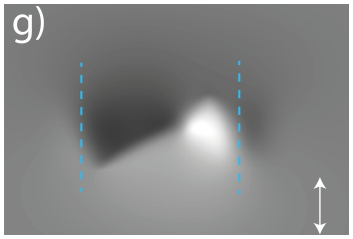

(g) Simulated β_y image of AVW

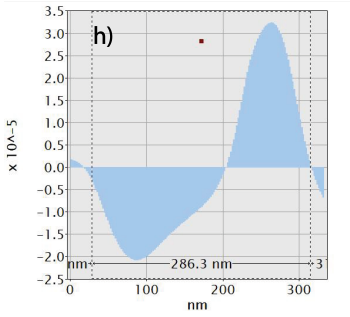

(h) Profile across DW in Figure 5.20g

Figure 5.20: DPC images of an AVW nucleated in a 90 nm wide Fe nanowire. a) and b) show the two induction components with the white arrows representing the induction mapping directions. c) shows a composite image of the a) and b) and is used to clearly visualise the change of magnetisation within the nanowire. d) shows the DPC sum image and e) is line profile measurement across the DW used to measure its extent.f) and g) show simulated DPC images of a AVW from a 130 nm $\times$ 65 nm HC nanowire. h) shows the line profile across g).

5.6.5 Transverse wall in L-shaped nanowire

The final DW that is discussed here was nucleated in the vertex of a 110 nm wide L-shaped Co nanowire and presented in 5.21. Again no direct thickness measurements are available for this nanowire, but based solely on the width value its geometry can be likened to a QC. By examining 5.21a, 5.21b and 5.21c, one can see that the region of the DW is relatively uniform with no specific variation in contrast. This suggest that the nanowire imaged there is most likely a TW. Additionally, comparison to the calculated DPC images of a micromagnetic simulation of a similar 110 nm wide L-shaped QC nanowire (5.21f and 5.21f) shows that the DW pictured in 5.21a and 5.21b is consistent with the stable TW structure consistently observed in the simulations described in Section 4.5. Similarly to the nanowires above a profile was taken across the DW from one of the induction components and used to display the variation of the deflections and measure the extent of the DW, which was found to be 124 ± 12 nm. This value compares favourably with the 110 ± 10 nm value obtained from the simulation.

5.7 Summary

This chapter presents an empirical study of nanowires with curved geometry and variable thickness fabricated using FEBID. Several qualitative and quantitative microscopy techniques were used to image them, measure their critical dimensions and obtain insight into the different DWs that they can support. These include DPC and and Fresnel mode imaging, which were used to identify a variety of different DWs in both the Co and Fe nanowires. Table 5.2 summarises the DW types observed in different Co and Fe nanowireS using both of these techniques. C-shaped nanowires were found to support a wider variety of unique DWs than their L and Z-shaped counterparts, in which only a TW was observed. A similar trend was observed in the simulation study presented in Chapter 3. Additionally, nucleation of DWs was found to be more difficult in S-shaped than in C- shaped nanowires as only two DWs were observed in Co-S-shaped nanowires, with none in the Fe ones. The intended formation of two DWs in the S-shaped nanowires was not observed. A possible explanation is a quick expulsion of the DWs after the external field is switched off [22]. Alternatively it is possible that a pair of DWs forming in such a structure would have opposite "charges" causing them to attract an annihilate each other if not pinned [22].

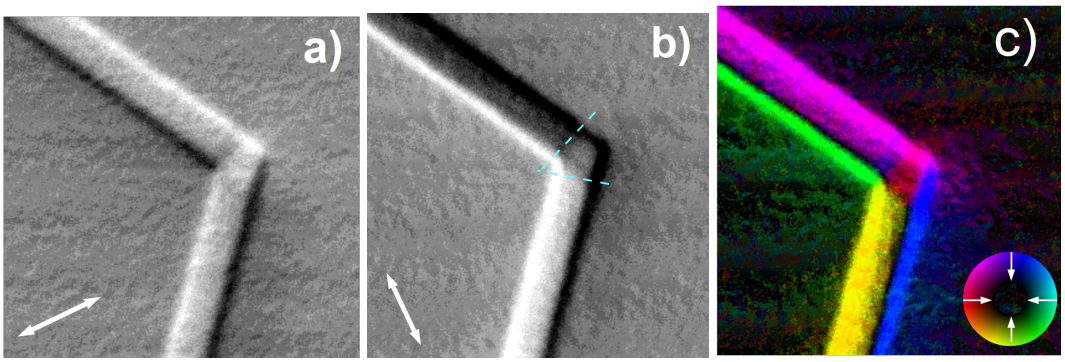

(a) DPC component 1 (b) DPC component 2 (c) Composite color image

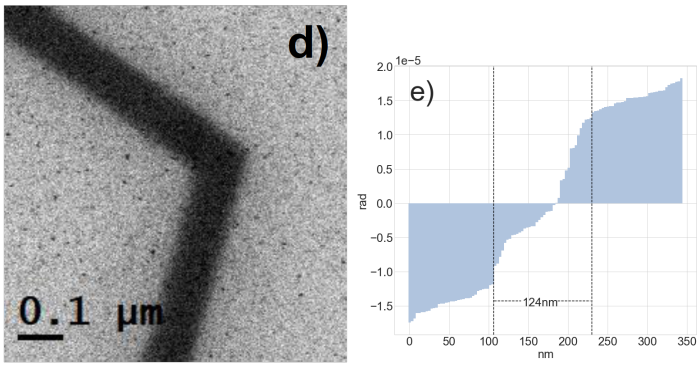

(d) DPC sum image (e) Profile across 5.21b

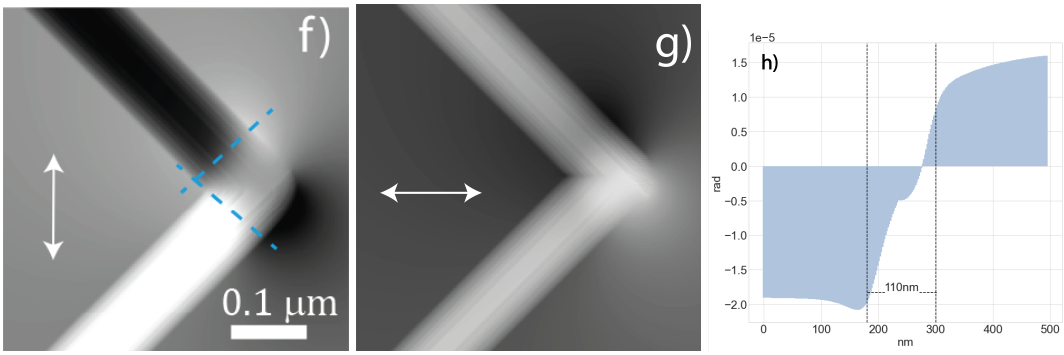

(f) Simulated DPC component 1 (g) Simulated DPC component 2 (h) Profile across5.21f

Figure 5.21: DPC images of a TW nucleated in a 110 nm wide Co nanowire. a) and b) show the two induction components with the white arrows representing the field mapping directions. c) shows a composite image of the a) and b) and is used to clearly visualise the change of magnetisation within the nanowire. d) shows the DPC sum image and e) is line profile measurement across the DW.

Table 5.2: DW types observed in curved Co and Fe nanowires fabricated using FEBID as observed by Fresnel and DPC imaging

	Co		**Fe**	
	Width (nm)	DW type	Width (nm)	DW type
L-shaped nanowire	72 HC	TW	220 N/A	TW
	110 QC	TW	250 N/A	TW
	150 QC	TW		
Z-shaped nanowire	60 HC	TW	180 N/A	TW
	71 HC	TW	200 N/A	TW
	110 QC	TW	251 N/A	TW
	130 QC	TW		
C-shaped nanowire	50 HC	TW	82 QC	AVW
	64 HC	TW	84 QC	VW
	72 HC	VW	90 QC	AVW
	83 QC	VW	103 QC	VW
	90 QC	TDVW	210 N/A	VW
			230 N/A	VW
S-shaped nanowire	60 HC	TDVW		
	120 QC	TW		

A surprising result was the successful nucleation of an AVW in the sub-100 nm wide C-shaped FE nanowire and a TDVW in the 60 nm Co S-shaped nanowire. Both of these DWs have a complex three-dimensional structure and an extent reaching up to three times the width of the nanowire they occupy. Furthermore, the AVW only stabilised in HC nanowires wider than 140 nm than in the simulations and while the TDVW stabilised in HC nanowires as narrow as 70 nm it was the ground state wall in nanowires wider than 110 nms. As the material parameters in the simulation closely match the ones measured in the physical nanowires it is most likely that the nanowire geometry is the main contributing factor to the nucleation of these DWs. In particular, the combination of a curved Gaussian profile and the in-plane curvature of the S and C-shape [23].

In addition to the Fresnel data images observations using DPC were made of a VW, an AVW and a TW in the C and L-shaped nanowires respectively. Measurements of the extent of the different DWs showed that as expected the VW and TW extended to sizes comparable to the width of the nanowires they occupy, while the AVW and TDVW were

significantly larger. Unfortunately, the more compact and desirable chiral walls discussed in Chapter 3, like the 1D wall and the FSW, were not observed. Despite that, the results presented here show that multiple DWs of varying extent and structure can be nucleated in curved Co and Fe nanowires of similar sizes in the sub - 100 nm range. In addition to the characterisation of DWs, a calculation of the saturation induction (B_s) of both the Co and Fe deposits was performed using the DPC data sets. This was achieved via two methods. The first was a more conventional method, using a Co square with minimal thickness variation.For the second method, before the B_s calculation was performed, the electrostatic contribution to the phase was separated and removed from the DPC image. From the saturation induction calculations, a deposit purity of 68 % for the Fe deposits and 73 % for the Co deposits was estimated. It must be noted that while both of these results are within the expected range they were obtained from limited data and even though every care was taken to make the deposition conditions consistent during each session small variations in the deposition environment were unavoidable.

5.8 Discussion

This research presents a unique contribution to the field of magnetic nanowires by exploring a previously unexamined geometry and directly classifying the observed DWs. This is significant because it is believed no prior studies have addressed DWs within this specific geometry. While numerous methods exist for characterizing magnetic and structural properties of nanowires [24], current literature on DWs in magnetic nanowires often lacks direct characterization of the DW type in the size studied in this thesis [25, 26]. [27], for instance, presents TEM images of the magnetic structure of FEBID fabricated nanowires with widths ranging from 70 to 100 nm, without classifying the DW types. Additionally, much of the research that does characterize DW types typically discusses nanowire geometries different from the one presented here. For example, planar nanostrips studied in [28][29] show Fresnel mode imaging of TWs and VWs in arched nanowires, similar to the C-shaped ones studied here. However, the discrepancy lies in the nanowire dimensions and shape, with both studies focusing on nanostrips that are 500-600 nm wide and 10-30 nm thick. Similarly sized L-shaped CoFeSi alloy nanostrips are also studied in [30], where TWs similar to the ones presented in Section 5.6.5 are observed at nanowire widths of 400 nm and thickness of approximately 30 nm. While many studies involving DPC imag-

ing of magnetic materials exist, they often focus on thin films [31] or skyrmions [32][33] rather than on nanowires. Unfortunately the 1DW or FSW described in the Chapter 4 were not successfully nucleated in the FEBID nanowires. This could be due to several factors including the external field application protocol, or even the bent geometry of the experimental structures. A more detailed discussion on this is presented in Chapter 6.

References

[1] S. Da Col, S. Jamet, M. Staňo, B. Trapp, S. Le Denmat, L. Cagnon, J. C. Toussaint, and O. Fruchart. Nucleation, imaging, and motion of magnetic domain walls in cylindrical nanowires. *Applied Physics Letters*, 109(6):062406, 2016.

[2] A. O. Adeyeye and R. L. White. Magnetoresistance behavior of single castellated Ni80Fe20 nanowires. *Journal of Applied Physics*, 95(4):2025–2028, 2004.

[3] B. Borie, A. Kehlberger, J. Wahrhusen, H. Grimm, and M. Kläui. Geometrical dependence of domain-wall propagation and nucleation fields in magnetic-domain-wall sensors. *Phys. Rev. Appl.*, 8:024017, 2017.

[4] J. D. Fowlkes and P. D. Rack. Fundamental electron-precursor-solid interactions derived from time-dependent electron-beam-induced deposition simulations and experiments. *ACS Nano*, 4(3):1619–1629, 2010.

[5] A. Fernández-Pacheco, J. M. De Teresa, R. Córdoba, and M. R. Ibarra. Magnetotransport properties of high-quality cobalt nanowires grown by focused-electron-beam-induced deposition. *Journal of Physics D: Applied Physics*, 42(5):055005, 2009.

[6] J. M. De Teresa and A. Fernández-Pacheco. Present and future applications of magnetic nanostructures grown by FEBID. *Applied Physics A*, 117(4):1645–1658, 2014.

[7] R. Córdoba, N. Sharma, S. Kölling, P. M. Koenraad, and B. Koopmans. High-purity 3D nano-objects grown by focused-electron-beam induced deposition. *Nanotechnology*, 27(35):355301, 2016.

[8] K. Mølhave, D. N. Madsen, A. M. Rasmussen, A. Carlsson, C. C. Appel, M. Brorson, C. J. H. Jacobsen, and P. Bøggild. Solid gold nanostructures fabricated by electron beam deposition. *Nano Letters*, 3(11):1499–1503, 2003.

[9] C. Brownlie, S. McVitie, J. N. Chapman, and C. D. W. Wilkinson. Lorentz microscopy studies of domain wall trap structures. *Journal of Applied Physics*, 100(3): 033902, 2006.

[10] L.A. Rodríguez, C. Magén, E. Snoeck, C. Gatel, L. Marín, L. Serrano-Ramón, J.L. Prieto, M. Muñoz, P.A. Algarabel, L. Morellon, J.M. De Teresa, and M.R. Ibarra.

Quantitative in situ magnetization reversal studies in lorentz microscopy and electron holography. *Ultramicroscopy*, 134:144–154, 2013.

[11] S. McVitie and M. Cushley. Quantitative fresnel lorentz microscopy and the transport of intensity equation. *Ultramicroscopy*, 106(4):423–431, 2006.

[12] M. Krajnak, D. McGrouther, D. Maneuski, V. O' Shea, and S. McVitie. Pixelated detectors and improved efficiency for magnetic imaging in STEM differential phase contrast. *Ultramicroscopy*, 165:42–50, 2016.

[13] Y. Li. *Dynamic magnetism and magnetisation topology in artificial spin ice*. University of Glasgow, 2018.

[14] T. Almeida, D. McGrouther, A. Kovács, R. Dunin-Borkowski, and S. Mcvitie. Effect of annealing on the magnetic states of FEBID-grown cobalt nanopatterns examined by off-axis electron holography. *Journal of Microscopy*, 279(3):217–221, 2020.

[15] J. Crangle and G. M. Goodman. The magnetization of pure iron and nickel. *Proceedings of the Royal Society of London. Series A, Mathematical and Physical Sciences*, 321:477–491, 1971.

[16] R. Córdoba, R. Lavrijsen, A. Fernández-Pacheco, M. R. Ibarra, F. Schoenaker, T. Ellis, B. Barcones-Campo, J. T. Kohlhepp, H. J. M. Swagten, B. Koopmans, J. J. L. Mulders, and J. M. De Teresa. Giant anomalous hall effect in Fe-based microwires grown by focused-electron-beam-induced deposition. *Journal of Physics D: Applied Physics*, 45(3):035001, 2011.

[17] J. M. De Teresa, A. Fernández-Pacheco, R. Córdoba, L. Serrano-Ramón, S. Sangiao, and M. R. Ibarra. Review of magnetic nanostructures grown by focused electron beam induced deposition (FEBID). *Journal of Physics D: Applied Physics*, 49(24): 243003, 2016.

[18] R. Lavrijsen, R. Córdoba, F. J. Schoenaker, T. H. Ellis, B. Barcones, J. T. Kohlhepp, H. J. M. Swagten, B. Koopmans, J. M. De Teresa, C. Magén, M. R. Ibarra, P. Trompenaars, and J. J. L. Mulders. Fe:O:C grown by focused-electron-beam-induced deposition: Magnetic and electric properties. *Nanotechnology*, 22(2):025302, 2010.

[19] J.A. Betancourt-Cantera, F. Sánchez-De Jesús, A. M. Bolarín-Miró, G. Torres-Villaseñor, and L. G. Betancourt-Cantera. Magnetic properties and crystal structure of elemental cobalt powder modified by high-energy ball milling. *Journal of Materials Research and Technology*, 8(5):4995–5003, 2019.

[20] C. Magén, J. Pablo-Navarro, and J. M. De Teresa. Focused-electron-beam engineering of 3D magnetic nanowires. *Nanomaterials*, 11(2):402, 2021.

[21] J. Pablo-Navarro, D. Sanz-Hernández, C. Magén, A. Fernández-Pacheco, and J. M. de Teresa. Tuning shape, composition and magnetization of 3d cobalt nanowires grown by focused electron beam induced deposition (FEBID). *Journal of Physics D: Applied Physics*, 50(18):18LT01, 2017.

[22] I. Purnama, C. S. Murapaka, W. S. Lew, and T. Ono. Remote driving of multiple magnetic domain walls due to topological interaction. *Applied Physics Letters*, 104 (9):092414, 2014.

[23] L. Skoric, C. Donnelly, C. Abert, A. Hierro-Rodriguez, D. Suess, and A. Fernández-Pacheco. Micromagnetic modeling of magnetic domain walls in curved cylindrical nanotubes and nanowires.

[24] H. Mohammed, J. A. Moreno, and J. Kosel. Advanced fabrication and characterization of magnetic nanowires. In Neeraj Panwar, editor, *Magnetism and Magnetic Materials*. Rijeka, 2017.

[25] S. Da Col, S. Jamet, N. Rougemaille, A. Locatelli, T. O. Mentes, B. Santos Burgos, R. Afid, M. Darques, L. Cagnon, J. C. Toussaint, and O. Fruchart. Observation of bloch-point domain walls in cylindrical magnetic nanowires. *Phys. Rev. B*, 89: 180405, 2014.

[26] A. Wartelle, J. Pablo-Navarro, M. Staňo, S. Bochmann, S. Pairis, M. Rioult, C. Thirion, R. Belkhou, J. M. de Teresa, C. Magén, and O. Fruchart. Transmission XMCD-PEEM imaging of an engineered vertical FEBID cobalt nanowire with a domain wall. *Nanotechnology*, 29(4):045704, 2017.

[27] F. Venturi, G. C. Gazzadi, A. H. Tavabi, A. Rota, R. E. Dunin-Borkowski, and S. Frabboni. Magnetic characterization of cobalt nanowires and square nanorings fabricated

by focused electron beam induced deposition. *Beilstein Journal of Nanotechnology*, 9:1040–1049, 2018.

[28] L. A. Rodríguez, C. Magén, E. Snoeck, L. Serrano-Ramón, C. Gatel, R. Córdoba, E. Martínez-Vecino, L. Torres, J. M. De Teresa, and M. R. Ibarra. Optimized cobalt nanowires for domain wall manipulation imaged by in situ Lorentz microscopy. *Applied Physics Letters*, 102(2):022418, 2013.

[29] D. Petit, H.T. Zeng, J. Sampaio, E. Lewis, L. O'Brien, A. Jausovec, D. Read, R. P. Cowburn, K. J. O'Shea, S. McVitie, and J. N. Chapman. Magnetic imaging of the pinning mechanism of asymmetric transverse domain walls in ferromagnetic nanowires. *Applied Physics Letters*, 97(23):233102, 2010.

[30] F. Lofink, A. Philippi-Kobs, M. R. Rahbar Azad, S. Hankemeier, G. Hoffmann, R. Frömter, and H. P. Oepen. Domain walls in bent nanowires. *Phys. Rev. Appl.*, 8:024008, 2017.

[31] T. P. Almeida, R. Temple, and J. Massey. Quantitative TEM imaging of the magnetostructural and phase transitions in ferh thin film systems. *Scientific Reports*, 7: 17835, 2017.

[32] F. Rendell-Bhatti, R. J. Lamb, and J. W. van der Jagt. Spontaneous creation and annihilation dynamics and strain-limited stability of magnetic skyrmions. *Nature Communications*, 11:3536, 2020.

[33] S. Pöllath, T. Lin, N. Lei, W. Zhao, J. Zweck, and C.H. Back. Spin structure relation to phase contrast imaging of isolated magnetic Bloch and Néel skyrmions. *Ultramicroscopy*, 212:112973, 2020.

6 Conclusions and Future Work

This thesis presented a micromagnetic and experimental exploration of the differen domain walls (DWs) that can stabilise in ferromagnetic nanowires with curved profiles in a head-to-head magnetisation configuration. The tools used to achieve this included finite-difference micromagnetic simulation coupled with experimental image generation, FEBID for physical nanowire fabrication and Lorentz microscopy for imaging and quantitative characterisation of the nanowire's magnetic properties. This chapter outlines the main research outcomes of the thesis and proposes opportunities for further research.

The subject of **Chapter 4** was the micromagnetic exploration of the different DWs that can stabilise in cylindrical segment nanowires. The main goal was to explore the parameter space of half and quarter cylinder (QC and HC) nanowires and map the DWs that stabilise, while noting any unique DWs with properties suitable for spintronic applications. To that end half and quarter-cylinder nanowires were simulated with varying thickness, width and material parameters in a head-to-head magnetisation configuration. Various DWs, such as the vortex wall (VW), transverse wall (TW), asymmetric vortex wall (AVW), and transverse/double vortex wall (TDVW), were observed in the cylindrical segment nanowires, exhibiting a structure similar to their planar nanowires counterparts. Furthermore, the impact of varying nanowire shape was investigated by simulating an L-shaped nanowire, a geometry commonly used for facilitating the nucleation of DWs in physical nanowires. This resulted in a smaller number of unique DWs observed with only a TW and VW stabilising across the entire simulation space. The results from all the simulations were used to produce phase diagrams and tables that display the expected DWs across the above-listed parameter space. Additionally, for each individual simulation, the extent of the resulting

DW was measured and plotted. Some of the DWs were found to have extents comparable to nanowire width, namely the VW and TW, while other were found to extend much more - the TDVW and AVW. Possibly the most interesting outcome of the chapter was the nucleation of the flower state wall (FSW) and one dimensional wall (1DW). This is because their chiral nature and compact size are properties sought after in the field of spintronics. The FSW was found to stabilise as a metastable state in both QC and HC nanowires in a wide range of sizes and to have a smaller extent than other DWs in the same nanowire size, save for the 1DW. To further study this unique DW the effect of iDMI was considered on nanowires where it would stabilise. It was observed that iDMI of strength (1×10^{-3} J/m^2), which is comparable to a thin platinum layer, while affecting the total exchange energy of the system showed no effect on the DW types observed in nanowires thicker than 20 nm except for a slight broadening of the vortex cores in the VW and AVW. In thinner QC nanowires (< 20 nm) it did however lead to the stabilisation of the other metastable chiral wall - the 1DW, whose name is derived from its simple, almost one-dimensional profile. Much like the FSW the 1DW was also found to be significantly narrower than other DWs. The rest of the chapter explored the generation of Fresnel mode and DPC images from the magnetisation data obtained from micromagnetic simulations. For the Fresnel mode images, different values of defocus were considered to show the effect of distortion in the imaging and to measure the effect of defocus on nanowire extent. As expected, the measured DW extent was found to be comparable to an extent value obtained from the curl of magnetisation for low defocus values (< 400 µm) and to increase with increasing defocus beyond that. A measure of the extent of the different DWs was also obtained from the simulated DPC images. There the DW extent measured from magnetic induction was found to be on average 10 % larger than the one measured directly from magnetisation. The most likely origin of which is the stray field generated by the DWs. Finally, the effect of mean inner potential and sample thickness (electrostatic contrast) was included in the calculation of the experimental images. This resulted in simulated images, where the contrast is dominated by the electrostatic contribution. More careful examination showed that the defining features of DWs are still discernible in the images and that electrostatic contrast had no significant effect on the DW extent measured from experimental images.

As the parameter space for simulation of cylindrical segment nanowires is quite vast the simulations performed in this chapter can be supplemented in many ways. In order to narrow down the options we can consider further simulations that might lead to a more

consistent stabilisation of the DWs of interest - that is the flower state wall (FSW) and one-dimensional wall (1DW). As mentioned before the parameter that was found to affect these greatly was the presence of iDMI. Therefore a more robust study of the effect of iDMI including a variation of the DMI interaction strength and the thickness of the nanowire could potentially lead to the discovery of nanowires where these walls are the ground-state.[1] and [2] show such studies for thin magnetic films, where larger values of the iDMI parameter contribute to the stability of the chiral DWs under an applied field. Additionally, other effects that contribute to the formation of chiral structures like crystalline anisotropy can be included in the simulation [3][4]. It should be noted that the simulations performed in this chapter were only static and contained no temperature effects. Therefore a natural continuation of the simulation research is to study the effect temperature has on DW formation in the structures presented here. This would make the simulations more comparable to the experimental results. Unfortunately, this is not a parameter that is present in most micromagnetic simulation packages. However, it was shown in [5] that temperature effects can be successfully included in some micromagnetic calculations with good agreement to theory. Finally, once the static simulation parameter space has been sufficiently explored, a dynamical study of the different DWs can be performed in order to determine their mobility under an applied field or a spin-polarised current. Many studies have been conducted on this topic - both for thin films and nanowires. In particular [6] and [7] demonstrate DW propagation speeds larger than 600 m/s and 300 m/s respectively for simulations of cylindrical nanowires.

Chapter 5 presented an empirical study of the DWs in curved nanowires. The first step in that was the fabrication of Co and Fe ferromagnetic nanowires and squares using FEBID. The deposition was a challenging and time-consuming process which involved the search for the best possible deposition parameters that result in defined nanowires with high content of magnetic material (Co or Fe). The resulting final nanowire deposits had maximum thicknesses varying between 20-35 nm and widths varying between 50 nm and 200 nm. They had curved Gaussian-like profiles and depending on the thickness-to-width ratio of the particular nanowire resembled either the half or quarter-cylinder nanowires that were studied using the simulations. The nanowires were then characterised in a TEM, where an external magnetic field was used to nucleate DWs, which were subsequently imaged using Fresnel and DPC mode Lorentz microscopy. With the help of micromagnetic simulations, several different DW types were identified in the physical nanowires. These include the

TW in both the L and C-shaped nanowires, and the AVW, VW and DVW in C and S-shaped nanowires. Where possible also their extent was measured. This was mostly done for the DPC images, because large the defocus used during Fresnel imaging (1 - 5 mm) caused significant "stretching" of the magnetic contrast. A combination of DPC, BF imaging and AFM was used to obtain a measure of the material purity of the nanowires- ~ 70 % for the Co and ~ 68 % for the Fe nanowires. To achieve this electrostatic contributions were subtracted from DPC images resulting in accurate induction maps. Unfortunately, the most interesting DWs, namely the FSW and 1DW, were not observed during the magnetic imaging. However, because of the presence of many different DWs in the nanowires, it may be possible to find a nanowire that supports them by carefully varying the geometry and material parameters.

A shortcoming of the research described in **Chapter 5** is the lack of a direct measurement of the chemical composition of the nanowires. Other recent studies of FEBID structures utilise energy dispersive x-ray mapping (EDX) [8] for that purpose. EDX was attempted on the structures described here inside the SEM after fabrication, however, the prolonged exposure to the low kV e-beam resulted in significant carbon contamination [9] which could not be distinguished from the already present carbon in the deposits. For this reason no EDX results were presented. Another option that could have provided the desired chemical map is STEM-EELS. Performing this technique was part of the original research plans as it is a great tool that can provide information both on the magnetic material content and on the thickness of the nanowires.[10] [11]. Unfortunately due to a combination of extremely limited laboratory access due to COVID and instrument downtime, it was not possible to perform it. Similar difficulties were encountered when performing AFM, which is the reason why not all the nanowires studied have direct thickness measurements. Additionally, while the section describing Fresnel imaging mentions electrostatic contrast, it does not provide a way to correct for it. This can be done by employing the same method described in the DPC section, which required the acquisition of multiple Fresnel images of the same nanowire. This was not performed as in the early stages of the project Fresnel imaging was intended to be a means for DW nucleation, quick initial DW identification and for preparation for DPC imaging.

Since the most interesting DWs were not successfully imaged steps could be undertaken to increase the chances of nucleating them. Firstly an alternative deposition method can be employed to fabricate nanowires in which the 1DW and FSW are more likely to sta-

bilise. Better control of the deposition resulting in narrower nanowires and more control of the nanowire shape can be achieved by using bespoke stream files for each structure as described in [12]. Another method for better control of nanowire structure and dimensions can be to include annealing. This step has been shown to reduce the content of carbon contamination in FEBID nanoparticles by 50 % in [13]. Including an annealing step in the deposition process would allow for the use of lower beam current and voltage, which would increase the achievable resolution of the structures and therefore give greater control over the final deposit. Typically, this would result in low-purity deposits, but the inclusion of annealing can effectively address this issue. Alternatively, different fabrication techniques could be explored. An example of one is two-photon lithography which allows for the fabrication of custom 3D magnetic structures [14][15]. It must be noted that the structures described in these papers are significantly larger than the ones deposited using FEBID, but optimisation of the technique can lead to deposition in the required sizes. Finally, since iDMI was found to affect the DWs stabilised in the nanowire simulations its effect can also be explored in the physical nanowires. [16] presents the results of several different studies that report DMI strength of 0.2-2.3 $\mathrm{mJ/m^2}$ in thin Co films with surface and capping layers of either Pt, Ir or Ta. To achieve this however, the thickness of the non-magnetic layer was often on the same scale as that of the magnetic layer and for the higher end of the range up to 5 times larger. It is also unclear how these values would translate to the FEBID deposited structures. An extensive experimental study coupled with further micromagnetic simulations would be required to fully explore this topic.

References

[1] Z. Sun, P. Fang, X. Shi, X. S. Wang, and F. Li. Field-driven side-by-side magnetic domain wall dynamics in ferromagnetic nanostrips. *Physical Review B*, 106(1):014412, 2022.

[2] S. K. Karna, M. Marshall, W. Xie, L. DeBeer-Schmitt, D. P. Young, I. Vekhter, W. A. Shelton, A. Kovács, M. Charilaou, and J. F. DiTusa. Annihilation and control of chiral domain walls with magnetic fields. *Nano Letters*, 21(3):1205–1212, 2021.

[3] L. G. Vivas, M. Vazquez, J. Escrig, S. Allende, D. Altbir, D. C. Leitao, and J. P. Araujo. Magnetic anisotropy in CoNi nanowire arrays: Analytical calculations and experiments. *Physical Review B*, 85(3):035439, 2012.

[4] T. Koyama, G. Yamada, H. Tanigawa, S. Kasai, N. Ohshima, S. Fukami, N. Ishiwata, Y. Nakatani, and T. Ono. Control of domain wall position by electrical current in structured Co/Ni wire with perpendicular magnetic anisotropy. *Applied Physics Express*, 1:101303, 2008.

[5] M. B. Hahn. Temperature in micromagnetism: cell size and scaling effects of the stochastic Landau–Lifshitz equation. *Journal of Physics Communications*, 3(7): 075009, 2019.

[6] M. Schöbitz, A. De Riz, S. Martin, S. Bochmann, C. Thirion, J. Vogel, M. Foerster, L. Aballe, T. O. Menteş, A. Locatelli, F. Genuzio, S. Le-Denmat, L. Cagnon, J. C. Toussaint, D. Gusakova, J. Bachmann, and O. Fruchart. 123(21):249901, 2019.

[7] J. A. Fernandez-Roldan and O. Chubykalo-Fesenko. Dynamics of chiral domain walls under applied current in cylindrical magnetic nanowires. *APL Materials*, 10 (11):111101, 2022.

[8] J. I. Goldstein, D. E. Newbury, J. R. Michael, N. W. M. Ritchie, J. H. J. Scott, and D. C. Joy. *Scanning Electron Microscopy and X-Ray Microanalysis*. Springer New York, 2018.

[9] M. Hugenschmidt, K. Adrion, A. Marx, E. Müller, and D. Gerthsen. Electron-beam-induced carbon contamination in STEM-in-SEM: Quantification and mitigation. *Microscopy and Microanalysis*, 29(1):219–234, 2022.

[10] J. Pablo-Navarro, C. Magén, and J. M. de Teresa. Three-dimensional core–shell ferromagnetic nanowires grown by focused electron beam induced deposition. *Nanotechnology*, 27(28):285302, 2016.

[11] C. Sanz-Martín, C. Magén, and J.M Teresa. High volume-per-dose and low resistivity of cobalt nanowires grown by Ga+ focused ion beam induced deposition. *Nanomaterials*, 9(12):1715, 2019.

[12] L. Skoric, D. Sanz-Hernández, F. Meng, C. Donnelly, S. Merino-Aceituno, and A. Fernández-Pacheco. Layer-by-layer growth of complex-shaped three-dimensional nanostructures with focused electron beams. *Nano Letters*, 20(1):184–191, 2019.

[13] T. Almeida, D. McGrouther, A. Kovács, R. Duni-Borkowski, and S. McVitie. Effect of annealing on the magnetic states of FEBID-grown cobalt nanopatterns examined by off-axis electron holography. *Journal of Microscopy*, 279(3):217–221, 2020.

[14] G. Williams, M. Hunt, B. Boehm, A. May, M. Taverne, D. Ho, S. Giblin, D. Read, J. Rarity, R. Allenspach, and S. Ladak. Two-photon lithography for 3D magnetic nanostructure fabrication. *Nano Research*, 11(2):845–854, 2017.

[15] J. Askey, M. O. Hunt, W. Langbein, and S. Ladak. Use of two-photon lithography with a negative resist and processing to realise cylindrical magnetic nanowires. *Nanomaterials*, 10(3):429, 2020.

[16] M. Kuepferling, A. Casiraghi, G. Soares, G. Durin, F. Garcia-Sanchez, L. Chen, C. H. Back, C. H. Marrows, S. Tacchi, and G. Carlotti. Measuring interfacial Dzyaloshinskii-Moriya interaction in ultrathin magnetic films. *Reviews of Modern Physics*, 95(1), 2023.

A Appendix

A.1 Micromagnetic simulation initialisation

The code in Figure A.1 shows an example of how a simulation for a QC straight nanowire is initialized. The geometry is achieved by manipulating Cylinder and Cuboid basic shapes available directly in the MuMax3 interface. The cylindrical segment geometry (QC in the example presented) is achieved by a Boolean subtraction operation between a cylinder and a cuboid structure. The starting state is head-to-head with transverse magnetization (in the y-direction) in the domain wall region. The size of the domains and domain walls is defined by the `defregion()` and `m.setregion()` functions.

A similar method is used to generate the L-shape geometry. Code is shown in Figure A.2. The geometry initialisation is done by placing two straight nanowires at a right angle with each other and filling the gap with a section of a sphere. Translation operations are applied to to keep the structures aligned. The domains and domain walls are generated by the same functions as in A.1.

```
setGridSize(1000, 50, 50)
setCellSize(2e-9, 2e-9, 2e-9)
```
Simulation cell number and size

```
a := cylinder(80e-9, 2000e-9)
b := rect(80e-9, 80e-9).transl(20e-9, 0, 0)
c := a.sub(b)
setgeom(c.roty(90 * pi / 180))
```
Generate Geometry

```
saveas(geom, "logicSub")
```

```
Msat = 860e3
Aex = 13e-12
alpha = 0.5
```
Set material parameters

```
defregion(1, xrange(-inf, -10e-9))
defregion(2, xrange(10e-9, inf))
defregion(3, xrange(-10e-9, 10e-9))
m.setregion(1, uniform(1, 0, 0))
m.setregion(2, uniform(-1, 0, 0))
m.setregion(3, uniform(0, 1, 0))
```
Define head-to-head magnetisation

```
save(regions)
```

```
OutputFormat = OVF1_TEXT
save(m)
relax()
save(m)
tableadd(Edens_total)
tableadd(Edens_exch)
tableadd(Edens_demag)
tablesave()
```
Define simulation solver and desired output

Figure A.1: Simulation of a QC straight nanowire with the different sections highlighted

```
setGridSize(450, 450, 30)
setCellSize(2e-9, 2e-9, 2e-9)
```
Simulation cell number and size

```
a := cylinder(100e-9, 800e-9).transl(-390e-9, 0, 0)
b := cylinder(100e-9, 800e-9).roty((90*pi)/180).transl(0, 0, 390e-9)
c := rect(900e-9, 100e-9).transl(0, -50e-9, 0)
g := a.add(b)
h := g.sub(c)
r := cuboid(100e-9, 100e-9, 100e-9).transl(50e-9, 0, 0)
r2 := cuboid(100e-9, 100e-9, 100e-9).transl(0, 0, -50e-9)
e := ellipsoid(100e-9, 100e-9, 100e-9).sub(c)
hs := e.sub(r).sub(r2).transl(-390e-9, 0, 390e-9)
geome := h.add(hs).transl(0, -30e-9, 0)
```
Generate L-shape Geometry

```
setgeom(geome.rotx(90 * pi / 180))
saveas(geom, "weird")
defregion(1, xrange(-inf, -300e-9))
defregion(2, cylinder(120e-9, 800e-9).transl(-390e-9, 0, 0).rotx(90*pi/180).transl(0, 50e-9, 0))
defregion(3, cylinder(120e-9, 800e-9).roty((90*pi)/180).transl(0, 0, 390e-9).rotx(90*pi/180).transl(50e-9, 0, 0))
m.setregion(1, uniform(0, 0, 1))
m.setregion(2, uniform(0, -1, 0))
m.setregion(3, uniform(-1, 0, 0))
```
Define head-to-head magnetisation in L-shape

```
OutputFormat = OVF2_TEXT
Msat = 860e3
Aex = 13e-12
EdgeSmooth = 8
alpha = 0.5
```
Set material parameters

```
saveas(m, "starting_state_permalloy_HtH_50nm")
relax()
saveas(m, "relaxed_state_permalloy_HtH50nm")
tableadd(Edens_total)
tableadd(Edens_exch)
tableadd(Edens_demag)
tablesave()
saveas(B_eff, "relaxed_state_permalloy_HTH_B_eff_50nm")
saveas(B_demag, "relaxed_state_permalloy_HTH_B_demag_50nm")
snapshot(B_eff)
OutputFormat = OVF2_TEXT
```
Define simulation solver and desired output

Figure A.2: Simulation of a HC L-shaped nanowire with the different sections highlighted.

A.2 Generating thickness and amplidude images

Figure A.3 shows Python code for generating the thickness and amplitude functions used to calculate Lorentz microscopy images in Chapter 4. The function takes several parameters as input, including the simulation output file containing the normalized magnetization, the dimensions and cell size of the simulation, the mean inner potential of the material, and the desired electron beam transmission (for the amplitude function). The function also provides options to rotate the images and add padding (empty space around the simulation geometry) to ease visualization. To check the results, the function offers an option to plot the resulting images. Comments in the code show what functions the different segments perform.

```python
@author: Hristo
"""

#Function to Generate Amplitude Image, Thickness image and EC phase image from mx,my,mz components from a mumax3 simulation.
#it allows for padding and rotation of the images, transm_param is a floating point defining the percentage of the transmited
#beam in the amplitude image calculation, V is the mean inner potential.
def EC_AmpImage(data,x,y,z, pad_w,transm_param,V, rotate,degrees,plot):
    from collections import namedtuple

    asd=[]#empty variable to fill during for loop
    #data is you simulation output that is already loaded into python in .csv or .txt form the next lines extract
    #the three components of magnetisation
    datax = data[:,0]
    datay = data[:,1]
    dataz = data[:,2]
    lambda_e=2.5e-12
    #x,y,z are the number of celss in each direction
    b=x*y*z
    #Code generating thickness function t(x,y)
    for i in range(0,b):
        profile = np.sqrt((datax[i]**2)+(datay[i]**2)+(dataz[i]**2))
        asd.append(profile) #loop creates a 1D dataset with value 1 for every point in the simulation that has magnetisation.

    profile2 = np.reshape(asd,(z,x*y))#reshape 1D dataset so that the thickness in z is separate from the x-y dimensions
    summedprofile=np.sum(profile2, 0) #Sum along z-direction
    rsp=np.reshape(summedprofile, (x,y))#Final reshape to get 2D  map of the simulation (not yet normalised for thickness)
    pad_wi = int(pad_w/2) #Define pad width
    txy=rsp*2e-9 #Multiply by cell size
    txy_pad=np.pad(txy, pad_wi, mode='constant', constant_values=0) #pad thicness image with zeros


    #Generate amplitude image
    ones = np.ones((x+pad_w,y+pad_w)) #Generate an image of ones based on the size of x,y dimension and the pad width
    rsp2=np.pad(rsp, pad_wi, mode='constant', constant_values=0)# Pad image with zeros
    tranms_port= transm_param/np.maximum(rsp)
    rsp_coeff= rsp2*tranms_port
    amp_image  = ones - rsp_coeff # Gives the amplitude imag


    #Calculate E_phase
    E_phase = ((np.pi*V))*(txy_pad)/(lambda_e*(200000))
    if rotate: # Rotate images if specified
        amp_image_r = sp.ndimage.rotate(amp_image, angle=degrees, axes=(-2, -1), reshape=False, order=1, mode='constant', cval=1.0, prefilter=True)
        txy_r = sp.ndimage.rotate(txy_pad, angle=degrees, axes=(-2, -1), reshape=False, order=1, mode='constant', cval=0.0, prefilter=True)
        E_phase_r = sp.ndimage.rotate(E_phase, angle=degrees, axes=(-2, -1), reshape=False, order=1, mode='constant', cval=0.0, prefilter=True)

    if plot: #Plot images if specified
        plt.matshow(amp_image_r)
        plt.matshow(txy_r)
        plt.matshow(E_phase_r)

    ImageResults = namedtuple('ImageResults',['E_phase','Amplitude_image','txy'])
    ec=ImageResults(E_phase_r, amp_image_r,txy_r)
    return ec
```

Figure A.3: Python code used to generate thickness function, amplitude function and electrostatic phase image for a given simulation.